PhD THESIS

Quantum Spin Liquids in SU(N) Heisenberg Models: Variational Monte Carlo Study of Dynamical Correlations

Dániel Vörös

Supervisor: Karlo Penc
HUN-REN Wigner Research Centre for Physics

Budapest University of Technology and Economics

2025.

Acknowledgements

I thank my supervisor, Karlo Penc, for his guidance, patience, invested time, and hard work during the years of my PhD studies.

I appreciate the financial support of the Budapest University of Technology and Economics and the HUN-REN Wigner Research Centre for Physics.

Finally, I would like to thank my parents and my brother for tolerating and supporting me through the years.

Publications related to the thesis

I. D. Vörös and K. Penc, *Dynamical structure factor of the SU(3) Heisenberg chain: Variational Monte Carlo approach* Physical Review B **104** 184426/1-19 (2021).

II. D. Vörös and K. Penc, *Dynamical structure factor of the SU(4) algebraic spin liquid on the honeycomb lattice* Physical Review B **108** 214407/1-10 (2023).

III. D. Vörös, P. Kránitz and K. Penc, The algebraic spin liquid in the SU(6) Heisenberg model on the kagome lattice, Physical Review B **110** 144437/1-29 (2024)

Publication not related to the thesis

IV. M. Kormos, D. Vörös, and G. Zaránd, *Finite-temperature dynamics in gapped one-dimensional models in the sine-Gordon family* Physical Review B **106** 205151/1-16 (2022).

Contents

Motivations

The traditional description of phase transitions, developed by Landau, relies on the concept of symmetry breaking. Each distinct phase is associated with a particular symmetry group, and a phase transition is accompanied by a symmetry breaking, in which the symmetry group of one phase is the subset of the symmetry group of the other phase. In this way, concepts like order parameters—quantities that vanish above the critical temperature but acquire a finite value below it—emerged as the universal hallmark of both classical and quantum phase transitions. In Landau's theory, all classical and quantum phase transitions arise from a form of symmetry breaking.

This well-established paradigm was challenged with the discovery of the fractional Quantum Hall effect [1], where multiple distinct phases share the same conventional symmetries. Realizing that such states of matter could not be understood within the symmetry-breaking framework, physicists began searching for "hidden" quantum orders that could distinguish these phases.

Quantum spin liquids (QSLs) represent a typical setting for these novel ideas in Mott insulators. A QSL is the ground state of a quantum spin system that remains fully symmetric—concerning the symmetries of the underlying lattice and of the Hamiltonian. Consequently, QSLs exhibit no conventional magnetic order of any kind (e.g. ferromagnetic or antiferromagnetic). While magnetically ordered ground states usually have bosonic excitations, like the spin-1 magnon, QSLs have fractionalized fermionic excitations, as the spin-1/2 spinons. The splitting of the bosonic excitation to a pair of fermionic quasiparticles is called fractionalization. Therefore, the existence of the QSL ground state and the fractionalized excitations is directly measurable through the dynamical spin structure factor, if at the lowest excitation energies we observe a continuum (implicating a pair of quasiparticles) instead of a single branch.

A promising approach to characterizing hidden quantum orders at the mean-field level involves the concept of the projective symmetry group (PSG). When the fluctuations beyond mean-field theory are weak, the mean-field quantum order (protected by the PSG) becomes the quantum order of the real ground state [2, Sec. 9.9.1]. If the mean-field one-particle energy spectrum is gapped, the quantum order is called topological order, and is characterized by the ground state degeneracy [2, Sec. 8.] [3]. If the one-particle energy spectrum is gapless, then the quantum order is characterized by the existence and location (in reciprocal space) of gapless excitation towers in the dynamical spin structure factor [2, Sec. 9.10.2]. Analogous to symmetry breaking protecting gapless excitations following Goldstone's theorem [4, Sec. 6.1], certain PSGs can protect gapless fermionic excitations and their reciprocal-space locations [2, Sec. 9.10.2]. Experimentally, the dynamical spin structure factor provides a tool to identify a gapless quantum spin liquid ground state [2, Sec. 9]. Quantum phase transitions can occur without conventional symmetry breaking, driven instead by changes in the PSG itself.

One-dimensional spin systems are archetypal examples of quantum spin liquids, where strong quantum fluctuations suppress all forms of magnetic order. In contrast, stabilizing a quantum spin liquid in two-dimensional systems is far more challenging and often requires enhanced fluctuations. Such enhancements can be achieved by geometric frustration (e.g., on the triangular or kagome lattice) or by introducing further-neighbor interactions. Another route is to enlarge the spin symmetry group, considering SU(N) or Sp(N) models with $N > 2$ [5], which increases quantum fluctuations and thereby helps to stabilize quantum spin liquids.

In this thesis, we seek new avenues to stabilize and characterize two-dimensional quantum spin liquids by considering models with higher symmetries. We implement a variational method to characterize excitations in one and two-dimensional SU(3), SU(4), and SU(6) symmetric Heisenberg models. We will calculate the experimentally relevant dynamical spin structure factor to facilitate their potential identification. We also show that the SU(6) symmetric Heisenberg model on the kagome lattice is a likely candidate for a gapless Dirac spin liquid.

Thesis statements

1. I computed the dynamical spin structure factor $S(k,\omega)$ of the SU(3) Heisenberg chain variationally using Gutzwiller projected particle-hole excitations of the Fermi sea. I showed that the low energy spectrum and the distribution of the spectral weights of the SU(3) Heisenberg chain can be well reproduced by this method, by comparing the $S(k,\omega)$ to exact diagonalization results for 18 sites, the two-soliton continuum of the Bethe Ansatz, and the DMRG results for 72 sites. Detailed analysis of the finite-size effects shows that the method captures the critical Wess-Zumino-Witten $SU(3)_1$ behavior and reproduces the correct exponent, except for the size dependence of the spectral weight in the bottom of the conformal tower. The extracted velocity of excitations and the central charge are very close to the exact results. These results are published in Ref. [I.].

2. I computed the dynamical spin structure factor $S(k,\omega)$ of the SU(4) Heisenberg model on the honeycomb lattice variationally, approximating the ground state by the Gutziller projected π-flux Fermi sea (motivated by Ref. [6]), called a Dirac spin liquid. I compared these results with non-interacting mean-field calculations. The two approaches produce qualitatively similar results, suggesting that the energy spectrum of the Gutzwiller projected excitations may also be a gapless continuum of fractionalized excitations. Quantitatively, the Gutzwiller projection shifts the spectral weight from higher to lower energies, thus emphasizing the lower edge of the continuum. The ratio of the sums $\left(\sum_{\mathbf{k}\in\mathrm{eBZ}} S^{33}_{\mathrm{MF}}(\mathbf{k})\right) / \left(\sum_{\mathbf{k}\in\mathrm{eBZ}} S^{33}(\mathbf{k})\right) = 1 - 1/N$ shows that the correlations are reduced in the mean-field case, since the charge fluctuations reduce the value of the quadratic Casimir operator, appearing in the sum rules. These results are published in Ref. [II.].

3. I proposed the Gutzwiller projected π-flux Fermi sea (another Dirac spin liquid) as the ground state of the SU(6) Heisenberg model on the Kagome lattice. To reach this conclusion, I investigated the energetical stability of the Dirac spin liquid (DSL) against perturbations of the mean-field ansatz and confirmed that the DSL remained the lowest energy singlet state. Furthermore, I found that finite values of the second-neighbor (J_2) and ring (K) exchange are necessary to destabilize the DSL, highlighting its resilience to further interactions. These results are published in Ref. [III.].

4. To characterize the DSL on the SU(6) kagome lattice, I calculated the dynamical spin structure factor $S(\mathbf{k},\omega)$ variationally using Gutzwiller projected particle-hole excitations of the π-flux Fermi sea, and compared these results with the non-interacting mean-field calculations. In the SU(6) case, the distribution of the spectral weights in the $S(\mathbf{k},\omega)$ shows a much better agreement between the variational and the mean-field calculations than in the SU(4) or SU(2) cases. I attribute the decreasing difference between the two approaches to the weakening of the fluctuations beyond the mean-field approximation as the SU(N) symmetry increases. Based on this similarity, I have studied the $S(\mathbf{k},\omega)$ in the mean-field approach for an extensive system with 3888 sites and found that the spectrum is a gapless continuum, where the gapless towers are centered at the Γ, Γ', M and M$'$ points in the extended Brillouin zone. The static spin structure factor $S(\mathbf{k})$ shows increased spectral weights in the form of triangular-shaped plateaus around the K$'$ points in the extended Brillouin zone. The static mean-field and the variational results differ in the sum rules and in the form of barely noticeable humps appearing in the variational calculations around the M$'$ points. The real space spin-spin correlations seem to decay algebraically with the distance, with a power between 3 and 4, similarly as in the SU(4) case (see Ref. [6]). These results are published in Ref. [III.].

Chapter 1

Models and their experimental realizations

1.1 SU(N) Hubbard model

1.1.1 SU(2) Hubbard model

In metals and band insulators the interaction between the electrons is negligible, so their energy spectra consist of bands. In both cases, the conduction electrons (if there are any) are completely delocalized in the material, so their wave functions are Bloch states. If the Fermi energy is inside a band, the material behaves as a metal, while if it is between two bands, the material is an insulator (since the conduction band is empty at $T = 0$). However, in certain materials, such as V_2O_3, Ti_2O_3, Sr_2IrO_4, $(BEDT\text{-}TTF)_2X$, the Fermi energy should be inside a band, yet they are strongly insulating. In these materials, called Mott insulators, the Coulomb repulsion between the electrons is strong enough to make them localized, destroying the metallic behavior. The Hubbard model (introduced in Refs. [7, 8, 9])) is the simplest many-body Hamiltonian describing these materials, encompassing two opposing tendencies:

1. the kinetic energy term (parametrized by the hopping amplitude t) tends to delocalize the electrons into Bloch states, causing a metallic behavior

2. the on-site repulsion term (approximating the Coulomb repulsion) with coupling $U \geq 0$ tends to localize the electrons to the lattice sites, leading to a Mott insulator.

Thus, increasing the on-site repulsion from $U = 0$, at some critical ratio U/t the ground state of the Hubbard model changes from a metallic state to a Mott insulator [4, Sec. 4]. This quantum phase transition is called the Mott transition. In the Hubbard model the screened Coulomb interaction between the electrons is simplified to the shortest possible range, on-site repulsion.

The SU(2) symmetric single-orbital Fermi Hubbard model is defined by the Hamiltonian

$$\mathcal{H}_{\text{Hub}}^{SU(2)} = -t \sum_{\langle i,j \rangle} \sum_{\sigma \in \{\uparrow,\downarrow\}} (c_{i,\sigma}^\dagger c_{j,\sigma} + \text{H.c.}) + U \sum_i n_{i,\uparrow} n_{i,\downarrow} + \sum_i \sum_{\sigma \in \{\uparrow,\downarrow\}} \varepsilon_i n_{i,\sigma}, \tag{1.1}$$

where $c_{i,\sigma}^\dagger$ creates a fermion with spin $\sigma \in \{\uparrow, \downarrow\}$ in the Wanier state localized at site i, $n_{i,\sigma} = c_{i,\sigma}^\dagger c_{i,\sigma}$ is the fermion number operator (with eigenvalues 0, 1), and ε_i is the external field at site i. Due to the Pauli exclusion principle, the occupation of a site (the eigenvalue of the total number operator $n_i = \sum_{\sigma \in \{\uparrow,\downarrow\}} c_{i,\sigma}^\dagger c_{i,\sigma}$) can be at most two.

1.1.2 Generalization to SU(N)

The SU(N) generalization allows for N different "spins" $\sigma \in \{1, \ldots, N\}$ of the particles $c_{i,\sigma}^\dagger |0\rangle$ ($|0\rangle$ being the vacuum), which will be called flavors. The SU(N) single-orbital Fermi-Hubbard model is defined by the Hamiltonian

$$\mathcal{H}_{\text{Hub}} = -t \sum_{\langle i,j \rangle, \sigma} (c_{i,\sigma}^\dagger c_{j,\sigma} + \text{H.c.}) + U \sum_{i, \sigma' > \sigma} n_{i,\sigma} n_{i,\sigma'} + \sum_{i,\sigma} \varepsilon_i n_{i,\sigma}, \tag{1.2}$$

which mainly differs from the SU(2) case in the interaction term, since here a site can be occupied at most by N particles. The fermion number operator $n_{i,\sigma} = c^\dagger_{i,\sigma} c_{i,\sigma}$ still has only two eigenvalues 0,1, but the eigenvalues of the total number operator $n_i = \sum_{\sigma=1}^{N} c^\dagger_{i,\sigma} c_{i,\sigma}$ can go from 0 to N.

The Hubbard Hamiltonian $\mathcal{H}_{\text{Hub}}$ has SU(N) spin rotation symmetry (see Appendix A.2), because permuting the flavors among each other does not change the Hamiltonian. The SU(N) spin rotation symmetry can be broken by introducing flavor-dependent hoppings t_σ or flavor-dependent on-site interactions $U_{\sigma,\sigma'}$.

In the large $U/t \to \infty$ limit, the leading order perturbation theory of the half-filled (one fermion per site on average) repulsive SU(2) symmetric Hubbard model gives rise to the antiferromagnetic SU(2) symmetric Heisenberg model in the spin 1/2 irreducible representation (see section 1.4.1. Similarly, in the large $U/t \to \infty$ limit, the leading order perturbation theory in t/U of the SU(N) Hubbard model with $m/N < 1$ filling (m fermions per site on average, where m is an integer) results in the SU(N) symmetric antiferromagnetic Heisenberg model. The m/N fractional filling of the Hubbard model determines the irreducible representation of the Heisenberg model on every site (see section 1.4.2, and appendix A.6).

The SU(N) symmetrical Hubbard model can describe fermionic cold atoms in optical lattices.

1.1.3 Experimental realization with optical lattices

Two counterpropagating interfering laser beams can create a standing wave, and more interfering laser beams can create a standing wave of almost any desired spatial periodicity. Such standing waves can trap neutral atoms, since the oscillating electric field of the lasers creates dipole momenta in the atoms, which interact with the electric field. In time average, the atoms are attracted either toward the high-intensity (antinode) or low-intensity (node) regions of the standing wave, depending on the applied frequency and the energy levels of the atoms. Thus, the neutral atoms feel a time-independent periodic potential that follows the spatial pattern of the laser field intensity, called an optical lattice [10, Sec. 3.1], where the atoms are localized in the potential wells, separated with potential barriers. Adjusting the frequency, polarization, and angle of the counterpropagating lasers, one can create almost any lattice geometry. A three-dimensional cubic optical lattice can be created by three pairs of counterpropagating laser beams in pairwise orthogonal directions, forming three orthogonal standing waves with orthogonal polarizations.

The atoms can tunnel through the potential barriers, corresponding to the hoppings t in Eq. (1.2). The repulsion between the atoms inside the same potential well corresponds to the on-site repulsion U. Both U and t depend on the intensity of the laser beams. Increasing the intensity we increase the potential barriers, therefore we simultaneously decrease t and increase U [11, 12, 13, 14]. The ε_i describes an additional external potential, which describes the energy offset of each lattice site [11].

If the intensity of the laser beams is the same in every direction, then the hoppings are equal in all directions. However, increasing the intensity of the pair of laser beams in one direction decreases the hopping along this direction, so for large enough intensity, we get almost decoupled two-dimensional layers [10, 11], simulating the two-dimensional Hubbard model on the square lattice.

Optical lattices of ultracold alkaline earth metal atoms, achieve near-perfect SU($N = 2I+1$) symmetry originating from the nuclear degrees of freedom. [15]. Here, I represents the nuclear spin, and N can be as high as 10, as demonstrated with ^{87}Sr isotopes exhibiting SU(10) symmetry [16, 17]. SU(6) symmetry can be realized by ^{173}Yb isotopes with $I = 5/2$ [18, 19, 20, 21, 22, 23, 24, 25, 26, 27]. SU(4) symmetry can be realized by atoms with $I = 3/2$ [28, 29]. Furthermore, it is possible to create a Mott insulator using ^{173}Yb isotopes [21], described by the physics of the SU(6) Heisenberg model.

A remaining issue is the temperature range achieved in experiments, which might be too high to compare the measurements with zero temperature calculations.

1.2 Orbital degeneracy, and the Kugel Khomskii model

The Hubbard model can be extended to allow for multiple orbitals at a given lattice site, giving an extra orbital index α to the fermionic operators $c^{\dagger}_{j,\alpha,\sigma}$. In this case, the hopping amplitudes acquire a dependence on the orbital indices as $t_{\alpha,\alpha'}$, and the Coulomb repulsion can also be different depending on whether two electrons occupy the same orbital (with antiparallel spins), or are placed on different orbitals (see [4, Sec. 5.4] and Refs. [30, 31, 32]). In the strong repulsion limit with one electron per site, the low energy effective theory will incorporate exchanges not only between the same orbitals on nearest neighbors, but also between different orbitals. In the case of two-fold orbital degeneracy, the low energy effective Hamiltonian can be reformulated in terms of the Pauli matrices τ^x, τ^y, and τ^z acting on the orbital degrees of freedom. Thus, the two orbitals $|1\rangle$ and $|2\rangle$ (called pseudospins) are the eigenstates of the τ^z operator with eigenvalues ± 1. An example of such a low energy Hamiltonian is

$$H_{\mathrm{KK}} = \sum_{\langle i,j \rangle} (u + \mathbf{S}_i \cdot \mathbf{S}_j) \times \left(v + \alpha[\tau_i^+ \tau_j^- + \tau_i^- \tau_j^+] + J'_z \tau_i^z \tau_j^z \right), \tag{1.3}$$

where the coefficients u, v, α, and J'_z are given in Refs. [31, 32]. The spin part is isotropic due to the SU(2) spin-rotational symmetry of the underlying two-orbital Hubbard model, but the orbital part is usually anisotropic because it depends on the relative orientation of the orbital wavefunctions on nearest neighbor sites. Bilinear terms of $\mathbf{S}$ and $\boldsymbol{\tau}$ like $S^x\tau^x$, $S^y\tau^y$, and $S^z\tau^z$ are absent in the low energy theory, due to the absence of the spin-orbit interactions in the underlying two-orbital Hubbard model. Since these models were first studied by Kugel and Khomskii in Ref. [30], these low-energy models are called Kugel Khomskii models.

For the special values of $\alpha = J'_z/2$, the orbital part also becomes SU(2) pseudo spin rotational symmetric. Furthermore, for the fine tuned parameters $u = v = 1/4$ and $2\alpha = J'_z = 1$ the Kugel Khomskii model becomes

$$H_{\mathrm{KK}} = \sum_{\langle i,j \rangle} \left(\frac{1}{4} + \mathbf{S}_i \cdot \mathbf{S}_j \right) \times \left(\frac{1}{4} + \boldsymbol{\tau} \cdot \boldsymbol{\tau} \right), \tag{1.4}$$

which is equivalent to the SU(4) Heisenberg model (discussed in section 1.4.2), since the four SU(4) spins (in the fundamental representation) are constructed as $|\uparrow\rangle \otimes |1\rangle$, $|\downarrow\rangle \otimes |1\rangle$, $|\uparrow\rangle \otimes |2\rangle$, and $|\downarrow\rangle \otimes |2\rangle$, and the $N^2 - 1 = 15$ SU(4) spin operators are constructed as $\{S^a, \tau^b, S^a\tau^b | a, b \in \{x, y, z\}\}$.

Unfortunately, the SU(4) symmetric point is never realized in real materials, since the relative orientation of the orbital wavefunctions on nearest neighbor sites is never optimal. However, in certain experiments, the Kugel Khomskii model describing the material is close to the SU(4) symmetric point, for example in magic-angle twisted graphene [33, 34] and metal dichalcogenide bilayers [35, 36, 37].

1.3 SU(4) Heisenberg model from spin-orbit coupled materials

The Kugel Khomskii model does not involve spin-orbit interactions. However, as argued in Refs. [38, 39] the strong spin-orbit interaction can give rise to the Kugel Khomskii model exactly at the SU(4) symmetric point. These arguments hold for a class of materials $\alpha - MX_3$, with $M \in \{\mathrm{Zr}, \mathrm{Hf}, \mathrm{Rf}\}$ and $X \in \{\mathrm{F}, \mathrm{Cl}, \mathrm{Br}, \mathrm{I}, \mathrm{At}\}$ where the M atoms form well-separated layers of almost ideal honeycomb lattices (based on Refs. [40, 41]). In particular, they focused on $\alpha-\mathrm{ZrCl_3}$,

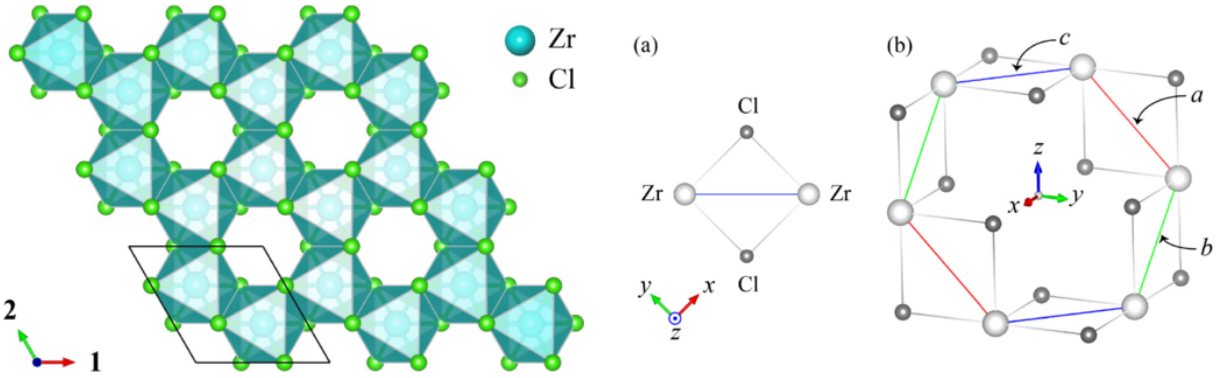

Figure 1.1: The left panel shows a single layer of $\alpha-ZrCl_3$, where the Zr atoms form a honeycomb lattice [38]. The right panel (b) shows the octahedral (cubic) environment of the Zr atoms (big spheres) formed by the Cl atoms (small spheres). The hexagon connecting the Zr atoms is one of the hexagons shown in the left panel [38]. The middle panel (a) shows the superexchange pathways, along which the Zr atoms can exchange electrons via the mediation of the Cl atoms [38]. Depending on the yz, zx, or xy planes of the superexchange, the nearest neighbor bonds in the Zr hexagons are colored by red, light green, or blue, which will be denoted by a, b, and c, respectively. All these figures were taken from Ref. [38].

though the arguments also work for the other possibilities. As shown in the left panel of Fig. 1.1 the Zr atoms form layers of honeycomb lattices, while the Cl atoms create an octahedral (cubic) environment for the Zr atoms (see the right panel (b) of Fig. 1.1). Consequently, the five-fold degenerate d orbitals of the Zr atoms are split by the octahedral crystal field to the two-fold degenerate e_g (the x^2-y^2 and $3z^2-r^2$ orbitals) and the three-fold degenerate t_{2g} orbitals (the d_{xy}, d_{yz}, and d_{zx} orbitals) [4, Sec. 3.5]. The Zr atoms have one electron in the d shells, which remains in the t_{2g} orbitals after the crystal field splitting. Thus, on every lattice site, the electron can be in two spin states $\sigma \in \{\uparrow,\downarrow\}$ and three orbitals $A \equiv d_{xy}$, $B \equiv d_{yz}$, $C \equiv d_{zx}$. To simplify the notations used in Refs. [38, 39] we denote the creation operators of these six states at site j as $c^\dagger_{j,\alpha,\sigma}$, where $\alpha \in \{A,B,C\}$, and $\sigma \in \{\uparrow,\downarrow\}$. The direct hopping of the electrons between the d_{xy}, d_{yz}, and d_{zx} orbitals of nearest Zr atoms is unlikely, the electrons are exchanged between Zr atoms via the mediation of the surrounding Cl atoms, as shown in Fig. 1.1(a), called superexchange [4, Sec. 5.2]. Consequently, the electrons can only hop between orbitals that are perpendicular to the plane of the superexchange, and have a large probability to find the electron around the Cl atoms. In the example shown in Fig. 1.1(a), the superexchange takes place in the xy plane, therefore the electrons of the Zr atoms can hop between the d_{yz} and d_{zx} orbitals only. Depending on the planes yz, zx, and xy of the superexchange, the nearest neighbor bonds of the Zr atoms are denoted as a, b, and c, respectively, as shown in Fig. 1.1(b). Therefore, the starting point of Refs. [38, 39] is the six-component Hubbard model with bond-dependent hoppings, which in our simplified notation reads,

$$\begin{aligned}\mathcal{H}_{\alpha-ZrCl_3} = -t\sum_{\sigma}\left(\sum_{\langle i,j\rangle_a} c^\dagger_{i,B,\sigma}c_{j,C,\sigma} + \sum_{\langle i,j\rangle_b} c^\dagger_{i,C,\sigma}c_{j,A,\sigma} + \sum_{\langle i,j\rangle_c} c^\dagger_{i,A,\sigma}c_{j,B,\sigma} + H.c.\right) \\ + \frac{U}{2}\sum_j \sum_{\sigma\neq\sigma'\in\{\uparrow,\downarrow\}} \sum_{\delta\neq\delta'\in\{A,B,C\}} n_{j,\delta,\sigma}n_{j,\delta',\sigma'}\end{aligned} \tag{1.5}$$

where t is a real-valued hopping parameter, U is the on-site Hubbard interaction, and $\sum_{\langle i,j\rangle_a}$ sums over nearest bonds of type a in Fig. 1.1(b). This Hamiltonian is not SU(4) symmetric, as it has 6 "flavors", and the hoppings from one orbital to another are bond dependent. However, due

to the spin independence of t and U, the Hamiltonian has an SU(2) spin rotational invariance. The six flavors create a six-dimensional on-site Hilbert space, which arises from the product of the two spins $\sigma \in \{\uparrow, \downarrow\}$ and the three orbitals $\alpha \in \{A, B, C\}$. The strong spin-orbit interaction $\propto \mathbf{L} \cdot \mathbf{S}$, splits this six-dimensional Hilbert space to a two- and a four-dimensional subspace, corresponding to the $s = \frac{1}{2}$ and the $s = \frac{3}{2}$ irreducible representations, respectively (see Sec. 1.4.1). Furthermore, the spin-orbit interaction lowers the energy of the $s = \frac{3}{2}$ four-dimensional subspace, which is occupied by a single electron (quarter filling) in the case of $\alpha - ZrCl_3$. Therefore, the low energy effective Hamiltonian can be reformulated using the quartet spinor fermionic creation operator $\psi_j^\dagger$ (in the $s = \frac{3}{2}$ subspace) with components $\psi_{j,\tau,\rho}^\dagger$, where $\tau \in \{\Uparrow, \Downarrow\}$ is the pseudo orbital index (not the $\alpha \in \{A, B, C\}$), and $\rho \in \{\overset{\uparrow}{\cdot\cdot}, \overset{\downarrow}{\cdot\cdot}\}$ is the pseudospin index, so that $\psi_j^\dagger = (\psi_{j,\Uparrow,\overset{\uparrow}{\cdot\cdot}}^\dagger, \psi_{j,\Uparrow,\overset{\downarrow}{\cdot\cdot}}^\dagger, \psi_{j,\Downarrow,\overset{\uparrow}{\cdot\cdot}}^\dagger, \psi_{j,\Downarrow,\overset{\downarrow}{\cdot\cdot}}^\dagger)^T$, where the components $\psi_{j,\tau,\rho}^\dagger$ are defined through the relations

$$\begin{aligned} c_{j,A,\sigma}^\dagger &= \frac{\sigma}{\sqrt{6}} \left(\psi_{j,\Uparrow,\bar{\sigma}}^\dagger - \sqrt{3} \psi_{j,\Downarrow,\sigma}^\dagger \right) \\ c_{j,B,\sigma}^\dagger &= \frac{i}{\sqrt{6}} \left(\psi_{j,\Uparrow,\bar{\sigma}}^\dagger + \sqrt{3} \psi_{j,\Downarrow,\sigma}^\dagger \right) \\ c_{j,C,\sigma}^\dagger &= \sqrt{\frac{2}{3}} \psi_{j,\Uparrow,\sigma}^\dagger, \end{aligned} \tag{1.6}$$

where the mixing of $\rho = \sigma$ and $\rho = \bar{\sigma}$ ($\bar{\sigma} \neq \sigma$) shows that the spin index σ is not the same as the pseudospin index ρ. Inserting Eqs. (1.6) into the Hamiltonian (1.5) we get

$$\mathcal{H}_{\alpha-ZrCl_3} = -\frac{t}{\sqrt{3}} \sum_{\langle i,j \rangle} \psi_i^\dagger U_{i,j} \psi_j + \frac{U}{2} \sum_j \psi_j^\dagger \psi_j (\psi_j^\dagger \psi_j - 1), \tag{1.7}$$

where $U_{i,j}$ is a 4×4 matrix defined as

$$U_{i,j} = \begin{cases} U^a = \boldsymbol{\tau}^y \otimes \boldsymbol{I}_2, & \langle i,j \rangle_a \\ U^b = -\boldsymbol{\tau}^x \otimes \boldsymbol{\rho}^z & \langle i,j \rangle_b \\ U^c = -\boldsymbol{\tau}^x \otimes \boldsymbol{\rho}^y & \langle i,j \rangle_c \end{cases}, \tag{1.8}$$

where $\boldsymbol{I}_2$ is a 2×2 identity matrix, $\boldsymbol{\tau}^\alpha$ and $\boldsymbol{\rho}^\alpha$ (with $\alpha \in \{x, y, z\}$) are the Pauli matrices acting on the pseudoorbital (τ) and pseudospin (ρ) indices of $\psi_{i,\tau,\rho}^\dagger$, respectively. More precisely, the τ and the ρ indices determine the eigenvalues of $\boldsymbol{\tau}^z$ and $\boldsymbol{\rho}^z$ for their simulatneous eigenstate $\psi_{i,\tau,\rho}^\dagger$. For example the $\psi_{i,\Uparrow,\overset{\downarrow}{\cdot\cdot}}^\dagger |0\rangle$ is an eigenstate of both $\boldsymbol{\tau}^z$ and $\boldsymbol{\rho}^z$ with eigenvalues $+1$ and -1, respectively. The $U^{a,b,c}$ are unitary and Hermitian, therefore $U_{j,i} = U_{i,j}^\dagger = U_{i,j}$. Interestingly, the flux of any elementary hexagonal plaquette p is $\prod_{\langle i,j \rangle \in p} U_{i,j} = U^a U^b U^c U^a U^b U^c = (U^a U^b U^c)^2 = -I_4$, where I_4 is a 4×4 identity matrix, corresponding to an Abelian phase π.

The Hamiltonian (1.7) is still not SU(4) symmetric, as $U_{i,j}$ is asymmetric in the quartet spinor space. However, a local SU(4) gauge transformation $\psi_j \to g_j \psi_j$, $U_{i,j} \to g_i U_{i,j} g_j^\dagger$ leaving the flux of every hexagonal plaquette invariant, can change the Hamiltonian (1.7) to the form

$$\begin{aligned} \mathcal{H}_{\alpha-ZrCl_3} &= -\frac{t}{\sqrt{3}} \sum_{\langle i,j \rangle} \eta_{i,j} \psi_i^\dagger \psi_j + \text{H.c.} + \frac{U}{2} \sum_j \psi_j^\dagger \psi_j (\psi_j^\dagger \psi_j - 1), \\ &= -\frac{t}{\sqrt{3}} \sum_{\substack{\langle i,j \rangle \\ \tau \in \{\Uparrow,\Downarrow\} \\ \rho \in \{\overset{\uparrow}{\cdot\cdot},\overset{\downarrow}{\cdot\cdot}\}}} \eta_{i,j} \psi_{i,\tau,\rho}^\dagger \psi_{j,\tau,\rho} + \text{H.c.} + \frac{U}{2} \sum_{\substack{j \\ \tau,\tau' \in \{\Uparrow,\Downarrow\} \\ \rho,\rho' \in \{\overset{\uparrow}{\cdot\cdot},\overset{\downarrow}{\cdot\cdot}\}}} \psi_{j,\tau,\rho}^\dagger \psi_{j,\tau,\rho} (\psi_{j,\tau',\rho'}^\dagger \psi_{j,\tau',\rho'} - 1), \end{aligned} \tag{1.9}$$

which is already invariant under global SU(4) rotations in the quartet spinor space. The $\eta_{i,j} \pm 1$ are arranged in a way to give a π flux for every elementary hexagonal plaquette p as $\prod_{\langle i,j \rangle \in p} \eta_{i,j} = -1$.

The specific form of these local gauge transformations g_j and the signs $\eta_{i,j}$ are detailed in the supplementary material of Ref. [38].

The Hamiltonian in Eq. (1.9) is equivalent to a Hubbard model with two-fold orbital degeneracy, leading to the Kugel-Khomskii model (1.4) right at the SU(4) symmetric point, which is equivalent to the antiferromagnetic SU(4) Heisenberg model.

The starting model in Eq. (1.5) assumed that $\alpha - ZrCl_3$ is formed by well-separated layers of ideal honeycomb lattices, based on Refs. [40, 41]. However, as pointed out in Ref. [42] the crystal structure in Refs. [40, 41] may be based on a misassigned powder pattern, so the honeycomb lattices may not be ideal. Furthermore, a recent density-functional theory calculation suggests that this material might be susceptible to dimerization of the honeycomb layers [43]. Consequently, it is possible that $\alpha - ZrCl_3$ is not a perfect realization of the SU(4) Heisenberg model.

Another possibility to realize the SU(4) Heisenberg model was suggested by Kugel and Khomskii, in materials having face-sharing MO_6 octahedra (M is a transition-metal ion) also using spin-orbital interactions in Ref. [44].

1.4 SU(N) Heisenberg model as a low energy effective model

We introduce the SU(N) symmetric Heisenberg model by comparing it to the well-known SU(2) Heisenberg model. Therefore, let us first briefly recapitulate the main features of the SU(2) case, where we also introduce the notion of an irreducible representation.

1.4.1 The SU(2) symmetric Heisenberg model

The Heisenberg model always emerges as an effective theory of an underlying model. For example, the SU(2) symmetric half-filled Hubbard model with non-degenerate orbitals leads to the antiferromagnetic SU(2) symmetric Heisenberg model in the $U/t \to \infty$ limit. Due to the strong on-site interactions, double occupancy is energetically unfavorable. At half filling, the low energy on-site Hilbert space reduces to a two-dimensional subspace spanned by the two basis states $|\uparrow\rangle \equiv c_\uparrow^\dagger|0\rangle$ and $|\downarrow\rangle \equiv c_\downarrow^\dagger|0\rangle$, which are called spins. The low energy Hamiltonian turns out to be the SU(2) symmetric Heisenberg model

$$\mathcal{H}^{SU(2)} = J\sum_{\langle i,j\rangle} \mathbf{S}_i \cdot \mathbf{S}_j = J\sum_{\langle i,j\rangle} \left(S_i^x S_j^x + S_i^y S_j^y + S_i^z S_j^z \right), \tag{1.10}$$

where summation is over the $\langle i,j\rangle$ nearest neighbor sites, and depending on the sign of J, the interaction is either antiferromagnetic ($J > 0$), or ferromagnetic ($J < 0$). If the Heisenberg model emerges from the SU(2) Hubbard model, then the spin operators are defined as

$$\begin{aligned} S_j^x &= \frac{1}{2}\left(f_{j,\uparrow}^\dagger f_{j,\downarrow} + f_{j,\downarrow}^\dagger f_{j,\uparrow} \right), \\ S_j^y &= \frac{i}{2}\left(-f_{j,\uparrow}^\dagger f_{j,\downarrow} + f_{j,\downarrow}^\dagger f_{j,\uparrow} \right), \\ S_j^z &= \frac{1}{2}\left(f_{j,\uparrow}^\dagger f_{j,\uparrow} - f_{j,\downarrow}^\dagger f_{j,\downarrow} \right) \end{aligned} \tag{1.11}$$

which can be abbreviated as

$$S_j^a = \frac{1}{2}\sum_{\rho,\rho' \in \{\uparrow,\downarrow\}} c_{j,\rho}^\dagger \sigma_{\rho,\rho'}^a c_{j,\rho'}, \tag{1.12}$$

where the σ^a with $a \in \{x, y, z\}$ are the Pauli matrices. This construction ensures that the spin operators satisfy the same commutation relations as the $\frac{1}{2}\sigma^a$ matrices, namely

$$[S_j^a, S_j^b] = i\hbar \sum_{c=1}^{3} \varepsilon_{a,b,c} S_j^c. \tag{1.13}$$

They are the generators of the su(2) Lie algebra at site j (we write the algebra with small letters and the group with big letters), and also the infinitesimal generators of SU(2) spin rotations (see Appendix A.2). The $\varepsilon_{a,b,c}$ are the Levi Civita symbols $\varepsilon_{123} = \varepsilon_{231} = \varepsilon_{312} = +1$ and $\varepsilon_{321} = \varepsilon_{213} = \varepsilon_{132} = -1$ (the rest are zeros). The spin operators on different sites commute, therefore they are bosonic operators. From now on, we will set $\hbar = 1$ for convenience.

In the above-mentioned example, the local Hilbert space of the Heisenberg model was two-dimensional, spanned by the two basis states $|\uparrow\rangle \equiv c_\uparrow^\dagger|0\rangle$ and $|\downarrow\rangle \equiv c_\downarrow^\dagger|0\rangle$, called the spin 1/2 representation [4, Sec. 5.1.5]. However, the on-site Hilbert space of the Heisenberg Hamiltonian (1.10) can be higher-dimensional, if it emerges from a different underlying model. The on-site Hilbert space of the Heisenberg model determines the matrices representing the spin operators and the representation of the Lie algebra.

A representation of the Lie algebra means that we exchange the spin operators for matrices, which obey the same commutation relations (1.13) as the spin operators (for the connection with the representations of the spin rotation group, see Appendix A.2). A representation is reducible, if all the matrices representing the spin operators can be simultaneously block diagonalized with a basis transformation. If they can not be simultaneously block diagonalized, then the representation is irreducible. In other words, in a reducible representation, the Hilbert space in which the matrices of the spin operators act, contains further closed subspaces (closed under the action of the spin operators). For example, in a six-dimensional reducible representation of the su(2) Lie algebra, we can simultaneously block diagonalize the 6×6 matrices representing the S^x, S^y, and S^z generators, to 2×2 ($s = 1/2$) and 4×4 block matrices ($s = 3/2$), which can not be further block diagonalized, so that there is a two- and a four-dimensional closed subspace, corresponding to a two- and a four-dimensional irreducible representation, respectively. In an irreducible representation, there are no further closed subspaces. One way to find all possible irreducible representations (all the smallest closed subspaces) is to find all operators $\hat{C}$ that simultaneously commute with all the spin operators because the eigensubspaces of these $\hat{C}$ are closed under the action of the spin operators. The $\hat{C}$ are called Casimir operators. In the SU(2) case, the only operator (except for 0 and the identity) commuting with all three spin operators at site j is

$$\hat{C}_j^{SU(2)} = \mathbf{S}_j \cdot \mathbf{S}_j \equiv (S_j^x)^2 + (S_j^y)^2 + (S_j^z)^2, \tag{1.14}$$

which can be interpreted as the length of the spin. The irreducible representations of the su(2) Lie algebra on a given site are the eigensubspaces of the Casimir operator $\hat{C}_j^{SU(2)}$, as these irreps emerge from the underlying model, the irrep is the same on every site. The eigenvalues of the $\hat{C}_j^{SU(2)}$ are $s(s+1)$ where $s \in \{0, \frac{1}{2}, 1, \frac{3}{2} \dots\}$ is either an integer, or a non-negative half-odd integer. s determines the dimension $d = 2s+1$ of the local Hilbert space of a single spin operator, and the size $d \times d = (2s+1) \times (2s+1)$ of the matrices representing the spin operators in this irrep. Therefore, s is a label for the irreps of the su(2) Lie algebra. When we talk about the spin 1/2 Heisenberg model, then the spin operators are in the $s = 1/2$ irrep, represented by the 2×2 Pauli matrices σ^a (given in Appendix A.3) as $S^a = \frac{1}{2}\sigma^a$ for $a \in \{x, y, z\}$.

As the spin operators do not commute with each other (see Eq. (1.13)), they can not be simultaneously diagonalized. The Casimir operator $\hat{C}_j^{SU(2)}$ commutes with all spin operators, so we can always choose a basis, in which we simultaneously diagonalize one of the spin operators (let us choose S^z) and the Casimir operator. These common eigenstates in the irrep labeled with s are the spin states (or simply spins) $|s, m\rangle$, where $m \in \{-s, -s+1 \dots s\}$, which form a $d = 2s+1$

dimensional basis for this irrep. In the $s = 1/2$ the spins are the $|\uparrow\rangle \equiv |s = 1/2, m = 1/2\rangle$ and the $|\downarrow\rangle \equiv |s = 1/2, m = -1/2\rangle$. A different irrep would be that of $s = 1$ (appearing in the spin 1 Heisenberg model), where the dimension of the local Hilbert space is $2s + 1 = 3$, and the spins are $|s = 1, m = 1\rangle$, $|s = 1, m = 0\rangle$,$|s = 1, m = -1\rangle$.

The SU(2) symmetry of the Hamiltonian (1.10) means that it is invariant under the simultaneous rotation of all spins around the same axis by the same angle ϕ, by the SU(2) operator $U = \prod_j e^{i\phi \mathbf{n}\cdot\mathbf{S}_j}$ (see Appendix A.2). Classically, one could argue that the $\mathbf{S}_i \cdot \mathbf{S}_j$ depends only on the relative orientation of two neighboring spins, which is not affected by a rotation that rotates every spin the same way. Quantum mechanically, we can argue that the SU(2) symmetry of $\mathcal{H}^{SU(2)}$ (1.10) means $U\mathcal{H}^{SU(2)}U^{-1} = \mathcal{H}^{SU(2)}$, which follows from the commutation of $\mathcal{H}^{SU(2)}$ with the total spin operators (proven in Appendix A.4)

$$S^x_{\mathrm{T}} \equiv \sum_{j=1}^{N_s} S^x_j, \qquad S^y_{\mathrm{T}} \equiv \sum_{j=1}^{N_s} S^y_j, \qquad S^z_{\mathrm{T}} \equiv \sum_{j=1}^{N_s} S^z_j, \tag{1.15}$$

where N_s is the number of lattice sites. These total spin operators also satisfy the commutations relations (1.13) as $[S^a_{\mathrm{T}}, S^b_{\mathrm{T}}] = i\hbar \sum_{c=1}^{3} \varepsilon_{a,b,c} S^c_{\mathrm{T}}$, so they are the generators of the Lie algebra of the total system.

The Casimir operator can also be evaluated on the total system containing multiple spins as

$$C^{SU(2)}_{\mathrm{T}} \equiv \mathbf{S}\cdot\mathbf{S} = (S^x_{\mathrm{T}})^2 + (S^y_{\mathrm{T}})^2 + (S^z_{\mathrm{T}})^2, \tag{1.16}$$

where the eigensubspaces labeled with S (having eigenvalue $S(S+1)$) define the irreducible representations of the su(2) Lie algebra generated by the total spin operators (1.15). This is useful, because the Hamiltonian $\mathcal{H}^{SU(2)}$ (1.10) commutes with all three components of the total spin operator in Eq. (1.15) (as shown in Appendix. A.4), therefore it also commutes with $C^{SU(2)}_{\mathrm{T}}$. Consequently, we can search for the eigenstates of the Hamiltonian $\mathcal{H}^{SU(2)}$ in the irreps (invariant eigensubspaces) of $C^{SU(2)}_{\mathrm{T}}$.

The connection of the irreducible representations of the Lie algebra on a single lattice site (labeled by s) to the irreducible representations of the Lie algebra on the total system (labeled by S) is given by the addition of angular momenta (and the Clebsch Gordon coefficients). In the simplest case of a two-site system, with the single spins $s_1 = s_2 = 1/2$, the possible irreps of the total system are $S \in \{|s_1 - s_2|, \dots s_1 + s_2\} = \{0, 1\}$, which are the $S = 0$ singlet (completely antisymmetric), and the $S = 1$ triplet (completely symmetric) irreps.

A quantum spin liquid ground state is expected not to break any symmetry of the Heisenberg Hamiltonian, meaning that it should be invariant under all transformations that leave invariant the Hamiltonian. In particular, the global spin rotational invariance means $\prod_j e^{i\phi \mathbf{n}\cdot\mathbf{S}_j}|\mathrm{GS}\rangle = |\mathrm{GS}\rangle$ for any ϕ and any $\mathbf{n}$. As explained in Appendix A.4, the infinitesimal global spin rotations will leave the $|\mathrm{GS}\rangle$ invariant, only if $\sum_j S^a_j|\mathrm{GS}\rangle = 0$ for all $a \in \{x, y, z\}$. In other words, the $|\mathrm{GS}\rangle$ serves as a basis for an irreducible representation of the total spin operators, where the 1×1 matrices representing the total spin operators are all zeros (zeros clearly satisfy the commutation relations (1.13)). Therefore, the total Casimir operator of this irrep is also 0, defining the singlet irreducible representation of the Lie algebra of the total system. The claim that the $|\mathrm{GS}\rangle$ serves as a basis for the singlet representation is sometimes rephrased as the $|\mathrm{GS}\rangle$ transforms under the action of the spin operators as a singlet. The $|\mathrm{GS}\rangle$ also serves as a basis for the singlet irrep of the SU(2) spin rotation group, where every spin rotation is represented by ones, as follows from $\prod_j e^{i\phi \mathbf{n}\cdot\mathbf{S}_j}|\mathrm{GS}\rangle = |\mathrm{GS}\rangle$. If a wavefunction transforming as a singlet is formed by two spins, then it must be antisymmetric under the exchange of any two spins (its Young tableau is a column of two boxes, as explained in Appendix. A.5). In general, a wavefunction transforming as a singlet must be formed by $2 \times L$ spins (L being a positive integer) since it must be composed of the

product of completely antisymmetric two-spin wavefunctions (its Young tableau is a rectangle of two rows and L number of columns, as explained in Appendix. A.5).

The interaction $\mathbf{S}_i \cdot \mathbf{S}_j$ in the Hamiltonian (1.10) can be rewritten with the exchange operator $\mathcal{P}_{ij}$ as

$$\mathbf{S}_i \cdot \mathbf{S}_j = \frac{1}{2}\mathcal{P}_{ij} - \frac{1}{4}\mathcal{I}, \tag{1.17}$$

where $\mathcal{I}$ is the identity, and the $\mathcal{P}_{ij}$ simply exchanges the spins on sites i and j. The expression (1.17) can be verified by matching the action of the two sides on the four possible spin configurations $|\uparrow\rangle_i \otimes |\uparrow\rangle_j$, $|\uparrow\rangle_i \otimes |\downarrow\rangle_j$, $|\downarrow\rangle_i \otimes |\uparrow\rangle_j$, $|\downarrow\rangle_i \otimes |\downarrow\rangle_j$.

1.4.2 Generalization to SU(N)

The SU(N) symmetric Heisenberg model is defined as

$$\mathcal{H} = J \sum_{\langle i,j \rangle} \mathbf{T}_i \cdot \mathbf{T}_j = J \sum_{\langle i,j \rangle} \sum_{a=1}^{N^2-1} T_i^a T_j^a, \tag{1.18}$$

where $J > 0$ ($J < 0$) describes antiferromagnetic (ferromagnetic) interaction, the $\langle i,j \rangle$ are nearest neighbor sites. The T_j^a (with $a \in \{1, 2, \dots N^2 - 1\}$) are the generalizations of the SU(2) spin operators (which we will call SU(N) spin operators) satisfying the commutation relations

$$[T_j^a, T_j^b] = i \sum_{c=1}^{N^2-1} f_{abc} T_j^c. \tag{1.19}$$

The f_{abc} are the structure constants of the algebra [45] (the analogs of the $\varepsilon_{a,b,c}$), which can be determined in the way explained in Appendix A.3. The SU(N) spin operators are the generators of the su(N) Lie algebra on site j, and also the infinitesimal generators of SU(N) spin rotations (see Appendix A.2). The SU(N) spin operators on different sites commute, therefore they are bosonic operators.

The SU(N) Heisenberg model can emerge from the SU(N) Hubbard model at $1/N$ filling (one fermion per site) at the limit of $U/t \to \infty$. In this case, the low energy on-site Hilbert space reduces to an N-dimensional subspace spanned by the SU(N) spins $c_{i,\sigma}^\dagger|0\rangle$ with $\sigma \in \{1 \dots N\}$, since multiple occupancy is energetically unfavorable, called the fundamental representation. The spin 1/2 representation of the su(2) Lie algebra is also its fundamental representation, where the two SU(2) spins are $|\uparrow\rangle \equiv c_\uparrow^\dagger|0\rangle$ and $|\downarrow\rangle \equiv c_\downarrow^\dagger|0\rangle$. In the case of the SU($N$) Hubbard model, the spin operators are constructed as

$$T_j^a = \frac{1}{2} \sum_{\sigma,\sigma'=1}^{N} c_{j,\sigma}^\dagger \lambda_{\sigma,\sigma'}^a c_{j,\sigma'}, \tag{1.20}$$

where the $\frac{1}{2}\lambda^a$ are the generalizations of the Pauli matrices having sizes $N \times N$, which represent the spin operators in the fundamental representation. In the SU(3) case, the eight λ^a matrices are called the Gell-Mann matrices [46], known from particle physics. The construction of the λ^a matrices for any N is explained in Appendix A.3, where we also list the eight Gell-Mann matrices. Just as in the case of SU(2), the SU(N) Heisenberg Hamiltonian can emerge in different irreducible representations, not only the fundamental one.

For $N > 2$, there are multiple operators commuting with all the SU(N) spin operators, called Casimir operators. These are functions of the spin operators, and their eigenvalues label the irrep together. However, there is an equivalent, simpler pictorial way to label the irreps (and calculate

their dimensions) by Young-tableaux (explained in Appendix A.5), therefore we will not specify the Casimir operators here. We mention only the quadratic Casimir operator

$$\hat{C}_{2j} = \mathbf{T}_j^2 = \mathbf{T}_j \cdot \mathbf{T}_j = \sum_{a=1}^{N^2-1} T_j^a T_j^a, \tag{1.21}$$

with its eigenvalues given in Appendix A.3. The Casimir operators can be simultaneously diagonalized together with $N-1$ SU(N) spin operators (for SU(2) it is only the S^z). Their common eigenstates provide a basis for a given irrep and will be called SU(N) spins (the analogs of spins). The number of these SU(N) spins equals the dimension of the local Hilbert space of a single SU(N) spin operator T_j^a on a given site, which is determined by the irrep (there is no simple formula as $2s+1$, but the dimension can be calculated from the Young tableau explained in Appendix A.5).

The SU(N) symmetry of the Hamiltonian (1.18) means that it is invariant under the simultaneous rotation of all SU(N) spins around the same axis (given by the unit vector $\mathbf{n}$) with the same angle ϕ, done with the SU(N) spin rotation operator $U = \prod_j e^{i\phi \sum_{a=1}^{N^2-1} n_a T_j^a}$ (see Appendix A.2), as $U\mathcal{H}U^{-1} = \mathcal{H}$. The proof is presented in Appendix A.4, relying on the commutation of $\mathcal{H}$ with the N^2-1 components of the total SU(N) spin operator $\sum_j T_j^a$ ($a \in \{1 \dots N^2-1\}$).

The Hamiltonian (1.18) commutes with all N^2-1 components of the total SU(N) spin operator $T_{\mathrm{T}}^a \equiv \sum_j T_j^a$ with $a \in \{1 \dots N^2-1\}$, therefore it also commutes with all Casimir operators of the total system. Consequently, we can search for the eigenstates of the Hamiltonian (1.18) in the irreps of the Lie algebra of the total system (generated by the total spin operators), which are the common eigensubspaces of the Casimir operators of the total system. The relation between the irreps of the Lie algebra on a single site and the irreps of the Lie algebra of the whole system is given by the Young tableaux; the simplest cases are explained in Appendix A.5.

As already mentioned in the SU(2) case, a quantum spin liquid ground state must be invariant under any global spin rotation as $\prod_j e^{i\phi \mathbf{n}\cdot\mathbf{T}_j}|\mathrm{GS}\rangle = |\mathrm{GS}\rangle$ for any ϕ and any $\mathbf{n}$, implying $\sum_j T_j^a|\mathrm{GS}\rangle = 0$ for all $a \in \{1 \dots N^2-1\}$ (explained in Appendix A.4). In other words, the $|\mathrm{GS}\rangle$ serves as a one-dimensional basis for an irreducible representation of the Lie algebra of the total system, where every total spin operator is trivially represented with 1×1 matrices which are all zeros, (and every SU(N) spin rotation is represented with ones). Consequently, the total quadratic Casimir operator

$$\hat{C}_{2\mathrm{T}} = \mathbf{T}_{\mathrm{T}} \cdot \mathbf{T}_{\mathrm{T}} = \sum_{a=1}^{N^2-1} \left(\sum_j T_j^a \right) \left(\sum_{j'} T_{j'}^a \right) \tag{1.22}$$

will have eigenvalue zero, which uniquely identifies the SU(N) singlet irrep (unlike other irreps) without the need to specify the eigenvalues of the other Casimir operators. We will abbreviate the above statements by saying that the $|\mathrm{GS}\rangle$ transforms (under the action of the SU(N) spin operators) as an SU(N) singlet. In general, a wavefunction transforming as an SU(N) singlet must be formed by $N \times L$ SU(N) spins since it must be a linear combination of L completely antisymmetrized wavefunctions composed of N SU(N) spins (its Young tableau is a rectangle of N rows and L columns, as explained in Appendix. A.5).

The $\mathbf{T}_i \cdot \mathbf{T}_j$ in the fundamental representation can be expressed by the exchange operator $\mathcal{P}_{i,j}$ as

$$\mathbf{T}_i \cdot \mathbf{T}_j = \frac{1}{2}\mathcal{P}_{i,j} - \frac{1}{2N}\mathcal{I}, \tag{1.23}$$

similarly as in the SU(2) case (1.17). The $\mathcal{I}$ is the identity operator and the effect of the P_{ij} is simply to exchange the SU(N) spins on sites i and j. The $\mathcal{P}_{i,j}$ also has SU(N) spin rotational symmetry, which can be understood even without knowing about the SU(N) spin rotational

invariance of the $\mathbf{T}_i \cdot \mathbf{T}_j$ term, since the $\mathcal{P}_{i,j}$ makes no difference between the SU(N) spins (so rotating them has no effect). Therefore, the SU(N) symmetric Heisenberg model can also be formulated as

$$\mathcal{H} = \frac{J}{2} \sum_{\langle i,j \rangle} \mathcal{P}_{i,j}, \tag{1.24}$$

up to a constant.

Chapter 2

Quantum spin liquids

In this section, we will first introduce the mean-field theory for quantum spin liquid ground states [2, Sec. 9.] arising from the SU($N > 2$) symmetric antiferromagnetic Heisenberg model (1.18) in the fundamental representation, then discuss how can we incorporate certain fluctuations beyond the mean-field approximation with Gutzwiller projection, and finally explain the notion of quantum order differentiating between different quantum spin liquids.

In the case of the SU(2) Heisenberg model, mean-field theory is done by rewriting the spin operators as $\mathbf{S}_i = \langle \mathbf{S}_i \rangle + (\mathbf{S}_i - \langle \mathbf{S}_i \rangle)$, and hope that the fluctuation $\delta \mathbf{S}_i \equiv (\mathbf{S}_i - \langle \mathbf{S}_i \rangle)$ is small. Thus, writing them back to the Hamiltonian $\mathcal{H} = J \sum_{\langle i,j \rangle} \mathbf{S}_i \cdot \mathbf{S}_j$ we can neglect the square of the fluctuations $\delta \mathbf{S}_i \delta \mathbf{S}_j$, arriving at the mean-field Hamiltonian $\mathcal{H} = -J \sum_{\langle i,j \rangle} \langle \mathbf{S}_i \rangle \langle \mathbf{S}_j \rangle + 2J \sum_{\langle i,j \rangle} \langle \mathbf{S}_i \rangle \cdot \mathbf{S}_j$. The expectation values $\langle \dots \rangle$ are taken self-consistently in the mean-field ground state.

However, a quantum spin liquid ground state neither breaks the SU(N) symmetry of the Hamiltonian (1.18), nor the symmetries of the underlying lattice, implying $\langle \mathbf{S}_j \rangle = 0 \ \forall j$, which makes the usual mean-field approximation impossible. The magnetic disorder of a quantum spin liquid ground state means, that the correlation functions of the spin operators in this state vanish for large distances. In contrast, in a magnetically ordered state, the correlation function approaches a finite value determined by the ordering pattern.

The way to do a mean-field approximation for a quantum spin liquid is through the projective construction (also known as the fermionic parton construction). Another type of projective construction is the bosonic parton construction (or Schwinger boson approach). We will use the former one because the latter always leads to gapped quantum spin liquids [2, Sec. 9.1].

2.1 Projective construction and mean-field theory

In the SU(2) fermionic projective construction (see [2, Sec. 9.1] and Refs. [47, 48, 49, 50, 51, 52, 53, 54]) the bosonic spin operators are decomposed into a pair of fermionic operators the same way as we defined them in section 1.4.1

$$S_j^a = \frac{1}{2} \sum_{\rho,\rho' \in \{\uparrow,\downarrow\}} f_{j,\rho}^\dagger \sigma_{\rho,\rho'}^a f_{j,\rho'}, \tag{2.1}$$

where the σ^a with $a \in \{x, y, z\}$ are the Pauli matrices. In the fundamental representation of su(N), the three Pauli matrices are replaced by the $N^2 - 1$ λ^a matrices having sizes $N \times N$ as

$$T_j^a = \frac{1}{2} \sum_{\sigma,\sigma'=1}^{N} f_{j,\sigma}^\dagger \lambda_{\sigma,\sigma'}^a f_{j,\sigma'}. \tag{2.2}$$

However, the fermionic operators $f_{j,\sigma}^\dagger$ - usually referred to as Abrikosov fermions - are not the same as the fermionic operators $c_{j,\sigma}^\dagger$ appearing in the SU(N) Hubbard model, since writing the spin operators with both, $\frac{1}{2} \sum_{\sigma,\sigma'=1}^{N} c_{j,\sigma}^\dagger \lambda_{\sigma,\sigma'}^a c_{j,\sigma'} = T_j^a = \frac{1}{2} \sum_{\sigma,\sigma'=1}^{N} f_{j,\sigma}^\dagger \lambda_{\sigma,\sigma'}^a f_{j,\sigma'}$, shows that there is a gauge redundancy in the definition of $f_{j,\sigma}^\dagger$. Namely, the fermionic operators can differ in a site-dependent, but flavor-independent phase $f_{j,\sigma}^\dagger = e^{i\phi_j} c_{j,\sigma}^\dagger$, since they yield the same spin operators. More complicated relations between the fermionic operators are also possible (like

flavor mixing gauge transformations shown in Eq. (2.35), the only requirement is that they have to yield the same spin operators.

In the basis $\{f^\dagger_{j,\sigma}|0\rangle\}$ with $\sigma \in \{1 \dots N\}$, the expectation values

$$\langle 0|f_{j,\sigma} T^a_j f^\dagger_{j,\sigma'}|0\rangle = \frac{1}{2}\sum_{\rho,\rho'}\langle 0| \underbrace{f_{j,\sigma}f^\dagger_{j,\rho}}_{\delta_{\sigma,\rho}-f^\dagger_{j,\rho}f_{j,\sigma}} \lambda^a_{\rho,\rho'} \underbrace{f_{j,\rho'}f^\dagger_{j,\sigma'}}_{\delta_{\rho',\sigma'}-f^\dagger_{j,\sigma'}f_{j,\rho'}} |0\rangle = \frac{1}{2}\lambda^a_{\sigma,\sigma'}, \tag{2.3}$$

where we used that both $f_{j,\rho'}|0\rangle = 0$ and $\langle 0|f^\dagger_{j,\rho} = 0$. Therefore, the states $\{f^\dagger_{j,\sigma}|0\rangle\}$ form an N-dimensional basis for the fundamental representation. Equivalently, we can write

$$T^a_j f^\dagger_{j,\sigma}|0\rangle = \sum_{\sigma'=1}^{N} \frac{1}{2}\lambda^a_{\sigma',\sigma} f^\dagger_{j,\sigma'}|0\rangle, \tag{2.4}$$

which shows that the action of the spin operator T^a_j on the states $\{f^\dagger_{j,\sigma}|0\rangle\}$ is equivalent to the multiplication with the matrix $\frac{1}{2}\lambda^a$. In the literature, people abbreviate this by saying that the states $\{f^\dagger_{j,\sigma}|0\rangle\}$ transform under the fundamental representation.

When we map the bosonic SU(N) spin operators (in the fundamental irrep) to fermions, the local Hilbert spaces should map to each other in a one-to-one correspondence, so their dimensions must be equal. However, the dimension of the former is simply N (the number of SU(N) spins), while the dimension of the latter is bigger because we can have $r \in \{0, 1, \dots N\}$ number of fermions on the same lattice site, giving a dimension $\sum_{r=0}^{N}\binom{N}{r}$. Just as in the case of the Hubbard model, one fermion per site corresponds to the fundamental representation of the Heisenberg model, and different fillings lead to different irreducible representations (see Appendix A.6). To achieve a one-to-one correspondence with the Hilbert space of the Heisenberg model in the fundamental representation, we have to impose on the fermions the single occupancy constraint

$$n_j \equiv \sum_{\sigma=1}^{N} f^\dagger_{j,\sigma} f_{j,\sigma} = 1, \tag{2.5}$$

on every site j, where n_j is the total fermion number operator. Requiring $n_j = 1\ \forall j$ excludes the possibility of empty or multiply occupied sites, reducing the dimension of the fermionic Hilbert space to N. This constraint accounts for the strong on-site repulsion $1 \ll U/t$ of the Hubbard model (1.2), which is also the reason why the Heisenberg Hamiltonian (1.18) appears as an effective model in the fundamental representation.

Substituting Eq. (2.2) into the Heisenberg Hamiltonian $\mathcal{H} = J\sum_{\langle i,j\rangle}\mathbf{T}_i \cdot \mathbf{T}_j$ (1.18) we get an interacting fermionic Hamiltonian (B.4) with terms like $f^\dagger f\ f^\dagger f$, as explained in Appendix B.

In the mean-field approximation, we replace a pair of fermionic operators with their expectation values (for details see Appendix B),

$$\mathcal{H}^{\mathrm{MF}} = \sum_{\langle i,j\rangle}\sum_{\sigma=1}^{N} t_{i,j} f^\dagger_{i,\sigma} f_{j,\sigma}, \tag{2.6}$$

where the hoppings $t_{i,j}$ can either be determined by the self-consistency equation

$$t_{i,j} = -J\sum_{\sigma=1}^{N}\langle \mathrm{FS}|f^\dagger_{i,\sigma} f_{j,\sigma}|\mathrm{FS}\rangle, \tag{2.7}$$

or by minimizing the mean-field variational energy $\langle \mathrm{FS}|\mathcal{H}^{\mathrm{MF}}|\mathrm{FS}\rangle/\langle \mathrm{FS}|\mathrm{FS}\rangle$, where $|\mathrm{FS}\rangle$ is the Fermi sea ground state of the mean-field Hamiltonian $\mathcal{H}^{\mathrm{MF}}$ (2.6). We will determine the $t_{i,j}$ by

minimizing the variational energy given in Eq. (2.14) in the next section. We will call the $\mathcal{H}^{\mathrm{MF}}$ and its hopping structure $t_{i,j}$ an ansatz.

Just like the Hubbard Hamiltonian (1.2), the $\mathcal{H}^{\mathrm{MF}}$ is also invariant under SU(N) spin rotations, because the hoppings $t_{i,j}$ are independent of σ, and the terms $f^\dagger_{i,\sigma}f_{j,\sigma}$ do not change the σ as $f^\dagger_{i,\sigma}f_{j,\bar{\sigma}}$.

In the mean-field approximation, we could take the expectation value of any pair of fermionic operators, which allows for pairing terms like $f^\dagger_{i,\sigma}f^\dagger_{j,\sigma'}$. In the context of the SU(2) symmetric Heisenberg model, these pairing terms $f^\dagger_{i,\uparrow}f^\dagger_{j,\downarrow}$ transform as a singlet and they appear in the mean-field Hamiltonians of Z_2 spin liquids [2, Secs. 9.2.1.1, 9.2.1.2]. However, in the fundamental representation of SU(N), we would have to take the product of N creation operators to form an operator transforming as an SU(N) singlet, which is beyond the mean-field description.

2.1.1 The Fermi sea

The Fermi sea is constructed by filling the lowest energy one-particle eigenstates $|\xi_{\mathbf{q},b}\rangle \equiv f^\dagger_{\mathbf{q},b,\sigma}|0\rangle$ (which are independent of σ, see Eq. (2.27)) of $\mathcal{H}^{\mathrm{MF}}$ up to the Fermi energy $\varepsilon_b(\mathbf{q}) < \varepsilon_{\mathrm{F}}$ as

$$|\mathrm{FS}\rangle = \prod_{\sigma=1}^{N} \prod_{\substack{\mathbf{q},b \\ \varepsilon_b(\mathbf{q})<\varepsilon_{\mathrm{F}}}} f^\dagger_{\mathbf{q},b,\sigma}|0\rangle, \tag{2.8}$$

where the ε_{F} is determined by the $1/N$ filling. In principle, the number of particles of different flavors N_σ might all differ, satisfying $\sum_\sigma N_\sigma = N_s$, where N_s is the number of lattice sites.

If $N_\sigma = N_s/N$ for all σ, and the Fermi sea is non-degenerate (achieved by antiperiod boundary conditions), then the single-particle eigenstates $|\xi_{\mathbf{q},b}\rangle$ with $\varepsilon_b(\mathbf{q}) < \varepsilon_{\mathrm{F}}$ are filled with fermions of every flavor σ as $\prod_{\sigma=1}^{N} f^\dagger_{\mathbf{q},b,\sigma}|0\rangle$, which is antisymmetric under the exchange of any two flavors. Consequently, the Fermi sea transforms as an SU(N) singlet, represented with a Young tableau of N rows and N_s/N columns. The eigenvalue of the total quadratic Casimir operator of Eq. (1.22) is zero for an SU(N) singlet.

We can rewrite the Fermi sea to real space using the basis

$$|x\rangle = \left(\prod_{\sigma=1}^{N} f^\dagger_{j_1^\sigma,\sigma}f^\dagger_{j_2^\sigma,\sigma}\cdots f^\dagger_{j_{N_\sigma}^\sigma,\sigma}\right)|0\rangle = f^\dagger_{j_1^1,1}f^\dagger_{j_2^1,1}\cdots f^\dagger_{j_{N_1}^1,1}\cdots f^\dagger_{j_1^N,N}f^\dagger_{j_2^N,N}\cdots f^\dagger_{j_{N_N}^N,N}|0\rangle, \tag{2.9}$$

where j_l^σ is the site of the l-th fermion of flavor σ, and $l \in \{1 \dots N_\sigma\}$. In this basis, the coefficients of the Fermi sea are Slater determinants [4, Sec. 9.2.1]

$$|\mathrm{FS}\rangle = \sum_{\{\{j^\sigma\}\}} \left(\prod_{\sigma=1}^{N} \mathrm{slat}_{\{j^\sigma\}} f^\dagger_{j_1^\sigma,\sigma}f^\dagger_{j_2^\sigma,\sigma}\cdots f^\dagger_{j_{N_\sigma}^\sigma,\sigma}\right)|0\rangle = \sum_x \left(\prod_{\sigma=1}^{N} \mathrm{slat}_{\{j^\sigma\}}\right)|x\rangle, \tag{2.10}$$

where $\{j^\sigma\}$ is the set of sites j_l^σ occupied by fermions of flavor σ (the number of sites in such a set is N_σ), and the $\sum_{\{\{j^\sigma\}\}}$ goes through all possible such sets. As multiply occupied sites are allowed in $|\mathrm{FS}\rangle$ the sets of sites $\{j^\sigma\}$ may overlap (e.g. $j_l^1 = j_{l'}^2 = 5$ means that at site 5 there are two fermions, one with flavor 1 and another with flavor 2). The ordering of fermionic operators with the same flavor is arbitrary, but must match the order of indices in the Slater determinant

$$\mathrm{slat}_{\{j^\sigma\}} = \begin{vmatrix} \xi_1(j_1^\sigma) & \xi_1(j_2^\sigma) & \cdots & \xi_1(j_{N_s/N}^\sigma) \\ \xi_2(j_1^\sigma) & \xi_2(j_2^\sigma) & \cdots & \xi_2(j_{N_s/N}^\sigma) \\ \vdots & \vdots & \ddots & \vdots \\ \xi_{N_s/N}(j_1^\sigma) & \xi_{N_s/N}(j_2^\sigma) & \cdots & \xi_{N_s/N}(j_{N_s/N}^\sigma) \end{vmatrix}, \tag{2.11}$$

where $\xi_n(j) = \langle 0|f_{j,\sigma}|\xi_n\rangle$, and $|\xi_n\rangle$ are the one-particle eigenstates of $\mathcal{H}^{\mathrm{MF}}$ sorted in energy $\varepsilon_b(\mathbf{q})$, so that the sets of states $\{|\xi_n\rangle\}$ and $\{|\xi_{\mathbf{q},b}\rangle\}$ are the same, and the smaller n index corresponds to smaller or equal eigen energy ε_n of $|\xi_n\rangle$.

If the hoppings $t_{i,j}$ are real, then the $\mathcal{H}^{\mathrm{MF}}$ is time-reversal symmetric, implying that its eigenstates $|\xi_{\mathbf{k}}\rangle$ and $|\xi_{-\mathbf{k}}\rangle$ are degenerate. Consequently, we can construct real one-particle eigenstates $|\xi_n\rangle$ as linear combinations of $|\xi_{\mathbf{k}}\rangle$ and $|\xi_{-\mathbf{k}}\rangle$. This choice makes the Slater determinants (2.11) real, making calculations faster.

2.2 Gutzwiller projection

The mean-field ground state $|\mathrm{FS}\rangle$ of Eq. (2.8) does not satisfy the single occupancy constraint of Eq. (2.5), as can be seen in Eq. (2.10) from the possible overlap of the sets of sites $\{j^\sigma\}$ occupied by flavor σ. Consequently, the Hilbert space of fermions does not represent correctly the Hilbert space of the original Heisenberg model (1.18). The single occupancy constraint (2.5) can be enforced by the Gutzwiller projector [55], defined as the hermitian operator

$$P_{\mathrm{G}} = \prod_{j=1}^{N_s} \frac{1}{(N-1)!} n_j \prod_{m=2}^{N} (m - n_j) \,, \tag{2.12}$$

where $n_j \equiv \sum_{\sigma=1}^{N} f_{j,\sigma}^\dagger f_{j,\sigma}$ is the total fermion number operator. The term $\prod_{m=2}^{N}(m-n_j)$ gives zero if the number of fermions on site j is larger than 1, while n_j gives zero when there is no fermion. The factor $\frac{1}{(N-1)!}$ is to get 1 when n_j gives an eigenvalue 1, so that P_{G} really acts as a projector. As we have a product for each lattice site, the Gutzwiller projector projects to zero all configuration states $|x\rangle$ defined in Eq. (2.9) where any of the sites is not singly occupied. Applying the Gutzwiller projector on the mean-field ground state of Eq. (2.10) eliminates all configurations $|x\rangle$ (2.9) violating the single occupancy constraint (2.5), so that we can write it similarly as in Eq. (2.10)

$$P_{\mathrm{G}}|\mathrm{FS}\rangle = \sum_{\{\{j^\sigma\}_{P_{\mathrm{G}}}\}} \left(\prod_{\sigma=1}^{N} \mathrm{slat}_{\{j^\sigma\}_{P_{\mathrm{G}}}} f_{j_1^\sigma,\sigma}^\dagger f_{j_2^\sigma,\sigma}^\dagger \dots f_{j_{N_\sigma}^\sigma,\sigma}^\dagger \right) |0\rangle = \sum_{x_{P_{\mathrm{G}}}} \left(\prod_{\sigma=1}^{N} \mathrm{slat}_{\{j^\sigma\}_{P_{\mathrm{G}}}} \right) |x_{P_{\mathrm{G}}}\rangle, \tag{2.13}$$

where $|x_{P_{\mathrm{G}}}\rangle$ are of the same form as in Eq. (2.9) with the difference that the sets of sites $\{j^\sigma\}_{P_{\mathrm{G}}}$ occupied by different flavors do not overlap. This equation shows us that any geometrical transformation commutes with the Gutzwiller projector since it does not matter whether we first eliminate configurations $|x\rangle$ (2.9) with multiply occupied sites and then apply a geometrical transformation or do it in the opposite order. Here, we showed it only for the Gutzwiller projected Fermi sea, but any Gutzwiller projected state can be written in the basis $|x_{P_{\mathrm{G}}}\rangle$, so we can repeat the same argument.

We could have introduced a chemical potential in the mean-field Hamiltonian (equivalent to fixing the filling), which would have ensured the single occupancy only in average $\langle \mathrm{FS}|n_j|\mathrm{FS}\rangle = 1$ (even if the chemical potential is site dependent) instead of $n_j = 1$ as in Eq. (2.5). The $n_j = 1$ single occupancy constraint could be achieved by a time-dependent chemical potential (see [2, Sec. 9.1.1] Eq. (9.1.8)), so that the effect of the Gutzwiller projector is to incorporate the temporal fluctuations of the chemical potential. Therefore, $P_{\mathrm{G}}|\mathrm{FS}\rangle$ is a better approximation for the real ground state of the Heisenberg Hamiltonian (1.18) than the mean-field ground state $|\mathrm{FS}\rangle$, and the $t_{i,j}$ hoppings of the mean-field Hamiltonian $\mathcal{H}^{\mathrm{MF}}$ (2.6) are determined by minimizing the variational energy

$$E_{P_{\mathrm{G}}|\mathrm{FS}\rangle} \equiv \frac{\langle \mathrm{FS}|P_{\mathrm{G}}\mathcal{H}P_{\mathrm{G}}|\mathrm{FS}\rangle}{\langle \mathrm{FS}|P_{\mathrm{G}}P_{\mathrm{G}}|\mathrm{FS}\rangle} \tag{2.14}$$

(where $\mathcal{H}$ is the original Heisenberg Hamiltonian (1.18)), instead of the mean-field variational energy $\langle \mathrm{FS}|\mathcal{H}^{\mathrm{MF}}|\mathrm{FS}\rangle/\langle \mathrm{FS}|\mathrm{FS}\rangle$. When optimizing the $t_{i,j}$ we do not have to care about the overall magnitude of the hoppings $\sum_{\langle i,j\rangle} |t_{i,j}|$, because these do not affect the wavefunction $P_{\mathrm{G}}|\mathrm{FS}\rangle$, only the relative ratios $t_{i,j}/t_{m,n}$ matter.

As the analytic evaluation of the Gutzwiller projection is too difficult, all expectation values as Eq. (2.14) in the Gutzwiller projected state are evaluated numerically, within a Monte Carlo calculation [56, 57]. In a Monte Carlo calculation, we visit configurations $|x\rangle$ of Eq. (2.9) with certain probabilities, and evaluate the expectation values as (2.14) in these configurations. The effect of the Gutzwiller projector is to visit only those configurations $|x\rangle$, where the sets of sites $\{j^\sigma\}_{P_{\mathrm{G}}}$ occupied by different flavors σ do not overlap, as explained in Appendix J.

In the following, we are going to make frequent citations of sections of the book [2] for easy comparison with the SU(2) case, where an ansatz is described by the $U_{i,j}$ containing both the $t_{i,j}$ and the SU(2) singlet pairing terms $f^\dagger_{i,\uparrow}, f^\dagger_{j,\downarrow}$ [2, Secs. 9.2.1.1, 9.2.1.2]

The Gutzwiller projector (2.12) is a function of the total fermion number operator $n_j = \sum_{\sigma=1}^{N} f^\dagger_{j,\sigma} f_{j,\sigma}$, so it commutes with the SU(N) spin operators of Eq. (2.2)

$$[P_{\mathrm{G}}, T^a_j] = 0 \tag{2.15}$$

, since the T^a_j have one $f^\dagger$ and one f that does not change the eigenvalue of n_j. Similarly, P_{G} also commutes with the total spin operators $T^a_{\mathrm{T}} = \sum_{j=1}^{N_s} T^a_j$. Therefore, it also commutes with all the Casimir operators on any site and also with the total Casimir operators since these are functions of the T^a_j and T^a_{T}, respectively. Consequently, applying the P_{G} on a wavefunction does not change the eigenvalues of the Casimir operators for that wavefunction. For example, if the Fermi sea transforms as an SU(N) singlet, identified with the zero eigenvalue of the total quadratic Casimir operator (1.22), then the $P_{\mathrm{G}}|\mathrm{FS}\rangle$ also transforms as an SU(N) singlet. If we have a set of states that serves as a basis for other irreducible representations, then the set of these Gutzwiller projected states will also serve as a basis for the same irreducible representation (see Appendix A.6.3).

2.3 Variational states

One would think that if we want to end up with a variational wavefunction $P_{\mathrm{G}}|\mathrm{FS}\rangle$, which is invariant under all symmetries of the Hamiltonian (1.18) and the underlying lattice, then the only way to achieve this is by starting from a mean-field Hamiltonian $\mathcal{H}^{\mathrm{MF}}$ with uniform equal hoppings $t_{i,j}$.

However, the decomposition of the SU(N) spin operators to fermions (2.2) does not unambiguously define the fermionic operators $f^\dagger_{i,\sigma}$, because a site-dependent, but flavor independent unitary gauge transformation [2, Eq. (9.1.11)]

$$G f^\dagger_{j,\sigma} G^{-1} = e^{i\phi(j)} f^\dagger_{j,\sigma} \tag{2.16}$$

leaves the SU(N) spin operators in Eq. (2.2) unchanged, since

$$G T^a_j G^{-1} = \frac{1}{2} \sum_{\sigma,\sigma'=1}^{N} e^{i\phi(j)} f^\dagger_{j,\sigma} \lambda^a_{\sigma,\sigma'} e^{-i\phi(j)} f_{j,\sigma'} = \frac{1}{2} \sum_{\sigma,\sigma'=1}^{N} f^\dagger_{i,\sigma} \lambda^a_{\sigma,\sigma'} f_{i,\sigma'} = T^a_j. \tag{2.17}$$

These gauge transformations do not affect the Gutzwiller projected wavefunctions, so we can use them to construct completely symmetric variational wavefunctions $P_{\mathrm{G}}|\mathrm{FS}\rangle$, even if the $\mathcal{H}^{\mathrm{MF}}$ breaks the symmetries of the lattice (this is the projective symmetry explained in section 2.4). Different mean-field Hamiltonians yield different completely symmetric variational wavefunctions

$P_G|\mathrm{FS}\rangle$. The optimal wavefunction is then selected by minimizing the variational energy defined in Eq. (2.14).

In the following two subsections, we present the mean-field Hamiltonians $\mathcal{H}^{\mathrm{MF}}_{\mathrm{DSL}}$ (2.6) of the Dirac spin liquid (DSL) variational states, which give a good approximation of the ground states of the SU(4) and SU(6) Heisenberg models on the honeycomb and kagome lattices, respectively. Both of these states share similar features, namely the hoppings $t_{i,j}$ of $\mathcal{H}^{\mathrm{MF}}$ are all real, their absolute values are equal, but their signs are such, that their product around any elementary plaquette is negative [49, 50]. We can associate a phase $t_{i,j} = |t_{i,j}|e^{i\phi_{i,j}}$ to every hopping ($\phi_{i,j} = \pi$ for negative hoppings), so that the product of the hoppings involves the sum of these phases $e^{i\sum_{\langle i,j\rangle}\phi_{i,j}}$ around an elementary plaquette modulo 2π. The sum $\sum_{\langle i,j\rangle}\phi_{i,j}$ can be interpreted as the integral of an imaginary vector potential around an elementary plaquette which is equal to the imaginary magnetic flux ϕ through the elementary plaquette. In general, the flux ϕ of a plaquette can be calculated as

$$e^{i\phi} = \prod_{\langle i,j\rangle\in\text{plaquette}} \frac{t_{i,j}}{|t_{i,j}|}, \tag{2.18}$$

In the case of complex hopping, the product should be taken with some orientation, e.g., clockwise. For real hoppings the orientation is irrelevant, and one can have only two inequivalent possibilities, 0-flux and π-flux, corresponding to positive and negative products, respectively. Therefore, both Dirac spin liquid ansätze have π fluxes in every elementary plaquette of their lattices, see Fig. 2.1 (a) and (c).

The π-flux hopping structure of the mean-field Hamiltonian $\mathcal{H}^{\mathrm{MF}}_{\mathrm{DSL}}$ (shown in Figs. 2.1 (a) and (c)) requires at least a doubled unit cell to accommodate the hoppings $t_{i,j}$ for both the honeycomb and the kagome lattices [6, 58]. Therefore in both cases the $\mathcal{H}^{\mathrm{MF}}_{\mathrm{DSL}}$ breaks (among others) the discrete translational symmetry of the underlying lattice in some direction, yet as explained in the next section 2.4 the Gutzwiller projected variational wave function $P_G|\pi\mathrm{FS}\rangle$ have all the symmetries of the lattice, justifying the name spin liquid.

Even though the hoppings of the π-flux $\mathcal{H}^{\mathrm{MF}}_{\mathrm{DSL}}$ could be accommodated in doubled unit cells, here we choose different hopping patterns requiring quadrupled unit cells, because these have more beautiful symmetries. The gauge equivalence of these choices is discussed in Appendix F.

2.3.1 The SU(4) π-flux Dirac Spin liquid on the Honeycomb lattice

The SU(4) Heisenberg model on the honeycomb lattice is an example where the π-flux $\mathcal{H}^{\mathrm{MF}}_{\mathrm{DSL}}$ (shown in Fig. 2.1 (a)), breaking the symmetries of the lattice, gives a variational wavefunction with better variational energy (2.14) than the 0-flux $\mathcal{H}^{\mathrm{MF}}$, which has all the symmetries of the honeycomb lattice. Based on Refs. [6, 59, 60, 61, 62, 63] the π-flux variational wavefunction is a good approximation of the ground state of the SU(4) Heisenberg model on the honeycomb lattice, though there are doubts about a possible gap opening [64, 65]. Although these articles discussed the π-flux $\mathcal{H}^{\mathrm{MF}}_{\mathrm{DSL}}$ with a doubled unit cell, here we will use the $\mathcal{H}^{\mathrm{MF}}_{\mathrm{DSL}}$ with the quadrupled unit cell shown in Fig. 2.1 (a). The equivalence of the two Hamiltonians is discussed in Appendix F.

The honeycomb lattice has two basis sites per unit cell, with basis vectors $\boldsymbol{\delta}_A = (0,0)$ and $\boldsymbol{\delta}_B = (0, \frac{1}{\sqrt{3}})$, and is periodic under translations by the primitive vectors $\mathbf{a}_1 = (1,0)$ and $\mathbf{a}_2 = (-1/2, \sqrt{3}/2)$, which span the triangular Bravais lattice $\mathbf{R} = R_1\mathbf{a}_1 + R_2\mathbf{a}_2$ with R_1, R_2 integers. The number of Bravais lattice vectors is equal to the number of unit cells N_C, which equals the number of wave vectors in the reciprocal unit cell (Brillouin zone). The lattice vector of any site j can be written as $\mathbf{r_j} = \mathbf{R}_j + \boldsymbol{\delta}_{s_j}$, where $s_j \in \{A, B\}$ is the sublattice index. The product of the number of basis sites $N_B = 2$ and the number of Bravais-lattice vectors N_C is always equal to the number of lattice sites $N_s = N_C \times N_B$.

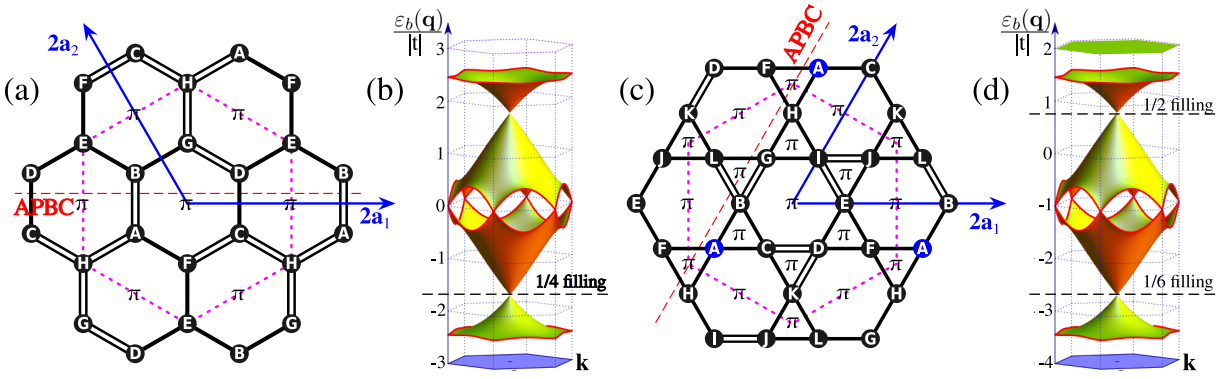

Figure 2.1: (a) and (c) shows the hopping structures of the π-flux mean-field Hamiltonians with quadrupled unit cells on the honeycomb and kagome lattices, respectively. The magenta dashed hexagons denote the quadrupled Wigner-Seitz unit cells. Every white bond is a positive hopping, and every black bond a negative one, so that the product of the hoppigs around every elementary plaquette is negative (hence the name π-flux, see Eq. (2.18)). All hoppings have the same absolute value $|t|$. (b) and (d) shows the one-particle energy spectrum given by Eqs. (2.26) and (2.31) on the honeycomb and kagome lattices, respectively. Every band is doubly degenerate, except the flat band with $\varepsilon = 2t$ in (d), which is four-fold degenerate. The single occupancy constraint (2.5) of the SU(N) mean-field Hamiltonian requires $1/N$ filling, which fills both band structures up to the tip of the lowest energy Dirac cones, resulting in Dirac Fermi points (hence the name Dirac spin liquid).

The quadrupled unit cell of the π-flux $\mathcal{H}^{\mathrm{MF}}$ shown in Figs. 2.1 (a) breaks the discrete translational symmetry of the honeycomb lattice, with a remaining symmetry for translations by the doubled primitive vectors $2\mathbf{a}_1$ and $2\mathbf{a}_2$, which span the mean-field Bravais lattice

$$\mathbf{R}^{\mathrm{MF}} = R_1^{\mathrm{MF}}(2\mathbf{a}_1) + R_2^{\mathrm{MF}}(2\mathbf{a}_2), \tag{2.19}$$

with $R_1^{\mathrm{MF}}, R_2^{\mathrm{MF}}$ integers. Consequently, the number of basis sites in the mean-field quadrupled unit cell is $N_B^{\mathrm{MF}} = 4 \times N_B = 8$. Again, the number of lattice sites $N_s = N_C^{\mathrm{MF}} \times N_B^{\mathrm{MF}}$, so that $N_C^{\mathrm{MF}} = N_C/4$, implying that the number of wave vectors in the mean-field Brillouin zone is a quarter of the number of wave vectors in the original Brillouin zone (for details see Appendix H). Thus we will call the mean-field Brillouin zone the reduced Brillouin zone (rBZ).

The lattice vector of any site j can be expressed using the mean-field vectors as

$$\mathbf{r}_j^{\mathrm{MF}} = \mathbf{R}_j^{\mathrm{MF}} + \boldsymbol{\delta}_{s_j^{\mathrm{MF}}}^{\mathrm{MF}}, \tag{2.20}$$

where $s_j^{\mathrm{MF}} \in \{A, B \dots H\}$ is the sublattice index of the quadrupled unit cell, with the mean-field basis vectors $\boldsymbol{\delta}_A^{\mathrm{MF}} = \boldsymbol{\delta}_A$, $\boldsymbol{\delta}_B^{\mathrm{MF}} = \boldsymbol{\delta}_B$, $\boldsymbol{\delta}_C^{\mathrm{MF}} = \boldsymbol{\delta}_A + \mathbf{a}_1$, $\boldsymbol{\delta}_D^{\mathrm{MF}} = \boldsymbol{\delta}_B + \mathbf{a}_1$, $\boldsymbol{\delta}_E^{\mathrm{MF}} = \boldsymbol{\delta}_A + \mathbf{a}_2$, $\boldsymbol{\delta}_F^{\mathrm{MF}} = \boldsymbol{\delta}_B + \mathbf{a}_2$, $\boldsymbol{\delta}_G^{\mathrm{MF}} = \boldsymbol{\delta}_A + \mathbf{a}_1 + \mathbf{a}_2$, $\boldsymbol{\delta}_H^{\mathrm{MF}} = \boldsymbol{\delta}_B + \mathbf{a}_1 + \mathbf{a}_2$.

Using the remaining discrete translational invariance of the π-flux $\mathcal{H}_{\mathrm{DSL}}^{\mathrm{MF}}$, we can Fourier transform the fermionic operators as

$$f_{j,\sigma}^\dagger = f_{\mathbf{R}_j^{\mathrm{MF}}, s_j^{\mathrm{MF}}, \sigma}^\dagger = \frac{1}{\sqrt{N_C^{\mathrm{MF}}}} \sum_{\mathbf{q} \in \mathrm{rBZ}} e^{-i\mathbf{q}\cdot\mathbf{R}_j^{\mathrm{MF}}} f_{\mathbf{q}, s_j^{\mathrm{MF}}, \sigma}^\dagger, \tag{2.21}$$

where we have relabeled site j to $\mathbf{R}_j^{\mathrm{MF}}, s_j^{\mathrm{MF}}$ based on Eq. (2.20), and the wave vectors $\mathbf{q}$ are in the reduced Brilloun-zone (rBZ). This allows us to rewrite the $\mathcal{H}^{\mathrm{MF}}$ in reciprocal space as

$$\mathcal{H}^{\mathrm{MF}} = \sum_{\mathbf{q} \in \mathrm{rBZ}} \sum_{\sigma=1}^{N} \sum_{s^{\mathrm{MF}}, \bar{s}^{\mathrm{MF}}} \mathcal{H}_{s^{\mathrm{MF}}, \bar{s}^{\mathrm{MF}}}^{\mathrm{MF}}(\mathbf{q}) f_{\mathbf{q}, s^{\mathrm{MF}}, \sigma}^\dagger f_{\mathbf{q}, \bar{s}^{\mathrm{MF}}, \sigma}, \tag{2.22}$$

where the $\mathcal{H}^{\mathrm{MF}}_{s^{\mathrm{MF}},\bar{s}^{\mathrm{MF}}}(\mathbf{q})$ is the $N_B^{\mathrm{MF}} \times N_B^{\mathrm{MF}}$ matrix

$$t\begin{pmatrix} 0 & 1 & 0 & 0 & 0 & -1 & 0 & e^{-i2\mathbf{q}\cdot\mathbf{a}_1} \\ 1 & 0 & 0 & 0 & -1 & 0 & -1 & 0 \\ 0 & 0 & 0 & -1 & 0 & 1 & 0 & 1 \\ 0 & 0 & -1 & 0 & -e^{i2\mathbf{q}\cdot\mathbf{a}_1} & 0 & 1 & 0 \\ 0 & -1 & 0 & -e^{-i2\mathbf{q}\cdot\mathbf{a}_1} & 0 & -e^{i2\mathbf{q}\cdot\mathbf{a}_2} & 0 & 0 \\ -1 & 0 & 1 & 0 & -e^{-i2\mathbf{q}\cdot\mathbf{a}_2} & 0 & 0 & 0 \\ 0 & -1 & 0 & 1 & 0 & 0 & 0 & e^{i2\mathbf{q}\cdot\mathbf{a}_2} \\ e^{i2\mathbf{q}\cdot\mathbf{a}_1} & 0 & 1 & 0 & 0 & 0 & e^{-i2\mathbf{q}\cdot\mathbf{a}_2} & 0 \end{pmatrix}\begin{matrix} |\mathrm{A}\rangle \\ |\mathrm{B}\rangle \\ |\mathrm{C}\rangle \\ |\mathrm{D}\rangle \\ |\mathrm{E}\rangle \\ |\mathrm{F}\rangle \\ |\mathrm{G}\rangle \\ |\mathrm{H}\rangle \end{matrix}, \tag{2.23}$$

where the basis states mean $|\mathrm{A}\rangle \equiv f^\dagger_{\mathbf{q},A,\sigma}|0\rangle$. The effect of the antiperiodic boundary condition can be thought of as shifting the wave vectors $\mathbf{q}$.

The characteristic polynomial $0 = \det\left(\mathcal{H}^{\mathrm{MF}}_{s^{\mathrm{MF}},\bar{s}^{\mathrm{MF}}}(\mathbf{q}) - \varepsilon_{\mathbf{q}}\mathcal{I}_{s^{\mathrm{MF}},\bar{s}^{\mathrm{MF}}}\right)$ providing the one-particle energies $\varepsilon_{\mathbf{q}}$ simplifies to

$$0 = \left(\varepsilon^4_{\mathbf{q}} - 6t^2\varepsilon^2_{\mathbf{q}} + t^4\gamma_{\mathbf{q}}\right)^2, \tag{2.24}$$

where

$$\gamma_{\mathbf{q}} = 3 + 2\cos 2\mathbf{q}\cdot\mathbf{a_1} + 2\cos 2\mathbf{q}\cdot\mathbf{a_2} + 2\cos 2\mathbf{q}\cdot[\mathbf{a_1}+\mathbf{a_2}]. \tag{2.25}$$

The squared form of the characteristic polynomial implies that every eigenvalue is doubly degenerate. The quartic polynomial in $\varepsilon_{\mathbf{q}}$ implies that we will get four energy eigenvalues for every $\mathbf{q}$, which span four energy bands in reciprocal space, shown in the reduced Brillouin zone of the quadrupled unit cell (see Appendix H) in Fig. 2.1 (b). The energy eigenvalues can be written as

$$\varepsilon_b(\mathbf{q}) = \pm|t|\sqrt{3 \pm \sqrt{6 - 2\cos(2\mathbf{q}\cdot\mathbf{a}_1) - 2\cos(2\mathbf{q}\cdot\mathbf{a}_2) - 2\cos\left(2\mathbf{q}\cdot(\mathbf{a}_1+\mathbf{a}_2)\right)}} \tag{2.26}$$

where $b \in \{1\ldots8\}$ is the band index, such that $b \in \{1,2\}$ are in the first band, $b \in \{3,4\}$ in the second, $b \in \{5,6\}$ in the third, and $b \in \{7,8\}$ in the fourth band, due to the double degeneracy of the eigenvalues.

The one-particle eigenstates of the matrix $\mathcal{H}^{\mathrm{MF}}_{s^{\mathrm{MF}},\bar{s}^{\mathrm{MF}}}(\mathbf{q})$ (2.23) can be written as

$$|\xi_{\mathbf{q},b}\rangle \equiv f^\dagger_{\mathbf{q},b,\sigma}|0\rangle = \sum_s v_{\mathbf{q},b,s} f^\dagger_{\mathbf{q},s,\sigma}|0\rangle = \frac{1}{\sqrt{N_C^{\mathrm{MF}}}}\sum_s v_{\mathbf{q},b,s}\sum_{\mathbf{R}^{\mathrm{MF}}} e^{i\mathbf{q}\mathbf{R}^{\mathrm{MF}}} f^\dagger_{\mathbf{R},s,\sigma}|0\rangle, \tag{2.27}$$

where $b \in \{1\ldots8\}$ is the band index, $s \in \{A\ldots H\}$ is the sublattice index, and the complex numbers $v_{\mathbf{q},b,s}$ are the coefficients of the eigenstate in the site basis $\{f^\dagger_{\mathbf{q},s,\sigma}|0\rangle\}$, which are normalized as $\sum_s |v_{\mathbf{q},b,s}|^2 = 1$. The one-particle eigenstates $|\xi_{\mathbf{q},b}\rangle$ are independent of σ (so that the σ index of $f^\dagger_{\mathbf{q},b,\sigma}$ can be anything), since the matrix $\mathcal{H}^{\mathrm{MF}}_{s^{\mathrm{MF}},\bar{s}^{\mathrm{MF}}}(\mathbf{q})$ of Eq. (2.23) is independent of σ.

When we construct the $|\pi\mathrm{FS}\rangle$ of Eq. (2.8), we create a product state of the lowest energy one-particle eigenstates of the $\mathcal{H}^{\mathrm{MF}}_{\mathrm{DSL}}$ which have the energies Eq. (2.26) smaller than the Fermi energy ε_F. Due to the $1/N$ filling corresponding to the single occupancy constraint of Eq. (2.5), only the lowest energy band is filled, so that the Fermi energy is $\varepsilon_{\mathrm{F}} = -\sqrt{3}|t|$, where the Dirac cones touch at $\mathbf{q} = 0$. This is the reason why the $P_{\mathrm{G}}|\pi\mathrm{FS}\rangle$ variational state is called a Dirac spin liquid (DSL), and it will be the reason for the existence of gapless excitations having linear dispersion at small energies (see Sec. 6). Since at the Fermi energy ε_{F} the cross-section of the bands is only a point, the tip of the Dirac cones, we will call the Fermi energy the Dirac Fermi point.

2.3.2 The SU(6) π-flux Dirac Spin liquid on the Kagome lattice

In Sec. 3 we will argue that the Dirac spin liquid state might also be a good approximation of the ground state of the SU(6) Heisenberg model in the fundamental representation on the kagome lattice.

In the kagome lattice we have $N_B = 3$ basis sites, with basis vectors $\boldsymbol{\delta}_A = (0,0)$, $\boldsymbol{\delta}_B = (1/2,0)$, and $\boldsymbol{\delta}_C = (1/4, \sqrt{3}/4)$. The periodicity of the kagome lattice is given by the primitive vectors $\mathbf{a_1} = (1,0)$ and $\mathbf{a}_2 = \left(\frac{1}{2}, \frac{\sqrt{3}}{2}\right)$. The mean-field Hamiltonian $\mathcal{H}^{\mathrm{MF}}_{\mathrm{DSL}}$ with a quadrupled unit cell (shown in Fig. 2.1) (c) breaks (among others) the discrete translational symmetry of the kagome lattice in both directions, with a remaining periodicity in $2\mathbf{a_1}$ and $2\mathbf{a_2}$. In this quadrupled unit cell, the number of basis sites is $N_B^{\mathrm{MF}} = 4N_B = 12$, therefore the reduced Brillouin zone is again the quarter of the original Brillouin zone. Using this remaining periodicity we can Fourier transform the fermionic operators just as in Eq. (2.21), and rewrite the $\mathcal{H}^{\mathrm{MF}}$ to reciprocal space just as in Eq. (2.22). We end up with the 12×12 matrix

$$\mathcal{H}^{\mathrm{MF}}_{b,\bar{b}}(\mathbf{q}) = t \begin{pmatrix} 0 & -1 & -1 & 0 & 0 & -\bar{r}_1 & 0 & -\bar{r}_2 & 0 & 0 & 0 & 0 \\ -1 & 0 & -1 & 0 & 0 & 0 & 1 & 0 & 0 & 0 & 0 & \bar{r}_1 \\ -1 & -1 & 0 & 1 & 0 & 0 & 0 & 0 & 0 & 0 & -\bar{r}_2 & 0 \\ 0 & 0 & 1 & 0 & -1 & -1 & 0 & 0 & 0 & 0 & \bar{r}_2 & 0 \\ 0 & 0 & 0 & -1 & 0 & -1 & 0 & 0 & 1 & -1 & 0 & 0 \\ -r_1 & 0 & 0 & -1 & -1 & 0 & 0 & -r_1\bar{r}_2 & 0 & 0 & 0 & 0 \\ 0 & 1 & 0 & 0 & 0 & 0 & 0 & -1 & -1 & 0 & 0 & -\bar{r}_1 \\ -r_2 & 0 & 0 & 0 & 0 & -r_2\bar{r}_1 & -1 & 0 & -1 & 0 & 0 & 0 \\ 0 & 0 & 0 & 0 & 1 & 0 & -1 & -1 & 0 & 1 & 0 & 0 \\ 0 & 0 & 0 & 0 & -1 & 0 & 0 & 0 & 1 & 0 & -1 & -1 \\ 0 & 0 & -r_2 & r_2 & 0 & 0 & 0 & 0 & 0 & -1 & 0 & -1 \\ 0 & r_1 & 0 & 0 & 0 & 0 & -r_1 & 0 & 0 & -1 & -1 & 0 \end{pmatrix}, \tag{2.28}$$

where $r_1 = e^{i\mathbf{q}\cdot 2\mathbf{a}_1}$ or $r_2 = e^{i\mathbf{q}\cdot 2\mathbf{a}_2}$ (the $\bar{r}_1 = e^{-i\mathbf{k}\cdot 2\mathbf{a}_1}$ and $\bar{r}_2 = e^{-i\mathbf{k}\cdot 2\mathbf{a}_2}$ are the complex conjugates).

The characteristic polynomial $0 = \det\left(\mathcal{H}^{\mathrm{MF}}_{s^{\mathrm{MF}},\bar{s}^{\mathrm{MF}}}(\mathbf{q}) - \varepsilon_{\mathbf{q}}\mathcal{I}_{s^{\mathrm{MF}},\bar{s}^{\mathrm{MF}}}\right)$ providing the one-particle energies $\varepsilon_{\mathbf{q}}$, simplifies to

$$0 = \left(\varepsilon_{\mathbf{q}}^4 + 4t\varepsilon_{\mathbf{q}}^3 - 8t^3\varepsilon_{\mathbf{q}} + 2t^4\gamma_{\mathbf{q}}\right)^2 (\varepsilon_{\mathbf{q}} - 2t)^4, \tag{2.29}$$

where

$$\gamma_{\mathbf{q}} = \cos 2\mathbf{q}\cdot\mathbf{a_1} + \cos 2\mathbf{q}\cdot\mathbf{a_2} + \cos 2\mathbf{q}\cdot[\mathbf{a_1} - \mathbf{a_2}] - 1. \tag{2.30}$$

The squared form of the quartic polynomial in $\varepsilon_{\mathbf{q}}$ again implies 4 doubly degenerate bands, while the $(\varepsilon_{\mathbf{q}} - 2t)^4$ term gives a four-fold degenerate flat band at $\varepsilon_{\mathbf{q}} = 2t$, shown in Fig. 2.1(d). Unlike in the zero-flux case, the dispersive bands are separated by a gap from the flat bands (implying that the flat band is not topological, unlike in the 0-flux case [66]), and the dispersive bands touch at Dirac points. Interestingly, the characteristic polynomial of the honeycomb lattice (2.24) can be mapped exactly to the first term of Eq. (2.29) not containing the flat bands, if we shift the $\varepsilon_{\mathbf{q}} \to \varepsilon_{\mathbf{q}} + t$ of the honeycomb lattice, and we change the primitive vector $\mathbf{a}_2 \to \mathbf{a}_1 + \mathbf{a}_2$ of the kagome lattice. Therefore, the 4 doubly degenerate energy eigenvalues of the $\mathcal{H}^{\mathrm{MF}}_{b,\bar{b}}(\mathbf{q})$ on the kagome lattice will be simply shifted by t relative to those on the honeycomb lattice (2.26)

$$\begin{aligned} &2\times\text{degen: } \varepsilon_b(\mathbf{q}) = -t \pm |t|\sqrt{3 \pm \sqrt{6 - 2\cos 2\mathbf{q}\cdot\mathbf{a_1} - 2\cos 2\mathbf{q}\cdot\mathbf{a_2} - 2\cos 2\mathbf{q}\cdot[\mathbf{a_1} - \mathbf{a_2}]}} \\ &4\times\text{degen: } \varepsilon_b(\mathbf{q}) = 2t, \end{aligned} \tag{2.31}$$

where in the first row, the band index $b \in \{1\ldots 8\}$, such that $b \in \{1,2\}$ are in the first band, $b \in \{3,4\}$ in the second, $b \in \{5,6\}$ in the third, and $b \in \{7,8\}$ in the fourth band, while in the second row $b \in \{9\ldots 12\}$.

Consequently, this band structure inherits the Dirac cone touchings of the honeycomb lattice. We call the $P_{\mathrm{G}}|\pi\mathrm{FS}\rangle$ a Dirac spin liquid (DSL) because due to the 1/6 filling, the Fermi energy is at $\varepsilon_{\mathrm{F}} = -t - \sqrt{3}|t|$, where the Dirac cones touch. The equivalent of this DSL ansatz with a doubled unit cell was proposed as a candidate for the ground state of the SU(2) Heisenberg model on the kagome lattice [58], which differs only in the filling of the band structure. In the SU(2) case the 1/2 filling requires filling the one-particle eigenstates in the lowest 3 bands up to the Fermi energy $\varepsilon_{\mathrm{F}}^{\mathrm{SU}(2)} = -t + \sqrt{3}|t|$, where the highest lying 2 Dirac cones touch (see Fig. 2.1(d)). Actually, the idea of trying this DSL state as a candidate for the SU(6) case came from the possibility of changing the filling so that the Fermi energy is lowered to the touching point of the lowest two Dirac cones, which required 1/6 filling.

It is important to note, that although in the case of the honeycomb lattice the change $t \to -t$ does not influence anything, here it changes a lot, since it changes the fluxes of the triangles from π to 0, keeping the π fluxes of the hexagons. It also changes the sign of t in the characteristic polynomial (2.29), which contains t contrary to the characteristic polynomial of the honeycomb lattice (2.24) containing only $|t|$. The effect of the $t \to -t$ is to turn the band structure of the DSL (Fig. 2.1 (d)) upside down, leaving the four-fold degenerate flat band at the bottom. The 1/6 filling fills only half of the flat band, therefore the Fermi energy is inside the flat band, and the Fermi sea of this ansatz is highly degenerate, making any calculation impossible. In the case of SU(2), the filling is 1/2 instead of 1/6, so that the Fermi energy is outside the flat band at the touching of two Dirac cones. Furthermore, in the SU(2) case the ansatz with 0 fluxes in the triangles and π fluxes in the hexagons is equivalent to the DSL ansatz with π-fluxes everywhere due to a symmetry under a combination of a spin-rotation and a time-reversal transformation [2, Sec. 9.2.7] [3]), but they are inequivalent in the case of SU(6).

2.4 Projective symmetry and Quantum orders

As mentioned in Sec.2.3 the π-flux hopping structure of $\mathcal{H}^{\mathrm{MF}}$ shown in Figs. 2.1 (a) and (c) break the discrete translational symmetry of the underlying lattice for translations T_1 and T_2 with primitive vectors $\mathbf{a}_1$ and $\mathbf{a}_2$, respectively, meaning that $\mathcal{H}^{\mathrm{MF}} \neq \mathsf{T}_i \mathcal{H}^{\mathrm{MF}} \mathsf{T}_i^{-1}$ for $i \in \{1,2\}$. $\mathcal{H}^{\mathrm{MF}}$ has a remaining translational symmetry for translations with $2\mathbf{a}_1$ and $2\mathbf{a}_2$, so that $\mathcal{H}^{\mathrm{MF}} = (\mathsf{T}_i)^2 \mathcal{H}^{\mathrm{MF}} (\mathsf{T}_i^{-1})^2$ for $i \in \{1,2\}$. The $\mathcal{H}^{\mathrm{MF}}$ also breaks the symmetries under the C_6 sixfold rotation and the σ reflection, which generate the D_6 point group of both the honeycomb and kagome lattices. Yet, the expectation values $\langle T_i^a \rangle$ of the SU(N) spin operators (2.2) and their correlation functions $\langle T_i^a T_j^a \rangle$ will possess all the symmetries of the underlying lattice in both states $|\pi\mathrm{FS}\rangle$ and $P_{\mathrm{G}}|\pi\mathrm{FS}\rangle$, due to the projective symmetry of $\mathcal{H}^{\mathrm{MF}}$ for the geometric transformations (assuming periodic boundary conditions, for APBC see E.2).

As discussed in section 2.3, a site-dependent, but flavor-independent gauge transformation $G f_{j,\sigma}^\dagger G^{-1} = e^{i\phi(j)} f_{j,\sigma}^\dagger$, defined in Eq. (2.16), leaves the spin operators invariant, as shown in Eq. (2.17). One can use this gauge redundancy of the projective construction to restore the symmetries of $\mathcal{H}^{\mathrm{MF}}$ under the geometrical transformations $\mathsf{g} \in \{\mathsf{C}_6, \sigma, \mathsf{T}_1, \mathsf{T}_2\}$, by applying suitable gauge transformations $G_{\mathsf{g}} \in \{G_{\mathsf{C}_6}, G_\sigma, G_{\mathsf{T}_1}, G_{\mathsf{T}_2}\}$ which undo the effects of the geometrical transformations $\mathsf{g}\mathcal{H}^{\mathrm{MF}}\mathsf{g}^{-1}$ as

$$\mathcal{H}^{\mathrm{MF}} = G_{\mathsf{g}} \mathsf{g} \mathcal{H}^{\mathrm{MF}} \mathsf{g}^{-1} G_{\mathsf{g}}^{-1} = \tilde{\mathsf{g}} \mathcal{H}^{\mathrm{MF}} \tilde{\mathsf{g}}^{-1}, \tag{2.32}$$

so that $\mathcal{H}^{\mathrm{MF}}$ is invariant under the combined operation $\tilde{\mathsf{g}} \equiv G_{\mathsf{g}} \mathsf{g}$, called projective symmetry (see [2, Sec. 9.4.2] and Refs. [67, 68, 69, 3]). For example, the π-flux $\mathcal{H}^{\mathrm{MF}}$ on the honeycomb lattice has a hopping structure (shown in Fig. 2.2(a)) which is not invariant under the translation T_1 by the primitive vector $\mathbf{a}_1$. However, we can change the signs of some $f_{j,\sigma}^\dagger$ on certain lattice sites j (shown in Fig. 2.2 (b)), to reverse the effect of T_1 on the hoppings, since changing the

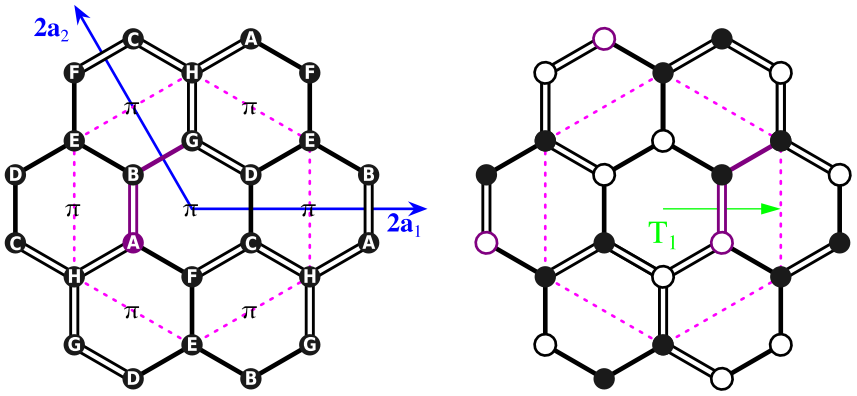

Figure 2.2: (a) The hopping structure of the π-flux $\mathcal{H}^{\mathrm{MF}}$ on the honeycomb lattice, white and black bonds correspond to positive and negative hoppings, respectively. (b) The hopping structure of $\mathcal{H}^{\mathrm{MF}}$ after the translation $\mathsf{T}_1\mathcal{H}^{\mathrm{MF}}\mathsf{T}_1^{-1}$ by the primitive vector $\mathbf{a}_1$. Since the hopping structures are different, $\mathcal{H}^{\mathrm{MF}}$ is not invariant under T_1. However, we can change the signs of some $f^\dagger_{j,\sigma}$ on certain lattice sites j (shown with the white circles in (b)), to reverse the effect of T_1 on the hoppings, since changing the sign of a $f^\dagger_{j,\sigma}$ is equivalent to changing the signs of the hoppings connected to site j. These sign changes correspond to the gauge transformation G_{T_1}, so that the π-flux $\mathcal{H}^{\mathrm{MF}}$ is invariant under the combined transformation $G_{\mathsf{T}_1}\mathsf{T}_1$, since G_{T_1} reverses the effect of T_1.

sign of a $f^\dagger_{j,\sigma}$ is equivalent to changing the signs of the hoppings connected to site j. These sign changes correspond to the gauge transformation G_{T_1}, so that the π-flux $\mathcal{H}^{\mathrm{MF}}$ is invariant under the combined transformation $G_{\mathsf{T}_1}\mathsf{T}_1$, since G_{T_1} reverses the effect of T_1 (for more details see Appendix E).

The set of all $\tilde{\mathsf{g}}$ satisfying Eq. (2.32) form a group, called the projective symmetry group (PSG) (see [2, Sec. 9.4.2] and Refs. [69, 3]). The gauge transformations $G_{\mathsf{C}_6}, G_\sigma, G_{\mathsf{T}_1}, G_{\mathsf{T}_2}$ for both the honeycomb and the kagome lattices are listed in Appendix E

We can use the gauge transformations of Eq. (2.16) to create an equivalence relation, as the following. Two Hamiltonians $\mathcal{H}_1^{\mathrm{MF}}$ and $\mathcal{H}_2^{\mathrm{MF}}$ are gauge equivalent, if there exists a G such that

$$\mathcal{H}_2^{\mathrm{MF}} = G\mathcal{H}_1^{\mathrm{MF}}G^{-1}, \tag{2.33}$$

so $\mathcal{H}_1^{\mathrm{MF}}$ and $\mathcal{H}_2^{\mathrm{MF}}$ are in the same equivalence class. Rephrasing Eq. (2.32), $\mathcal{H}^{\mathrm{MF}}$ is invariant under the combined transformation $G_{\mathsf{g}}\mathsf{g}$, if $\mathcal{H}^{\mathrm{MF}}$ and $\mathsf{g}\mathcal{H}^{\mathrm{MF}}\mathsf{g}^{-1}$ are gauge equivalent. It is important to emphasize that not all mean-field Hamiltonians are gauge equivalent, for example, the 0-flux and the π-flux Hamiltonians can not be connected by gauge transformations, they are in different equivalence classes. Furthermore, one can construct ansätze of staggered 0 and π-fluxes, which again form separate equivalence classes. These equivalence classes are what define the hidden quantum order of the quantum spin liquid state at the mean-field level [3, 69]. On a given lattice, all the ansätze having π-fluxes in every plaquette are gauge equivalent, so that the quantum order at the mean-field level is the π-flux structure of the $t_{i,j}$ in Eq. (2.6).

One could ask, how can we exclude the possibility that there exists a gauge transformation connecting the 0-flux, and π-flux cases, just because we could not find any? There are simple ways to exclude this possibility, for example, to compare the one-particle energy spectra, which are the same for two gauge equivalent mean-field Hamiltonians $\mathcal{H}_2^{\mathrm{MF}} = G\mathcal{H}_1^{\mathrm{MF}}G^{-1}$, since

$$\begin{aligned}
\mathcal{H}_1^{\mathrm{MF}}|\xi^1_{\mathbf{q},b}\rangle &= E^{\mathrm{MF}}_{\mathbf{q},b}|\xi^1_{\mathbf{q},b}\rangle \\
G\mathcal{H}_1^{\mathrm{MF}}G^{-1}G|\xi^1_{\mathbf{q},b}\rangle &= E^{\mathrm{MF}}_{\mathbf{q},b}G|\xi^1_{\mathbf{q},b}\rangle \\
\mathcal{H}_2^{\mathrm{MF}}|\xi^2_{\mathbf{q},b}\rangle &= E^{\mathrm{MF}}_{\mathbf{q},b}|\xi^2_{\mathbf{q},b}\rangle,
\end{aligned} \tag{2.34}$$

where $|\xi^1_{\mathbf{q},b}\rangle$ and $|\xi^2_{\mathbf{q},b}\rangle = G|\xi^1_{\mathbf{q},b}\rangle$ are one-particle eigenstates of $\mathcal{H}_1^{\mathrm{MF}}$ and $\mathcal{H}_2^{\mathrm{MF}}$, respectively, with the same energy $E^{\mathrm{MF}}_{\mathbf{q},b}$.

An equivalence class can be characterized by the PSGs of its ansätze, which are slightly different for every ansatz within one equivalence class, but they can be connected via gauge transformations [2, Sec. 9.4.2]. If the mean-field ansatz is stable and the fluctuations are weak (as explained in the next section 2.5), then the quantum order of the mean-field ansatz might survive the fluctuations and become the quantum order of the real ground state [2, Sec. 9.9.1], which is then measurable. In the case of a Dirac spin liquid, the quantum order is measurable through the gapless excitations of the dynamical spin structure factor at certain wave vectors [2, Sec. 9.7].

Every element of the PSG is of the form $G\mathsf{g}$, but these also include pure geometrical transformations like $(\mathsf{T}_1)^2$ and $(\mathsf{T}_2)^2$ (for which the corresponding gauge transformations $G_{(\mathsf{T}_1)^2}$ and $G_{(\mathsf{T}_2)^2}$ are identity), and pure gauge transformations as I and $-\mathsf{I}$, which multiply every fermionic operator by $+1$ and -1, respectively (the geometrical transformations g for all these are identity). The pure gauge transformations form a normal subgroup of the PSG called an invariant gauge group (IGG) [2, Sec. 9.4.2], meaning that the quotient group PSG/IGG = SG contains only the geometric transformations g. For a quantum spin liquid ansatz, SG is the symmetry group of the Heisenberg Hamiltonian of Eq. (1.18), containing all symmetries of the lattice. In the literature, people refer to the quantum spin liquid ansätze through their IGG (in the SU(2) case these are typically Z_2, $U(1)$, and $SU(2)$), because it turns out that the IGG characterizes the low energy gauge fluctuations, and determine whether the ansatz is stable against fluctuations, or not (see [2, Sec. 9.2.2], and Sec. 2.5). Here we will not determine the IGG of any ansatz (so we will not construct the full PSGs either), because that would require knowing *all* pure gauge transformations leaving $\mathcal{H}^{\mathrm{MF}}$ invariant. However, there might be gauge transformations mixing different flavors of fermions (in Eq. (2.16) we used only flavor independent U(1) gauge transformations), which leave the spin operators of Eq. (2.2) invariant, and may also be elements of the IGG (if they leave invariant the mean-field Hamiltonian as well). In the SU(2) case, the most general such gauge transformation $G \in \mathrm{SU}(2)$, which leaves the S^x, S^y, S^z spin operators of Eq. (2.2) invariant, is

$$\begin{array}{ll} f_{j,\uparrow} \to a_j f_{j,\uparrow} + b_j f^\dagger_{j,\downarrow} & f_{j,\downarrow} \to a_j f_{j,\downarrow} - b_j f^\dagger_{j,\uparrow} \\ f^\dagger_{j,\uparrow} \to a^*_j f^\dagger_{j,\uparrow} + b^*_j f_{j,\downarrow} & f^\dagger_{j,\downarrow} \to a^*_j f^\dagger_{j,\downarrow} - b^*_j f_{j,\uparrow}, \end{array} \quad \leftrightarrow \quad G \begin{pmatrix} f_{j,\uparrow} \\ f^\dagger_{j,\downarrow} \end{pmatrix} = \begin{pmatrix} a_j & b_j \\ -b^*_j & a^*_j \end{pmatrix} \begin{pmatrix} f_{j,\uparrow} \\ f^\dagger_{j,\downarrow} \end{pmatrix}, \tag{2.35}$$

where $|a_j|^2 + |b_j|^2 = 1$ [50, 52] (see the SU(2) projective construction in [2, Sec. 9.2]).

In the SU(2) case, all possible different equivalence classes can be listed by the projective symmetry group classification [3, 70, 71]. We can not do such a classification for the SU($N > 2$) case here, because that would require constructing the full PSGs (including the full IGGs) of the ansätze. However, at least certain equivalence classes can be distinguished, for example by different one-particle energy spectra (see Eq. (2.34)).

2.4.1 Invariance of the Gutzwiller projected state under the symmetries of the lattice

Here we will show that Gutzwiller projecting the Fermi sea ground states of two gauge equivalent mean-field Hamiltonians results in variational wavefunctions that differ only in a global phase, and are therefore physically equivalent [2, Eq. (9.1.14))]. In other words, each ansatz in the same equivalence class results in the same Gutzwiller projected wavefunction, while different equivalence classes are believed to give rise to different Gutzwiller projected wavefunctions. Furthermore, even if a mean-field Hamiltonian is not invariant under some geometrical transformation g, if there exists a combined transformation $G_{\mathsf{g}}\mathsf{g}$ leaving $\mathcal{H}^{\mathrm{MF}}$ invariant, then its Gutzwiller projected Fermi seas will be invariant under g (up to a global phase).

If the mean-field ground states $|\mathrm{FS}_1\rangle$ and $|\mathrm{FS}_2\rangle$ of the gauge equivalent Hamiltonians $\mathcal{H}_1^{\mathrm{MF}}$ and $\mathcal{H}_2^{\mathrm{MF}}$ are non-degenerate, we can show (see Appendix D) that they are related as

$$|\mathrm{FS}_2\rangle = G|\mathrm{FS}_1\rangle. \tag{2.36}$$

Our purpose is to prove that

$$P_{\mathrm{G}}|\mathrm{FS}_2\rangle = P_{\mathrm{G}}G|\mathrm{FS}_1\rangle = e^{i\varphi}P_{\mathrm{G}}|\mathrm{FS}_1\rangle, \tag{2.37}$$

where $e^{i\varphi}$ is a *global* (site and configuration independent) phase, which cancels in every expectation value

$$\langle \mathrm{FS}_2|P_{\mathrm{G}}T_i^a P_{\mathrm{G}}|\mathrm{FS}_2\rangle = \langle \mathrm{FS}_1|P_{\mathrm{G}}e^{-i\varphi}T_i^a e^{i\varphi}P_{\mathrm{G}}|\mathrm{FS}_1\rangle = \langle \mathrm{FS}_1|P_{\mathrm{G}}T_i^a P_{\mathrm{G}}|\mathrm{FS}_1\rangle, \tag{2.38}$$

and is thus unphysical. To see how Eq. (2.37) follows let us write the Fermi sea in real space as in Eq. (2.13)

$$P_{\mathrm{G}}G|\mathrm{FS}_1\rangle = \sum_{\{j\}_{P_{\mathrm{G}}}} \left(\prod_{\sigma=1}^{N} \mathrm{slat}_{\{j^\sigma\}_{P_{\mathrm{G}}}} G f^\dagger_{j_1^\sigma,\sigma} G^{-1} G f^\dagger_{j_2^\sigma,\sigma} G^{-1} \dots G f^\dagger_{j_{N_s/N}^\sigma,\sigma} G^{-1} \right) G|0\rangle, \tag{2.39}$$

where the sets of sites $\{j^\sigma\}_{P_{\mathrm{G}}}$ occupied by different colors do not overlap. Due to the single occupancy constraint of Eq. (2.5) the number of fermions is equal to the number of lattice sites N_s, therefore the sets $\{j^\sigma\}_{P_{\mathrm{G}}}$ are disjoint subsets of the set $\{1, 2 \dots N_s\}$. Since the gauge transformation G of Eq. (2.16) is flavor independent, every fermionic operator will bring in a phase $G f^\dagger_{j,\sigma} G^{-1} = e^{i\phi(j)} f^\dagger_{j,\sigma}$, and the product of the N_s fermionic operators will bring in the product of phases $e^{i\phi(1)} e^{i\phi(2)} \dots e^{i\phi(N_s)}$, which is independent of the subsets of sites $\{j^\sigma\}$ occupied by different flavors. Therefore, these phases can be factored out as the global phase $e^{i\varphi} = e^{i\phi(1)} e^{i\phi(2)} \dots e^{i\phi(N_s)}$ [2, Eq. 9.1.14]. This is unlike in the unprojected case, where the subsets of sites $\{j^\sigma\}$ might overlap, therefore the product of the phases depends on the $\{j^\sigma\}$ (in case of the $m > 1$ times occupied site j the phase $e^{i\phi(j)}$ will appear as $e^{i\phi(j)m}$, and the phases of empty sites will be missing). Furthermore, any Gutzwiller projected state (not just the Fermi sea) can be written in the real space basis with singly occupied configurations as in Eq. (2.10), therefore the above arguments can be repeated for any state, implying that P_G eliminates any gauge transformation of the form (2.16) (in the sense that it converts it to an unimportant global phase). The claim that the gauge equivalent ansätze give rise to physically equivalent Gutzwiller projected wavefunctions can also be proven in the case of flavor mixing SU(2) gauge transformations of Eq. (2.35) [2, Sec. 9.2.1.3].

Now that we have proven that all gauge equivalent Hamiltonians result in physically equivalent Gutzwiller projected wavefunctions, we can prove that the Gutzwiller projected Fermi seas are invariant under the geometric transformations g. If $\mathcal{H}_1^{\mathrm{MF}}$ is gauge equivalent to $\mathcal{H}_2^{\mathrm{MF}} = \mathsf{g}\mathcal{H}_1^{\mathrm{MF}}\mathsf{g}^{-1}$ (meaning that $\mathcal{H}_1^{\mathrm{MF}}$ is invairant under $G_{\mathsf{g}}\mathsf{g}$), then their ground states are related as $|\mathrm{FS}_2\rangle = \mathsf{g}|\mathrm{FS}_1\rangle$ (as argued in Appendix D). However, as the $\mathcal{H}_1^{\mathrm{MF}}$ and $\mathcal{H}_2^{\mathrm{MF}}$ are gauge equivalent, we can also use Eq. (2.37) as

$$e^{i\varphi}P_{\mathrm{G}}|\mathrm{FS}_1\rangle = P_{\mathrm{G}}|\mathrm{FS}_2\rangle = P_{\mathrm{G}}\mathsf{g}|\mathrm{FS}_1\rangle = \mathsf{g}P_{\mathrm{G}}|\mathrm{FS}_1\rangle \tag{2.40}$$

where in the last step we used that the Gutzwiller projector commutes with any geometrical transformation g (as argued after Eq. (2.13)). The meaning of Eq. (2.40) is that $P_{\mathrm{G}}|\mathrm{FS}_1\rangle$ is invariant under the action of the geometrical transformation g (up to an unimportant global phase), therefore every expectation value taken in this state will also be invariant under g. To see this, let us rewrite Eq. (2.40) as $P_{\mathrm{G}}|\mathrm{FS}_1\rangle = e^{i\varphi}\mathsf{g}^{-1}P_{\mathrm{G}}|\mathrm{FS}_1\rangle$, so that

$$\langle \mathrm{FS}_1|P_{\mathrm{G}}T_i^a P_{\mathrm{G}}|\mathrm{FS}_1\rangle = \langle \mathrm{FS}_1|P_{\mathrm{G}}\mathsf{g}e^{-i\varphi}T_i^a e^{i\varphi}\mathsf{g}^{-1}P_{\mathrm{G}}|\mathrm{FS}_1\rangle = \langle \mathrm{FS}_1|P_{\mathrm{G}}T_{\mathsf{g}(i)}^a P_{\mathrm{G}}|\mathrm{FS}_1\rangle, \tag{2.41}$$

and similarly for the equal time correlation function

$$\langle \mathrm{FS}_1|P_{\mathrm{G}}T_i^a T_j^a P_{\mathrm{G}}|\mathrm{FS}_1\rangle = \langle \mathrm{FS}_1|P_{\mathrm{G}}\mathsf{g}e^{-i\varphi}T_i^a \mathsf{g}^{-1}\mathsf{g}T_j^a e^{i\varphi}\mathsf{g}^{-1}P_{\mathrm{G}}|\mathrm{FS}_1\rangle = \langle \mathrm{FS}_1|P_{\mathrm{G}}T_{\mathsf{g}(i)}^a T_{\mathsf{g}(j)}^a P_{\mathrm{G}}|\mathrm{FS}_1\rangle. \tag{2.42}$$

Eq. (2.40) is surprising, because the $|\mathrm{FS}\rangle$ (without Gutzwiller projection) inherits the symmetries of $\mathcal{H}^{\mathrm{MF}}$, therefore it is not invariant under the geometric transformations $\mathsf{C}_6, \sigma, \mathsf{T}_1, \mathsf{T}_2$. In fact, just like $\mathcal{H}^{\mathrm{MF}}$, $|\mathrm{FS}\rangle$ is invariant only under the combined transformations $\tilde{\mathsf{g}} \in \{G_{\mathsf{C}_6}\mathsf{C}_6, G_\sigma\sigma, G_{\mathsf{T}_1}\mathsf{T}_1, G_{\mathsf{T}_2}\mathsf{T}_2\}$. However, as we show in Appendix G, the invariance of $\mathcal{H}^{\mathrm{MF}}$ under $G_{\mathsf{g}}\mathsf{g}$ implies that

$$\langle \mathrm{FS}|T_i^a|\mathrm{FS}\rangle = \langle \mathrm{FS}|T_{\mathsf{g}(i)}^a|\mathrm{FS}\rangle, \quad \langle \mathrm{FS}|T_i^a T_j^a|\mathrm{FS}\rangle = \langle \mathrm{FS}|T_{\mathsf{g}(i)}^a T_{\mathsf{g}(j)}^a|\mathrm{FS}\rangle, \tag{2.43}$$

just like for the Gutzwiller projected state.

Antiperiodic boundary condition can spoil projective symmetries for some g, therefore the Gutzwiller projected expectation values will not be invariant under these g (see Appendix E.2). However, as it is only a boundary condition, the asymmetries disappear in the thermodynamic limit.

2.5 What about the fluctuations?

The excited eigenstates of the mean-field Hamiltonian (2.6), which preserve the total particle number, can be constructed by removing a fermion of flavor σ from the Fermi sea, and adding a fermion of flavor σ' on a higher energy band as $f^\dagger_{\mathbf{k}+\mathbf{q},b',\sigma'} f_{\mathbf{q},b,\sigma}|\mathrm{FS}\rangle$, with $\varepsilon_b(\mathbf{q}) \leq \varepsilon_{\mathrm{F}}$ and $\varepsilon_{b'}(\mathbf{q}) > \varepsilon_{\mathrm{F}}$. These excited states are called particle-hole excitations. The states $f^\dagger_{\mathbf{k}+\mathbf{q},b',\sigma'}|\mathrm{FS}\rangle$ and $f_{\mathbf{q},b,\sigma}|\mathrm{FS}\rangle$ are also eigenstates of the mean-field Hamiltonian (2.6), but these do not preserve the total particle number. In the SU(2) case, both the $f^\dagger_{\mathbf{k}+\mathbf{q},b',\sigma'}|\mathrm{FS}\rangle$ and the $f_{\mathbf{q},b,\sigma}|\mathrm{FS}\rangle$ are called spinons, so that the particle-hole excitation could be called a two-spinon excitation. In the SU(N) case, the $f^\dagger_{\mathbf{k}+\mathbf{q},b',\sigma'}|\mathrm{FS}\rangle$ and the $f_{\mathbf{q},b,\sigma}|\mathrm{FS}\rangle$ could be called a flavoron, and an antiflavoron, respectively. At the mean-field level, these are true eigenstates of $\mathcal{H}^{\mathrm{MF}}$, so we can call them quasiparticles.

The SU(N) spin operators are bosonic operators, so when the ground state is magnetically ordered (e.g. ferromagnetic or antiferromagnetic), the quasiparticles are also bosonic, like the already mentioned $s = 1$ magnon in the SU(2) case. The decomposition of the bosonic SU(N) spin operators into fermionic operators in Eq. (2.2) is a mathematical formalism, but it allows for the existence of such fermionic quasiparticles. In the mean-field approximation we neglected the fluctuations that mediate interactions between the flavorons and the antiflavorons (see Appendix B). If the interaction between these fermionic mean-field quasiparticles is short-ranged and weak, then the quasiparticles (excited eigenstates) of the SU(N) Heisenberg model are similar to the fermionic mean-field quasiparticles. In other words, the bosonic excited states of the ordered state are split into a pair of fermionic quasiparticles, which is called fractionalization. In this case, the existence of fermionic quasiparticles is directly measurable in the dynamical spin structure factor, since at the lowest excitation energies we will see a continuum (implicating a pair of quasiparticles) instead of a single branch. On the other hand, if the interactions between the flavorons and the antiflavorons are strong, then the real quasiparticles of the Heisenberg model will be their bosonic bound states, so the decomposition of Eq. (2.2) remains a mere mathematical formalism without any physical content. As an example from the SU(2) case, the $s = 1$ bosonic magnon can be thought of as a bound state of two $s = 1/2$ fermionic spinons.

The interactions are called short-ranged, when the ratio of the interaction energy and the kinetic energy goes to zero for large distances (low energy), as explained in the book [2, Sec. 9.1.4]. In this case, the interaction is an irrelevant perturbation in the RG sense, and the mean-field ansatz is said to be *stable*. If the ratio of the interaction energy and the kinetic energy goes to a constant, then the interaction is a marginal perturbation (stability is questionable), and if it diverges it is a relevant perturbation (the mean-field ansatz is *unstable*). However, not even a stable mean-field ansatz is guaranteed to give a good approximation of the real ground state, because even the short-range interactions might be strong enough to change the ground state and the excitations. In the SU(2) case, it is argued, that Z_2 spin liquids (having an IGG forming a Z_2 group [2, Secs. 9.2.6, 9.9.2, 9.9.4], and chiral spin liquids (having fluxes different from 0 and π, achieved by complex hoppings $t_{i,j}$ [2, Sec. 9.1.6]) are stable, but even these have typically short-range interactions which are not weak [2, Sec. 9.8]. However, the interaction between the fermions can be weakened by enhancing the symmetry of the Heisenberg model from SU(2) to Sp($2N$) [5], which means introducing N copies of both the $\uparrow$ and $\downarrow$ spins [2, Sec. 9.8]. Consequently, in the large-N limit of the Sp($2N$) symmetric model, the stable and marginal mean-field ansätze can become the real ground states of the Sp($2N$) Heisenberg model. However, our large-N limit is different, since we are interested in the SU(N) symmetric Heisenberg model in the fundamental representation. In the self-conjugate representation of the SU(N) Heisenberg model, some fluctuations were already argued to become weaker with an increasing N [49, 50], but this is again not the large-N limit we need. Here we hope that the fluctuations are also weakened in the SU(N) symmetric large-N limit in the fundamental representation. This is in agreement with the decreasing difference between the mean-field and the Gutzwiller projected results presented in the following sections, although the Gutzwiller projection takes into account only the temporal fluctuations of the chemical potential, and not the interactions between the fermions [2, Sec. 9.1.1, Eq. (9.1.8)].

Furthermore, in 2+1 dimensions, field-theoretical arguments involving N species of Dirac fermions suggest that for $N > N_c$, the Dirac fermions become deconfined, stabilizing the Dirac spin liquid [72, 73, 74, 75]. However, the precise value of N_c is debated, and the connection with our models is not fully understood.

As already mentioned in section 2.4, if the mean-field ansatz is stable (and weakly interacting), the mean-field quantum order protected by the PSG survives the fluctuations, and becomes the quantum order of the real ground state [2, Sec. 9.9.1]. If the mean-field one-particle energy spectrum is gapped, the quantum order is called topological order, and is characterized by the ground state degeneracy [2, Sec. 8.] [3]. If the one-particle energy spectrum is gapless, then the quantum order is characterized by the existence and location (in reciprocal space) of gapless excitation towers in the dynamical spin structure factor [2, Sec. 9.10.2]. In Dirac spin liquids, the measurement of the dynamical spin structure factor serves as an experimental verification of the quantum order and of the stability of the mean-field ansatz [2, Sec. 9.7]. However, we have not proven that the π-flux quantum order and its PSG protects gapless fermionic excitations at certain wave vectors. Yet, the dynamical spin structure factors of the ansätze presented in section 2.3 do have gapless excitations at certain wave vectors. Every ansatz in the same equivalence class should give the same dynamical spin structure factor, since the SU(N) spin operators are insensitive to the gauge transformations connecting different ansätze (2.17). It is reasonable to believe that the PSG should indeed require the existence of gapless excitation towers at certain wave vectors. Thus, instead of analyzing the fluctuations and the stability of the ansätze, we present the dynamical spin structure factors of these ansätze in sections 5, 6 and 6, and the possible ways to experimentally measure them in real systems in section 4.1.

2.6 Symmetry breaking quantum phase transitions

Before turning to quantum phase transitions without symmetry breaking, let us first recapitulate Landau's symmetry-breaking theory. A quantum phase transition happens, when while tuning some parameter of a Hamiltonian (for example the transverse field h in Eq. (2.44)), the ground state changes from one state $|\mathrm{GS}_1\rangle$ to another $|\mathrm{GS}_2\rangle$, where the first state is invariant under the transformations $\mathsf{g} \in \mathrm{SG}_1$, while the second is invariant under $\mathsf{g} \in \mathrm{SG}_2$. A symmetry breaking quantum phase transition means that either $\mathrm{SG}_1 \subset \mathrm{SG}_2$, or $\mathrm{SG}_2 \subset \mathrm{SG}_1$. If $\mathrm{SG}_1 \subset \mathrm{SG}_2$, then $|\mathrm{GS}_1\rangle$ is not invariant under some of the transformations $\mathsf{g} \in \mathrm{SG}_2$ missing from $\mathsf{g} \notin \mathrm{SG}_1$. The simplest example of such a quantum phase transition is perhaps of the transverse field ferromagnetic Ising model [76, Sec. 1.4.1]

$$\mathcal{H}_I = -J \sum_{\langle i,j \rangle} \hat{\sigma}_i^z \hat{\sigma}_j^z - Jh \sum_i \hat{\sigma}_i^x, \tag{2.44}$$

where $\hat{\sigma}^a$ are the Pauli matrices. $\mathcal{H}_I$ has a discrete Z_2 symmetry, it is invariant under the unitary operator $U = \prod_i \hat{\sigma}_i^x$, meaning $\mathcal{H}_I = U\mathcal{H}_I U^{-1}$, where U rotates with π around the x axis, since $\hat{\sigma}_i^x \hat{\sigma}_i^z \hat{\sigma}_i^x = -\hat{\sigma}_i^z$ and $\hat{\sigma}_i^x \hat{\sigma}_i^x \hat{\sigma}_i^x = \hat{\sigma}_i^x$. There are two phases, separated by a quantum phase transition. For large $h > h_c$ (paramagnetic phase) there is one non-degenerate ground state $|\mathrm{GS}_1\rangle = \prod_i |\rightarrow\rangle_i = \frac{1}{\sqrt{2}} \prod_i (|\uparrow\rangle_i + |\downarrow\rangle_i)$, which is invariant under U as $U|\mathrm{GS}_1\rangle = |\mathrm{GS}_1\rangle$, so $U \in \mathrm{SG}_1$. $|\mathrm{GS}_1\rangle$ is also invariant under all other transformations leaving $\mathcal{H}_I$ invariant, like translations, complex conjugation (time reversal), and so on, therefore this phase is called paramagnetic. Therefore, the symmetry group SG_1 of $|\mathrm{GS}_1\rangle$ is just the symmetry group of $\mathcal{H}_I$, $\mathrm{SG}_1 = \mathrm{SG}_{\mathcal{H}_I}$. For small $h < h_c$ (ferromagnetic phase) $\mathcal{H}_I$ has two degenerate ground states, $|\uparrow\rangle = \prod_i |\uparrow\rangle_i$ and $|\downarrow\rangle = \prod_i |\downarrow\rangle_i$, where $|\uparrow\rangle_i$ and $|\downarrow\rangle_i$ are the two eigenstates of $\hat{\sigma}_i^z$. Neither $|\uparrow\rangle$, nor $|\downarrow\rangle$ are invariant under U, meaning that the ground states have lower symmetries than the Hamiltonian, called symmetry breaking. In this case, it is a Z_2 symmetry breaking, so $\mathrm{SG}_2 \subset \mathrm{SG}_1$. Symmetry breaking necessarily brings about ground state degeneracy in the thermodynamic limit, because the eigenvalue equation $\mathcal{H}|\uparrow\rangle = E_\uparrow|\uparrow\rangle$ can be multiplied with U as $U\mathcal{H}|\uparrow\rangle = UE_\uparrow|\uparrow\rangle$, and the symmetry of $\mathcal{H}$ under U ($[\mathcal{H}, U] = 0$) implies $\mathcal{H}U|\uparrow\rangle = E_\uparrow U|\uparrow\rangle$. However, if there is a symmetry breaking, $|\uparrow\rangle$ is not invariant under U, so $U|\uparrow\rangle$ is a linearly independent state with the same energy eigenvalue $E_\uparrow$. In the case of the Ising model, $U|\uparrow\rangle = |\downarrow\rangle$ and $U|\downarrow\rangle = |\uparrow\rangle$. The local order parameter distinguishing the two phases is $\langle \mathrm{GS}|\hat{\sigma}_i^z|\mathrm{GS}\rangle$ taken on any site i, which is finite in the ferromagnetic phase (where $|\mathrm{GS}\rangle$ is either $|\uparrow\rangle$ or $|\downarrow\rangle$) and zero in the paramagnetic phase.

In $\mathcal{H}_I$ (2.44) the broken symmetry was a discrete Z_2 symmetry, so we got two degenerate ground states connected with the transformation U. However, if the broken symmetry is continuous, as the $\mathrm{SU}(N)$ spin rotation symmetry of the $\mathrm{SU}(N)$ Heisenberg model (1.18), then the number of degenerate states is larger. If the Hamiltonian has only short-range interactions, then the Goldstone theorem implies that the spectrum has to be gapless (see page 273 in [4, Sec. 6.1.2]), which can be understood as an infinitesimal excitation turning one ground state to another. The simplest example is the SU(2) ferromagnetic Heisenberg model, where the degenerate ground states are fully polarized, just as for the Ising model, but a small rotation of the polarization of all spins gives another ground state. Such a small rotation can be achieved with a magnon having zero wave vector, so there will be gapless excitations at $\mathbf{q} = \mathbf{0}$.

2.7 Quantum phase transitions without symmetry breaking

A quantum phase transition can also happen without symmetry breaking, meaning that both $|\mathrm{GS}_1\rangle$ and $|\mathrm{GS}_2\rangle$ are invariant under the same transformations $g \in \mathrm{SG}$, where in case of quantum spin liquids SG is the symmetry group of the Hamiltonian. What changes from one

state (phase) to another is some hidden quantum order, which influences measurable quantities, like the dynamical spin structure factor.

Some of these quantum phase transitions can be described by projective symmetry groups, provided that both $|\mathrm{GS}_1\rangle$ and $|\mathrm{GS}_2\rangle$ are well approximated with the stable mean-field ansätze $|\mathrm{GS}_1\rangle \approx P_\mathrm{G}|\mathrm{FS}_1\rangle$ and $|\mathrm{GS}_2\rangle \approx P_\mathrm{G}|\mathrm{FS}_2\rangle$ with mean-field Hamiltonians $\mathcal{H}_1^\mathrm{MF}$ and $\mathcal{H}_2^\mathrm{MF}$, respectively. $\mathcal{H}_1^\mathrm{MF}$ and $\mathcal{H}_2^\mathrm{MF}$ can not be gauge equivalent, since then $|\mathrm{GS}_1\rangle$ and $|\mathrm{GS}_2\rangle$ would be the same, so there would not be any quantum phase transition. The mean-field Hamiltonians should not be confused with the original Hamiltonian $\mathcal{H}$ having some coupling, which can be tuned to change the ground state from $|\mathrm{GS}_1\rangle$ to $|\mathrm{GS}_2\rangle$. For example, $\mathcal{H}$ can be the $J_1 - J_2$ SU(2) Heisenberg model

$$\mathcal{H}_{J_1-J_2} = J_1 \sum_{\langle i,j\rangle} \mathbf{S}_i \cdot \mathbf{S}_j + J_2 \sum_{\langle\langle i,j\rangle\rangle} \mathbf{S}_i \cdot \mathbf{S}_j, \tag{2.45}$$

where we can fix $J_1^2 + J_2^2 = 1$. The mean-field Hamiltonians $\mathcal{H}_1^\mathrm{MF}$ and $\mathcal{H}_2^\mathrm{MF}$ are only used to construct the variational wavefunctions approximating the two lowest energy eigenstates of $\mathcal{H}_{J_1-J_2}$, namely $|\mathrm{GS}_1\rangle \approx P_\mathrm{G}|\mathrm{FS}_1\rangle$ and $|\mathrm{GS}_2\rangle \approx P_\mathrm{G}|\mathrm{FS}_2\rangle$. For example, let us suppose that $\mathcal{H}_1^\mathrm{MF}$ and $\mathcal{H}_2^\mathrm{MF}$ are the 0-flux, and π-flux hopping Hamiltonians (2.6), respectively. The variational energy $E(J_2/J_1) = \langle \mathrm{FS}|P_\mathrm{G}\mathcal{H}P_\mathrm{G}|\mathrm{FS}\rangle / \langle \mathrm{FS}|P_\mathrm{G}P_\mathrm{G}|\mathrm{FS}\rangle$ of every ansatz is a smooth function of J_2/J_1. Thus, we can compare the variational energies $E_{0-\mathrm{flux}}(J_2/J_1)$ and $E_{\pi-\mathrm{flux}}(J_2/J_1)$ for different values of J_2/J_1. The simplest example of a quantum phase transition is when the variational energy of the 0-flux ansatz is smaller $E_{0-\mathrm{flux}}(J_2/J_1) < E_{\pi-\mathrm{flux}}(J_2/J_1)$ for $J_2 < J_{2C}$, but it becomes bigger $E_{0-\mathrm{flux}}(J_2/J_1) > E_{\pi-\mathrm{flux}}(J_2/J_1)$ for $J_2 > J_{2C}$. Thus, J_{2C} is a critical coupling, where $E_{0-\mathrm{flux}}(J_{2C}/J_1) = E_{\pi-\mathrm{flux}}(J_{2C}/J_1)$. Therefore, for $J_2 < J_{2C}$ the ground state is approximated by the 0-flux ansatz, while for $J_2 > J_{2C}$ by the π-flux ansatz. If these mean-field ansätze are stable, then their quantum orders become the quantum orders of the eigenstates $|\mathrm{GS}_1\rangle$ and $|\mathrm{GS}_2\rangle$ of $\mathcal{H}_{J_1-J_2}$, so the quantum order is changed at the transition point J_{2C}.

A quantum phase transition is of first order, if the slopes of the variational energies $\partial E/\partial J_2$ are unequal at the transition point J_{2C}, and second order, if the slopes are equal (continuous transition) [5]. In a second order transition the mean-field ansätze $\mathcal{H}_1^\mathrm{MF}$ and $\mathcal{H}_2^\mathrm{MF}$ can be connected with a small perturbation as $\mathcal{H}_2^\mathrm{MF} = \mathcal{H}_1^\mathrm{MF} + \delta\mathcal{H}^\mathrm{MF}$, which transfers to the hoppings as $t_{i,j}^2 = t_{i,j}^1 + \delta t_{i,j}$. The transition between the 0-flux and the π-flux ansätze is not second-order, since the mean-field Hamiltonians can not be connected with a small perturbation. Let us denote the projective symmetry groups of $\mathcal{H}_1^\mathrm{MF}$ and $\mathcal{H}_2^\mathrm{MF}$ by PSG_1 and PSG_2, respectively. In a second-order transition either $\mathrm{PSG}_2 \subset \mathrm{PSG}_1$, or $\mathrm{PSG}_1 \subset \mathrm{PSG}_2$ [5] [2, Sec. 9.5]. Since both states $|\mathrm{GS}_1\rangle$ and $|\mathrm{GS}_2\rangle$ must be invariant under all elements of the symmetry group SG of the original Hamiltonian, both PSG_1 and PSG_2 must contain a combined transformation $G_\mathtt{g}\mathtt{g}$ for every element $\mathtt{g} \in \mathrm{SG}$ (otherwise it would be a symmetry breaking quantum phase transition). Let us denote the invariant gauge groups of the two ansätze with IGG_1 and IGG_2, which satisfy $\mathrm{PSG}_1/\mathrm{IGG}_1 = \mathrm{SG} = \mathrm{PSG}_2/\mathrm{IGG}_2$. Thus, the condition $\mathrm{PSG}_2 \subset \mathrm{PSG}_1$ implies $\mathrm{IGG}_2 \subset \mathrm{IGG}_1$. Consequently, the $\delta\mathcal{H}$ breaks some pure gauge transformations $G_{\mathrm{IGG}_1} \in \mathrm{IGG}_1$, and the combinations $G_{\mathrm{IGG}_1}G_\mathtt{g}\mathtt{g}$ (in every coset of IGG_1), where $\mathtt{g}$ is not the identity. The possible ways of lowering the IGG_1 of an ansatz to $\mathrm{IGG}_2 \subset \mathrm{IGG}_1$ determines all possible second-order quantum phase transitions at the mean-field level [5].

Finally, we would like to note that there are quantum phase transitions that are not accompanied by any symmetry breaking, yet they can not be described by projective symmetry groups because GS_1 and GS_2 may not be described by stable mean-field ansätze. One such example is the Mott transition, introduced in section 1.1.1.

Chapter 3

The stability of the SU(6) Dirac spin liquid on the kagome lattice

The SU(2) Heisenberg model on the kagome lattice was argued to be magnetically disordered [77], therefore we expect the SU(6) Heisenberg model to also exhibit disorder due to increased quantum fluctuations.

We propose that the ground state of this model may be well described by the Dirac spin-liquid (DSL) ansatz introduced in Sec. 2.3.2, previously suggested for the SU(2) case [58]. To support our claim, we search for possible perturbations of the Dirac spin liquid ansatz, meaning that we modify the hoppings $t_{i,j}^{\mathrm{DSL}}$ of the DSL mean-field Hamiltonian, $\mathcal{H}_{\mathrm{DSL}}(\mathbf{k})$ in Eqs. (2.6) and (2.28), as

$$t_{i,j} = t_{i,j}^{\mathrm{DSL}}(1 + \delta\tilde{t}_{i,j}), \tag{3.1}$$

where $0 < \delta \ll 1$, $|\tilde{t}_{i,j}| = \mathcal{O}(1)$. The Gutzwiller projected ground state of such a perturbed mean-field Hamiltonian yields a modified wavefunction $|\psi_{\tilde{t}_{i,j}}\rangle$. We then compute the variational energy $\langle\psi_{\tilde{t}_{i,j}}|\mathcal{H}|\psi_{\tilde{t}_{i,j}}\rangle/\langle\psi_{\tilde{t}_{i,j}}|\psi_{\tilde{t}_{i,j}}\rangle$ for the perturbed wavefunctions. If the variational energy of any perturbed ansatz is lower than that of the DSL, this indicates that the DSL is no longer the ground state, and we say that the DSL is locally unstable against the perturbations in Eq. (3.1). If the DSL has the lowest variational energy, then we say that the DSL is energetically stable against the perturbations considered here.

We note that two forms of stability can be distinguished for a fermionic mean-field ansatz: energetic stability and quantum field-theoretical stability. The latter requires that interactions between fermions become irrelevant in the renormalization group sense, leading to deconfined fermions, as discussed in Sec. 2.5. While we have not explicitly checked quantum field-theoretical stability for the SU(6) case, the large-N value is certainly beneficial. For the remainder of this chapter, 'stability' will refer exclusively to energetic stability.

3.1 Real-valued $\tilde{t}_{i,j}$ perturbations of the DSL

There are many ways to perturb the DSL ansatz. Here, we consider only real-valued perturbations periodic in the quadrupled unit cell of 12-sites. These include some valence bond like patterns discussed in Refs. [78, 79, 75, 80]. As shown in in ref. [III.], the symmetry group of the 12-site unit cell is isomorphic to the O_h group, so the irreducible representations of the $\tilde{t}_{i,j}$ can be classified using the character table of the O_h group. We show the hopping structures of some perturbed ansätze transforming under the irreps of the O_h group in the first row of Fig. 3.1 and the first column of Fig. 3.2. These real perturbations modify the absolute values of the hoppings, but leave their signs identical to those of the DSL, keeping the $\pi_{\hexagon}\pi_{\triangle}\pi_{\triangledown}$ flux structure unchanged.

We also take advantage of the fact that the center of the O_h group is the identity and the inversion that constitute a normal subgroup. Consequently, the irreducible representations of the O_h are either even (gerade) or odd (ungerade) under the inversion. The inversion in the O_h group corresponds to the twofold rotation C_2 around the center of a hexagon in the wallpaper group, so $\tilde{t}_{C_2(i,j)} = +\tilde{t}_{i,j}$ in an even (gerade, g) irreducible representation, and $\tilde{t}_{C_2(i,j)} = -\tilde{t}_{i,j}$ in an odd (ungerade, u) one. For each irreducible representation, there is a gerade and an ungerade one.

In Fig. 3.1 we show the single-parameter ansätze $T^1_{2g} - T^2_{2g} - T^3_{2g}$, T^1_{2g}, $T^1_{2u} - T^2_{2u} - T^3_{2u}$, T^1_{2u}, and A_{1u} with the parameter δ (here we allow negative δ, which is like multiplying the $\tilde{t}_{i,j}$ by -1). The $T^1_{2g} - T^2_{2g} - T^3_{2g}$ (first column in figure) coincides with the famous "pinwheel" pattern in deformed kagome material $Rb_2Cu_3SnF_{12}$ [81]. We do not plot the A_{1g} since it changes the hoppings uniformly, leaving the wave function equivalent to the DSL.

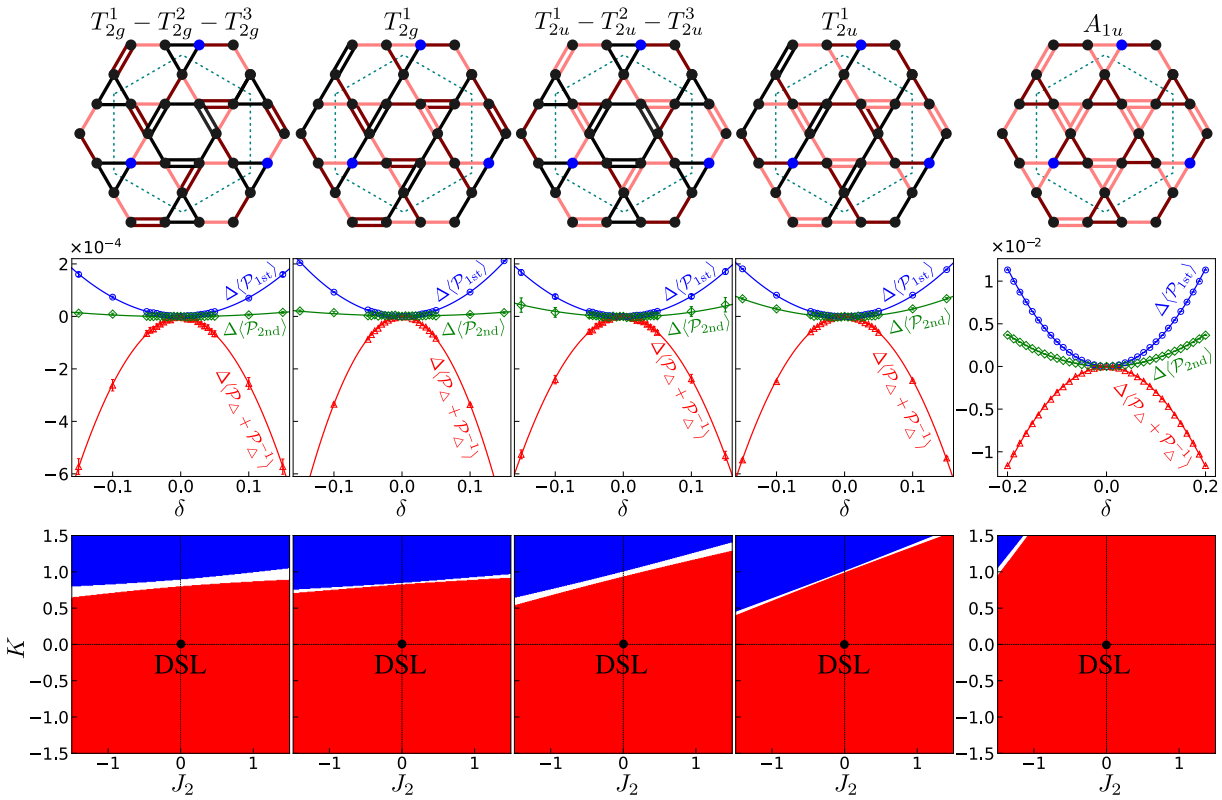

Figure 3.1: In the first row, we show the hopping structure of the real perturbations of the Dirac spin liquid having a single free parameter δ. Different shades represent different absolute values of the hoppings. The empty bonds stand for positive hoppings, while the solid bonds for negative hoppings (each ansatz has a $\pi_\bigcirc\pi_\triangle\pi_\bigtriangledown$ flux structure, just as the DSL). The black bonds have absolute value 1, the dark red hoppings $1+\delta$, and the light reds $1-\delta$. In the midle row, the red points show the $\Delta\langle\mathcal{P}_\triangle + \mathcal{P}_\triangle^{-1}\rangle$, the blue points $\Delta\langle\mathcal{P}_{1st}\rangle$, and the green points $\Delta\langle\mathcal{P}_{2nd}\rangle$ defined in Eq. (3.5), while the solid lines are the fitted parabolas. The bottom row shows the local stability of these ansätze (as explained in sec. 3.2.1), as a function of K and J_2, fixing $J_1 = 1$. The DSL is the lowest energy state in the red region, and the perturbation wins in the blue region. All these results were calculated for a cluster of 192 sites with APBC.

In Fig. 3.2 we show the two-parameter ansätze $-T^1_{1g} + T^2_{1g} + T^3_{1g}$, T^3_{1g}, $-T^1_{1u} + T^2_{1u} + T^3_{1u}$, T^3_{1u}, $v_1E^1_g + v_2E^2_g$, and $v_1E^1_u + v_2E^2_u$. To make the comparison of the different ansätze in Fig. 3.2 unambiguous, we have collected the different hopping amplitudes in Tab. 3.1.

We can identify the $-T^1_{1g} + T^2_{1g} + T^3_{1g}$ ansatz with the David star ansatz studied in [78] for the SU(2) case. There, it had a single parameter δ, which is identical to $\alpha = 1$ and $\beta = 0$ in our notation, so that each bond on the edge of a David star is strengthened as $t_{i,j} = t^{\mathrm{DSL}}_{i,j}(1+\delta)$, while all other hoppings are weakened as $t_{i,j} = t^{\mathrm{DSL}}_{i,j}(1-\delta)$ (see Tab. 3.1). Some linear combinations are equivalent, for example, $T^1_{1g} - T^2_{1g} + T^3_{1g}$ is a David star shifted in $\mathbf{a}_2$ direction. Allowing for

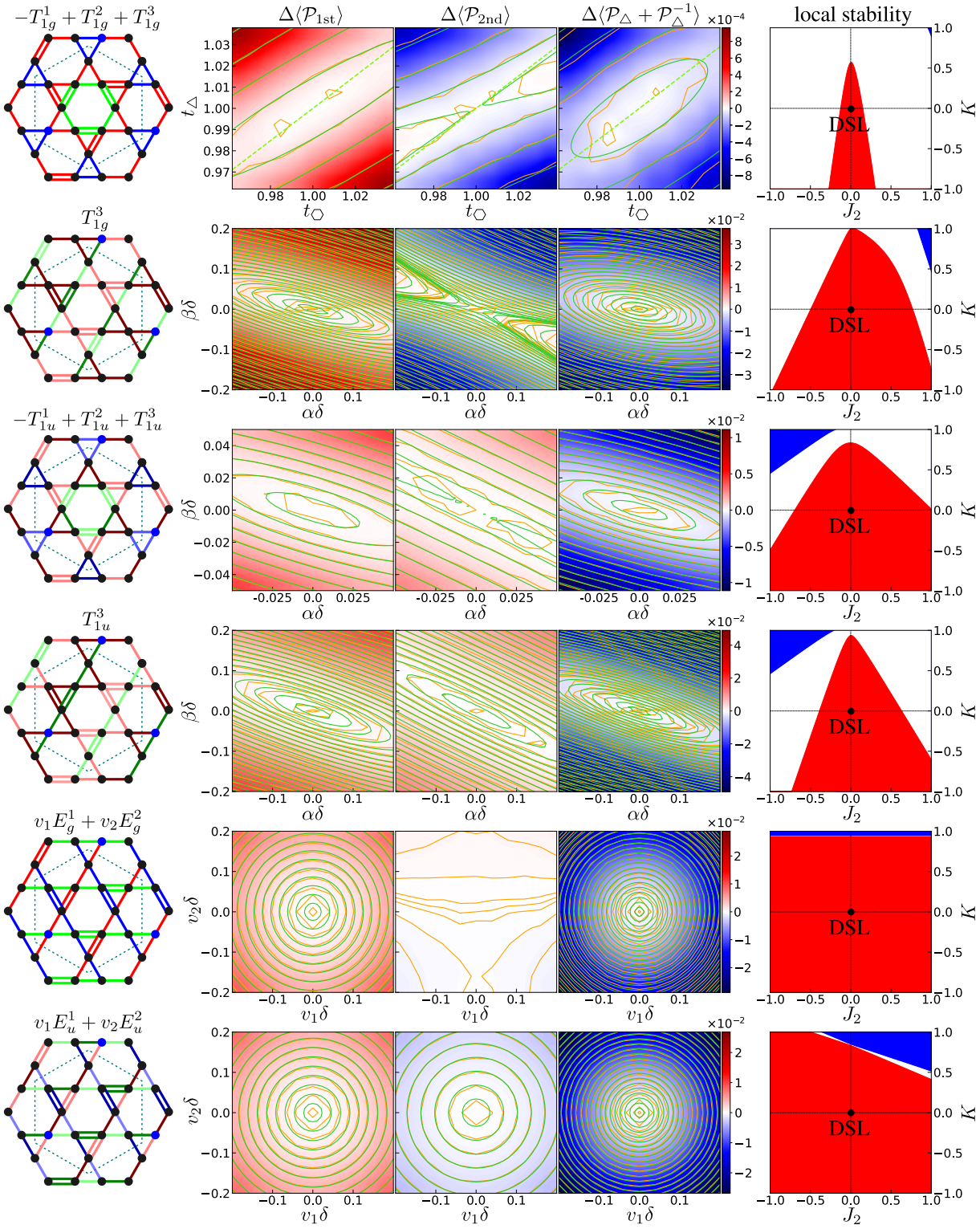

Figure 3.2: In the first column, we show the hopping structure of the real perturbations of the Dirac spin liquid having two free parameters. Different colors represent different absolute values of the hoppings listed in Tab. 3.1 for the denoted irreducible representation. The empty bonds stand for positive hoppings, while the solid bonds for negative hoppings (each ansatz has a $\pi_\hexagon\pi_\triangle\pi_\triangledown$ flux structure, just as the DSL). The second column shows the $\Delta\langle\mathcal{P}_{1\mathrm{st}}\rangle$, the third $\Delta\langle\mathcal{P}_{2\mathrm{nd}}\rangle$, and the fourth $\Delta\langle\mathcal{P}_{\triangle} + \mathcal{P}^{-1}_{\triangle}\rangle$ defined in Eq. (3.5), calculated by VMC for a cluster of 192 sites with APBC, the $\delta = 0$ is the DSL. The effect of the APBC is visible only in the $\Delta\langle\mathcal{P}_{2\mathrm{nd}}\rangle$ of $\alpha E^1_g + \beta E^2_g$ (which becomes flat after averaging over all APBC orientations). The contours of the fitted ellipsoids are shown in light green, while the contours of the data are orange. The fifth column shows the local stability of these ansätze (see Sec. 3.2.1), as a function of K and J_2, keeping $J_1 = 1$. The DSL has the lowest energy in the red region and the perturbed ansatz of the given row in the blue region.

ansatz	color	relative hoppings $t_{i,j}/t_{i,j}^{\mathrm{DSL}}$
$-T_{1g}^1+T_{1g}^2+T_{1g}^3$	red	$t_{\hexagram}\approx 1$
	green	$t_{\hexagon}\approx 1+2(\beta-\alpha)\delta$
	blue	$t_{\triangle}\approx 1-2(\beta+\alpha)\delta$
T_{1g}^3	dark green	$1+\alpha\delta$
	light green	$1-\alpha\delta$
	dark red	$1+\beta\delta$
	light red	$1-\beta\delta$
$-T_{1u}^1+T_{1u}^2+T_{1u}^3$	dark green	$1+(2\beta-\alpha)\delta$
	light green	$1-(2\beta-\alpha)\delta$
	dark red	$1+\alpha\delta$
	light red	$1-\alpha\delta$
	light blue	$1+(2\beta+\alpha)\delta$
	dark blue	$1-(2\beta+\alpha)\delta$
T_{1u}^3	dark green	$1+\alpha\delta$
	light green	$1-\alpha\delta$
	dark red	$1+\beta\delta$
	light red	$1-\alpha\delta$
$\alpha\|E_g^1\rangle+\beta\|E_g^2\rangle$	green	$1+(\alpha-\beta)\delta$
	red	$1+2\beta\delta$
	blue	$1-(\alpha+\beta)\delta$
$\alpha\|E_u^1\rangle+\beta\|E_u^2\rangle$	dark red	$1+2\beta\delta$
	light red	$1-2\beta\delta$
	dark blue	$1+(\alpha+\beta)\delta$
	light blue	$1-(\alpha+\beta)\delta$
	light green	$1+(\alpha-\beta)\delta$
	dark green	$1-(\alpha-\beta)\delta$

Table 3.1: The hopping amplitudes for all two-parameter ansätze in Fig. 3.2 are listed in the third column, with their colors in the second column. The first column is the label of the irreducible representation of the O_h group, identifying the perturbed ansatz.

$\beta \neq 0$, we consider a more general David star ansatz,

$$t_{i,j}^{\text{☆}} = t_{i,j}^{\text{DSL}}(1+\alpha\delta) \tag{3.2a}$$
$$t_{i,j}^{\triangle} = t_{i,j}^{\text{DSL}}\left[1-(2\beta+\alpha)\delta\right] \tag{3.2b}$$
$$t_{i,j}^{\hexagon} = t_{i,j}^{\text{DSL}}\left[1+(2\beta-\alpha)\delta\right], \tag{3.2c}$$

shown in the first row of Fig. 3.2. The $t_{i,j}^{\text{☆}}$ denotes the hoppings amplitudes on the edge of the David star (red bonds in Fig. 3.2), the $t_{i,j}^{\triangle}$ on the interstar triangles (blue) and $t_{i,j}^{\hexagon}$ on the hexagon within the star (shown by green). After Gutzwiller projecting the ground state of the David star mean-field Hamiltonian (2.6), only the ratios of the hopping amplitudes remain essential. Therefore, using the notations $t_{i,j}^{\text{☆}} = t_{i,j}^{\text{DSL}} t_{\text{☆}}$, $t_{i,j}^{\triangle} = t_{i,j}^{\text{DSL}} t_{\triangle}$, and $t_{i,j}^{\hexagon} = t_{i,j}^{\text{DSL}} t_{\hexagon}$, we can divide with $1+\alpha\delta$, getting $t_{\text{☆}} = 1$, and use $t_{\triangle} \approx 1-2(\beta+\alpha)\delta$ and $t_{\hexagon} \approx 1+2(\beta-\alpha)\delta$ as the two free parameters (also listed in Tab. 3.1), instead of $\alpha\delta$ and $\beta\delta$. The David star is special because, for weak $t_{\triangle}$ hoppings, the nearly decoupled 12 sites tend to transform as an SU(6) singlet, with a Young tableau of two columns and six rows (see Appendix A.5). This can be contrasted with the A_{1u} configuration, which results in almost decoupled triangles - an ideal starting point for the trimerized phase of the SU(3) Heisenberg model [82, 83]. Another interesting case is $|t_{\text{☆}}| < |t_{\triangle}|$ and $|t_{\text{☆}}| < |t_{\hexagon}|$ when the six spins in the hexagon tend to transform as an SU(6) singlet (with a Young tableau of a single column of 6 boxes) and the spins in the decoupled triangles as the 20-dimensional self-conjugate irreducible representation (with a Young tableau of a single column of 3 boxes).

In the T_{1g}^3 ansatz, the hopping amplitudes alternate along parallel lines while the rest of the bonds remain unchanged (shown in the second row of Fig. 3.2). Refs. [78, 79, 79] also considered this dimerized ansatz for the SU(2) case, setting $\alpha = 1$ and $\beta = 0$. Allowing for $\beta \neq 0$ we consider a more general pattern, for which the hoppings are given in Tab. 3.1.

Both the ungerade David star ansatz $-T_{1u}^1 + T_{1u}^2 + T_{1u}^3$ and T_{1u}^3 are shown in the third and fourth rows of Fig. 3.2. They have only two free parameters $\alpha\delta$ and $\beta\delta$, despite parametrizing six and four different hoppings, respectively, which are given in Tab. 3.1.

The ansatz $v_1 E_g^1 + v_2 E_g^2$ is shown in the fifth row of Fig. 3.2, for which the hoppings are given in Tab. 3.1. For $v_1 = 0$ and $v_2 = 1$ it describes anisotropic chains with hoppings $t_{i,j} = t_{i,j}^{\text{DSL}}(1+2\delta)$ along one direction and $t_{i,j} = t_{i,j}^{\text{DSL}}(1-\delta)$ along the other two. The linear combinations with $v_1 = \pm\sqrt{3}v_2$ rotate the chains with different hoppings. For $v_1 = 1$ and $v_2 = 0$, the lines in the three different directions have three different strengths $t_{i,j} = t_{i,j}^{\text{DSL}}(1+\xi\delta)$, with $\xi \in \{-1, 0, 1\}$. Here again, the $v_2 = \pm\sqrt{3}v_1$ rotates the unequivalent chains.

For the ungerade E_u we show the ansatz $v_1 E_u^1 + v_2 E_u^2$ in the sixth row of Fig. 3.2 and Tab. 3.1.

The A_{1g}, A_{1u}, E_g, E_u ansätze are gapless and have a two-fold degenerate Dirac Fermi point at $\mathbf{k} = 0$, similarly to the DSL. Among the real perturbations, only the T_{1g} and T_{2g} open a gap. However, for the T_{1g} the gap closes along a curve going through the $t_H = t_T = t$ and the $(t_T = 0, t_H = -t/\sqrt{2})$ point (shown with the dashed green line in Fig. 3.2), and a Dirac cone appears. The T_{1u} and T_{2u} have two Dirac Fermi points at non-zero $\mathbf{k}_D$ and $-\mathbf{k}_D$ values, each non-degenerate. In the projective sense, the translational symmetry is restored for the A_1 and E ansätze, but they break the point group symmetries. The T_{1g} and T_{2g} keep some of the point group projective symmetries but break translation symmetries, while the T_{1u} and T_{2u} break both the translations and point group symmetries.

As we will show in Figs. 3.1 and 3.2, all of these real perturbations increase the variational energy, so the Dirac spin liquid remains the lowest energy state.

3.2 Stability of the DSL

The Heisenberg Hamiltonian of Eq. (1.18) is a result of the leading order perturbation theory of the repulsive Hubbard Hamiltonian of Eq. (1.2) for $U/t \to \infty$. However, we can incorporate further terms so that the effective Hamiltonian reads

$$\mathcal{H} = J_1 \sum_{\langle i,j \rangle} \mathcal{P}_{i,j} + J_2 \sum_{\langle\langle i,j \rangle\rangle} \mathcal{P}_{i,j} + K \sum_{\langle i,j,k \rangle} (\mathcal{P}_{i,j,k} + \mathcal{P}_{i,j,k}^{-1}), \tag{3.3}$$

where the $\langle\langle i,j \rangle\rangle$ denotes second nearest neighbor sites and the $\mathcal{P}_{i,j,k}$ is the ring exchange operator acting on elementary triangles $\langle i,j,k \rangle$. The J_1 is of the order $\frac{t^2}{U}$ and usually positive (antiferromagnetic), $K \propto \frac{t^3}{U^2}$, and $J_2 \propto \frac{t^4}{U^3}$ in case it arises from nearest neighbor hoppings. Written explicitly, P_{ij} and P_{ijk} are defined through their action on the local basis states, $P_{ij}|\sigma_1\rangle_i \otimes |\sigma_2\rangle_j = |\sigma_2\rangle_i \otimes |\sigma_1\rangle_j$ and $P_{ijk}|\sigma_1\rangle_i \otimes |\sigma_2\rangle_j \otimes |\sigma_3\rangle_k = |\sigma_3\rangle_i \otimes |\sigma_1\rangle_j \otimes |\sigma_2\rangle_k$, for a fixed orientation of the triangle i, j, k. The variational energy per lattice site of the effective Hamiltonian (3.3) can be written as

$$\begin{aligned} \frac{E}{N_s} &= \frac{1}{N_s} \frac{\langle\psi|\mathcal{H}|\psi\rangle}{\langle\psi|\psi\rangle} \\ &= 2J_1\langle\mathcal{P}_{1\text{st}}\rangle + 2J_2\langle\mathcal{P}_{2\text{nd}}\rangle + \frac{2}{3}K\langle\mathcal{P}_{\triangle} + \mathcal{P}_{\triangle}^{-1}\rangle, \end{aligned} \tag{3.4}$$

where the $\langle\mathcal{P}_{1\text{st}}\rangle$ is the averaged expectation value of the permutation operator between the nearest neighbor sites, the $\langle\mathcal{P}_{2\text{nd}}\rangle$ between the second neighbor sites, and $\langle\mathcal{P}_{\triangle} + \mathcal{P}_{\triangle}^{-1}\rangle$ of the ring exchange on the triangles. The coefficients consider that there are twice as many first- and second-neighbor bonds than sites and two triangles for every three sites. The expectation values of these exchange operators were evaluated by Monte Carlo sampling the wavefunctions $|\psi\rangle$ of the ansätze discussed in section 3.1, for details see Appendix J. Figures 3.1 and 3.2 show the expectation values relative to the DSL, i.e.,

$$\Delta\langle\mathcal{P}_{1\text{st}}\rangle = \langle\mathcal{P}_{1\text{st}}\rangle - \langle\mathcal{P}_{1\text{st}}\rangle_{\text{DSL}} \tag{3.5a}$$

$$\Delta\langle\mathcal{P}_{2\text{nd}}\rangle = \langle\mathcal{P}_{2\text{nd}}\rangle - \langle\mathcal{P}_{2\text{nd}}\rangle_{\text{DSL}} \tag{3.5b}$$

$$\Delta\langle\mathcal{P}_{\triangle} + \mathcal{P}_{\triangle}^{-1}\rangle = \langle\mathcal{P}_{\triangle} + \mathcal{P}_{\triangle}^{-1}\rangle - \langle\mathcal{P}_{\triangle} + \mathcal{P}_{\triangle}^{-1}\rangle_{\text{DSL}} \tag{3.5c}$$

for all ansätze as a function of the perturbation strength. On the one hand, we will see that the $\langle\mathcal{P}_{1\text{st}}\rangle$ is minimal for the DSL for small perturbations for all the ansätze we considered. We call this the local stability of the DSL. On the other hand, comparing with the expectation values $\langle\mathcal{P}_{2\text{nd}}\rangle$ and $\langle\mathcal{P}_{\triangle} + \mathcal{P}_{\triangle}^{-1}\rangle$ we find that the values of J_2/J_1 and K/J_1 needed to destabilize the DSL are not small, as explained in the next section.

3.2.1 Calculation of the threshold values of J_2 and K

To assess the stability of the DSL, we calculated the minimum values of J_2 and K (fixing $J_1 = 1$) needed to locally destabilize the DSL in favor of the real perturbations discussed in Sec. 3.1. Specifically, we determined the threshold values of J_2 and K in the Hamiltonian (3.3) where the variational energy of the DSL becomes indistinguishable from that of a perturbed ansatz up to the Monte Carlo error. The results, presented in the last row of Fig. 3.1 and the last column of Fig.3.2, indicate that the DSL remains locally stable over a relatively large parameter region.

First, we considered the ansätze with two free parameters. We fitted a quadratic surface (ellipsoid) to the expectation values of the exchanges $X = \langle\mathcal{P}_{1\text{st}}\rangle$, $\langle\mathcal{P}_{2\text{nd}}\rangle$, and $\langle\mathcal{P}_{\triangle} + \mathcal{P}_{\triangle}^{-1}\rangle$ for small δ values around the DSL point,

$$f(\alpha\delta, \beta\delta)_X = a_X(\alpha\delta)^2 + b_X(\beta\delta)^2 + 2c_X\alpha\beta\delta^2 \,. \tag{3.6}$$

The data sets consisted of 11×11 points in the $\alpha\delta, \beta\delta$ plane, all having a Monte Carlo error, which we considered in the fitting procedure and transferred to the parameters a_X, b_X, and c_X. Fig. 3.2 shows the results of this analysis. To facilitate the comparison between the calculated and fitted values, the contours of the Monte Carlo data are shown in orange, and the contours of the fitted surface in green (we use the same quadratic contour level spacing for every figure, both for the contours of the fitted ellipsoids and the contours of the Monte Carlo data). For the nearest neighbor exchange $\langle \mathcal{P}_{1\text{st}} \rangle$, the expectation value is the smallest for $\delta = 0$, thus providing numerical evidence for the local stability of DSL. However, the expectation values of the second neighbor and ring exchanges show a different picture: the $\langle \mathcal{P}_{2\text{nd}} \rangle$ can lose or gain energy depending on the perturbed ansatz, but the $\langle \mathcal{P}_\triangle + \mathcal{P}_\triangle^{-1} \rangle$ will always gain energy with perturbations (assuming $K > 0$).

To calculate the threshold values J_2 and K, we calculated the curvatures of the ellipsoid

$$f(\alpha\delta, \beta\delta)_E = \left(a_1 + a_2 + \frac{1}{3}a_\triangle\right)(\alpha\delta)^2 + \left(b_1 + b_2 + \frac{1}{3}b_\triangle\right)(\beta\delta)^2 + 2\left(c_1 + c_2 + \frac{1}{3}c_\triangle\right)\alpha\beta\delta^2 \,. \tag{3.7}$$

which fits on the variational energy per site $E/(2N_s) = \langle \mathcal{P}_{1\text{st}} \rangle + J_2 \langle \mathcal{P}_{2\text{nd}} \rangle + \frac{1}{3}K \langle \mathcal{P}_\triangle + \mathcal{P}_\triangle^{-1} \rangle$ of Eq. 3.4. The curvatures are the eigenvalues of the matrix

$$\begin{pmatrix} J_1 a_1 + J_2 a_2 + \frac{K}{3} a_\triangle & J_1 c_1 + J_2 c_2 + \frac{K}{3} c_\triangle \\ J_1 c_1 + J_2 c_2 + \frac{K}{3} c_\triangle & J_1 b_1 + J_2 b_2 + \frac{K}{3} b_\triangle \end{pmatrix}. \tag{3.8}$$

If both of these curvatures are positive, then the DSL has the lowest variational energy for these J_2 and K values (red region). If at least one of the curvatures becomes negative, the DSL is certainly unstable (blue region), since some perturbed ansätze have lower variational energies. If the curvatures can not be distinguished from 0 up to the Monte Carlo error, then we can not conclude (white region).

For the ansätze with a single free parameter δ, shown in Fig. 3.1, we fit a simple parabola to $\Delta E/N_s$ instead of a quadratic surface, and the coefficient of the δ^2 takes the role of the eigenvalues discussed above. We repeat the same procedure to get the regions of stability.

For the David star shown in the first row of Fig. 3.2, we used $t_\hexagon$, and $t_\triangle$ (given in Tab. 3.1) instead of $\alpha\delta$ and $\beta\delta$. For this ansatz, there are sizeable contributions in δ^3, so we considered only a tiny neighborhood around the $t_\hexagon = t_\triangle = 1$ DSL point to fit the quadratic surface. The energy differences were also tiny, with large relative errors, explaining the large white region. However, we expect the same local stability figure as we obtained for the T_{1g}^3, where the δ^3 are absent. Indeed, the calculations give a smaller relative error in that case and a smaller white region.

Summary

In this chapter, we showed that the Dirac spin liquid ansatz is energetical stable against its real-valued perturbations in the quadrupled 12-site unit cell. Furthermore, we found that the values of the second-neighbor (J_2) and ring (K) exchanges necessary to destabilize the DSL are not small relative to J_1, highlighting its resilience to further interactions. However, our study cannot exclude an SU(6) symmetry-breaking ground state of some form.

These results were published in Ref. [III.], where we have also shown that the Dirac spin liquid is globally stabile against every possible David star ansatz, chiral ansätze in the 12-site unit cell, and also chiral ansätze in larger unit cells.

Chapter 4

Dynamical spin structure factor

The dynamical spin structure factor gives precious information about the magnetic excitations and the nature of the ground state of a material. It is always associated with a Hamiltonian, describing the system of interest. The dynamical spin structure factor at $T = 0$ K is the Fourier transform of the dynamic spin correlation function

$$S^{ab}(\mathbf{k},\omega) \equiv \frac{1}{N_B}\sum_{s,\bar{s}} e^{-i\mathbf{k}\cdot(\boldsymbol{\delta}_s-\boldsymbol{\delta}_{\bar{s}})}\frac{1}{N_C}\sum_{\mathbf{R},\bar{\mathbf{R}}} e^{-i\mathbf{k}\cdot(\mathbf{R}-\bar{\mathbf{R}})}\frac{1}{2\pi}\int_{-\infty}^{\infty} e^{i\omega t}\langle \mathrm{GS}|T^a_{\mathbf{R},s}(0)T^b_{\bar{\mathbf{R}},\bar{s}}(t)|\mathrm{GS}\rangle dt, \quad (4.1)$$

where $|\mathrm{GS}\rangle$ is the ground state of the Hamiltonian $\mathcal{H}$, $T^b_{\bar{\mathbf{R}},\bar{s}}(t) \equiv e^{-i\mathcal{H}t}T^b_{\bar{\mathbf{R}},\bar{s}}e^{i\mathcal{H}t}$, $a, b \in \{1 \dots N^2 - 1\}$, the SU($N$) spin operators are taken on sites with lattice vectors $\mathbf{R}+\boldsymbol{\delta}_s$ and $\bar{\mathbf{R}}+\boldsymbol{\delta}_{\bar{s}}$, $\mathbf{R}$ and $\bar{\mathbf{R}}$ are the Bravais lattice vectors of the unit cells, $\boldsymbol{\delta}_s$ and $\boldsymbol{\delta}_{\bar{s}}$ are basis vectors, s and $\bar{s}$ are sublattice indices, N_C is the number of unit cells and N_B is the number of basis sites in a unit cell (the number of possible sublattice indices), so that $N_B \times N_C = N_s$ is the number of lattice sites. Defining the Fourier transform of an SU(N) spin operator as

$$T^a_{\mathbf{k}} \equiv \frac{1}{\sqrt{N_s}}\sum_{\mathbf{R},s} e^{i\mathbf{k}\cdot(\mathbf{R}+\boldsymbol{\delta}_s)}T^a_{\mathbf{R},s}, \quad (4.2)$$

we can rewrite $S^{ab}(\mathbf{k},\omega)$ as

$$S^{ab}(\mathbf{k},\omega) = \frac{1}{2\pi}\int_{-\infty}^{\infty} e^{i\omega t}\langle \mathrm{GS}|T^a_{-\mathbf{k}}(0)T^b_{\mathbf{k}}(t)|\mathrm{GS}\rangle dt = \sum_f \frac{1}{2\pi}\int_{-\infty}^{\infty} e^{i\omega t}\langle \mathrm{GS}|T^a_{-\mathbf{k}}(0)|f\rangle\langle f|T^b_{\mathbf{k}}(t)|\mathrm{GS}\rangle dt \quad (4.3)$$

where we inserted the identity as $\mathcal{I} = \sum_f |f\rangle\langle f|$ with the sum going through the eigenstates $|f\rangle$ of the Hamiltonian, so that $e^{i\mathcal{H}t}|f\rangle = e^{iE_f t}|f\rangle$. Using $\langle f|T^b_{\mathbf{k}}(t)|\mathrm{GS}\rangle = \langle f|e^{-i\mathcal{H}t}T^b_{\mathbf{k}}e^{i\mathcal{H}t}|\mathrm{GS}\rangle = e^{i(E_{\mathrm{GS}}-E_f)t}\langle f|T^b_{\mathbf{k}}|\mathrm{GS}\rangle$ and $\int_{-\infty}^{\infty} e^{i\omega t}e^{i(E_{\mathrm{GS}}-E_f)t}dt = 2\pi\delta(\omega + E_{\mathrm{GS}} - E_f)$, we get

$$S^{ab}(\mathbf{k},\omega) = \sum_f \langle \mathrm{GS}|T^a_{-\mathbf{k}}|f\rangle\langle f|T^b_{\mathbf{k}}|\mathrm{GS}\rangle\delta(\omega - (E_f - E_{\mathrm{GS}}))\ , \quad (4.4)$$

or for the $a = b$ case

$$S^{aa}(\mathbf{k},\omega) = \sum_f |\langle f|T^a_{\mathbf{k}}|\mathrm{GS}\rangle|^2\,\delta(\omega - (E_f - E_{\mathrm{GS}}))\ , \quad (4.5)$$

where the matrix elements $|\langle f|T^a_{\mathbf{k}}|\mathrm{GS}\rangle|^2$ are called the spectral weights.

In case of the SU(N) symmetric Heisenberg Hamiltonian (1.18), $S^{ab}(\mathbf{k},\omega) = \delta_{a,b}S^{ab}(\mathbf{k},\omega)$. Due to the SU($N$) spin rotational symmetry of the Heisenberg Hamiltonian (1.18) and its mean-field hopping Hamiltonian (2.6), the $S^{aa}(\mathbf{k},\omega)$ is the same for all $a \in \{1 \dots N^2 - 1\}$ in both cases. It is convenient to calculate the $S^{aa}(\mathbf{k},\omega)$ only for the diagonal SU(N) spin operators. Using the convention of the SU(N) spin operators in the fundamental representation presented in Appendix A.3, the

$$T^3_{\mathbf{k}} = \frac{1}{\sqrt{N_s}}\sum_{\mathbf{R},s} e^{i\mathbf{k}\cdot(\mathbf{R}+\boldsymbol{\delta}_s)}\frac{1}{2}\left(f^\dagger_{\mathbf{R},s,1}f_{\mathbf{R},s,1} - f^\dagger_{\mathbf{R},s,2}f_{\mathbf{R},s,2}\right) \quad (4.6)$$

will always be diagonal (the generalization of S^z) so that we will calculate $S^{33}(\mathbf{k},\omega)$.

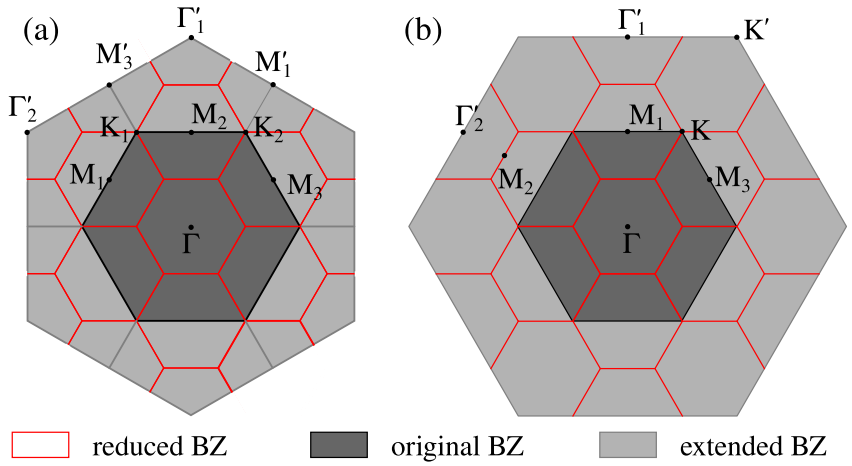

Figure 4.1: The original, extended, and reduced Brillouin zones of the honeycomb (a) and kagome lattices (b), with the color codes shown at the bottom. The dynamical structure factor is periodic only in the extended Brillouin zone, because neither the honeycomb, nor the kagome lattices are Bravais lattices.

If the underlying lattice of the Hamiltonian is a Bravais lattice (having one basis site in its unit cell $N_B = 1$), then the $S^{aa}(\mathbf{k}, \omega)$ will be periodic in the original Brillouin zone. However, if the underlying lattice is not a Bravais lattice (meaning that $N_B > 1$), which is the case of the honeycomb ($N_B = 2$) and the kagome ($N_B = 3$) lattices, then the $S^{aa}(\mathbf{k}, \omega)$ will not be periodic in the original Brillouin zone, due to the term $e^{i\mathbf{k}\cdot\boldsymbol{\delta}_s}$ in Eq. (4.2). Instead, the $S^{aa}(\mathbf{k}, \omega)$ will be periodic only in the extended Brillouin zone shown in Fig. 4.1 (for an explanation see Appendix H). Therefore, to have all the information about the $S^{aa}(\mathbf{k}, \omega)$, we have to calculate it in the extended Brillouin zone $\mathbf{k} \in eBZ$ instead of the original Brillouin zone.

4.1 Measurement of the dynamical spin structure factor in real materials

The $S^{aa}(\mathbf{k}, \omega)$ can be measured, among others, in inelastic neutron scattering, Bragg spectroscopy, resonant inelastic X-ray scattering, electron spin resonance, and light absorption experiments.

4.1.1 Inelastic neutron scattering experiments

In inelastic neutron scattering experiments, a small (a few mm^3) sample is irradiated with a beam of unpolarised neutrons of incident wave vectors $\mathbf{k}_i$, which are scattered on the sample and acquire final wave vectors $\mathbf{k}_f$ [84, Chap. 3.]. The momentum of a neutron is $\mathbf{p} = \hbar\mathbf{k}$ and its kinetic energy is $E = \hbar^2\mathbf{k}^2/(2m)$, where m is the neutron mass. The conservation of momentum and energy implies, that the neutron has transferred momentum $\Delta p = \hbar(\mathbf{k_i} - \mathbf{k_f})$ and energy $\Delta E = \hbar^2(\mathbf{k_i}^2 - \mathbf{k_f}^2)/(2m) = \hbar\omega$ to the sample, where $\mathbf{k} \equiv \mathbf{k_i} - \mathbf{k_f}$ is called the scattering vector and $\Delta E = \hbar\omega$ the energy transfer, these are the arguments of $S^{ab}(\mathbf{k}, \omega)$. For $|\mathbf{k_i}| = |\mathbf{k_f}|$ the $\Delta E = 0$, this is called elastic neutron scattering. The scattering is inelastic, if the energy transferred is finite. Such experiments measure the partial differential cross section $d^2\sigma/(d\Omega dE)$, which is the number of neutrons scattered per second per unit incident flux, into a range of solid angle $d\Omega$ and with a range of energies between E and $E + dE$. Neutrons are scattered by atomic nuclei and the total magnetic moments of the electrons (including spin and orbital angular momentum). The contribution of the atomic nuclei can be separated, and the $d^2\sigma/(d\Omega dE)$

originating from the total magnetic moments of the electrons turns out to be directly related to the dynamical spin structure factor $S^{ab}(\mathbf{k},\omega)$. At a sufficiently low temperature, the $S^{ab}(\mathbf{k},\omega)$ extracted from the experimental data should coincide with the zero temperature expression of Eq. (4.5).

4.1.2 Bragg spectroscopy for ultracold atoms

Regarding optically trapped ultracold atomic experiments, inelastic neutron scattering is not possible, but for atoms with spin 1/2, the dynamical spin structure factor can be measured with Bragg spectroscopy (see Ref. [85, 86], and for a general description of Bragg spectroscopy [10, Sec. 14.4]).

In such an experiment, the sample is illuminated with two phase-locked laser beams with wave vectors $\mathbf{k}_1$ and $\mathbf{k}_2$, and frequencies ω_1 and ω_2, enclosing an angle θ. The atoms absorb photons from one beam and emit photons into the second beam. Meanwhile, their momenta change as $\Delta\mathbf{p}_{\text{Bragg}} = \hbar(\mathbf{k}_1 - \mathbf{k}_2)$ and their energy change as $\Delta E_{\text{Bragg}} = \hbar(\omega_2 - \omega_1)$. The transfer of momentum can be tuned independently of the energy transfer by changing the angle θ between the two beams.

In the coherent momentum transfer method (CMTM, [87], [10, Sec. 14.4]) the confining potential is turned off immediately after the application of the Bragg pulses, followed by the free expansion of the atoms. Using light absorption images at different times after the release of the atoms (called time-of-flight absorption imaging), it is possible to determine the momentum Δp_{Bragg} transferred to a fraction of the atoms, as a function of the ΔE_{Bragg} [10, Sec. 14.2]. However, this method was initially applied only for the measurement of the dynamical density structure factor. It was generalized to measure the dynamical spin structure factor of ^{6}Li atoms in the experiment of Ref. [85] (and later used in Ref. [86]), where the two Bragg lasers were detuned close to resonance. Every ^{6}Li atom has two degenerate ground states, labeled as $|F = 1/2, m_f = 1/2\rangle$ and $|F = 1/2, m_f = -1/2\rangle$. In this experiment, the CMTM method was applied so that $t_\uparrow$ time after turning off the confinement potential a light absorption image was taken of the atoms in state $|F = 1/2, m_f = 1/2\rangle$. The imaging laser frequency was then rapidly switched and a second image was taken of atoms in state $|F = 1/2, m_f = -1/2\rangle$, time $t_\downarrow$ after the first. Taking separate images of each spin state at different times allowed them to measure the differential center of mass cloud displacement (from which Δp_{Bragg} can be calculated), which is insensitive to fluctuations in the trap position, and the order of the images.

Unfortunately, such measurements were not yet performed for atoms with SU(N) spins (e.g. the ^{173}Yb isotopes with SU(6) symmetric nuclear spins mentioned in Sec. 1.1.3).

4.2 $S^{33}(\mathbf{k},\omega)$ of the mean-field hopping Hamiltonian

The $S^{aa}(\mathbf{k},\omega)$ of Eq. (4.5) can be calculated exactly for the mean-field hopping Hamiltonian $\mathcal{H}^{\text{MF}}$ of Eq. (2.6), for any hoppings $t_{i,j}$, which will serve as comparison with the Gutzwiller projected case (allowing us to interpret the Gutzwiller projected results), and also as a guide for building the Gutzwiller projected particle-hole excitations in section 4.3.

The exact ground state of the noninteracting $\mathcal{H}^{\text{MF}}$ is the Fermi sea $|\text{GS}\rangle = |\text{FS}\rangle$, (see Eqs. (2.8) and (2.27)), and the exact excited eigenstates $|f\rangle$ are particle-hole excitations

$$f^\dagger_{\mathbf{k}+\mathbf{q},b',\sigma} f_{\mathbf{q},b,\sigma} |\pi\text{FS}\rangle, \tag{4.7}$$

where a particle of flavor σ and wave vector $\mathbf{q}$ is transferred from an occupied band of the Fermi sea with band index b, to one of the unoccupied bands with band index b', to wave vector $\mathbf{k}+\mathbf{q}$.

In Appendix I (see also Ref. [II.]) we derive the simple formula

$$S^{33}_{\mathrm{MF}}(\mathbf{k},\omega) = \frac{1}{2N_s}\sum_{\mathbf{q}\in\mathrm{rBZ}}\sum_{\substack{b,b'\\ \varepsilon_{b'}(\mathbf{k}+\mathbf{q})>\varepsilon_{\mathrm{F}}\\ \varepsilon_{b}(\mathbf{q})<\varepsilon_{\mathrm{F}}}}\left|\sum_{s\in\{A,B\ldots\}} e^{i\mathbf{k}\cdot\boldsymbol{\delta}_s} v^{*}_{\mathbf{k}+\mathbf{q},b',s} v_{\mathbf{q},b,s}\right|^2 \times \delta\left(\omega-\varepsilon_{b'}(\mathbf{k}+\mathbf{q})+\varepsilon_{b}(\mathbf{q})\right)\ , \tag{4.8}$$

where the complex numbers $v_{\mathbf{q},b,s}$ are the coefficients of the band eigenstates $\{f^{\dagger}_{\mathbf{q},b,\sigma}|0\rangle\}$ in the site basis $\{f^{\dagger}_{\mathbf{q},s,\sigma}|0\rangle\}$ (see Eq. 2.27), normalized as $\sum_s |v_{\mathbf{q},b,s}|^2 = 1$. The Dirac delta in Eq. 4.5 implies $\omega = E_f - E_{\mathrm{GS}}$, where both E_f and E_{GS} are sums of the filled one-particle energies, and they differ only due to the particle-hole excitation of Eq. (4.7), implying $\omega = \varepsilon_{b'}(\mathbf{k}+\mathbf{q}) - \varepsilon_b(\mathbf{q})$.

For the π-flux $\mathcal{H}^{\mathrm{MF}}$ introduced in sections 2.3.1 and 2.3.2, the exact ground state is the $|\pi\mathrm{FS}\rangle$, where only the two-fold degenerate lowest band is occupied (see Eqs. (2.26) and (2.31)). As mentioned in sections 2.3.1 and 2.3.2, the π-flux $\mathcal{H}^{\mathrm{MF}}$ has a quadrupled unit cell (see Fig. 2.1 (a) and (c)), implying that one-particle spectrum is periodic in the reduced Brillouin zone (rBZ), which is a quarter of the original Brillouin zone, as shown in Fig. 4.1 (for details see Appendix H). However, the SU(N) Heisenberg Hamiltonian (1.18) does not break any symmetry of the lattice, therefore the wave vector $\mathbf{k}$ in the associated $S^{aa}(\mathbf{k},\omega)$ in Eq. (4.5) has to be in the extended Brillouin zone of the lattice, as argued in section 4 and Appendix H. To be able to compare the $S^{aa}_{\mathrm{MF}}(\mathbf{k},\omega)$ of the π-flux $\mathcal{H}^{\mathrm{MF}}$ and the $S^{aa}(\mathbf{k},\omega)$ of the SU(N) Heisenberg Hamiltonian (1.18), the wave vector $\mathbf{k}$ has to be in the extended Brillouin zone in both cases. Consequently, even if $\mathbf{q}\in\mathrm{rBZ}$, $\mathbf{k}+\mathbf{q}$ will be in the extended Brillouin zone. Since the one-particle spectrum is periodic in the rBZ, we can turn back the $\mathbf{k}+\mathbf{q}$ to the rBZ by adding a reciprocal lattice vector $\mathbf{Q}$ as $\mathbf{k}+\mathbf{q}+\mathbf{Q}\in\mathrm{rBZ}$, as explained in Appendix I.

The $S^{33}_{\mathrm{MF}}(\mathbf{k},\omega)$ will be gapless due to the term $\delta\left(\omega-\varepsilon_{b'}(\mathbf{k}+\mathbf{q})+\varepsilon_b(\mathbf{q})\right)$, since in the thermodynamic limit $\varepsilon_{b'}(\mathbf{k}+\mathbf{q}) = \varepsilon_b(\mathbf{q})$ when a particle is excited from the top of the Fermi sea (with $b\in\{1,2\}$) to the bottom of the Dirac cone in the second band ($b'\in\{3,4\}$) (see Figs. 2.1(b), 2.1(d), and 6.2(d)). This happens not only at the relative wave vector $\mathbf{k}=(0,0)\in\mathrm{eBZ}$ (the Γ point), but also at the M, M', and Γ' points of the eBZ, because when turned back to the rBZ, these are equivalent to $\mathbf{k}=(0,0)\in\mathrm{rBZ}$, which we will call the Γ_{MF} point (the centers of the red hexagons in Figs. 4.1(a) and (b), all of which host Dirac Fermi points).

4.3 Variational method: Gutzwiller projected particle-hole excitations

Let us consider first translationally symmetric mean-field Hamiltonians (0-flux case) and Bravais lattices (with one basis site per unit cell), like a one-dimensional chain, the two-dimensional square and triangular lattices, so we don't have to carry the sublattice (or band) indices.

4.3.1 Translationally invariant mean-field ansätze on Bravais lattices

Following Refs. [88, 89, 90], as an analogy of the mean-field particle-hole excitations of Eq. (4.7), we can define the Gutzwiller projected particle-hole excitations as

$$|\mathbf{k},\mathbf{q},\sigma\rangle \equiv P_{\mathrm{G}} f^{\dagger}_{\mathbf{k}+\mathbf{q},\sigma} f_{\mathbf{q},\sigma}|\mathrm{FS}\rangle. \tag{4.9}$$

We can rewrite these states to real space using Eq. (2.27) (which has only one band now, with $v_{\mathbf{q},1,1} = 1$) as

$$P_{\mathrm{G}} f^{\dagger}_{\mathbf{k}+\mathbf{q},\sigma} f_{\mathbf{q},\sigma} |\mathrm{FS}\rangle = \frac{1}{N_C} \sum_{\mathbf{R},\mathbf{R}'} e^{i(\mathbf{k}+\mathbf{q})\mathbf{R}} e^{-i\mathbf{q}\mathbf{R}'} P_{\mathrm{G}} f^{\dagger}_{\mathbf{R},\sigma} f_{\mathbf{R}',\sigma} |\mathrm{FS}\rangle \tag{4.10}$$
$$= \frac{1}{N_C} \sum_{\mathbf{R},\mathbf{R}'} e^{i(\mathbf{k}+\mathbf{q})\mathbf{R}} e^{-i\mathbf{q}\mathbf{R}'} \sum_{x} \left(\prod_{\sigma=1}^{N} \mathrm{slat}_{\{j^{\sigma}\}} \right) P_{\mathrm{G}} f^{\dagger}_{\mathbf{R},\sigma} f_{\mathbf{R}',\sigma} |x\rangle,$$

where in the second line we have substituted the real space expression of $|\mathrm{FS}\rangle$ from Eq. (2.10). This expression shows us that the configurations $|x\rangle$ giving non-zero weights are those which have one hole at $\mathbf{R}$ and two fermions at $\mathbf{R}'$, so that $|x'\rangle = f^{\dagger}_{\mathbf{R},\sigma} f_{\mathbf{R}',\sigma} |x\rangle$ has only singly occupied sites, otherwise the Gutzwiller projector would kill $|x'\rangle$.

Eq. (4.10) also explains why we can not have excitations like $f^{\dagger}_{\mathbf{k}+\mathbf{q},\sigma} f_{\mathbf{q},\sigma} P_{\mathrm{G}} |\mathrm{FS}\rangle$ since these would have terms like $f^{\dagger}_{\mathbf{R},\sigma} f_{\mathbf{R}',\sigma} P_{\mathrm{G}} |x\rangle$, where $P_{\mathrm{G}}|x\rangle$ is a product state of singly occupied sites, so the $f^{\dagger}_{\mathbf{R},\sigma} f_{\mathbf{R}',\sigma} P_{\mathrm{G}} |x\rangle$ have a doubly occupied site at $\mathbf{R}$, and an empty site at $\mathbf{R}'$. Consequently, the state $f^{\dagger}_{\mathbf{R},\sigma} f_{\mathbf{R}',\sigma} P_{\mathrm{G}} |x\rangle$ violates the single occupancy constraint (2.5), implying that the Hilbert spaces of fermions and SU(N) spins would not be mapped to each other in a one-to-one correspondence.

If the mean-field ansatz is stable (the interactions between the fermions are short-ranged and weak), then the $P_{\mathrm{G}}|\mathrm{FS}\rangle$ and the above-defined excitations are expected to give a good approximation of the low-energy excited eigenstates of the Heisenberg Hamiltonian (1.18). In other words, the real ground state and its lowest energy excitations are expected to be similar to the Gutzwiller projected mean-field ground state, and its Gutzwiller projected particle-hole excitations. However, this qualitative similarity is not expected to give quantitatively perfect answers, since the fluctuations can cause small changes even if the mean-field ansatz is stable. Still, the existence and location of the gapless towers in the dynamical spin structure factor allows the identification of a gapless quantum spin liquid.

Although we call the states in Eq. (4.9) excitations, these states are not eigenstates of the Heisenberg Hamiltonian (1.18), they are not even all linearly independent. However, in $S^{aa}(\mathbf{k},\omega)$ of Eq. (4.5) the $|f\rangle$ must be eigenstates of the Hamiltonian. We can construct approximating eigenstates, by projecting the Heisenberg Hamiltonian onto the subspace of these Gutzwiller projected particle-hole excitations as $\tilde{\mathcal{H}} \equiv \langle \mathbf{k},\mathbf{q},\sigma|\mathcal{H}|\mathbf{k}',\mathbf{q}',\sigma'\rangle$, and solving the generalized eigenvalue problem $\tilde{\mathcal{H}}|f\rangle = E_f \tilde{\mathcal{O}}|f\rangle$, where $\tilde{\mathcal{O}} \equiv \langle \mathbf{k},\mathbf{q},\sigma|\mathbf{k}',\mathbf{q}',\sigma'\rangle$ is the overlap matrix (it appears because the states $|\mathbf{k},\mathbf{q},\sigma\rangle$ are not orthonormal). These $|f\rangle$ are only approximate eigenstates of $\mathcal{H}$ because the subspace of the states $|\mathbf{k},\mathbf{q},\sigma\rangle$ is not closed under the action of $\mathcal{H}$.

We can project the Hamiltonian on a different set of states without changing the energy eigenvalues E_f or the spectral weights, provided that the new set of states span the same subspace as the $|\mathbf{k},\mathbf{q},\sigma\rangle$. In other words, transforming the Hamiltonian and the overlap matrices by a unitary operator U does not change the eigenvalues E_f, and the eigenstates $|f\rangle$ are simply rotated as $U|f\rangle$, since $U\tilde{\mathcal{H}}U^{-1}U|f\rangle = E_f U\tilde{\mathcal{O}}U^{-1}U|f\rangle$. If the $\mathcal{H}$ and $\mathcal{O}$ matrices are evaluated exactly, we obtain exactly the same eigenvalues E_f and spectral weights for any set of states spanning the same subspace. Therefore, instead of projecting the Hamiltonian to the states $|\mathbf{k},\mathbf{q},\sigma\rangle$, we can project it to the real-space states

$$|\mathbf{R},\mathbf{R}',\sigma\rangle \equiv P_{\mathrm{G}} f^{\dagger}_{\mathbf{R},\sigma} f_{\mathbf{R}',\sigma} |\mathrm{FS}\rangle, \tag{4.11}$$

as $\tilde{\mathcal{H}} \equiv \langle \mathbf{R},\mathbf{R}',\sigma|\mathcal{H}|\bar{\mathbf{R}},\bar{\mathbf{R}}',\sigma'\rangle$ with $\tilde{\mathcal{O}} \equiv \langle \mathbf{R},\mathbf{R}',\sigma|\bar{\mathbf{R}},\bar{\mathbf{R}}',\sigma'\rangle$, and solving the generalized eigenvalue problem $\tilde{\mathcal{H}}|f\rangle = E_f\tilde{\mathcal{O}}|f\rangle$ for these matrices. The unitary transformation connecting these

states with the previous ones can be read off from Eq. (4.10) to be

$$|\mathbf{k},\mathbf{q},\sigma\rangle = \frac{1}{N_C}\sum_{\mathbf{R},\mathbf{R}'} e^{i(\mathbf{k}+\mathbf{q})\mathbf{R}} e^{-i\mathbf{q}\mathbf{R}'} |\mathbf{R},\mathbf{R}',\sigma\rangle. \tag{4.12}$$

Following Ref. [91], we can project out the eigenstates of the translation operator from the states $|\mathbf{R},\mathbf{R}',\sigma\rangle$, using the projector

$$\frac{1}{\sqrt{N_C}}\sum_{\mathbf{R}'} e^{i\mathbf{k}\cdot\mathbf{R}'}\mathsf{T}_{\mathbf{R}'}, \tag{4.13}$$

where $\mathsf{T}_{\mathbf{R}'} \equiv \mathsf{T}_1^{R_1'}\mathsf{T}_2^{R_2'}$ is the translation operator translating by the Bravais lattice vector $\mathbf{R}' = R_1'\mathbf{a}_1 + R_2'\mathbf{a}_2$, while T_1 and T_2 translates by the primitive vectors $\mathbf{a}_1$ and $\mathbf{a}_2$, respectively. This projector projects a state to the eigensubspace of the translation operator $\mathsf{T}_{\mathbf{R}}$ with eigenvalue $e^{-i\mathbf{k}\cdot\mathbf{R}}$, since

$$\mathsf{T}_{\mathbf{R}}\sum_{\mathbf{R}'} e^{i\mathbf{k}\cdot\mathbf{R}'}\mathsf{T}_{\mathbf{R}'}\cdots = \sum_{\mathbf{R}'} e^{i\mathbf{k}\cdot\mathbf{R}'}\mathsf{T}_{\mathbf{R}'+\mathbf{R}}\cdots = \sum_{\tilde{\mathbf{R}}'} e^{i\mathbf{k}\cdot(\tilde{\mathbf{R}}'-\mathbf{R})}\mathsf{T}_{\tilde{\mathbf{R}}'}\cdots = e^{-i\mathbf{k}\cdot\mathbf{R}}\sum_{\tilde{\mathbf{R}}'} e^{i\mathbf{k}\cdot\tilde{\mathbf{R}}'}\mathsf{T}_{\tilde{\mathbf{R}}'}\cdots \tag{4.14}$$

where in the third step we changed the summation variable to $\tilde{\mathbf{R}}' \equiv \mathbf{R}' + \mathbf{R}$. Consequently, applying this projector on the real space state $|\mathbf{R},\mathbf{0},\sigma\rangle$ of Eq. (4.11) results in an eigenstate of the translation operator, with the hole and the doubly occupied site being separated by $\mathbf{R}$, as

$$\begin{aligned}
|\mathbf{k},\mathbf{R},\sigma\rangle &\equiv \frac{1}{\sqrt{N_C}}\sum_{\mathbf{R}'} e^{i\mathbf{k}\cdot\mathbf{R}'}\mathsf{T}_{\mathbf{R}'}|\mathbf{R},0,\sigma\rangle = \frac{1}{\sqrt{N_C}}\sum_{\mathbf{R}'} e^{i\mathbf{k}\cdot\mathbf{R}'}\mathsf{T}_{\mathbf{R}'}P_{\mathrm{G}}f^\dagger_{\mathbf{R},\sigma}f_{0,\sigma}|\mathrm{FS}\rangle \\
&= \frac{1}{\sqrt{N_C}}\sum_{\mathbf{R}'} e^{i\mathbf{k}\cdot\mathbf{R}'}P_{\mathrm{G}}\mathsf{T}_{\mathbf{R}'}f^\dagger_{\mathbf{R},\sigma}\mathsf{T}^{-1}_{\mathbf{R}'}\mathsf{T}_{\mathbf{R}'}f_{0,\sigma}\mathsf{T}^{-1}_{\mathbf{R}'}\mathsf{T}_{\mathbf{R}'}|\mathrm{FS}\rangle \\
&= \frac{1}{\sqrt{N_C}}\sum_{\mathbf{R}'} e^{i\mathbf{k}\cdot\mathbf{R}'}P_{\mathrm{G}}f^\dagger_{\mathbf{R}+\mathbf{R}',\sigma}f_{\mathbf{R}',\sigma}\mathsf{T}_{\mathbf{R}'}|\mathrm{FS}\rangle = \frac{1}{\sqrt{N_C}}\sum_{\mathbf{R}'} e^{i\mathbf{k}\cdot\mathbf{R}'}P_{\mathrm{G}}f^\dagger_{\mathbf{R}+\mathbf{R}',\sigma}f_{\mathbf{R}',\sigma}|\mathrm{FS}\rangle,
\end{aligned} \tag{4.15}$$

where in the second row we used that the P_{G} commutes with $\mathsf{T}_{\mathbf{R}}$ (as argued at Eq. (2.13)), and in the last step we used that the $|\mathrm{FS}\rangle$ inherits the symmetries of $\mathcal{H}^{\mathrm{MF}}$, which is supposed to be translationally invariant in this section. These states are connected to the original ones as $|\mathbf{k},\mathbf{q},\sigma\rangle = \frac{1}{\sqrt{N_C}}\sum_{\mathbf{R}} e^{i(\mathbf{k}+\mathbf{q})\cdot\mathbf{R}}|\mathbf{k},\mathbf{R},\sigma\rangle$. This relation does not hold for the π-flux ansatz, because the π flux Fermi sea is not translationally invariant (the $|\pi\mathrm{FS}\rangle$ is discussed in section 4.3.3).

The Heisenberg Hamiltonian (1.18) does not change the eigenvalue of the translation operator because it is translationally invariant. Therefore, if the Hamiltonian and the overlap matrices were calculated exactly (which we will call the exact variational method, see Appendix J), then they would be exactly block diagonal in $\mathbf{k}$ as $\tilde{\mathcal{H}} = \langle\mathbf{k},\mathbf{q},\sigma|\mathcal{H}|\mathbf{k}',\mathbf{q}',\sigma'\rangle = \delta_{\mathbf{k},\mathbf{k}'}\langle\mathbf{k},\mathbf{q},\sigma|\mathcal{H}|\mathbf{k}',\mathbf{q}',\sigma'\rangle$ and $\tilde{\mathcal{O}} = \langle\mathbf{k},\mathbf{q},\sigma|\mathbf{k}',\mathbf{q}',\sigma'\rangle = \delta_{\mathbf{k},\mathbf{k}'}\langle\mathbf{k},\mathbf{q},\sigma|\mathbf{k}',\mathbf{q}',\sigma'\rangle$ and similarly for the $|\mathbf{k},\mathbf{R},\sigma\rangle$ states. The states $|\mathbf{R},\mathbf{R}',\sigma\rangle$ would not yield block diagonal $\tilde{\mathcal{H}}$ and $\tilde{\mathcal{O}}$, but they give the same results. However, if the $\tilde{\mathcal{H}}$ and $\tilde{\mathcal{O}}$ are evaluated by Monte Carlo sampling (which we will call the Variational Monte Carlo method, see Appendix J), the Hamiltonian and the overlap matrices will not be perfectly block diagonal, the matrix elements connecting subspaces with different wave vectors (which should be zero) will be of the order of the Monte Carlo error. We can significantly reduce the errors of the E_f and the spectral weights, if instead of solving the generalized eigenvalue problem for the full Hamiltonian and overlap matrices as $\tilde{\mathcal{H}}|f\rangle = E_f\tilde{\mathcal{O}}|f\rangle$, we solve it separately for the block matrices $\tilde{\mathcal{H}}^{\mathbf{k}} \equiv \langle\mathbf{k},\mathbf{R},\sigma|\mathcal{H}|\mathbf{k},\mathbf{R}',\sigma'\rangle$ and $\tilde{\mathcal{O}}^{\mathbf{k}} \equiv \langle\mathbf{k},\mathbf{R},\sigma|\mathbf{k},\mathbf{R}',\sigma'\rangle$ as

$$\tilde{\mathcal{H}}^{\mathbf{k}}|f^{\mathbf{k}}\rangle = E_f^{\mathbf{k}}\tilde{\mathcal{O}}^{\mathbf{k}}|f^{\mathbf{k}}\rangle, \tag{4.16}$$

since this trick eliminates the Monte Carlo errors connecting subspaces of different wave vectors. This way, the eigenstates $\{|f\rangle\}$ are separated into the eigensubspaces of the translation operator exactly, which is useful because the eigenstates giving non-zero overlaps in $\langle f|T^a_{\mathbf{k}}|\mathrm{GS}\rangle$ are those having wave vectors $\mathbf{k}$ (as explained in Section 4.3.4). This is why the states $|\mathbf{R},\mathbf{R}',\sigma\rangle$ are less useful in the VMC method since they produce much bigger Monte Carlo results.

4.3.2 Translationally invariant mean-field ansätze on non-Bravais lattices

For a non-Bravais lattice (where the number of basis sites in the unit cell is larger than one), like the honeycomb ($N_B = 2$) or the kagome lattices ($N_B = 3$), the states $|\mathbf{k},\mathbf{R},\sigma\rangle$ and $|\mathbf{R},\mathbf{R}',\sigma\rangle$ get additional sublattice indices as

$$|\mathbf{R},\mathbf{R}',s,\bar{s},\sigma\rangle \equiv P_{\mathrm{G}} f^\dagger_{\mathbf{R},s,\sigma} f_{\mathbf{R}',\bar{s},\sigma}|\mathrm{FS}\rangle, \tag{4.17}$$

and

$$|\mathbf{k},\mathbf{R},s,\bar{s},\sigma\rangle \equiv \frac{1}{\sqrt{N_C}}\sum_{\mathbf{R}'} e^{i\mathbf{k}\cdot\mathbf{R}'}\mathsf{T}_{\mathbf{R}'} P_{\mathrm{G}} f^\dagger_{\mathbf{R},s,\sigma} f_{\mathbf{R}',\bar{s},\sigma}|\mathrm{FS}\rangle \tag{4.18}$$

$$= \frac{1}{\sqrt{N_C}}\sum_{\mathbf{R}'} e^{i\mathbf{k}\cdot\mathbf{R}'} P_{\mathrm{G}} f^\dagger_{\mathbf{R}+\mathbf{R}',s,\sigma} f_{\mathbf{R}',\bar{s},\sigma}\mathsf{T}_{\mathbf{R}'}|\mathrm{FS}\rangle, \tag{4.19}$$

where again $\mathsf{T}_{\mathbf{R}'}|\mathrm{FS}\rangle = |\mathrm{FS}\rangle$ for a translationally invariant $\mathcal{H}^{\mathrm{MF}}$.

The states $|\mathbf{k},\mathbf{q},\sigma\rangle$ would in principle acquire band indices as $|\mathbf{k},\mathbf{q},b,\bar{b},\sigma\rangle$ although we have not tried using them.

The way to calculate the spectral weights $|\langle f|T^3_{\mathbf{k}} P_{\mathrm{G}}|\pi\mathrm{FS}\rangle|^2$ for $S^{33}(\mathbf{k},\omega)$ is discussed in Appendix K.

4.3.3 π-flux mean-field ansätze

If the mean-field Hamiltonian is not invariant under some translations (as the π-flux $\mathcal{H}^{\mathrm{MF}}$), then the $\mathsf{T}_{\mathbf{R}'}|\mathrm{FS}\rangle \neq |\mathrm{FS}\rangle$ for some $\mathbf{R}'$. In this case, Eq. (4.19) becomes more complicated. The trick (used in Refs. [92, 93], but explained only in Appendix F.3 of the thesis https://hdl.handle.net/20.500.11767/103865) is that if the $\mathcal{H}^{\mathrm{MF}}$ is invariant under the combined transformation $G_{\mathsf{T}_{\mathbf{R}'}}\mathsf{T}_{\mathbf{R}'}$ for any $\mathbf{R}'$, then $|\mathrm{FS}\rangle$ inherits this invariance, meaning $G_{\mathsf{T}_{\mathbf{R}'}}\mathsf{T}_{\mathbf{R}'}|\mathrm{FS}\rangle = |\mathrm{FS}\rangle$ for any $\mathbf{R}'$ (the $G_{\mathsf{T}_{\mathbf{R}'}}$ is specified in Appendix E). Furthermore, as argued in section 2.4.1 the Gutzwiller projection eliminates any Gauge transformation (in the sense that it converts it to an unimportant global phase $e^{i\varphi}$), so we can insert $G_{\mathsf{T}_{\mathbf{R}'}}$ right before applying P_{G} in Eq. (4.19) as

$$\begin{aligned}
&|\mathbf{k},\mathbf{R},s,\bar{s},\sigma\rangle \qquad\qquad (4.20)\\
&= \frac{1}{\sqrt{N_C}}\sum_{\mathbf{R}'} e^{i\mathbf{k}\cdot\mathbf{R}'}\mathsf{T}_{\mathbf{R}'} P_{\mathrm{G}} f^\dagger_{\mathbf{R},s,\sigma} f_{0,\bar{s},\sigma}|\pi\mathrm{FS}\rangle\\
&= \frac{1}{\sqrt{N_C}} e^{i\varphi}\sum_{\mathbf{R}'} e^{i\mathbf{k}\cdot\mathbf{R}'} P_{\mathrm{G}} G_{\mathsf{T}_{\mathbf{R}'}}\mathsf{T}_{\mathbf{R}'} f^\dagger_{\mathbf{R},s,\sigma} f_{0,\bar{s},\sigma}|\pi\mathrm{FS}\rangle\\
&= \frac{e^{i\varphi}}{\sqrt{N_C}}\sum_{\mathbf{R}'} e^{i\mathbf{k}\cdot\mathbf{R}'} P_{\mathrm{G}} \underbrace{G_{\mathsf{T}_{\mathbf{R}'}}\mathsf{T}_{\mathbf{R}'} f^\dagger_{\mathbf{R},s,\sigma}\mathsf{T}^{-1}_{\mathbf{R}'}G^{-1}_{\mathsf{T}_{\mathbf{R}'}}}_{e^{i\phi_{\mathsf{T}_{\mathbf{R}'}}(\mathbf{R}+\mathbf{R}',s)} f^\dagger_{\mathbf{R}+\mathbf{R}',s,\sigma}} \underbrace{G_{\mathsf{T}_{\mathbf{R}'}}\mathsf{T}_{\mathbf{R}'} f_{0,\bar{s},\sigma}\mathsf{T}^{-1}_{\mathbf{R}'}G^{-1}_{\mathsf{T}_{\mathbf{R}'}}}_{e^{-i\phi_{\mathsf{T}_{\mathbf{R}'}}(\mathbf{R}',\bar{s})} f_{\mathbf{R}',\bar{s},\sigma}} \underbrace{G_{\mathsf{T}_{\mathbf{R}'}}\mathsf{T}_{\mathbf{R}'}|\pi\mathrm{FS}\rangle}_{|\pi\mathrm{FS}\rangle}\\
&= \frac{e^{i\varphi}}{\sqrt{N_C}}\sum_{\mathbf{R}'} e^{i\mathbf{k}\cdot\mathbf{R}'} e^{i\phi_{\mathsf{T}_{\mathbf{R}'}}(\mathbf{R}+\mathbf{R}',s)} e^{-i\phi_{\mathsf{T}_{\mathbf{R}'}}(\mathbf{R}',\bar{s})} P_{\mathrm{G}} f^\dagger_{\mathbf{R}+\mathbf{R}',s,\sigma} f_{\mathbf{R}',\bar{s},\sigma}|\pi\mathrm{FS}\rangle,
\end{aligned}$$

where the additional phases $e^{i\phi_{\mathsf{T}_{\mathbf{R}'}}(\mathbf{R}+\mathbf{R}',s)}e^{-i\phi_{\mathsf{T}_{\mathbf{R}'}}(\mathbf{R}',\bar{s})}$ turn out to be plus minus signs (specified in Eq. (E.10) of Appendix E) for the π-flux ansätze Ref. [II.], and the global phase $e^{i\varphi}$ can be left off for convenience.

4.3.4 Transformation properties under the action of the SU(N) spin operators

The spectral weights $|\langle f|T^a_{\mathbf{k}}|\mathrm{GS}\rangle|^2$ appearing in Eq. (4.5) are non-zero only if the states $|f\rangle$ transform under the same irreducible representation as the $T^a_{\mathbf{k}}|\mathrm{GS}\rangle$.

The $T^a_{\mathbf{k}}|\mathrm{GS}\rangle$ is the eigenstate of the translation operator $\mathsf{T}_{\mathbf{R}}$ with eigenvalue $e^{-i\mathbf{k}\cdot\mathbf{R}}$, since

$$\begin{aligned}\mathsf{T}_{\mathbf{R}}T^a_{\mathbf{k}}|\mathrm{GS}\rangle &= \frac{1}{\sqrt{N_s}}\sum_{\mathbf{R}',s} e^{i\mathbf{k}\cdot(\mathbf{R}'+\boldsymbol{\delta}_s)}\mathsf{T}_{\mathbf{R}}T^a_{\mathbf{R}',s}\mathsf{T}^{-1}_{\mathbf{R}}\underbrace{\mathsf{T}_{\mathbf{R}}|\mathrm{GS}\rangle}_{|\mathrm{GS}\rangle} = \frac{1}{\sqrt{N_s}}\sum_{\mathbf{R}',s} e^{i\mathbf{k}\cdot(\mathbf{R}'+\boldsymbol{\delta}_s)}T^a_{\mathbf{R}+\mathbf{R}',s}|\mathrm{GS}\rangle \\ &= \frac{1}{\sqrt{N_s}}\sum_{\tilde{\mathbf{R}},s} e^{i\mathbf{k}\cdot(\tilde{\mathbf{R}}-\mathbf{R}+\boldsymbol{\delta}_s)}T^a_{\tilde{\mathbf{R}},s}|\mathrm{GS}\rangle = e^{-i\mathbf{k}\cdot\mathbf{R}}T^a_{\mathbf{k}}|\mathrm{GS}\rangle, \end{aligned} \tag{4.21}$$

where we supposed that the ground state is translationally invariant $\mathsf{T}_{\mathbf{R}}|\mathrm{GS}\rangle = |\mathrm{GS}\rangle$, as expected from a quantum spin liquid, and we changed the summation variable to $\tilde{\mathbf{R}} \equiv \mathbf{R}+\mathbf{R}'$.

The translation operators $\mathsf{T}_{\mathbf{R}}$ form a commutative group, which has only one-dimensional irreps labeled by $\mathbf{k}$, where the 1×1 matrices representing the translation operators are the eigenvalues $e^{-i\mathbf{k}\cdot\mathbf{R}}$. Therefore, the initial statement of this section can be rephrased as the eigenstates of $\mathsf{T}_{\mathbf{R}}$ with different eigenvalues (different $\mathbf{k}$) are orthogonal to each other.

Thus, in the spectral weight $|\langle f|T^a_{\mathbf{k}}|\mathrm{GS}\rangle|^2$, we project out the eigenstate of $\mathsf{T}_{\mathbf{R}}$ with eigenvalue $e^{-i\mathbf{k}\cdot\mathbf{R}}$ from $|f\rangle$. Therefore, it is reasonable to construct the states $|f\rangle$ as eigenstates of $\mathsf{T}_{\mathbf{R}}$, which is exactly what we achieve by solving the generalized eigenvalue problem $\tilde{\mathcal{H}}^{\mathbf{k}}|f^{\mathbf{k}}\rangle = E^{\mathbf{k}}_f\tilde{\mathcal{O}}^{\mathbf{k}}|f^{\mathbf{k}}\rangle$ (4.16) for the block matrices $\tilde{\mathcal{H}}^{\mathbf{k}}$ and $\tilde{\mathcal{O}}^{\mathbf{k}}$. In principle, we could solve the generalized eigenvalue problem $\tilde{\mathcal{H}}|f\rangle = E\tilde{\mathcal{O}}|f\rangle$ for the full Hamiltonian and overlap matrices even in the real space basis $|\mathbf{R},\mathbf{R}',\sigma\rangle$ of Eq. (4.11), since the eigenstate of $\mathsf{T}_{\mathbf{R}}$ is projected out anyway, but this would increase the Monte Carlo error.

Furthermore, as explained in Appendix A.6, the states $T^a_{\mathbf{k}}|\mathrm{GS}\rangle$ transform under the N^2-1 dimensional adjoint representation of SU(N), meaning that the action of the total spin operators on these states is equivalent to a matrix multiplication

$$T^a_{\mathrm{T}}T^b_{\mathbf{k}}|\mathrm{GS}\rangle = \sum_{c=1}^{N^2-1}\Gamma^a_{c,b}T^c_{\mathbf{k}}|\mathrm{GS}\rangle, \tag{4.22}$$

where the $(N^2-1)\times(N^2-1)$ matrices $\Gamma^a_{c,b} \equiv if_{abc}$ represent the total spin operators T^a_{T} in the adjoint representation (f_{abc} are the structure constants in Eq. (1.19)). Consequently, the spectral weight $|\langle f|T^a_{\mathbf{k}}|\mathrm{GS}\rangle|^2$ will be non-zero only if there is a part in $|f\rangle$ which transforms under the same irrep. Here we will argue that the Gutzwiller projected particle-hole excitations $f^\dagger_{\mathbf{R}+\mathbf{R}',s,\sigma}f_{\mathbf{R}',\bar{s},\bar{\sigma}}|\pi\mathrm{FS}\rangle$ transform under the adjoint representation, implying that the states $|f\rangle$ transform the same way, since they are linear combinations of the formers.

The $|\pi\mathrm{FS}\rangle$ transforms as an SU(N) singlet, the set of fermionic creation operators $\{f^\dagger_{\mathbf{R}+\mathbf{R}',s,\sigma}|\sigma\in\{1\dots N\}\}$ transforms under the fundamental representation (here we will denote it as $\mathbf{N}$), while the set of fermionic annihilation operators $\{f_{\mathbf{R}',\bar{s},\sigma}|\sigma\in\{1\dots N\}\}$ transform under the conjugate representation at site $\mathbf{r} = \mathbf{R}'+\boldsymbol{\delta}_{\boldsymbol{s}}$ (here we will denote it as $\bar{\mathbf{N}}$). Therefore, the set of states $\{f^\dagger_{\mathbf{R}+\mathbf{R}',s,\sigma}f_{\mathbf{R}',\bar{s},\bar{\sigma}}|\pi\mathrm{FS}\rangle|\sigma,\bar{\sigma}\in\{1\dots N\}\}$ transform under the reducible representation $\mathbf{N}\otimes\bar{\mathbf{N}}$ (note that here we allow for different σ and $\bar{\sigma}$, unlike in Eq. (4.20)). This reducible representation can be decomposed to irreducible representations as $\mathbf{N}\otimes\bar{\mathbf{N}} = \mathbf{1}\oplus(\mathbf{N^2-1})$, where $\mathbf{1}$

denotes the one-dimensional SU(N) singlet, and $\mathbf{N^2-1}$ the adjoint representation (for an argument using the Young tableau see Fig. A.1(c)). The meaning of this decomposition is, that we can form linear combinations from the states $\{f^\dagger_{\mathbf{R}+\mathbf{R}',s,\sigma}f_{\mathbf{R}',\bar{s},\bar{\sigma}}|\pi\mathrm{FS}\rangle|\sigma,\bar{\sigma}\in\{1\dots N\}\}$ which transform either under the SU(N) singlet or under the adjoint representations Ref. [I.]. The state transforming as a singlet is simply $\sum_{\sigma=1}^N f^\dagger_{\mathbf{R}+\mathbf{R}',s,\sigma}f_{\mathbf{R}',\bar{s},\sigma}|\pi\mathrm{FS}\rangle$, while as argued in Eq. (A.39) of Appendix A.6.3,

$$T^a_{\mathrm{T}}\sum_{\sigma,\sigma'=1}^{N}\lambda^b_{\sigma,\sigma'}f^\dagger_{\mathbf{R}+\mathbf{R}',s,\sigma}f_{\mathbf{R}',s',\sigma'}|\pi\mathrm{FS}\rangle=\sum_{c=1}^{N^2-1}\Gamma^a_{c,b}\sum_{\sigma,\sigma'=1}^{N}\lambda^c_{\sigma,\sigma'}f^\dagger_{\mathbf{R}+\mathbf{R}',s,\sigma}f_{\mathbf{R}',s',\sigma'}|\pi\mathrm{FS}\rangle, \tag{4.23}$$

so the states transforming under the adjoint irrep are $\{\sum_{\sigma,\bar{\sigma}=1}^N\lambda^a_{\sigma,\bar{\sigma}}f^\dagger_{\mathbf{R}+\mathbf{R}',s,\sigma}f_{\mathbf{R}',\bar{s},\bar{\sigma}}|\pi\mathrm{FS}\rangle|a\in\{1\dots N^2-1\}\}$, where $\lambda^a_{\sigma,\bar{\sigma}}$ are the $N\times N$ matrices representing the SU(N) spin operators in the fundamental representation. When calculating the structure factor $S^{aa}(\mathbf{k},\omega)$ for a given a, the spectral weights $|\langle f|T^a_{\mathbf{k}}|\mathrm{GS}\rangle|^2$ will be non-zero, only if the states $|f\rangle$ also transform under the adjoint irrep, which is ensured if they are formed from the linear combinations of $\sum_{\sigma,\bar{\sigma}=1}^N\lambda^a_{\sigma,\bar{\sigma}}f^\dagger_{\mathbf{R}+\mathbf{R}',s,\sigma}f_{\mathbf{R}',\bar{s},\bar{\sigma}}|\pi\mathrm{FS}\rangle$ for the same index a. However, these linear combinations are formed during the solution of the generalized eigenvalue problem, so we don't need to deal with them. For the diagonal generators satisfying $\lambda^a_{\sigma,\sigma'}=\delta_{\sigma,\sigma'}\lambda^a_{\sigma,\sigma}$ (where a can be any of the $N-1$ indices of diagonal generators) the states

$$\begin{aligned}|(\mathbf{N^2-1})_a,\mathbf{k},\mathbf{R},s,\bar{s}\rangle&\equiv\sum_{\sigma=1}^{N}\lambda^a_{\sigma,\sigma}|\mathbf{k},\mathbf{R},s,\bar{s},\sigma\rangle \\ &=\frac{1}{\sqrt{N_C}}\sum_{\mathbf{R}',\sigma}e^{i\mathbf{k}\cdot\mathbf{R}'}e^{i\phi_{\mathrm{T}_{\mathbf{R}'}}(\mathbf{R}+\mathbf{R}',s)}e^{-i\phi_{\mathrm{T}_{\mathbf{R}'}}(\mathbf{R}',\bar{s})}\lambda^a_{\sigma,\sigma}P_{\mathrm{G}}f^\dagger_{\mathbf{R}+\mathbf{R}',s,\sigma}f_{\mathbf{R}',\bar{s},\sigma}|\pi\mathrm{FS}\rangle\end{aligned} \tag{4.24}$$

transform under the adjoint irrep (since they are linear combinations of the states $\sum_{\sigma=1}^N\lambda^a_{\sigma,\sigma}f^\dagger_{\mathbf{R}+\mathbf{R}',s,\sigma}f_{\mathbf{R}',\bar{s},\bar{\sigma}}|\pi\mathrm{FS}\rangle$), while the state

$$|\mathbf{1},\mathbf{k},\mathbf{R},s,\bar{s}\rangle\equiv\sum_{\sigma=1}^{N}|\mathbf{k},\mathbf{R},s,\bar{s},\sigma\rangle \tag{4.25}$$

transforms as the SU(N) singlet irrep. For example, in the SU(3) case, the diagonal generators are

$$\lambda^3=\begin{pmatrix}1&0&0\\0&-1&0\\0&0&0\end{pmatrix},\qquad\lambda^8=\frac{1}{\sqrt{3}}\begin{pmatrix}1&0&0\\0&1&0\\0&0&-2\end{pmatrix} \tag{4.26}$$

(see Appendix A.3), so we have the states

$$|(\mathbf{N^2-1})_3,\mathbf{k},\mathbf{R},s,\bar{s}\rangle\equiv\sum_{\sigma=1}^{N}\left(|\mathbf{k},\mathbf{R},s,\bar{s},1\rangle-|\mathbf{k},\mathbf{R},s,\bar{s},2\rangle\right) \tag{4.27}$$

and

$$|(\mathbf{N^2-1})_8,\mathbf{k},\mathbf{R},s,\bar{s}\rangle\equiv\sum_{\sigma=1}^{N}\frac{1}{\sqrt{3}}\left(|\mathbf{k},\mathbf{R},s,\bar{s},1\rangle+|\mathbf{k},\mathbf{R},s,\bar{s},2\rangle-2|\mathbf{k},\mathbf{R},s,\bar{s},3\rangle\right). \tag{4.28}$$

Projecting the Hamiltonian onto the subspaces of these states as

$$\begin{aligned}\tilde{\mathcal{H}}^{\mathbf{k},(\mathbf{N^2-1})_a}&\equiv\langle(\mathbf{N^2-1})_a,\mathbf{k},\mathbf{R},s,\bar{s}|\mathcal{H}|(\mathbf{N^2-1})_a,\mathbf{k},\mathbf{R}',s',\bar{s}'\rangle,\\ \tilde{\mathcal{O}}^{\mathbf{k},(\mathbf{N^2-1})_a}&\equiv\langle(\mathbf{N^2-1})_a,\mathbf{k},\mathbf{R},s,\bar{s}|(\mathbf{N^2-1})_a,\mathbf{k},\mathbf{R}',s',\bar{s}'\rangle,\\ \tilde{\mathcal{H}}^{\mathbf{k},\mathbf{1}}&\equiv\langle\mathbf{1},\mathbf{k},\mathbf{R},s,\bar{s}|\mathcal{H}|\mathbf{1},\mathbf{k},\mathbf{R}',s',\bar{s}'\rangle,\\ \tilde{\mathcal{O}}^{\mathbf{k},\mathbf{1}}&\equiv\langle\mathbf{1},\mathbf{k},\mathbf{R},s,\bar{s}|\mathbf{1},\mathbf{k},\mathbf{R}',s',\bar{s}'\rangle,\end{aligned} \tag{4.29}$$

where

$$0 = \langle(\mathbf{N^2}-\mathbf{1})_a, \mathbf{k}, \mathbf{R}, s, \bar{s}|\mathcal{H}|\mathbf{1}, \mathbf{k}, \mathbf{R}', s', \bar{s}'\rangle \text{ and } 0 = \langle(\mathbf{N^2}-\mathbf{1})_a, \mathbf{k}, \mathbf{R}, s, \bar{s}|\mathbf{1}, \mathbf{k}, \mathbf{R}', s', \bar{s}'\rangle, \quad (4.30)$$

not only reduces the sizes of these matrices, but also allows us to separate the approximating eigenstates $|f^{\mathbf{k}}\rangle$ and their energies $E_f^{\mathbf{k}}$ into subspaces of these irreps, by solving the generalized eigenvalue problems separately as

$$\tilde{\mathcal{H}}^{\mathbf{k},(\mathbf{N^2}-\mathbf{1})_a}|f^{\mathbf{k}}_{(\mathbf{N^2}-\mathbf{1})_a}\rangle = E^{\mathbf{k}}_{f,(\mathbf{N^2}-\mathbf{1})_a}\tilde{\mathcal{O}}^{\mathbf{k},(\mathbf{N^2}-\mathbf{1})_a}|f^{\mathbf{k}}_{(\mathbf{N^2}-\mathbf{1})_a}\rangle \text{ and } \tilde{\mathcal{H}}^{\mathbf{k},\mathbf{1}}|f^{\mathbf{k}}_{\mathbf{1}}\rangle = E^{\mathbf{k}}_{f,\mathbf{1}}\tilde{\mathcal{O}}^{\mathbf{k},\mathbf{1}}|f^{\mathbf{k}}_{\mathbf{1}}\rangle. \quad (4.31)$$

Due to the SU(N) symmetry, the matrices $\tilde{\mathcal{H}}^{\mathbf{k},(\mathbf{N^2}-\mathbf{1})_a}$ and $\tilde{\mathcal{O}}^{\mathbf{k},(\mathbf{N^2}-\mathbf{1})_a}$ are equal (up to the Monte Carlo error) for every diagonal generator, so we can reduce the Monte Carlo errors by averaging these matrices, and solving the generalized eigenvalue problem for the averaged matrices

$$\tilde{\mathcal{H}}^{\mathbf{k},\langle\mathbf{N^2}-\mathbf{1}\rangle} = \frac{1}{N-1}\sum_a \tilde{\mathcal{H}}^{\mathbf{k},(\mathbf{N^2}-\mathbf{1})_a}$$
$$\tilde{\mathcal{O}}^{\mathbf{k},\langle\mathbf{N^2}-\mathbf{1}\rangle} = \frac{1}{N-1}\sum_a \tilde{\mathcal{O}}^{\mathbf{k},(\mathbf{N^2}-\mathbf{1})_a}. \quad (4.32)$$
$$(4.33)$$

For example, in the SU(3) case, $\tilde{\mathcal{H}}^{\mathbf{k},\langle\mathbf{N^2}-\mathbf{1}\rangle} = \frac{1}{2}\left(\tilde{\mathcal{H}}^{\mathbf{k},(\mathbf{N^2}-\mathbf{1})_3} + \tilde{\mathcal{H}}^{\mathbf{k},(\mathbf{N^2}-\mathbf{1})_8}\right)$ and $\tilde{\mathcal{O}}^{\mathbf{k},\langle\mathbf{N^2}-\mathbf{1}\rangle} = \frac{1}{2}\left(\tilde{\mathcal{O}}^{\mathbf{k},(\mathbf{N^2}-\mathbf{1})_3} + \tilde{\mathcal{O}}^{\mathbf{k},(\mathbf{N^2}-\mathbf{1})_8}\right)$.

4.3.5 Calculation of spectral weights $|\langle f|T^a_{\mathbf{k}}P_{\mathbf{G}}|\mathbf{GS}\rangle$ for diagonal SU(N) spin operators

Solving the generalized eigenvalue problem of Eq. (4.16) and Eq. (4.31) gives the approximating eigenstates

$$|f^{\mathbf{k}}\rangle = \sum_{\mathbf{R},s,\bar{s},\sigma} A^{f,\mathbf{k}}_{\mathbf{R},s,\bar{s},\sigma}|\mathbf{k}, \mathbf{R}, s, \bar{s}, \sigma\rangle, \quad (4.34)$$

and

$$|f^{\mathbf{k}}_{(\mathbf{N^2}-\mathbf{1})_3}\rangle = \sum_{\mathbf{R},s,\bar{s},\sigma} A^{f,\mathbf{k},(\mathbf{N^2}-\mathbf{1})_3}_{\mathbf{R},s,\bar{s},\sigma}|(\mathbf{N^2}-\mathbf{1})_3\mathbf{k}, \mathbf{R}, s, \bar{s}, \sigma\rangle, \quad (4.35)$$

respectively. Either of these can be used for the calculation of the weights, as will be outlined below. However, the construction of these states is not so simple, since the generalized eigenvalue problem requires the overlap matrix to have only positive (non-zero) eigenvalues, which is not true, because not all $|\mathbf{k}, \mathbf{R}, s, \bar{s}, \sigma\rangle$ are linearly independent, resulting in 0 eigenvalues of the overlap matrix. This issue can be resolved in a way explained in Appendix (K). In this subsection, we suppose that this issue was already resolved and have constructed the states $|f^{\mathbf{k}}\rangle$ or $|f^{\mathbf{k}}_{(\mathbf{N^2}-\mathbf{1})_3}\rangle$.

Following Ferrari *et al.* [91], and using Eq. (4.6), we can write:

$$\begin{aligned}
T^3_{\mathbf{k}}P_{\mathrm{G}}|\mathrm{FS}\rangle &= \frac{1}{\sqrt{N_s}}\sum_{\mathbf{R}',s} e^{i\mathbf{k}\cdot(\mathbf{R}'+\boldsymbol{\delta}_s)}T^3_{\mathbf{R}',s}P_{\mathrm{G}}|\mathrm{FS}\rangle \\
&= \frac{1}{\sqrt{N_s}}\sum_{\mathbf{R}',s} e^{i\mathbf{k}\cdot(\mathbf{R}'+\boldsymbol{\delta}_s)}P_{\mathrm{G}}\frac{1}{2}\left(f^\dagger_{\mathbf{R}',s,1}f_{\mathbf{R}',s,1} - f^\dagger_{\mathbf{R}',s,2}f_{\mathbf{R}',s,2}\right)|\mathrm{FS}\rangle \\
&= \frac{1}{2\sqrt{N_B}}\sum_s e^{i\mathbf{k}\cdot\boldsymbol{\delta}_s}\left(|\mathbf{k}, \mathbf{R}=\mathbf{0}, s, s, 1\rangle - |\mathbf{k}, \mathbf{R}=\mathbf{0}, s, s, 2\rangle\right), \\
&= \frac{1}{\sqrt{N_B}}\sum_s e^{i\mathbf{k}\cdot\boldsymbol{\delta}_s}|(\mathbf{N^2}-\mathbf{1})_3, \mathbf{k}, \mathbf{R}=\mathbf{0}, s, s\rangle \quad (4.36)
\end{aligned}$$

where in the second row we used that $[T^3_{\mathbf{R}',s}, P_{\mathrm{G}}] = 0$ on any site (see Eq. (2.15)), and we wrote $\mathbf{R} = \mathbf{0}$, since in the definition of the states $|\mathbf{k}, \mathbf{R}, s, \bar{s}, \sigma\rangle$ the $\mathbf{R}$ (4.20) is the the relative Bravais lattice vector separating the fermionic operators $f^\dagger_{\mathbf{R}+\mathbf{R}',s,\sigma} f_{\mathbf{R}',\bar{s},\sigma}$. Consequently, the overlap in the spectral weights for $S^{33}(\mathbf{k},\omega)$ can be expressed as

$$\begin{aligned}
\langle f^{\mathbf{k}}|T^3_{\mathbf{k}} P_{\mathrm{G}}|\mathrm{FS}\rangle &= \frac{1}{2\sqrt{N_B}} \sum_s e^{i\mathbf{k}\cdot\boldsymbol{\delta}_s} \Big(\langle f^{\mathbf{k}}|\mathbf{k}, \mathbf{R}=\mathbf{0}, s, \bar{s}=s, \sigma=1\rangle - |\mathbf{k}, \mathbf{R}=\mathbf{0}, s, \bar{s}=s, \sigma=2\rangle \Big) \\
&= \frac{1}{2\sqrt{N_B}} \sum_s e^{i\mathbf{k}\cdot\boldsymbol{\delta}_s} \sum_{\mathbf{R}',s',\bar{s}',\sigma'} (A^{f,\mathbf{k}}_{\mathbf{R}',s',\bar{s}',\sigma'})^* (\tilde{\mathcal{O}}^{\mathbf{k}}_{\mathbf{R}',s',\bar{s}'\sigma';\mathbf{0},s,s,1} - (\tilde{\mathcal{O}}^{\mathbf{k}}_{\mathbf{R}',s',\bar{s}'\sigma';\mathbf{0},s,s,2}) \\
&= \frac{1}{2\sqrt{N_B}} \sum_s e^{i\mathbf{k}\cdot\boldsymbol{\delta}_s} \sum_{\mathbf{R}',s',\bar{s}',\sigma'} (A^{f,\mathbf{k},(\mathbf{N^2-1})_3}_{\mathbf{R}',s',\bar{s}',\sigma'})^* \tilde{\mathcal{O}}^{\mathbf{k},(\mathbf{N^2-1})_3}_{\mathbf{R}',s',\bar{s}'\sigma';\mathbf{0},s,s,1},
\end{aligned} \tag{4.37}$$

where the states are ordered in some way, so the $\mathbf{R}', s', \bar{s}'\sigma'$ corresponds to an index i and the $\mathbf{0}, s, s, 1$ corresponds to another index j so that $\tilde{\mathcal{O}}^{\mathbf{k}}_{\mathbf{R}',s',\bar{s}'\sigma';\mathbf{0},s,s,1} = \tilde{\mathcal{O}}^{\mathbf{k}}_{i,j}$. To get the correct spectral weights for $S^{33}(\mathbf{k},\omega)$, we normalize it to satisfy the sum rule given in Eq. (6.2). The normalization is needed, because the approximating ground state $P_{\mathrm{G}}|\mathrm{FS}\rangle$ is not normalized ($|\mathrm{FS}\rangle$ is supposed to be normalized, and the action of the P_{G} decreases its norm). Analogous equations hold for the spectral weights of $S^{aa}(\mathbf{k},\omega)$ for any diagonal generator T^a.

To reduce Monte Carlo errors we can solve the generalized eigenvalue problem for the averaged Hamiltonian and overlap matrices of Eqs. (4.33), which yields more precise approximating eigenstates analogous to Eq. (4.35) and more precise spectral weights as in Eq. (4.37).

Summary

In section 4.2, we presented the formula for the calculation of the mean-field dynamical spin structure factor, dervied in Appendix I. In section 4.3, we introduced the dynamical variational Monte Carlo method developed in Ref. [90] for the SU(2) case, which makes use of Gutzwiller projected particle-hole excitations of the Fermi sea. In section 4.3.3, we have constructed the Gutzwiller projected particle-hole excitations for the π-flux ansätze, which contains additional gauge phases (presented in Appendix E) relative to the 0-flux case. In section 4.3.4, we gave a group theoretical argument on why this method can be used for the calculation of the dynamical spin structure factor for the SU(N) Heisenberg model with arbitrary N.

Chapter 5

The $S^{33}(k,\omega)$ of the SU(3) Heisenberg chain

The SU(3) Heisenberg chain is defined by the Hamiltonian

$$\mathcal{H} = J\sum_{i=1}^{N_s} \mathbf{T}_i \cdot \mathbf{T}_{i+1} = J\sum_{i=1}^{N_s}\sum_{a=1}^{8} T_i^a T_{i+1}^a = \frac{J}{2}\sum_{i=1}^{N_s}\left(\mathcal{P}_{i,i+1} - \frac{1}{3}\mathcal{I}\right), \tag{5.1}$$

where we set $J = 1$ below. The model is exactly solvable in the fundamental representation with Bethe ansatz and it can be simulated with Density Matrix Renormalization Group (DMRG) method and quantum Monte Carlo methods without sign problem. Its critical field theory is the $SU(3)_1$ Wess-Zumino-Witten model [94]. The ground state of the SU(3) Heisenberg chain in the fundamental representation is well approximated using the Gutzwiller projected Fermi sea of the uniform hopping Hamiltonian

$$\mathcal{H}^{\mathrm{MF}} = t\sum_{i=1}^{L}\sum_{\sigma=1}^{3}\left(f_{i,\sigma}^\dagger f_{i+1,\sigma} + f_{i+1,\sigma}^\dagger f_{i,\sigma}\right) = \sum_{k,\sigma}\underbrace{2t\cos(k)}_{\varepsilon(k)} f_{k,\sigma}^\dagger f_{k,\sigma}, \tag{5.2}$$

as was shown by comparing the variational energy per site with Bethe ansatz, and the static structure factor with quantum Monte Carlo simulation in [95].

Here besides ground state properties, we also calculate the dynamical structure factor $S^{33}(\mathbf{k},\omega)$ of Eq. (4.5) at $T = 0$, and compare it with exact diagonalization (ED), Bethe ansatz, DMRG, and conformal field theory (see Ref. [I.]).

First, we calculated the $S^{33}(k,\omega)$ for a chain of length $N_s = L = 18$ sites by exact evaluation of the Hamiltonian and overlap matrices $\tilde{\mathcal{H}}^{\mathbf{k}}_{\mathbf{R},\sigma;\mathbf{R}',\sigma'}$ and $\tilde{\mathcal{O}}^{\mathbf{k}}_{\mathbf{R},\sigma;\mathbf{R}',\sigma'}$ (exact variational method, see Appendix J). The result is shown in Fig. 5.1(a), together with the dynamical structure factor calculated by exact diagonalization (ED), with the help of the standard Lánczos algorithm [96].

The lowest energy excitations are located at wave vectors $k = 0$ and $k = \pm 2\pi/3$, which can be understood from the 1/3 filled one-particle spectrum $\varepsilon(k) \equiv 2t\cos(k)$ of the mean-field Hamiltonian (5.2) shown in Fig. 5.1(e), where a particle is hopped from the highest energy occupied state to the lowest energy unoccupied state. The relative wave vectors $k = 0$ and $k = \pm 2\pi/3$ of these particle-hole excitations determine the locations of the low-energy excitations in the mean-field case (see Fig. 5.1(c)). Eventually, in the variational calculation, we get the low-energy excitations at the same wave vectors. With an increasing cluster size the available one-particle states move closer to each other, so that the excitation energies of these particle-hole excitations get smaller. Consequently, in the thermodynamic limit, the mean-field spectrum will have gapless excitations at wave vectors $k = 0$ and $k = \pm 2\pi/3$. To see whether the Gutzwiller projected spectrum is also gapless, we show the finite-size scaling of the gap Δ in Fig. 5.2, where the convergence of $L\Delta(L)$ in the $L \to \infty$ limit, shows that the gap closes. For these calculations, we used the averaged Hamiltonian and overlap matrices of Eq. (4.33) to reduce the Monte Carlo errors.

We also compared the $S^{33}(k,\omega)$ with the $S^{88}(k,\omega)$, and as expected from the SU(3) spin rotation symmetry of the Heisenberg Hamiltonian, the two dynamical structure factors were in perfect correspondence (T^3 and T^8 are the two diagonal SU(3) spin operators, see Appendix A.3).

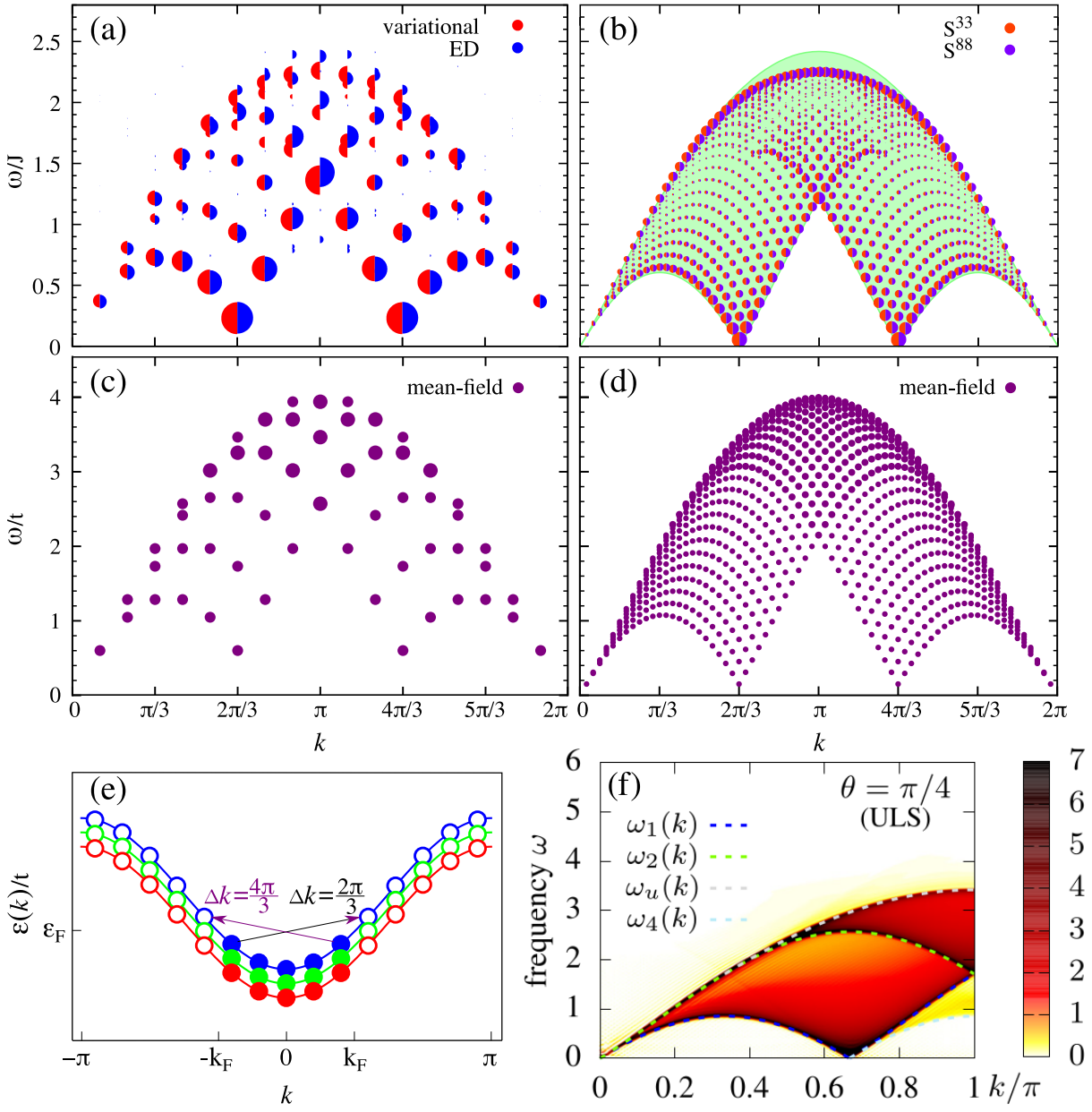

Figure 5.1: (a) Comparing $S^{33}(k,\omega)$ for a chain of length $L = 18$ calculated using the exact variational method (red) and by ED (blue). The area of the circles is proportional to the spectral weights $|\langle f|T^3_{\mathbf{k}}P_{\mathrm{G}}|\mathrm{FS}\rangle|^2$ (red) and $|\langle f|T^3_{\mathbf{k}}|\mathrm{GS}\rangle|^2$ (blue). (b) $S^{33}(k,\omega)$ and $S^{88}(k,\omega)$ for $L = 72$ calculated by VMC. The green background shows the two soliton continuum $(k,\omega) = (q_{\mathbf{3\bar{3}}}, \varepsilon_{\mathbf{3\bar{3}}})$ of the Bethe Ansatz solution, Eqs. (5.4) and (5.5), in the thermodynamic limit. In (c) and (d) we show the mean-field results for chains of lengths $L = 18$ and $L = 72$, respectively. (e) The one-particle energy spectrum $\varepsilon(k) = 2t\cos(k)$ of the uniform $\mathcal{H}^{\mathrm{MF}}$ in Eq. (5.2), showing how the particle-hole excitations lead to gapless excitations (in the thermodynamic limit) at relative wave vectors 0, $2\pi/3$ and $4\pi/3$ (equivalent to $-2\pi/3$). (f) DMRG results for $S^{33}(k,\omega)$ from Ref. [97], showing that the distribution of the spectral weights at low energies is similar to that in panel (b). The dashed lines show the boundaries of the two soliton continuum (5.5) of the Bethe-Ansatz. The difference in the ω spectra is due to different choice of exchange coupling $J_{\mathrm{DMRG}} = \sqrt{2}J$ in Ref. [97]. Reprinted figure with permission from [Moritz Binder and Thomas Barthel, Physical Review B, Vol. 102, 014447 (2020)] Copyright (2024) by the American Physical Society.

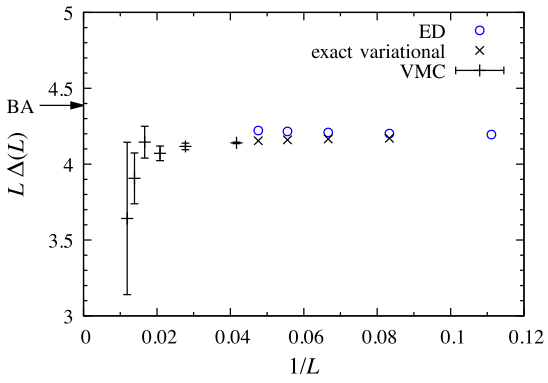

Figure 5.2: Finite-size scaling of the gap Δ at the $k = 2\pi/3$ multiplied by the chain length L, as a function of $1/L$. The blue circles show the ED gap, the exact variational results are shown with black crosses, and the VMC results with black lines with error bars. The convergence of $L\Delta$ to a finite value in the $L \to \infty$ implies that the gap closes, since if the gap remained finite, $L\Delta$ would diverge. The arrow points to $\pi\eta v_{\mathrm{BA}} = 4\pi^2/9$, the exact value in the thermodynamic limit using $\eta = 4/3$ and $v_{\mathrm{BA}} = \pi/3$, the velocity from the Bethe Ansatz, Eq. (5.7).

We can compare these results with mean-field calculations in Figs. 5.1(c) and (d), where Eq. (4.8) simplifies to

$$S^{33}_{\mathrm{MF}}(k,\omega) = \frac{1}{2L} \sum_{\substack{q \\ \varepsilon(q)<\varepsilon_{\mathrm{F}} \\ \varepsilon(k+q)>\varepsilon_{\mathrm{F}}}} \delta\left(\omega - \varepsilon(k+q) + \varepsilon(q)\right) \ , \tag{5.3}$$

since in the uniform hopping Hamiltonian the eigenstates are simply $f^\dagger_{k,\sigma}|0\rangle$ and there is only one band (so $v_{k,1,1} = 1$ in Eq. (4.8)). Eq. (5.3) shows that every excitation has equal spectral weights, and the excitation energies are simply the differences of one-particle energies $\omega = \varepsilon(k+q) - \varepsilon(q)$. Thus, we expect every circle in Figs. 5.1(c) and (d) to have equal area. However, certain excitations are degenerate, so their areas sum up. The effect of the Gutzwiller projector is to shift the spectral weights towards lower energies (giving a much better agreement with ED), and lowering the range of the excitation energies (the range of ω/J in Fig. 5.1(a) is lower than the range of ω/t in Fig. 5.1(c)).

Next, using the VMC method discussed in the previous section and in Appendices J and K, we calculated the $S^{33}(k,\omega)$ and $S^{88}(k,\omega)$ for a chain of length $L = 72$, shown in Fig. 5.1(b) (the difference between $S^{33}(k,\omega)$ and $S^{88}(k,\omega)$ is barely noticeable). The results can be qualitatively compared with mean-field theory (shown in Fig. 5.1(d)), DMRG calculations of Ref. [97] (shown in Fig. 5.1(f)), and with Bethe-Ansatz results (shown as the background in Fig. 5.1(b)).

The elementary excitations from the Bethe-Ansatz solution are two types of solitons, the $\mathbf{3}$ and the $\bar{\mathbf{3}}$, denoting the fundamental and the conjugate irreps of SU(3), respectively, with dispersions

$$\varepsilon_{\mathbf{3}}(k) = \frac{2\pi}{3\sqrt{3}}\left[\cos\frac{\pi}{3} - \cos\left(k + \frac{\pi}{3}\right)\right], \qquad 0 \le k \le \frac{4\pi}{3} \ , \tag{5.4a}$$

$$\varepsilon_{\bar{\mathbf{3}}}(k) = \frac{2\pi}{3\sqrt{3}}\left[\cos\left(\frac{\pi}{3} - k\right) - \cos\frac{\pi}{3}\right], \qquad 0 \le k \le \frac{2\pi}{3} \ , \tag{5.4b}$$

in the thermodynamic limit [98]. The two-soliton continuum shown in the background of Fig. 5.1(b) is spanned by

$$q_{\mathbf{3}\bar{\mathbf{3}}} = k_{\mathbf{3}} + k_{\bar{\mathbf{3}}} \ , \tag{5.5a}$$

$$\varepsilon_{\mathbf{3}\bar{\mathbf{3}}} = \varepsilon_{\mathbf{3}}(k_{\mathbf{3}}) + \varepsilon_{\bar{\mathbf{3}}}(k_{\bar{\mathbf{3}}}) \ , \tag{5.5b}$$

where $k_{\mathbf{3}} \in [0, 2\pi/3]$ and $k_{\bar{\mathbf{3}}} \in [0, 4\pi/3]$. The solitons with $\varepsilon_{\mathbf{3}}(k)$ correspond to particles, and those with $\varepsilon_{\bar{\mathbf{3}}}(k)$ are analogs of holes. As mentioned in Sec. 4.3.4, particle-hole excitations

(including those changing particle flavor like $f^\dagger_{\mathbf{k}+\mathbf{q},\sigma} f_{\mathbf{q},\sigma'}|\mathrm{FS}\rangle$) provide a basis for the reducible representation $3 \otimes \bar{3}$, just like the two soliton excitations discussed above.

The interactions between the flavorons $f^\dagger_{\mathbf{k}+\mathbf{q},b',\sigma'}|\pi\mathrm{FS}\rangle$ and the antiflavorons $f_{\mathbf{q},b,\sigma}|\pi\mathrm{FS}\rangle$ are hidden in the fluctuations beyond the mean-field solution (B). These interactions could make the mean-field ansatz unstable, and open a gap. However, from the Bethe-Ansatz solution we know, that the spectrum is indeed gapless, and the gapless excitation towers are at the same wave vectors as in the mean-field calculations. Therefore, we conclude that the interactions between the flavorons and antiflavorons are weak (they are almost the true quasiparticles of the SU(3) Heisenberg chain), and the simple hopping Hamiltonian (5.2) yields a stable quantum spin liquid $P_\mathrm{G}|\mathrm{FS}\rangle$.

Overall, the low-energy spectrum is in good agreement with ED, Bethe-Ansatz, and DMRG results as well, with the exception of the missing arc around $k = \pi$, which would correspond to two particle-hole excitations in the variational approach and four-soliton excitations in the Bethe-Ansatz (shown with $\omega_4(k)$ in Fig. 5.1(f)). However, the DMRG results in Fig. 5.1(f) show that the spectral weight of the four soliton excitations is much smaller than that of the two soliton excitations, and the distribution of the spectral weights is also similar to those in Fig. 5.1(b) at low energies.

We would like to remark that the correspondence would not be so good in the SU(4) Heisenberg chain, which has 4 gapless excitation towers, at $k \in \{0, \pi/4, \pi, 3\pi/4\}$ (see Ref. [99] Fig. 3.(b)). Three of these at ($k \in \{0, \pi/4, 3\pi/4\}$) can be reproduced with single particle-hole excitations of the 1/4 filled Fermi sea, similar to those shown in Fig. 5.1(e), but the tower at $k = \pi$ would require two particle-hole excitations. This can be understood as hopping a particle from one edge of the Fermi sea to the other produces a relative wave vector $\pi/2$, while hopping two particles gives an excitation of a relative wave vector $\pi/2 + \pi/2 = \pi$.

In contrast, the two particle-hole excitations of the SU(3) model do not create new gapless towers, because hopping two particles from the same edge results in an excitation of wave vector $2\pi/3 + 2\pi/3 = 4\pi/3$, which is equivalent to $-2\pi/3$.

5.1 The low-energy structure of a tower

The $\mathrm{SU}(3)_1$ Wess-Zumino-Witten conformal field theory determines the finite-size scaling of the spectral weight of the lowest energy peak in a tower as $S^{(0,0)} \propto L^{-1/3}$, and the ratios of the spectral weights of the lowest energy peaks as $S^{(1,0)}/S^{(0,0)} = S^{(0,1)}/S^{(0,0)} = S^{(1,1)}/S^{(1,0)} = S^{(1,1)}/S^{(0,1)} = 2/3$ and $S^{(2,0)}/S^{(0,0)} = S^{(0,2)}/S^{(0,0)} = 5/6$ in the thermodynamic limit (for the notation of the peaks see the inset of Fig. 5.3(a)). The variational approach fails to reproduce the scaling of the lowest peak, as we observe $S^{(0,0)} \propto L^{-1/4}$ (see Fig. 5.3(a)), but this does not contradict the stability of the quantum spin liquid $P_\mathrm{G}|\mathrm{FS}\rangle$ because even the weak interactions between the flavorons and antiflavorons may modify the exponents. Surprisingly, the ratios $S^{(1,0)}/S^{(0,0)}$, $S^{(0,1)}/S^{(0,0)}$, $S^{(2,0)}/S^{(0,0)}$, and $S^{(0,2)}/S^{(0,0)}$ approach the correct results (as shown in Fig. 5.3(b)), but the ratios $S^{(1,1)}/S^{(1,0)}$ and $S^{(1,1)}/S^{(0,1)}$ seem to be wrong.

Finally, we calculate the central charge c, which characterizes the universality class of the model. According to the conformal field theory [100, 101, 102] , the finite-size scaling of the ground state energy is given by

$$E(L) = L\varepsilon^\infty - \frac{\pi}{6L} vc \,, \tag{5.6}$$

where c is the central charge and v is the velocity of the excitations, and $\varepsilon^\infty \equiv \lim_{L\to\infty} E(L)/L$ is the ground state energy density. Bethe-Ansatz provides exact results (see Ref. [98]) for both the velocity

$$v_\mathrm{BA} = \frac{\pi}{3} \approx 1.0472 \tag{5.7}$$

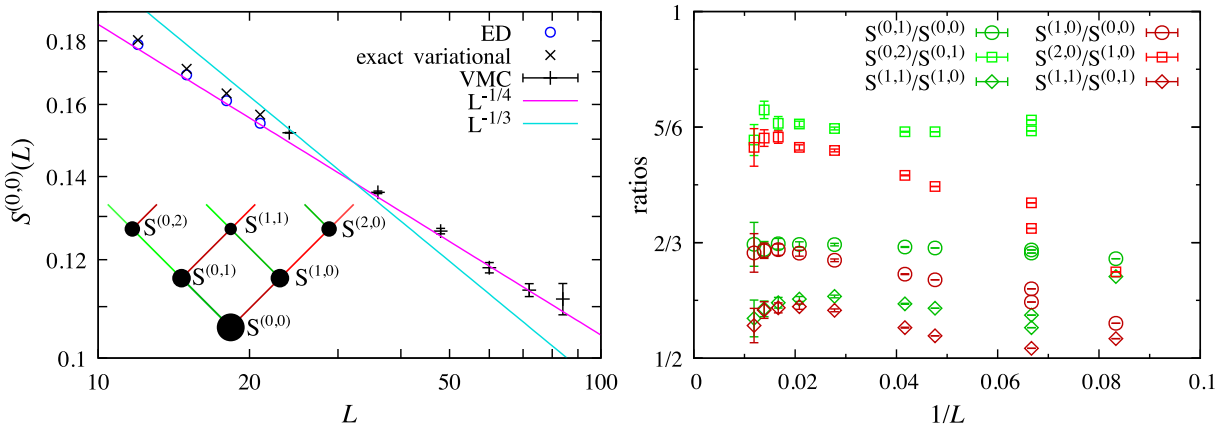

Figure 5.3: (a) The log-log plot of the finite-size scaling of the lowest peak $S^{(0,0)}$ (at wave vectors $\pm 2\pi/3$), shown in the inset. The variational means the numerically exact and the VMC the Monte Carlo evaluations of the $\tilde{\mathcal{H}}^{\mathbf{k}}$ and $\tilde{\mathcal{O}}^{\mathbf{k}}$ matrices in Eq. (4.16), (explained in App. J). Unlike the exact diagonal (ED) calculations, the variational results seem to follow an $L^{-1/4}$ scaling (the purple line is a guide to the eye), instead of the $L^{-1/3}$ behavior known from the $SU(3)_1$ Wess-Zumino-Witten conformal field theory [94] Ref. [I.]. Note the slight downward bending of the ED data suggesting that the exponent is indeed smaller than $-1/4$, tending toward $-1/3$. (b) The ratios of the spectral weights of the lowest energy peaks should approach the values $S^{(1,0)}/S^{(0,0)} = S^{(0,1)}/S^{(0,0)} = 2/3$ and $S^{(2,0)}/S^{(0,0)} = S^{(0,2)}/S^{(0,0)} = 5/6$ determined by the $SU(3)_1$ Wess-Zumino-Witten model [94], Ref. [I.]

and the ground state energy density

$$\varepsilon_{\mathrm{BA}}^{\infty} = \frac{1}{3} - \frac{\pi}{6\sqrt{3}} - \frac{\ln 3}{2} \approx -0.518273 \tag{5.8}$$

in the thermodynamic limit.

The velocity v can be calculated from the dynamical structure factor of the Gutzwiller projected particle-hole excitations as the slope $\Delta\omega/\Delta k$ of the continuum at $k = 0$ in the thermodynamic limit. In Fig. 5.4 we show the finite-size scaling of the slopes, and the fitting of the quadratic polynomial $v_{\mathrm{dyn}}(L) = v_{\mathrm{dyn}}^{\infty} + b_{\mathrm{dyn}}L^{-1} + c_{\mathrm{dyn}}L^{-2}$ yields $v_{\mathrm{dyn}}^{\infty} \approx 1.0901 \pm 8 \cdot 10^{-4}$, $b_{\mathrm{dyn}} \approx -0.13 \pm 0.02$, and $c_{\mathrm{dyn}} \approx -3.5 \pm 0.15$, where $v_{\mathrm{dyn}}^{\infty}$ differs from the exact value (5.7) only with 4%.

To calculate the central charge, we also need the finite-size scaling of the ground state energy. We plot the finite-size scaling of the variational energy $E = \langle \mathrm{FS}|P_{\mathrm{G}}\mathcal{H}P_{\mathrm{G}}|\mathrm{FS}\rangle / \langle \mathrm{FS}|P_{\mathrm{G}}P_{\mathrm{G}}|\mathrm{FS}\rangle$ in

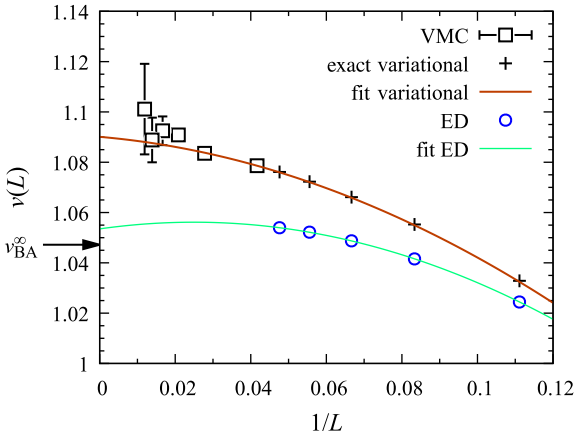

Figure 5.4: Finite-size scaling of the slopes $\Delta\omega/\Delta k$ of the dynamical structure factor at $k = 0$, where $\Delta k = 2\pi/L$. The + markers show the exact variational results, the squares the variation Monte Carlo results, and the circles the exact diagonalization results. We fitted a quadratic polynomial on both the variational, and the exact diagonalization results, to estimate the thermodynamic limit, which is known to be $\pi/3 \approx 1.0472$ from Bethe Ansatz calculations [98].

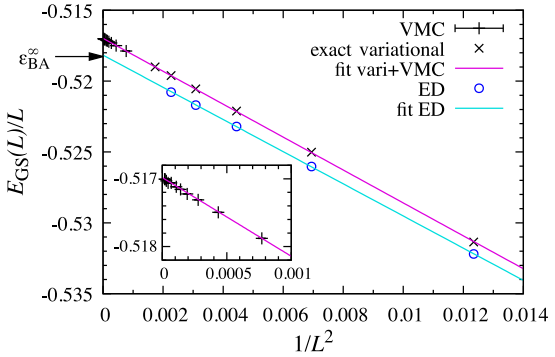

Figure 5.5: Finite-size scaling of the ground state energy density, calculated for the approximating variational ground state $P_G|FS\rangle$ (variational and VMC denotes the points calculated numerically exactly and with Monte Carlo, respectively), and compared with exact diagonalization results (ED). The arrow shows the exact energy density in the thermodynamic limit obtained from Bethe Ansatz, Eq. (5.8).

Fig. 5.5. To extract ε^{∞} and the product vc in Eq. (5.6) we fitted the function $b - a/L^2$ on E/L, shown in Fig. (5.5). From this fit we get the ground state energy density $\varepsilon^{\infty} = b \approx -0.516981 \pm 2 \cdot 10^{-6}$ (with a relative error of 0.3%), and $\frac{\pi}{6}vc = a \approx 1.1612 \pm 3 \cdot 10^{-4}$, so $vc \approx 2.2178 \pm 6 \cdot 10^{-4}$ with a relative error of 6%.

Using Eq. (5.6), the velocity $v^{\infty}_{\mathrm{dyn}} \approx 1.0901 \pm 8 \cdot 10^{-4}$, and the $\varepsilon^{\infty} = b \approx -0.516981 \pm 2 \cdot 10^{-6}$, we get $c \approx 2.034 \pm 0.002$, which is within a relative error of 2% to the exact value $c = 2$ from the $SU(3)_1$ Wess-Zumino-Witten model [94].

Summary

In this chapter, we computed the dynamical spin structure factor $S^{33}(k,\omega)$ of the SU(3) Heisenberg chain with this method. We showed that the low energy spectrum and the distribution of the spectral weights of the SU(3) Heisenberg chain can be well reproduced by this method, comparing the $S(k,\omega)$ to exact diagonalization results for 18 sites, to the two-soliton continuum of the Bethe Ansatz, and DMRG results for 72 sites. Detailed analysis of the finite-size effects showed that the method captures the critical Wess-Zumino-Witten $SU(3)_1$ behavior, and reproduces the correct exponent, except for the size dependence of the weight of the bottom of the conformal tower. We also calculated the velocity of excitations, and the central charge, which turn out to be very close to the exact results.

We conclude, that the $P_G|\rangle$ is a stable quantum spin liquid in the sense that the fluctuations beyond the mean-field approximation are not strong enough to open a gap, as can be seen from the Bethe-Ansatz solution. However, these fluctuations can modify the exponents, as seems to be the case in the finite-size scaling of the lowest spectral weight $S^{(0,0)} \propto L^{-1/4}$ in the gapless towers at $q = \pm 2\pi/3$.

These results were published in Ref. [I.], in which we also calculated the dynamical spin structure factor of the SU(3) Haldane-Shastry model, which is special, because the Gutzwiller projected Fermi sea is its exact ground state. Furthermore, we also calculated the single mode approximation for both the SU(3) Heisenberg model and the SU(3) Haldane-Shastry model, which gave a slightly worse approximation of the velocity of excitations than the slope of the dynamical structure factor at $k = 0$. For brevity, we have not included these additional results here.

Chapter 6

The $S^{33}(\mathbf{k},\omega)$ of the SU(4) and SU(6) Dirac spin liquids

In the case of the one-dimensional SU(3) Heisenberg chain, we saw that the spectrum of Gutzwiller projected particle-hole excitations is a gapless continuum, where the location of the gapless towers can be understood from mean-field theory. Thus, it is reasonable to expect that the spectrum of the Gutzwiller projected particle-hole excitations will be similar to the mean-field spectrum even in the two-dimensional case. In sections 2.3.1 and 2.3.2 we saw that the one-particle spectra of the two-dimensional Dirac spin liquids are gapless, so we expect gapless towers in the mean-field dynamical spin structure factors, similarly to the one-dimensional case.

The features of the $S^{33}(\mathbf{k},\omega)$ of the SU(4) and SU(6) Dirac spin liquids on the honeycomb and kagome lattices are very similar, therefore we will discuss them together. The complication relative to the one-dimensional case is that $S^{33}(\mathbf{k},\omega)$ is periodic in the extended Brillouin zone, while the mean-field band structure is periodic in the reduced Brillouin zone, as shown in Fig. 6.1(c) (for an explanation see App. H). In the mean-field case, we expect gapless excitations in the thermodynamic limit at all relative wave vectors connecting Dirac-Fermi points, since these correspond to particle-hole excitations $f^{\dagger}_{\mathbf{k}+\mathbf{q},b'}f_{\mathbf{q},b}|\pi\mathrm{FS}\rangle$ from the top of the Fermi sea ($b \in \{1,2\}$) to the lowest unoccupied states at the bottom of the Dirac cone in the second band ($b' \in \{3,4\}$), highlighted by the arrow labeled ω_{M}, see Figs. 6.1(d), 6.2(d), and 2.1(d). These relative wave vectors are all the Γ, Γ', M and M$'$ points in the extended Brillouin zone.

However, in a finite-size cluster, the antiperiodic boundary condition shifts the available wave vectors of one-particle states so that no particle can reside at the Dirac-Fermi point. Therefore, in a finite-size cluster, the lowest energy excitations are not gapless. In the mean-field case, the finite-size gap corresponds to the energy difference of the one-particle states closest to the Dirac-Fermi point, see Fig. 6.1(d). As the available wave vectors move closer to the Dirac-Fermi point with increasing system size, the finite-size gap disappears in the thermodynamic limit as $\Delta \propto N_s^{-1/2}$.

We show the $S^{33}(\mathbf{k},\omega)$ for the SU(4) and SU(6) Heisenberg models in Figs. 6.2(a) and 6.3(a), respectively. The mean-field $S^{33}_{\mathrm{MF}}(\mathbf{k},\omega)$ for the SU(4) and SU(6) models are shown in Figs. 6.2(b) and 6.3(b), respectively. In all cases, we can recognize towers at low energies centered at the Γ, Γ', M, and M$'$ points in the extended Brillouin zones, at the same wave vectors where we expect gapless excitations in the thermodynamic limit of the mean-field case. The shape of the energy spectrum is similar in the mean-field and variational calculations, so it is reasonable to expect that the variational results would become a gapless continuum in the thermodynamic limit, just as in the mean-field case. However, the excitations have lower energies in the variational calculations than in the mean-field results. We show the gapless mean-field spectra in the thermodynamic limit of the SU(4) and SU(6) models in the backgrounds of Figs. 6.2(b) and 6.3(c), respectively. The experimental observation of the gapless excitation towers at the Γ, Γ', M, and M$'$ points would indicate the stability of the Dirac spin liquid, the existence of fractionalized fermionic quasiparticles and the existence of the mean-field quantum order.

Comparing the $S^{33}_{\mathrm{MF}}(\mathbf{k},\omega)$ and $S^{33}(\mathbf{k},\omega)$ in Figs. 6.5, 6.2, and 6.3, we can see that the Gutzwiller projector shifts the spectral weights $|\langle f|T^3_{\mathbf{k}}P_{\mathrm{G}}|\mathrm{FS}\rangle|^2$ towards the lower edges of the continuum, relative to the mean-field spectral weights $|\langle f|T^3_{\mathbf{k}}|\mathrm{FS}\rangle|^2$. However, this difference decreases with increasing N, as the distributions of the spectral weights in the SU(6) case are almost identical for a 48 site cluster shown in Figs. 6.3(a) and (b). These results suggest that the distribution of the spectral weights becomes identical in the large-N limit of SU(N) models in the

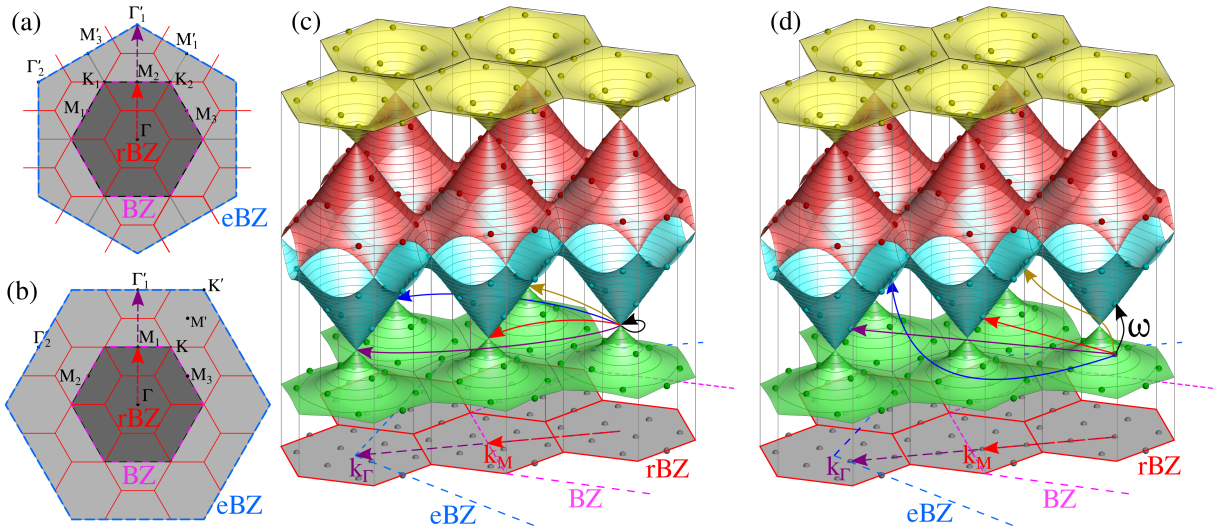

Figure 6.1: (c) The mean-field band structure of the π-flux $\mathcal{H}^{\mathrm{MF}}$ on the honeycomb lattice (2.1) shown in the extended Brillouin zone (eBZ) (dashed blue hexagons). The band structure is periodic in the reduced Brillouin zone (rBZ, shown with red hexagons), which fits multiple times into the eBZ. There are Dirac Fermi points at the center of every rBZ. The solid arrows in panel (c) show the gapless particle-hole excitations in the thermodynamic limit, a particle hops between Dirac-Fermi points (from the tip of the lowest Dirac cone to the tip of the Dirac cone above it). In panels (a) and (b), we show all Brillouin zones of the honeycomb and kagome lattices, respectively (see App. H). In the thermodynamic limit of the mean-field calculations, we expect gapless excitations in $S^{33}_{\mathrm{MF}}(\mathbf{k},\omega)$ at all relative wave vectors that connect Dirac-Fermi points (the centers of the red hexagons). These are all the Γ, Γ', M, and M$'$ points of the eBZ. Due to the anitperiodic boundary condition, in a finite size cluster, the available wave vectors for one-particle states are shifted, so that no one-particle state is available at the Dirac-Fermi point. The available wave vectors are shown with circles on the band structure in panels (c) and (d), for a 72-site cluster on the honeycomb lattice. In panel (d), we show the lowest energy particle-hole excitations in this 72-site cluster, where the particle is hopped from the highest energy occupied state to the lowest energy unoccupied state. At the mean-field level, the excitation energy ω is simply the difference of the one-particle energies.

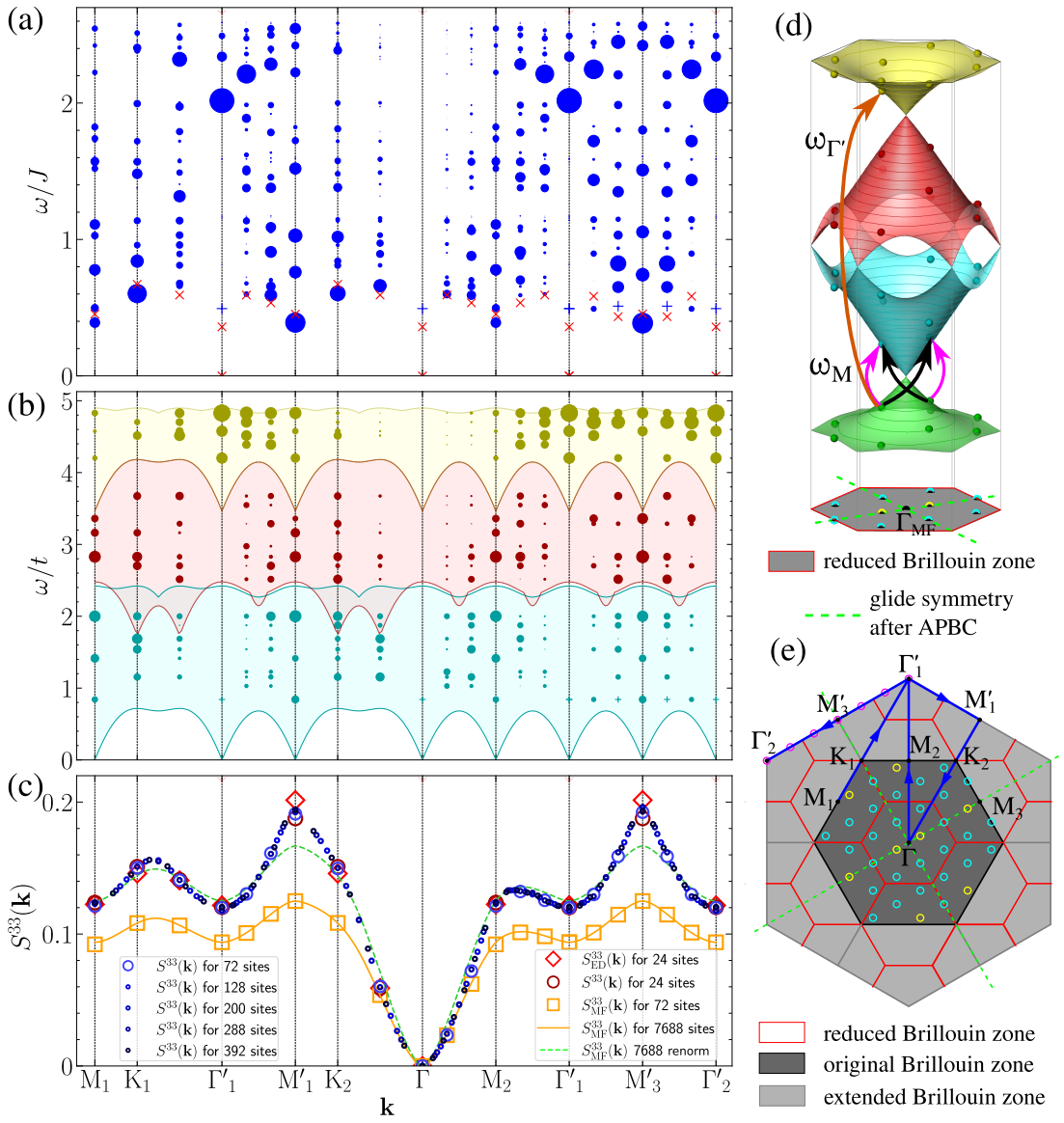

Figure 6.2: The $S^{33}(\mathbf{k},\omega)$ calculated by VMC is shown in (a) and the mean-field $S^{33}_{\mathrm{MF}}(\mathbf{k},\omega)$ of Eq. (4.8) in (b), for $N_s = 72$, along the blue path in the extended Brillouin zone shown in (e). The area of the circles in (a) and (b) is proportional to the spectral weights. The colors of the circles and the background in (b) correspond to the colors of the bands of the one-particle spectrum of Eq. (2.26) shown in (d), where the circles on the bands show the available one-particle states for the 72-site cluster in the reduced Brillouin zone. In the Fermi sea, the lowest band is completely filled and the higher energy bands are empty. Both the cyan and the yellow circles in (d) and (e) show the wave vectors of the available one-particle states (shifted by the APBC), but only the yellows are the closest to the Dirac-Fermi points located in the centers of every red hexagon (the reduced Brillouin zones) in panel (e). The blue plusses and the red crosses in (a) and (b) denote the lowest energy excitations with zero spectral weights transforming as the adjoint $|f^{\mathbf{k}}_{(\mathbf{15})_3}\rangle$ and as the singlet $|f^{\mathbf{k}}_{\mathbf{1}}\rangle$ representations (see Eq. (4.31)), respectively. The relative wave vectors on the $\Gamma'_1 - \mathrm{M}'_3 - \Gamma'_2$ path are shown with magenta circles in (e), which are not shifted by the APBC. The mean-field peaks in (b) are degenerate on this path, because all these relative wave vectors correspond to moving a particle between the wave vectors closest to Dirac points (marked with yellow circles). (c) Comparison of the static structure factor $S^{33}(\mathbf{k}) = \int S^{33}(\mathbf{k},\omega)d\omega$ for the projected (blue), mean-field (orange), renormalized mean-field (dashed green), and ED (red diamonds, from Ref. [6]) calculations. The Monte Carlo errors in (a) and (c) are smaller than the symbol sizes.

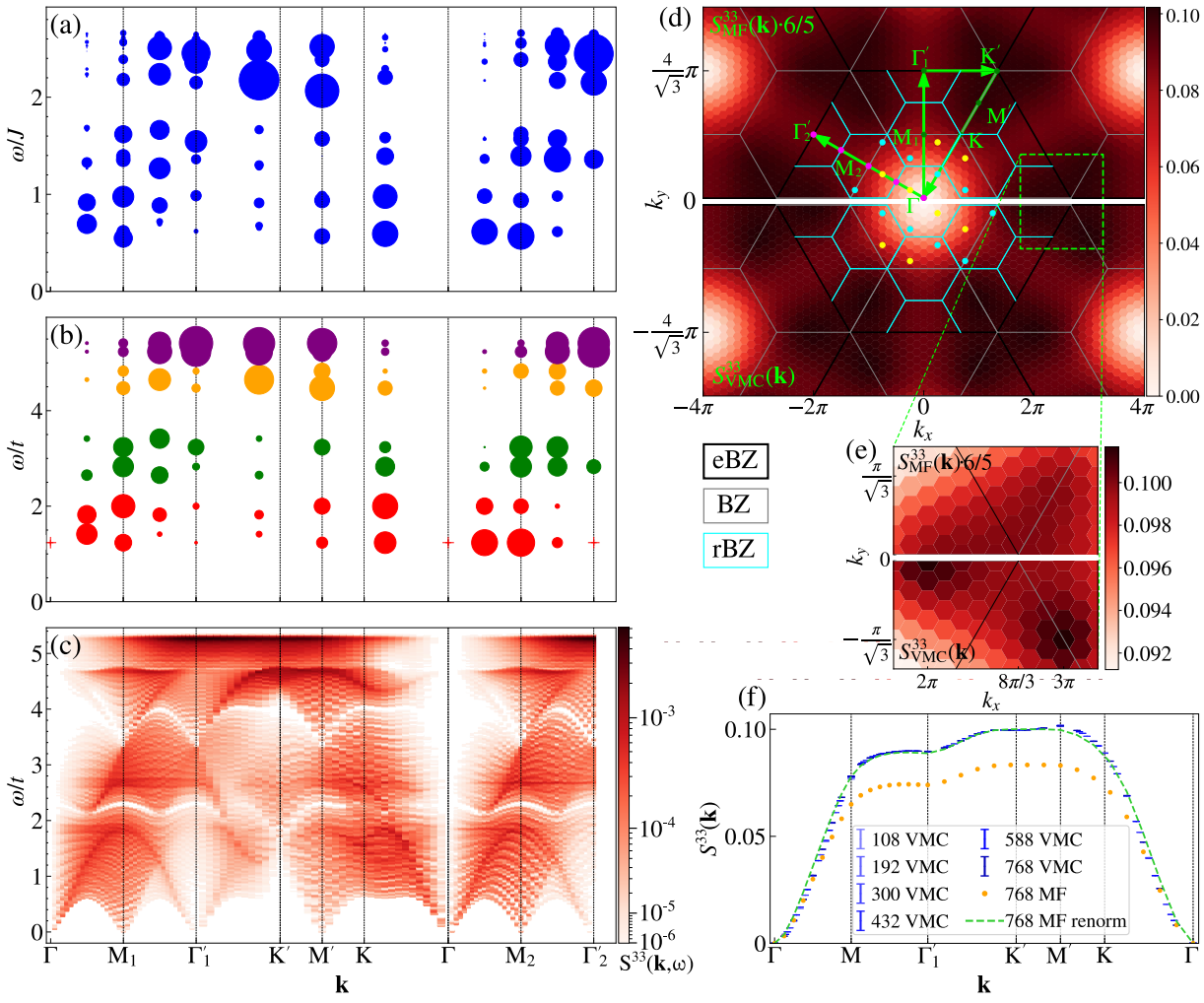

Figure 6.3: (a) the $S^{33}(\mathbf{k},\omega)$ calculated by VMC for $N_s = 48$, (b) the $S^{33}_{\mathrm{MF}}(\mathbf{k},\omega)$ mean-field calculations of Eq. (4.8) for $N_s = 48$ and (c) the $S^{33}_{\mathrm{MF}}(\mathbf{k},\omega)$ for $N_s = 3888$, all along the light green path in the extended Brillouin zone shown in (d). The area of the circles in (a) and (b) is proportional to the spectral weights. Both the cyan and the yellow circles in (d) show the wave vectors of the available one-particle states (shifted by the APBC), but only the yellows are the closest to the Dirac-Fermi points located in the centers of every cyan hexagon (the reduced Brillouin zones). The relative wave vectors on the $\Gamma - \mathrm{M}_2 - \Gamma'_2$ path are shown with magenta circles in (d), which are not shifted by the APBC. The mean-field peaks in (b) are degenerate on this path, because all these relative wave vectors correspond to moving a particle between the wave vectors closest to Dirac points (marked with yellow circles). These excitations remain degenerate even in larger systems as in (c), but only those at the M, and M′ points remain of finite spectral weights. We expect gapless towers in real experiments at every M, M′, Γ and Γ′ point of the extended Brillouin zone since all these correspond to Γ_{MF} points (the centers of the cyan hexagons), where the one-particle spectrum is gapless (see Figs. 6.2(d) and 2.1(d)). In (d), (e), and (f) we compare the static structure factor $S^{33}(\mathbf{k}) = \int S^{33}(\mathbf{k},\omega)d\omega$ for the projected (upper halves in (d) and (e)) and renormalized mean-field (lower halves) cases, both having the same sum rules. Both show triangular-shaped plateaus around the K′ points, with the difference that in the projected case, there are humps at the corners of these triangles at the M′ points, as can be seen in the zoomed figure in (e). In (f), we show the mean-field results without renormalization (orange), showing the decreased correlations due to charge fluctuations (see Appendix C.1). The Monte Carlo errors in (a), (d), and (f) are smaller than the symbol sizes.

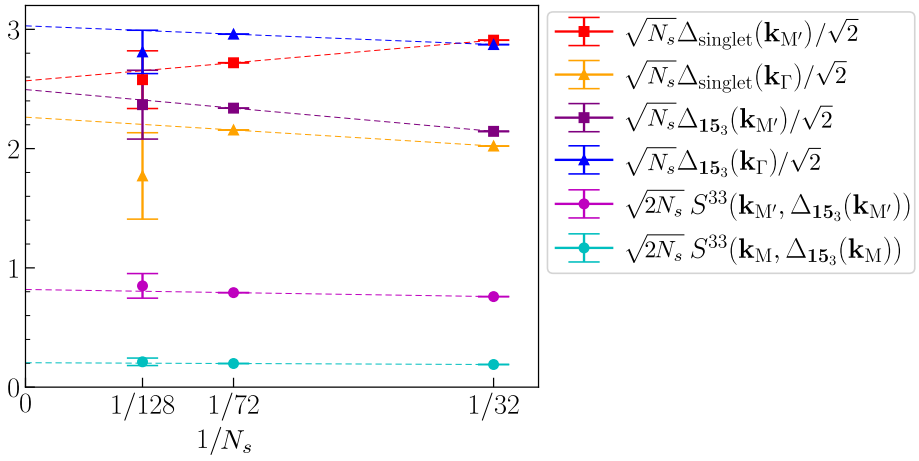

Figure 6.4: In the variational calculation, the $\sqrt{N_s}\Delta(\mathbf{k})$ at the M′ and Γ points tend to a finite value in the $N_s \to \infty$ limit, indicating that the gap probably vanishes as $\Delta(\mathbf{k}) \propto N_s^{-1/2}$, just like in the mean-field case. If the gap remained finite, $\sqrt{N_s}\Delta(\mathbf{k})$ would diverge. Due to the large Monte Carlo errors, we can not exclude this possibility with certainty, but the data make such a scenario unlikely. Similarly, the weights at the bottom of the towers at the M′ and M points probably scale as $S^{33}(\mathbf{k},\Delta(\mathbf{k})) \propto N_s^{-1/2}$, unlike in the mean-field case, where they scale as $S^{33}_{\text{MF}}(\mathbf{k},\Delta(\mathbf{k})) \propto N_s^{-1}$. However, the error bars in both cases are too big to draw definitive conclusions. The straight lines go through the 32- and 72-site results and serve as a guide to the eye.

fundamental representation. Maybe even the interactions between the flavorons $f^\dagger_{\mathbf{k}+\mathbf{q},b',\sigma'}|\pi\text{FS}\rangle$ and the antiflavorons $f_{\mathbf{q},b,\sigma}|\pi\text{FS}\rangle$ vanish in the large-N limit, just like in the large-N limit of Sp($2N$) Heisenberg models [2, Sec. 9.8]).

We were not able to calculate the $S^{33}(\mathbf{k},\omega)$ for a cluster larger than 48 sites in the SU(6) case, because the Monte Carlo errors increase with an increasing SU(N) symmetry. A 48-site cluster is too small to conclude about the thermodynamic limit, so we calculated the $S^{33}_{\text{MF}}(\mathbf{k},\omega)$ in the SU(6) case for a 3888-site cluster on the kagome lattice (shown in Fig. 6.3(c)). Such calculation is less useful in the SU(4) case, since the distribution of the spectral weights is less similar, and Fig. 6.2(a) already gives a feeling about the distribution of the spectral weights in the thermodynamic limit.

The similarity of the mean-field and variational spectra in finite systems does not prove that the projected spectrum becomes gapless in the thermodynamic limit. To be sure, we should analyze the finite-size scaling of the gap shown in Fig. 6.4. The results suggest a $\Delta(\mathbf{k}) \propto N_s^{-1/2} + \mathcal{O}(N_s^{-3/2})$ like scaling, which indicates a gapless spectrum at the M′ and Γ points, just like in the mean-field case. However, the error bars are too large to draw definitive conclusions. The projected spectrum may be gapped only if the Gutzwiller projector can open a gap. Since the differences between the projected and mean-field calculations become smaller with increasing N, if the Gutzwiller projector cannot open a gap in the SU(2) case, we do not expect a gap in the SU(4) and SU(6) cases either. While we are not aware of a finite-size scaling analysis of the gap in the SU(2) case, the gapless feature of the projected spectrum is quite convincing in References [91, 103, 92, 104, 105].

The antiperiodic boundary condition breaks the D_6 projective symmetry of the mean-field Hamiltonian, therefore $S^{33}(\mathbf{k},\omega)$ and $S^{33}_{\text{MF}}(\mathbf{k},\omega)$ are only D_2 symmetric, as argued in Appendix. E.2. This can be seen from the differences of the spectral weights at the M'_1 and M'_2 points at higher energies in Figs. 6.2(a) and (b). However, since this D_6 projective symmetry breaking is due to the boundary condition, the D_6 symmetry of $S^{33}(\mathbf{k},\omega)$ and $S^{33}_{\text{MF}}(\mathbf{k},\omega)$ is restored in the

thermodynamic limit.

In the mean-field band structure, the APBC shifts the available wave vectors of one-particle states (shown with circles in Fig. 6.2(d)), so that no one-particle state is available at the Dirac-Fermi point. The Dirac-Fermi points are located at the centers of the reduced Brillouin zones, which we call the Γ_{MF} point. Consequently, the arrangement of the wave vectors around the Γ_{MF} point is D_2 symmetric, there are remaining reflection symmetries around the dashed green lines in Fig. 6.2(d) and (e) and the line connecting the Γ and Γ_2' points in Fig. 6.3(d). The two highest-energy occupied one-particle states in the vicinity of the Dirac-Fermi point in the lowest band are located at the two wave vectors closest to the Γ_{MF} point (the yellow circles in Figs. 6.2(e) and 6.3(d)). Similarly, the two lowest energy unoccupied states in the vicinity of the Dirac-Fermi point in the next band are also located at these wave vectors. A fermion can hop from these two occupied one-particle states to the two unoccupied one-particle states in four possible ways, shown with black and magenta arrows in Fig. 6.2(d). All four possible ways of hopping correspond to different particle-hole excitations with the same excitation energy ω_{M}. Two such particle-hole excitations have relative wave vectors Γ_{MF}, the particle jumps upwards in Fig. 6.2(d), shown with magenta arrows. The other two particle-hole excitations have relative wave vectors surrounding the Γ_{MF} point, shown with the black arrows in Fig. 6.2(d). Thus, two out of these four particle-hole excitations have relative wave vector Γ_{MF}, while the other two have relative wave vectors surrounding the Γ_{MF} point. Therefore, in the mean-field $S^{33}_{\mathrm{MF}}(\mathbf{k},\omega)$, we will have three degenerate excitations around every Γ_{MF} point with excitation energy ω_{M}. As we show in Figs. 6.1, the center of every reduced Brillouin zone is a Γ_{MF} point since there is a Dirac-Fermi point. Therefore, all of the M, M$'$, Γ or Γ' points of the extended Brillouin zone are also Γ_{MF} points in the reduced Brillouin zone. Consequently, there are three degenerate points around every M, M$'$, Γ or Γ' point in the extended Brillouin zone, which are visible only if we go through them in the correct direction (specified by the APBC). In the case of the honeycomb lattice, we can see these excitations along the Γ_1' – M_3' – Γ_2' path in Fig. 6.2(b), but we see 7 degenerate excitations instead of 3, because each of the Γ_1', M_3', and Γ_2' points is surrounded with two degenerate excitations (shown with the magenta circles in Fig. 6.2(e)), giving a total of 9 excitations, but only 7 are visible in this path. In the case of the kagome lattice, we see these degenerate excitations in the Γ – M_2 – Γ_2' path, here we also have 5 instead of 3 for the same reason. These excitations are also present in the variational calculation on both lattices (Figs. 6.2(a) and 6.3(a)), but in these cases, the degeneracy is lifted, the excitations in the Γ_{MF} points have lower energies than the excitations surrounding them.

At the Γ' points, we get high-energy excitations in both the SU(4) and SU(6) cases, originating from particle-hole excitations $c^\dagger_{\mathbf{k}_{\Gamma'}+\mathbf{q},b'}c_{\mathbf{q},b}|\pi\mathrm{FS}\rangle$ with a fermion being hopped from the top of the Fermi sea ($b \in \{1,2\}$) to the bottom of the higher energy Dirac cone ($b' \in \{7,8\}$), indicated by the $\omega_{\Gamma'}$ arrow in Fig. 6.2(d). The available one-particle states move towards the Dirac-Fermi point with increasing system size, so that $\omega_{\Gamma'} \to 2\sqrt{3}t$ (from the dispersions (2.26) and (2.31)) in the thermodynamic limit.

Finally, let us turn to the question of whether we get all the gapless towers from single particle-hole excitations. Let us recall that in the one-dimensional case, we got all the towers for the SU(3) Heisenberg model (at $q = 0$ and $\pm 2\pi/3$), while for the SU(4), the single particle-hole states give only the $q = 0$ and the $\pm\pi/2$ and the tower at the $q = \pi$ originates from two particle-hole excitations. In the two-dimensional case, the relative wave vectors connecting the Dirac-Fermi points (the Γ, Γ', M, and M$'$ points) generate a triangular lattice in the reciprocal space, as can be seen from Figs. 6.2(e) and 6.3(d)). Thus, all the wave vectors of the two particle-hole excitations are also accessible by single particle-hole excitations.

The stability of the gapless quantum spin liquid, the existence of fractionalized fermionic quasiparticles, and the mean-field quantum order can be verified through the existence and location of gapless excitation towers in the experimentally measured dynamical spin structure

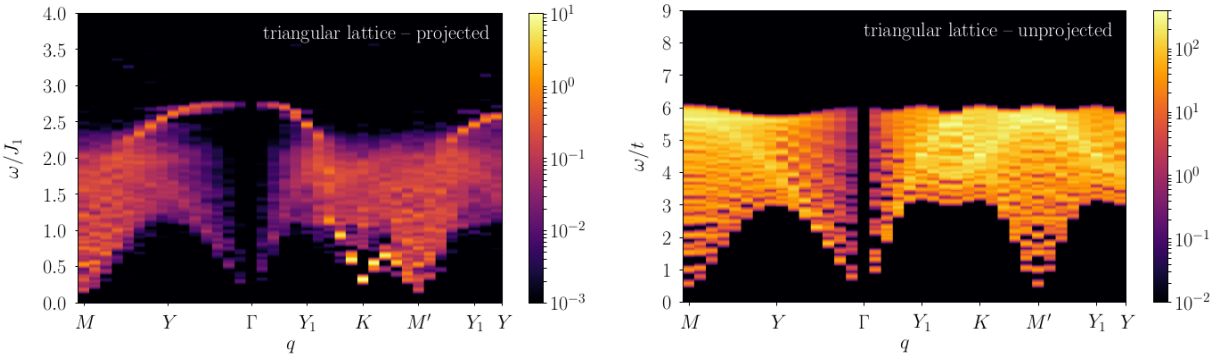

Figure 6.5: The dynamical spin structure factor $S^{33}(\mathbf{k},\omega)$ of the SU(2) symmetric $J_1 - J_2$ Heisenberg model (2.45) on the triangular lattice in the quantum spin liquid regime. These figures were taken from Ref. [92] (Figs. 8. and 9.). The Figures labeled as "projected" are the same as the variational calculations (explained in Sec. 4.3) we used in Figs. 6.2(a) and 6.3(a), and those labeled as "unprojected" correspond to the mean-field calculations (explained in Sec. 4.2) used in Figs. 6.2(b) and 6.3(b) and 6.3(c). We included these figures, to show that the Gutzwiller projector can create new gapless excitations (the low energy excitation at the K point of the "triangular lattice-projected" panel), which are not present in the mean-field calculations. Furthermore, the distribution of the spectral weights differs more than in the SU(4) and SU(6) cases (shown in Figs. 6.2 and 6.3).

factor. However, we saw that the Gutzwiller projected variational spectrum seems to be gapless at the same wave vectors as the mean-field calculations. If this was always the case, there would be no need for the variational calculations for the experimental identification of a gapless quantum spin liquid. However, this is not always the case, as was shown for the staggered-flux SU(2) Dirac spin liquid on the triangular lattice, where the Gutzwiller projector creates a gapless excitation, which is not present in the mean-field case [92] (we show their Figure in Fig. 6.5 for comparison). What we have to compare with experiments to conclude about the stability of a gapless quantum spin liquid is the Gutzwiller projected spectrum. We believe that the similarity of the Gutzwiller projected and mean-field spectra in our cases is due to the increased SU(N) symmetries.

However, even in the SU(2) case, the Gutzwiller projected spectrum can be very similar to the mean-field result, as was shown in Ref. [93] (and also included in [92]) on the square lattice, though the distribution of the spectral weights is very different (we also show this Figure in Fig. 6.5).

We also compared the finite-size scaling of the lowest energy spectral weights of $S^{33}_{\mathrm{MF}}(\mathbf{k},\omega)$ and $S^{33}(\mathbf{k},\omega)$ in the SU(4) case, which seems to be different. Namely, the $S^{33}_{\mathrm{MF}}(\mathbf{k},\omega)$ at the M′ points scales as $\frac{2}{3}N_s^{-1} + \mathcal{O}\left(N_s^{-2}\right)$, and at the M points as $\frac{5}{12}N_s^{-1} + \mathcal{O}\left(N_s^{-2}\right)$, while in the projected case the scaling seems to be $S^{33}(\mathbf{k},\Delta(\mathbf{k})) \propto N_s^{-1/2} + \mathcal{O}(N_s^{-3/2})$, as shown in Fig. 6.4. Unfortunately, the large error bars do not allow a more precise determination of the finite-size scalings.

So far there was no indication that the $S^{33}(\mathbf{k},\omega)$ calculated by the variational method would indeed be similar to the real dynamical spin structure factor of the SU(4) Heisenberg model. Therefore, we compared our results with exact diagonalization (ED) for a small cluster of 16 sites in Fig. 6.6. For the ED, we used periodic boundary conditions, while for the variational method, we had to impose APBC to make the Fermi sea non-degenerate. The orientation of the APBC in a C_6 symmetric cluster causes a simple rotation of the data, but since this cluster is not C_6 symmetric, the orientations of the APBC are not equivalent. For one of the APBC orientations, (Fig. 6.6(c)) the lowest energy excitations seem to be quite similar to the ED results.

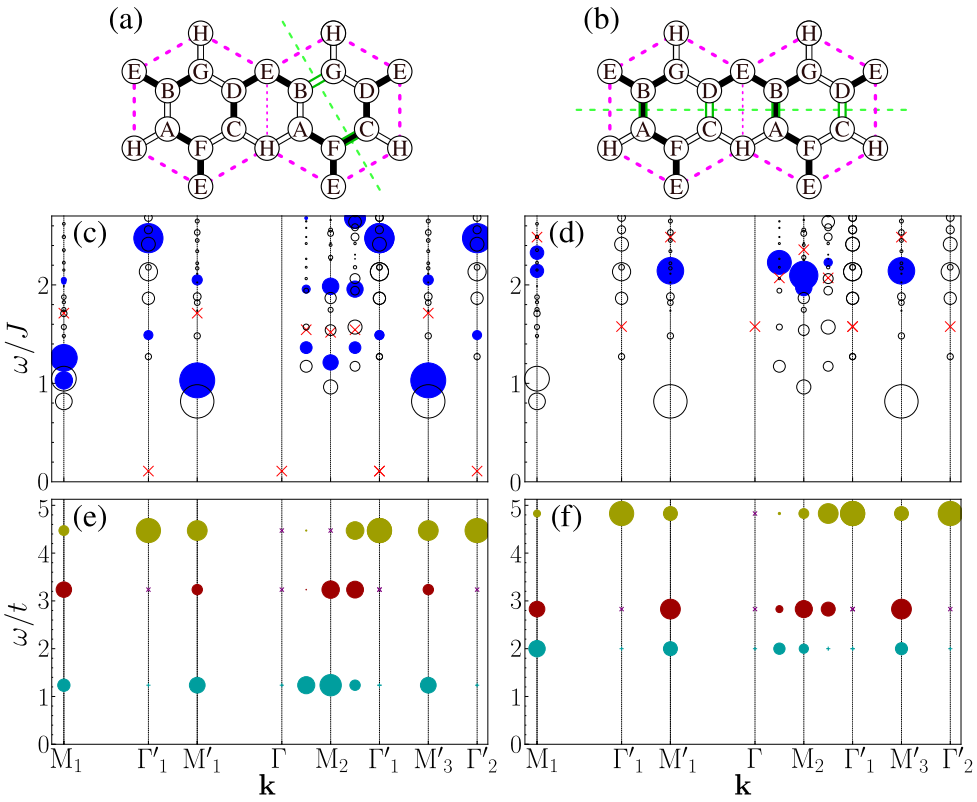

Figure 6.6: (a) and (b) the $N_s = 16$ site clusters with different antiperiodic boundaries (dashed green lines), which reverse the sign of the hoppings they cross. (c) The $S^{33}(\mathbf{k},\omega)$ for the 16-site cluster in (a), calculated by variational method (blue circles) and by exact diagonalization (black circles). The red crosses indicate the lowest energy states transforming as SU(N) singlets, from which we can see that the variational ground state energy of the $|\pi\text{FS}\rangle$ state is close to the ED ground state energy, which is at $\omega = 0$. (d) The $S^{33}(\mathbf{k},\omega)$ for the 16-site cluster in (b), in this case, the agreement is not so good. We expect the sensitivity to the boundary conditions to decrease with larger clusters. (e) and (f) show the mean-field $S^{33}_{\text{MF}}(\mathbf{k},\omega)$ for the clusters in (a) and (b), respectively. The crosses in panels (c)-(f) show excitations with zero spectral weights.

One could argue that we should have chosen the same boundary conditions for the two methods, so if we had chosen periodic boundary conditions for the ED, then we should have also used PBC for the variational method. However, choosing APBC for the variational method means multiplying by -1 the fermions that are beyond the boundary, and this sign change cancels from the definition of the spin operators in Eq. (2.2), so the boundary condition of Heisenberg chain remains periodic.

In the SU(4) case, we also found that at low energies, the local $S^{33}_{\text{MF}}(\omega) = \sum_{\mathbf{k}} \int S^{33}_{\text{MF}}(\mathbf{k},\omega)$ within a tower above the M and M$'$ points is proportional to the degeneracy (the number of particle-hole excitations with the same ω), ignoring finite-size corrections. Consequently, the $\int_0^{\omega} S^{33}_{\text{MF}}(\omega')\text{d}\omega' \propto \omega^4$ and from this the $S^{33}_{\text{MF}}(\omega) \propto \omega^3$ follows. However, the matrix elements in Eq. (4.8) are not all equal at a given ω.

6.1 The static spin structure factor

The static spin structure factor at zero temperature is defined as

$$\begin{aligned} S^{aa}(\mathbf{k}) &\equiv \frac{1}{N_s}\sum_{\mathbf{R},s}\sum_{\bar{\mathbf{R}},\bar{s}} e^{-i\mathbf{k}\cdot(\mathbf{R}+\boldsymbol{\delta}_s)} e^{i\mathbf{k}\cdot(\bar{\mathbf{R}}+\boldsymbol{\delta}_{\bar{s}})} \langle \mathrm{GS}|T^a_{\mathbf{R},s}T^a_{\bar{\mathbf{R}},\bar{s}}|\mathrm{GS}\rangle \\ &= \langle \mathrm{GS}|T^a_{-\mathbf{k}}T^a_{\mathbf{k}}|\mathrm{GS}\rangle = \int S^{aa}(\mathbf{k},\omega)d\omega, \end{aligned} \tag{6.1}$$

where we approximate $|\mathrm{GS}\rangle$ with the $P_{\mathrm{G}}|\pi\mathrm{FS}\rangle$ for the Heisenberg model (variational method), and $|\pi\mathrm{FS}\rangle$ in the mean-field case.

In the SU(4) case, both the projected $S^{33}(\mathbf{k})$ and the mean-field $S^{33}_{\mathrm{MF}}(\mathbf{k})$ have maxima only at the M′ points in the form of a hump (see Fig. 6.2(c)). In the SU(6) case, both $S^{33}(\mathbf{k})$ and $S^{33}_{\mathrm{MF}}(\mathbf{k})$ have triangular-shaped plateaus around the K′ points (see Fig. 6.3(d)), with the corners located at the M′ points. The difference between $S^{33}(\mathbf{k})$ and $S^{33}_{\mathrm{MF}}(\mathbf{k})$ in the SU(6) model is that the former has small humps at the M′ points (shown in the zoomed panel of Fig. 6.3(e), and in Fig. 6.3(f)), similarly to the SU(4) case.

The shapes of $S^{33}_{\mathrm{MF}}(\mathbf{k})$ (the orange curves in Figs.6.2(c) and 6.3(f)) are similar to the shapes of the Gutzwiller projected $S^{33}(\mathbf{k})$, with a difference in their normalizations, meaning that the correlations are reduced in the mean-field case. The normalization of the Fourier transformed spin operators in Eq. (4.2) and the static structure factor in Eq. (6.1) (consistent with the normalization of the dynamical structure factor in Eq. (4.5)) implies the sum rules

$$\sum_{\mathbf{k}\in\mathrm{eBZ}} S^{33}(\mathbf{k}) = \sum_{\mathbf{k}\in\mathrm{eBZ}}\int d\omega S^{33}(\mathbf{k},\omega) = \frac{N_{\mathbf{k}}}{N_s}\sum_{\mathbf{R},s}\frac{C_2}{N^2-1} = \frac{N_{\mathbf{k}}}{2N}, \tag{6.2}$$

and

$$\sum_{\mathbf{k}\in\mathrm{eBZ}} S^{33}_{\mathrm{MF}}(\mathbf{k}) = \sum_{\mathbf{k}\in\mathrm{eBZ}}\int d\omega S^{33}_{\mathrm{MF}}(\mathbf{k},\omega) = \frac{N_{\mathbf{k}}}{N_s}\sum_{\mathbf{R},s}\frac{C_2^{\mathrm{MF}}}{N^2-1} = \frac{N_{\mathbf{k}}}{2N}\left(1-\frac{1}{N}\right), \tag{6.3}$$

as derived in Appendix C (see also Ref. [II.]), where $N_{\mathbf{k}}$ is the number of wave vectors in the extended Brillouin zone, C_2 and C_2^{MF} are the quadratic Casimir operators of the Heisenberg model and its mean-field theory, $N_{\mathbf{k}} = \frac{3}{2}N_s$ on the honeycomb lattice, and $N_{\mathbf{k}} = \frac{4}{3}N_s$ on the kagome lattice. The relative factor $\left(\sum_{\mathbf{k}\in\mathrm{eBZ}} S^{33}_{\mathrm{MF}}(\mathbf{k})\right) / \left(\sum_{\mathbf{k}\in\mathrm{eBZ}} S^{33}(\mathbf{k})\right) = 1 - 1/N$ comes from the different values of the quadratic Casimir operators $C_2^{\mathrm{MF}} = C_2\left(1-\frac{1}{N}\right)$, as argued in Appendix C.1. The eigenvalue of the quadratic Casimir operator is determined by the irreducible representation of the Heisenberg model, which depends on the local Hilbert spaces. In the Gutzwiller projected treatment every site is singly occupied corresponding to the fundamental representation, so $C_2 = (N^2-1)/(2N)$ (as derived in App. A.3). However, in the mean-field approach, any site can be simultaneously occupied by multiple fermions, mixing different irreducible representations (for details see App. C.1). Thus, the charge fluctuations of the mean-field approach violate the single occupancy constraint of Eq. (2.5) and reduce the correlations. However, even though the multiple occupancy persists for any N, the difference between the sum rules vanishes in the large-N limit, showing the decreasing difference between the mean-field and Gutzwiller projected results with an increasing N.

We can divide the $S^{33}_{\mathrm{MF}}(\mathbf{k})$ with $(1-1/N)$, so that the sum rule of this renormalized $S^{33}_{\mathrm{MF}}(\mathbf{k})/(1-1/N)$ is the same as that of the projected $S^{33}(\mathbf{k})$. The renormalized $S^{33}_{\mathrm{MF}}(\mathbf{k})/(1-1/N)$ is shown with dashed light green in Figs. 6.2(c) and 6.3(f), and in the upper halves of Figs. 6.3(d), and 6.3(e). Comparing the renormalized mean-field $S^{33}_{\mathrm{MF}}(\mathbf{k})/(1-1/N)$ with the Gutzwiller projected $S^{33}(\mathbf{k})$, we can see that the differences are much smaller in the SU(6) case than in the SU(4) case, again indicating that the projected and mean-field calculations become equal in the large-N limit.

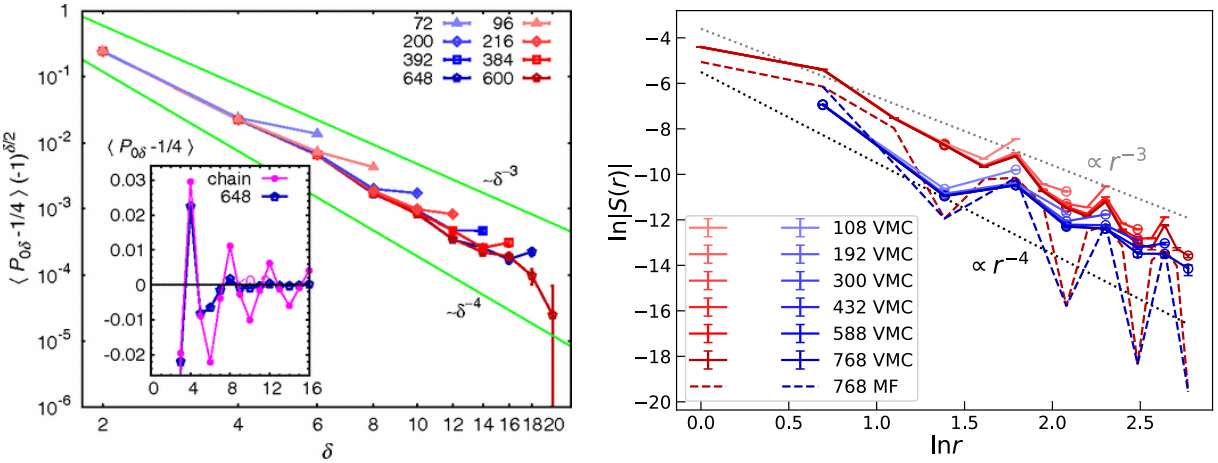

Figure 6.7: In the left panel we show on a logarithmic scale the decay of the SU(4) spin correlations $\langle P_{0\delta} - 1/4\rangle(-1)^{\delta/2} = 30\langle \pi\mathrm{FS}|P_\mathrm{G}T_0^3T_\delta^3P_\mathrm{G}|\pi\mathrm{FS}\rangle(-1)^{\delta/2}$ of the SU(4) Heisenberg model on a zig-zag chain of the honeycomb lattice, taken from Ref. ([6]). In the right panel we show the logarithm of the SU(6) spin correlations $|S(r)| \equiv \sum_{a=1}^{35}|\langle\pi\mathrm{FS}|P_\mathrm{G}T_0^aT_\delta^aP_\mathrm{G}|\pi\mathrm{FS}\rangle|$ of the SU(6) Heisenberg model on the kagome lattice calculated by VMC (solid lines with error bars) as a function of the logarithm of distance. In both panels, the approximately linear decay of the correlation function on the log-log scale suggests a power-law dependence on the distance, but perhaps the achievable distances were not large enough to see the exponential decay. On the right panel, we also plot the mean-field correlation function $|S_\mathrm{MF}(r)| \equiv \sum_{a=1}^{35}|\langle\pi\mathrm{FS}|T_0^aT_\delta^a|\pi\mathrm{FS}\rangle|$ with dashed-lines, which is known to approach a $\propto r^{-4}$ decay for large r. The colors of the right panel encode different directions: the red along the edges of the triangles and the blue in the directions crossing the centers of the hexagons. We average over equivalent directions to eliminate the anisotropy effect of the antiperiodic boundary condition. The absolute values of $S(r)$ take care of the alternating sign structure along the edges of the triangles (we put empty circles for $S(r) > 0$). At the same time, $S(r)$ is always positive along the directions through the centers of the hexagons. The mean-field results are negative for all $r > 0$. The dotted lines with r^{-3} and r^{-4} are guides for the eye. In both panels, the VMC results seem to decay algebraically with a power between 3 and 4, while the mean-field correlations of a Dirac spin liquid always approach a $\propto r^{-4}$ decay.

The mean-field static spin correlation function decays as a power law $|\langle\pi\mathrm{FS}|T_\mathbf{r}^aT_{\bar{\mathbf{r}}}^a|\pi\mathrm{FS}\rangle| \propto |\mathbf{r}-\bar{\mathbf{r}}|^{-4}$ at large enough $|\mathbf{r}-\bar{\mathbf{r}}|$, which is typical for every system with a Dirac-Fermi point [49, 106] Ref. [II.]. We also calculated the static spin correlation function in the Gutzwiller projected Fermi sea $|\langle\pi\mathrm{FS}|P_\mathrm{G}T_\mathbf{r}^aT_{\bar{\mathbf{r}}}^aP_\mathrm{G}|\pi\mathrm{FS}\rangle|$ in the SU(6) case, shown in the right panel of Fig. 6.7. In the left panel of Fig. 6.7, we show the $|\langle\pi\mathrm{FS}|P_\mathrm{G}T_\mathbf{r}^aT_{\bar{\mathbf{r}}}^aP_\mathrm{G}|\pi\mathrm{FS}\rangle|$ in the SU(4) case, taken from Ref. [6]. In both cases, the decay seems linear in log-log scales, suggesting a power law decay, just as in the mean-field case ($S(r) = cr^{-\alpha} \to \ln S(r) = \ln c - \alpha \ln r$). However, we can not exclude that the cluster sizes were not large enough, and the real decay is exponential. The exponential decay is usually accompanied by a gapped spectrum, while a power law decay is usually accompanied by a gapless spectrum. We plotted the finite size scaling of the finite size gap of the Gutzwiller projected spectrum in the SU(4) case in Fig. 6.4, which suggests a gapless spectrum, but again, due to the large Monte Carlo errors, this is not a proof. The steepness of the line in the log-log plot determines the exponent of the power law decay, and in both the SU(4) and the SU(6) cases the steepness seems to be between -3 and -4, so that the decay of $|\langle\pi\mathrm{FS}|P_\mathrm{G}T_\mathbf{r}^aT_{\bar{\mathbf{r}}}^aP_\mathrm{G}|\pi\mathrm{FS}\rangle|$ seems to be proportional to $|\mathbf{r}-\bar{\mathbf{r}}|^{-\alpha}$ with a power $3 \leq \alpha \leq 4$. Again, in the mean-field approximation we get $\alpha = 4$ in both the SU(4) and SU(6) cases.

What really matters is not the decay of $|\langle\pi\mathrm{FS}|P_\mathrm{G}T_\mathbf{r}^aT_{\bar{\mathbf{r}}}^aP_\mathrm{G}|\pi\mathrm{FS}\rangle|$, but instead the decay of

$|\langle \mathrm{GS}|T^a_{\mathbf{r}}T^a_{\bar{\mathbf{r}}}|\mathrm{GS}\rangle|$, where $|\mathrm{GS}\rangle$ is the ground state of the SU(N) Heisenberg model in the fundamental representation. If $|\langle \mathrm{GS}|T^a_{\mathbf{r}}T^a_{\bar{\mathbf{r}}}|\mathrm{GS}\rangle|$ also decays as a power law, then the spectrum of the SU(N) Heisenberg model should be gapless, and if the gapless towers are at the same locations as in the variational calculation, then the $P_{\mathrm{G}}|\pi\mathrm{FS}\rangle$ is stable. However, even if $P_{\mathrm{G}}|\pi\mathrm{FS}\rangle$ is stable, and both $|\langle \pi\mathrm{FS}|P_{\mathrm{G}}T^a_{\mathbf{r}}T^a_{\bar{\mathbf{r}}}P_{\mathrm{G}}|\pi\mathrm{FS}\rangle| \propto |\mathbf{r}-\bar{\mathbf{r}}|^{-\alpha}$ and $|\langle \mathrm{GS}|T^a_{\mathbf{r}}T^a_{\bar{\mathbf{r}}}|\mathrm{GS}\rangle| \propto |\mathbf{r}-\bar{\mathbf{r}}|^{-\beta}$ decay as power laws, their exponents might be different $\alpha \neq \beta$. The reason for this is that the interactions between the flavorons $f^\dagger_{\mathbf{k}+\mathbf{q},b',\sigma'}|\pi\mathrm{FS}\rangle$ and the antiflavorons $f_{\mathbf{q},b,\sigma}|\pi\mathrm{FS}\rangle$ (hidden in the fluctuations beyond the mean-field approximation) can change the exponent, even if these interactions are weak, and the mean-field ansatz is stable.

In the SU(4) case, the humps at the M′ points correspond to a short-range four-sublattice order, as shown in Ref. [6]. In the SU(6) case, the alternating sign structure of the static spin correlation function in the directions $\mathbf{r}_i - \mathbf{r}_j$ along the edges of the triangles (shown with the empty circles in Fig. 6.7) can be reproduced by $\sum_{l=1}^{6} e^{i\mathbf{k}_{\mathrm{M}'_l}\cdot(\mathbf{r}_i-\mathbf{r}_j)}$, where $\mathbf{k}_{\mathrm{M}'_l}$ are the wave vectors of the M′ ∈ eBZ points.

Summary

We computed the dynamical spin structure factor $S^{33}(k,\omega)$ of the SU(4) and SU(6) Heisenberg models on the honeycomb and kagome lattices, respectively. For these variational calculations, we approximated the ground state by the Gutzwiller projected π-flux Fermi sea, and the excited states by Gutzwiller projected particle-hole excitations of the π-flux Fermi sea, as explained in section 4.3. We compared these variational results with non-interacting mean-field calculations. The two approaches produce qualitatively similar results, suggesting that the energy spectrum of the Gutzwiller projected excitations may also be a gapless continuum of fractionalized excitations (see Figs. 6.2 and 6.3), with the gapless towers located at the M, M′, Γ and Γ′ points of the extended Brillouin zone.

Quantitatively, the Gutzwiller projection shifts the spectral weight $|\langle f|T^3_{\mathbf{k}}|\pi\mathrm{FS}\rangle|^2$ from higher to lower energies, thus emphasizing the lower edge of the continuum. The distributions of the mean-field and variational spectral weights show a much better agreement in the SU(6) case than in the SU(4) case. We attribute the decreasing difference between the two approaches to the increased SU(N) symmetry. However, while in the SU(4) case we could calculate the $S^{33}(\mathbf{k},\omega)$ variationaly for a 72-site cluster, in the SU(6) case we were limited to a cluster of 48-sites. Relying on the similarity of the variational and mean-field calculations in the SU(6) case, we calculated the $S^{33}(\mathbf{k},\omega)$ in the mean-field approach for an extensive system with 3888 sites, to assess the thermodynamic limit.

In the mean-field approach of the SU(4) case, we obtained the $1/\mathrm{r}^4$ decay of the spin correlation function, and the local correlations show $S^{33}_{\mathrm{MF}}(\omega) \propto \omega^3$ behavior.

For both the SU(4) and SU(6) cases, the static spin structure factor $S^{33}(\mathbf{k}) = \int d\omega S^{33}(\mathbf{k},\omega)$ has maxima at the M′ points of the extended Brillouin zone. However, in the SU(6) case, there are increased weights in the form of triangular-shaped plateaus around the K′ points of the extended Brillouin zone, which are not present in the SU(4) calculations. The differences between the static variational and mean-field calculations are the reduced sum rules and the reduced maxima of the mean-field results.

The ratio of the sums $\left(\sum_{\mathbf{k}\in\mathrm{eBZ}} S^{33}_{\mathrm{MF}}(\mathbf{k})\right) / \left(\sum_{\mathbf{k}\in\mathrm{eBZ}} S^{33}(\mathbf{k})\right) = 1 - 1/N$ shows that the correlations are reduced in the mean-field case. As argued in Appendix C.1, the reason is that the charge fluctuations reduce the value of the quadratic Casimir operator, appearing in the sum rules. However, even though the charge fluctuations persist for any N, the difference between the mean-field and VMC sum rules vanishes in the large-N limit.

The real space spin-spin correlations decay algebraically with the distance, with a power between 3 and 4, similarly as in the SU(4) case Ref. [6].

These results were published in Refs. Ref. [II.] and Ref. [III.].

Appendix A

Details of the SU(N) spin operators: the generators of the su(N) Lie algebra

A.1 Rotations in 3D, the SO(3) group and the so(3) Lie algebra

Before calculating the SU(N) spin rotation operator, let us recapitulate the properties of classical rotations. In this section, we follow sections I.3 and IV.2 of the book [107].

A rotation operator $\mathcal{R}$ is expected to preserve the norm of a vector $\mathbf{r}$, in the sense that $\mathbf{r}^T \cdot \mathbf{r} = (\mathcal{R}\mathbf{r})^T \cdot (\mathcal{R}\mathbf{r}) = (\mathbf{r}^T\mathcal{R}^T) \cdot (\mathcal{R}\mathbf{r})$ and also the angle between any two vectors $\mathbf{u}$ and $\mathbf{v}$, which depends on their inner product $\mathbf{u}^T \cdot \mathbf{v} = (\mathcal{R}\mathbf{u})^T \cdot (\mathcal{R}\mathbf{v}) = (\mathbf{u}^T\mathcal{R}^T) \cdot (\mathcal{R}\mathbf{v})$, implying that $\mathcal{R}$ must be orthogonal $\mathcal{R}^T\mathcal{R} = \mathcal{I}$ (giving the O in SO(3)). The condition that $\mathcal{R}$ must be orthogonal does not uniquely specify rotations because reflections also satisfy $\mathcal{R}^T\mathcal{R} = \mathcal{I}$. Taking the determinant of this relation $\det\left(\mathcal{R}^T\mathcal{R}\right) = \det\left(\mathcal{R}^T\right)\det(\mathcal{R}) = (\det(\mathcal{R}))^2 = \det(\mathcal{I}) = 1$, so that $\det\left(\mathcal{R}^T\right) = \pm 1$. To uniquely specify rotations, we have to add the condition $\det(\mathcal{R}) = +1$ (giving the S in SO(3) as "special") because the $\det(\mathcal{R}) = -1$ specifies reflections. The set of orthogonal operators with unit determinants form the SO(3) rotation group. So far, we have been talking about rotation operators. When we take a set of matrices satisfying the same multiplication relations as the rotation operators, then we have a representation of the rotation operators with matrices. The size of the matrices representing the SO(3) rotations depends on the representation. An irreducible representation is when the rotation matrices can not be simultaneously block diagonalized with basis transformations. In the fundamental representation (sometimes called defining representation) of SO(3) these become 3×3 matrices, describing the rotation of vectors in 3 dimensions (3 linearly independent vectors serve as a basis for this irrep).

The condition to have $\det(\mathcal{R}) = +1$ also allows us to use Taylor expansion for the infinitesimal rotation around the identity as

$$\mathcal{R}(\phi) = \mathcal{I} + \phi\mathcal{A} + \mathcal{O}(\phi^2), \tag{A.1}$$

where ϕ is a small angle. A reflection with $\det(\mathcal{R}) = -1$ can not be continuously connected to the identity. $\mathcal{R}$ have to satisfy the orthogonality condition in every power of ϕ,

$$\mathcal{R}^T \cdot \mathcal{R} = (\mathcal{I} + \phi\mathcal{A} + \mathcal{O}(\phi^2))^T(\mathcal{I} + \phi\mathcal{A} + \mathcal{O}(\phi^2)) = \mathcal{I} + \phi(\mathcal{A}^T + \mathcal{A}) + \mathcal{O}(\phi^2), \tag{A.2}$$

so $\mathcal{A}^T = -\mathcal{A}$ must hold, meaning that $\mathcal{A}$ is antisymmetric (and real since $\mathcal{R}$ is real). Any finite rotation $\mathcal{R}$ can be separated into a series of many small rotations as $\mathcal{R}(\theta) = \mathcal{R}(\theta/m)^m$, where θ is not a small angle, but for a large m, θ/m is small. Therefore, we can use the expression of the infinitesimal rotations as

$$\mathcal{R}(\theta) = \lim_{m\to\infty} \mathcal{R}(\theta/m)^m = \lim_{m\to\infty} \left(\mathcal{I} + \frac{\theta}{m}\mathcal{A}\right)^m = \exp\left(\theta\mathcal{A}\right). \tag{A.3}$$

We can take a set of real antisymmetric matrices $\{\mathcal{B}_j\}$ serving as a basis, so that any real antisymmetric matrix can be written as their linear combination $\mathcal{A} = \sum_j \mathcal{B}_j$. To know how many such matrices we need, we have to count how many independent real numbers $\mathcal{A}$ can have. Its diagonal has zeros (since $\mathcal{A}_{i,i} = -\mathcal{A}_{i,i}$), and the off diagonals satisfy $\mathcal{A}_{i,j} = -\mathcal{A}_{j,i}$. Therefore, only three real numbers are independent, so we can choose the three matrices

$$\mathcal{B}_1 = \begin{pmatrix} 0 & 0 & 0 \\ 0 & 0 & -1 \\ 0 & 1 & 0 \end{pmatrix} \quad \mathcal{B}_2 = \begin{pmatrix} 0 & 0 & 1 \\ 0 & 0 & 0 \\ -1 & 0 & 0 \end{pmatrix} \quad \mathcal{B}_3 = \begin{pmatrix} 0 & -1 & 0 \\ 1 & 0 & 0 \\ 0 & 0 & 0 \end{pmatrix} \tag{A.4}$$

as a basis. If we further express the real antisymmetric matrices $\mathcal{B}_j = -i\mathcal{L}_j$ with hermitian matrices $\mathcal{L}_j^\dagger = \mathcal{L}_j$, then the $\mathcal{L}_j$ become the operators of angular momentum (divided by $\hbar$) $L_x/\hbar$, $L_y/\hbar$ and $L_z/\hbar$. These satisfy the commutation relations $[L_i, L_j] = i\hbar\sum_k \varepsilon_{i,j,k}L_k$, so they are the generators of the so(3) Lie algebra. With these, we can write an infinitesimal rotation (with angle ϕ) and a finite rotation (with angle θ)

$$\mathcal{R}(\phi) = \mathcal{I} + \frac{i}{\hbar}\phi\sum_j n_j\mathcal{L}_j + \mathcal{O}(\phi^2) \qquad\qquad \mathcal{R} = \exp\left(\frac{i}{\hbar}\theta\sum_j n_j L_j\right), \tag{A.5}$$

therefore the L_j are also called infinitesimal generators of rotations. The norm $\sum_j |n_j|^2$ can be melted into θ, so that we can interpret the $\sum_j n_j L_j = \mathbf{n}\cdot\mathbf{L}$ as the inner product of the unit vector $\mathbf{n}$ (specifying the axis of rotation through the right-hand rule) with the vector operator $\mathbf{L}$.

Eq. (A.5) shows that the sizes of the matrices of angular momenta L_j and the size of the rotation matrices $\mathcal{R}$ are the same. In the fundamental irrep of SO(3) every matrix is 3 dimensional. However, higher-dimensional irreps of SO(3) exist labeled by the integer j, where the dimension is given by $d = 2j+1$, which equals the number of basis states for this irrep. The three-dimensional fundamental irrep has $j = 1$, with basis vectors $|j = 1, m = 1\rangle$, $|j = 1, m = 0\rangle$, $|j = 1, m = -1\rangle$, where m is the eigenvalue of L^z. For a general j the basis states can be labeled with $m \in \{-j \dots j\}$ integers, and serve as a basis for both the rotation matrices (forming the SO(3) group) and the angular momentum operators L_x, L_y and L_z (being the generators of the so(3) Lie algebra). The main point is that even though the number of generators L_x, L_y, and L_z came from the number of linearly independent 3×3 hermitian matrices (which turns out to be 3), it remains the same for any irrep j, regardless of its dimension. In other words, the number of generators L_x, L_y, and L_z is always deduced from the fundamental irrep of a given algebra (and group), and remains the same for any other irrep, only the dimension of the matrices increases. The number of generators changes, if we change the group (and the algebra with it), for example to SO($N > 3$).

A.2 Spin rotations and the SU(N) group

In the preceding section, we presented the SO(3) group of rotations and its so(3) Lie algebra, to be able to compare the followings with something well known. In this section, we follow section IV.4. of the book [107].

SU(N) spins are the wave functions that serve as a basis for the local Hilbert space of the SU(N) Heisenberg model in a given irreducible representation (see Sec. 1.4.2 and Appendix A.5). In the fundamental representation, there are N such wave functions, which can be taken to be $\{c^\dagger_{j,\sigma}|0\rangle|\sigma \in \{1\dots N\}\}$, where $c^\dagger_{j,\sigma}$ are the fermionic creation operators of the SU(N) Hubbard model (1.2) on site j. The rotation of a wavefunction $|\psi\rangle$ by an operator U is expected to leave invariant its norm $\langle\psi|\psi\rangle = \langle\psi|U^\dagger U|\psi\rangle$, and the inner product of any two wavefunctions $|\psi\rangle$ and $|\phi\rangle$ as $\langle\psi|\phi\rangle = \langle\psi|U^\dagger U|\phi\rangle$, therefore the U has to be unitary (giving the letter U in SU(N)), meaning $U^\dagger U = \mathcal{I}$. Taking the determinant of this relation we get $\det\big(U^\dagger U\big) = \det\big(U^\dagger\big)\det(U) = |\det(U)|^2 = \det(\mathcal{I}) = 1$, implying that $\det(U) = e^{i\varphi}$ is a phase. Similarly, as in the case of SO(3) rotations, we expect an SU(N) rotation to be continuously connected to the identity because an infinitesimal rotation is almost like doing nothing. Therefore, we will set $\det(U) = +1$ (giving the letter S in SU(N), as "special"). Unitary operators with unit determinants form the SU(N) group, describing the transformations of wavefunctions with the properties we expect from an SO(3) rotation. The $\det(U) = +1$ condition allows us to use Taylor expansion for an SU(N) rotation with the infinitesimal angle ϕ as

$$U(\phi) = \mathcal{I} + \phi\mathcal{A} + \mathcal{O}(\phi^2), \tag{A.6}$$

where the unitarity condition

$$U^\dagger U = (\mathcal{I} + \phi\mathcal{A} + \mathcal{O}(\phi^2))^\dagger(\mathcal{I} + \phi\mathcal{A} + \mathcal{O}(\phi^2)) = \mathcal{I} + \phi(\mathcal{A}^\dagger + \mathcal{A}) + \mathcal{O}(\phi^2) \tag{A.7}$$

requires $\mathcal{A}^\dagger = -\mathcal{A}$, so that $\mathcal{A}^\dagger$ is antihermitian. Writing $\mathcal{A} = i\mathcal{B}$ the $\mathcal{B}$ becomes hermitian. We can write a finite SU(N) rotation $U(\theta)$ as a sequence on infinitesimal SU(N) rotations, and use the above expansion to get

$$U(\theta) = \lim_{m\to\infty}(U(\theta/m))^m = \lim_{m\to\infty}\left(\mathcal{I} + i\frac{\theta}{m}\mathcal{B}\right)^m = \exp(i\theta\mathcal{B})\,. \tag{A.8}$$

We can use the relation $\det\exp(A) = \exp(\operatorname{Tr} A)$ as $+1 = \det U = \det[\exp(i\theta\mathcal{B})] = \exp(i\theta\operatorname{Tr}\mathcal{B})$, to deduce $\operatorname{Tr}\mathcal{B} = 0$. Therefore, we can take a basis of traceless hermitian operators $\{T^a\}$, in which basis we can write $\mathcal{B} = \sum_a n_a T^a$. The number of linearly independent basis operators $\{T^a\}$ is equal to the number of independent real numbers in an $N\times N$ traceless hermitian matrix. There are N real numbers in its diagonal, and $(N^2-N)/2$ complex numbers in its upper right off-diagonal (the lower left off-diagonals are the complex conjugate of these), where every complex number is counted as two independent real numbers. The traceless condition reduces the N independent real numbers in the diagonal by one, so in total there are $N-1+2(N^2-N)/2 = N^2-1$ independent real numbers. For example, in the su(3) Lie algebra we have $3^2-1=8$ linearly independent operators $\{T^a\}$, which are called the Gell-Mann matrices [46], presented in Appendix A.3. These matrices can be constructed in different ways, one of them is presented in Appendix A.3. Independently of their choice, the T^a matrices are called the generators of the su(N) Lie algebra, and they satisfy the commutation relations $[T^a, T^b] = i\sum_c f_{abc}T^c$ of Eq. (1.19). The reason for this is that the commutator $[T^a, T^b]$ is itself antihermitian ($[T^a, T^b]^\dagger = [(T^b)^\dagger, (T^a)^\dagger] = [T^b, T^a] = -[T^a, T^b]$) and traceless ($\operatorname{Tr}\big[T^a, T^b\big] = \operatorname{Tr} T^aT^b - \operatorname{Tr} T^bT^a = 0$), therefore it can be written as a linear combination of the antihermitian traceless matrices iT^c, where f_{abc} are the coefficients in the linear combination. Of course, the f_{abc} depends on the particular construction of the T^a. In summary, an infinitesimal SU(N) rotation with a small angle ϕ, and a finite SU(N) rotation with an angle θ can be written with the generators T^a as

$$U(\phi) = \mathcal{I} + i\phi\sum_{a=1}^{N^2-1} n_a T^a + \mathcal{O}(\phi^2) \qquad\qquad U(\theta) = exp\left(i\theta\sum_{a=1}^{N^2-1} n_a T^a\right). \tag{A.9}$$

These equations show that the sizes of the matrices of the generators T^a and the matrices of SU(N) rotations U are the same in any representation. The number of generators T^a was determined in the fundamental irrep of the su(N) Lie algebra (which is also the fundamental irrep of the SU(N) group), but it remains the same for any other irrep of su(N), only the size of the matrices T^a is changed.

The norm $\sum_{a=1}^{N^2-1}|n_a|^2$ can be melted into the angles ϕ and θ, so that $\sum_{a=1}^{N^2-1} n_a T^a = \mathbf{n}\cdot\mathbf{T}$ can be interpreted as the inner product of the unit vector $\mathbf{n}$ (specifying the axis of SU(N) rotation in an N^2-1 dimensional spin space through the right-hand rule) and the vector operator $\mathbf{T}$.

Eq. (A.9) expresses the rotation of a single SU(N) spin, the simultaneous rotation of all SU(N) spins around the same axis $\mathbf{n}$ with the same angle ϕ is given by the SU(N) operator $U = \prod_{j=1}^{N_s} e^{i\phi\mathbf{n}\cdot\mathbf{T}_j}$, where j is the site index.

A.3 The matrices representing the SU(N) spin operators in the fundamental representation

As argued in Appendix A.2, the generators of the su(N) Lie algebra in the fundamental irreducible representation form a basis in the space of $N\times N$ traceless hermitian matrices,

therefore there should be N^2-1 generators. These can be constructed in different ways, here we follow the convention from section V.3 of the book [107] and [108]. In this convention, the generators are orthonormalized as

$$\operatorname{Tr} T^a T^b = \frac{1}{2}\delta_{a,b}, \tag{A.10}$$

where $\operatorname{Tr} A^\dagger B$ can be viewed as an inner product in the vector space of matrices. Furthermore, we set the generators S^x, S^y, S^z of the su(2) Lie algebra to be $S^a = \frac{1}{2}\sigma^a$ in the fundamental representation, where σ^a are the Pauli matrices

$$\sigma^x = \begin{pmatrix} 0 & 1 \\ 1 & 0 \end{pmatrix}, \sigma^y = \begin{pmatrix} 0 & -i \\ i & 0 \end{pmatrix}, \sigma^z = \begin{pmatrix} 1 & 0 \\ 0 & -1 \end{pmatrix}. \tag{A.11}$$

In case of su(3), the $3^2-1=8$ generators are again of the form $S^a = \frac{1}{2}\lambda^a$, where in this convention the λ^a are

$$\begin{aligned} \lambda^1 &= \begin{pmatrix} 0 & 1 & 0 \\ 1 & 0 & 0 \\ 0 & 0 & 0 \end{pmatrix} \quad \lambda^2 = \begin{pmatrix} 0 & -i & 0 \\ i & 0 & 0 \\ 0 & 0 & 0 \end{pmatrix} \quad \lambda^3 = \begin{pmatrix} 1 & 0 & 0 \\ 0 & -1 & 0 \\ 0 & 0 & 0 \end{pmatrix} \\ \lambda^4 &= \begin{pmatrix} 0 & 0 & 1 \\ 0 & 0 & 0 \\ 1 & 0 & 0 \end{pmatrix} \quad \lambda^5 = \begin{pmatrix} 0 & 0 & -i \\ 0 & 0 & 0 \\ i & 0 & 0 \end{pmatrix} \\ \lambda^6 &= \begin{pmatrix} 0 & 0 & 0 \\ 0 & 0 & 1 \\ 0 & 1 & 0 \end{pmatrix} \quad \lambda^7 = \begin{pmatrix} 0 & 0 & 0 \\ 0 & 0 & -i \\ 0 & i & 0 \end{pmatrix} \quad \lambda^8 = \frac{1}{\sqrt{3}} \begin{pmatrix} 1 & 0 & 0 \\ 0 & 1 & 0 \\ 0 & 0 & -2 \end{pmatrix} \end{aligned}, \tag{A.12}$$

called the Gell-Mann matrices [46]. The first three Gell-Mann matrices are simply the Pauli matrices complemented with zeros, they form an su(2) subalgebra of su(3). The λ^1, λ^4 and λ^6 in the first column are basically σ^x in the $1-2$, $1-3$ and $2-3$ sectors, respectively. Similarly, the λ^2, λ^5 and λ^7 contain the σ^y in these sectors. If we had three diagonal matrices containing the σ^z in these sectors, then the su(3) algebra would be equal to the product of three non-overlapping su(2) subalgebras as $\mathrm{su}(2) \otimes \mathrm{su}(2) \otimes \mathrm{su}(2)$. However, there are only two diagonal matrices λ^3 and λ^8, therefore these su(2) subalgebras overlap, and their missing σ^z like matrices are linear combinations of λ^3 and λ^8.

From the su(3) case above, we can deduce how to construct the generators $T^a = \frac{1}{2}\lambda^a$ in the fundamental representation of any su(N) Lie algebra in this convention. First, take the λ^a matrices in the fundamental irrep of the $su(N-1)$ Lie algebra and complete every matrix with one row and one column of zeros. Then, add σ^x and σ^y in all possible sectors which were not included yet. The number of diagonal matrices should be $N-1$ in the su(N) Lie algebra, so when complementing the matrices of su($N-1$) to su(N), we have to add one more diagonal matrix. Let us denote the indices a of the diagonal matrices λ^a as $D(n)$, so that $n \in \{1 \dots N-1\}$, and the $D(n)$ iterates through the diagonal indices (for example, in the su(3) case $D(1)=3$, and $D(2)=8$). The new diagonal matrix $\lambda^{D(N-1)}$ should be orthogonal to all previous diagonal matrices as $\operatorname{Tr} \lambda^{D(N-1)} \lambda^{D(n)} = 0$ with $n < N-1$, which is easily achieved by setting its first $N-1$ diagonal elements to 1. Then we make it traceless by setting the last element to $-(N-1)$, and finally normalize the matrix so that it satisfies $\operatorname{Tr} \lambda^{D(N-1)} \lambda^{D(N-1)} = 2$ (the normalization of the λ^a follows from Eq. (A.10) after dividing both sides with 4).

In reality, we first construct the matrices λ^a in the fundamental representation, which determine the structure constants f_{abc} through the commutation relations

$$\left[\frac{1}{2}\lambda^a, \frac{1}{2}\lambda^b\right] = i \sum_{c=1}^{N^2-1} f_{abc} \frac{1}{2}\lambda^c, \tag{A.13}$$

and then we build in these matrices into the operators $T^a_j = \frac{1}{2}\sum_{\sigma,\sigma'} f^\dagger_{j,\sigma}\lambda^a_{\sigma,\sigma'}f_{j,\sigma'}$ of Eq. (2.2), to get the same commutation relations for the T^a as for the $\frac{1}{2}\lambda^a$. Consequently, the structure constants f_{abc} depend on the specific construction of the matrices λ^a. For the construction described here, the structure constants of the su(2) Lie algebra are the Levi Civita symbols $\varepsilon_{123} = \varepsilon_{231} = \varepsilon_{312} = +1$ and $\varepsilon_{321} = \varepsilon_{213} = \varepsilon_{132} = -1$ (all others like ε_{112} are zeros), while in the su(3) case, these are

$$\begin{aligned} f^{123} &= 1 \\ f^{147} &= -f^{156} = f^{246} = f^{257} = f^{345} = -f^{367} = \frac{1}{2} \\ f^{458} &= f^{678} = \frac{\sqrt{3}}{2}, \end{aligned} \tag{A.14}$$

where the ones not listed are zeros.

Once the f_{abc} were fixed, the matrices λ^a of all the other irreducible representations are constructed in a way to satisfy the commutation relations (A.13) for the same f_{abc}, and their spin operators are constructed in some basis by building the λ^a into their definitions.

The eigenvalue of the quadratic Casimir operator $\hat{C}_2 \equiv \sum_{a=1}^{N^2-1} T^a T^a$ of Eq. (1.21) is diagonal in every irreducible representation (since the eigenvalues of the Casimir operators determine the irrep), which can be written as $\hat{C}_2 = C_2\mathbf{I}$. We can get the eigenvalue C_2 by taking the trace $\operatorname{Tr}\hat{C}_2 = C_2 \operatorname{Tr}\mathbf{I} = C_2 d$, where d is the dimension of the irrep. In the fundamental representation $d = N$, and using the normalization of spin operators $\operatorname{Tr} T^a T^b = \frac{1}{2}\delta_{a,b}$ of Eq. (A.10) we get $\operatorname{Tr}\hat{C}_2 = \sum_{a=1}^{N^2-1} \operatorname{Tr} T^a T^a = (N^2-1)/2$, so

$$C_2 = \frac{N^2-1}{2N}. \tag{A.15}$$

In the su(N) case there are $N-1$ simultaneously diagonal matrices (λ^3 and λ^8 in the su(3) case), which means that the simultaneous eigenstates of these diagonal matrices can be parametrized by $N-1$ quantum numbers $|m_{D(1)}, \dots m_{D(N-1)}\rangle$ (in the su(3) case these states have quantum numbers $|m_3, m_8\rangle$). These states are what we call SU(N) spins in section 1.4.2. In the su(2) case, the only quantum number is m, which forms the states $|j, m\rangle$ in the irrep labeled by j. The irrep label is not written explicitly in the $|m_{D(1)}, \dots m_{D(N-1)}\rangle$, it would either involve the eigenvalues of all Casimir operators or the young tableau of the irrep. The range of the $m_1, \dots m_{N-1}$ quantum numbers depends on the irrep, just as in the su(2) case, where $m \in \{-j \dots j\}$. In the fundamental representation of su(3) these eigenstates (the su(3) spins) are $|m_3 = 0, m_8 = -\frac{1}{\sqrt{3}}\rangle$, $|m_3 = \frac{1}{2}, m_8 = \frac{1}{2\sqrt{3}}\rangle$ and $|m_3 = -\frac{1}{2}, m_8 = \frac{1}{2\sqrt{3}}\rangle$, which form a triangle (called weight diagram) in the space where the horizontal axis is m_3 and the vertical axis is m_8. In the fundamental representation of su(N) the number of states $|m_{D(1)}, \dots m_{D(N-1)}\rangle$ is N, spaning the N dimensional Hilbert space of this irrep.

The non-diagonal matrices can be separated into $[N^2 - 1 - (N-1)]/2 = N(N-1)/2$ pairs (the σ^x and σ^y in a given sector) to form raising and lowering operators similar to S^+ and S^-, with the difference that these do not raise or lower the single value m, but the $N-1$ quantum numbers $m_1, \dots m_{N-1}$ simultaneously. In the su(3) case, these are the followings:

$$I_\pm = T^1 \pm iT^2 \qquad V_\pm = T^4 \pm iT^5 \qquad V_\pm = T^6 \pm iT^7, \tag{A.16}$$

which have the following commutation relations with the diagonal T^3 and T^8:

$$[T^3, I_\pm] = \pm I_\pm \qquad [T^3, U_\pm] = \mp\frac{1}{2}U_\pm \qquad [T^3, V_\pm] = \pm\frac{1}{2}V_\pm \tag{A.17}$$

$$[T^8, I_\pm] = 0 \qquad [T^8, U_\pm] = \pm\frac{\sqrt{3}}{2}U_\pm \qquad [T^8, V_\pm] = \pm\frac{\sqrt{3}}{2}V_\pm. \tag{A.18}$$

Consequently, the operators $I_\pm$, $U_\pm$ and $V_\pm$ iterate between the simultaneous eigenstates $|m_3, m_8\rangle$ of λ^3 and λ^8 as

$$\begin{aligned} I_\pm|m_3, m_8\rangle &\propto |m_3 \pm 1, m_8\rangle \\ U_\pm|m_3, m_8\rangle &\propto |m_3 \mp \frac{1}{2}, m_8 \pm \frac{\sqrt{3}}{2}\rangle \\ V_\pm|m_3, m_8\rangle &\propto |m_3 \pm \frac{1}{2}, m_8 \pm \frac{\sqrt{3}}{2}\rangle, \end{aligned} \tag{A.19}$$

in any irreducible representation of su(3).

A.4 SU(N) spin rotational symmetry of the Heisenberg model

The SU(N) symmetry of the Heisenberg Hamiltonian (1.10) means that it is invariant under the simultaneous rotation of all SU(N) spins around the same axis $\mathbf{n}$ with the same angle ϕ, which is done by the global SU(N) spin rotation operator $U = \prod_{j=1}^{N_s} e^{i\phi\mathbf{n}\cdot\mathbf{T}_j}$ (see the end of Appendix A.2) as

$$U\mathcal{H}U^{-1} = \prod_{j=1}^{N_s} e^{i\phi\mathbf{n}\cdot\mathbf{T}_j}\mathcal{H}\prod_{j=1}^{N_s} e^{-i\phi\mathbf{n}\cdot\mathbf{T}_j} = \mathcal{H}, \tag{A.20}$$

which is equivalent to $[U, \mathcal{H}] = 0$.

Before turning to the proof, let us mention why is this symmetry important. Firstly, we have seen in Sec. 2.6 that if the ground state is not invariant under some transformation U, which leaves the Hamiltonian invariant (called symmetry breaking), then the ground state must be degenerate. We also saw that breaking a continuous symmetry can lead to gapless excitations due to the Goldstone theorem. If the ground state becomes ferromagnetic or antiferromagnetic, then the continuous SU(N) spin rotation symmetry is broken, and the operator U can transform one ground state into a linear combination of the others.

Secondly, if the ground state does not break any symmetry, it is also invariant under any global SU(N) spin rotation as $U|\mathrm{GS}\rangle = |\mathrm{GS}\rangle$. As shown in Appendix A.2, an infinitesimal SU(N) spin rotation can be Taylor expanded around the identity (A.9), so we can do the same with the global SU(N) spin rotation

$$U(\phi) = \prod_{j=1}^{N_s} e^{i\phi\mathbf{n}\cdot\mathbf{T}_j} = e^{i\phi\mathbf{n}\cdot\sum_{j=1}^{N_s}\mathbf{T}_j} = e^{i\phi\mathbf{n}\cdot\mathbf{T}_T} = e^{i\phi\sum_{a=1}^{N^2-1} n^a T_T^a} \tag{A.21}$$

for $\phi \ll 1$ as

$$U(\phi) = \mathcal{I} + i\phi\sum_{a=1}^{N^2-1} n^a T_T^a + \mathcal{O}(\phi^2), \tag{A.22}$$

where $T_T^a \equiv \sum_{j=1}^{N_s} T_j^a$. We can choose the axis of rotations $\mathbf{n}$ so, that it points into the direction of one of the SU(N) spin operators, say T^b, simplifying the above equation to

$$U(\phi) = \mathcal{I} + i\phi T_T^b + \mathcal{O}(\phi^2). \tag{A.23}$$

Consequently, $U(\phi)|\mathrm{GS}\rangle = |\mathrm{GS}\rangle$ for any U implies $T_T^b|\mathrm{GS}\rangle = 0$ for any b. Therefore, the total quadratic Casimir operator $\sum_{a=1}^{N^2-1} T_T^a T_T^a$ (1.22) also takes on an eigenvalue 0, so that the ground state transforms as an SU(N) singlet.

Now let us turn to the proof of $[U,\mathcal{H}]=0$ for the global SU(N) spin rotations U defined in Eq. (A.21) for any axis of rotation $\mathbf{n}$ and any angle ϕ. It is helpful to expand the exponential to a power series

$$U = e^{i\phi\sum_{a=1}^{N^2-1} n_a T_T^a} = \sum_{n=0}^{\infty} \frac{(-1)^n}{n!} \left(\phi \sum_{a=1}^{N^2-1} n_a T_T^a \right)^n . \tag{A.24}$$

If T_T^a commutes with $\mathcal{H}$ for all $a \in \{1 \dots N^2-1\}$, then every power of T_T^a commutes with $\mathcal{H}$, and so will U.

The Heisenberg Hamiltonian (1.18) can be rewritten as

$$\begin{aligned} \mathcal{H} &= J \sum_{\langle i,j \rangle} \sum_{a=1}^{N^2-1} T_i^a T_j^a = \frac{J}{2} \sum_{\langle i,j \rangle} \sum_{a=1}^{N^2-1} \left((T_i^a + T_j^a)^2 - (T_i^a)^2 - (T_j^a)^2 \right) \\ &= \frac{J}{2} \sum_{\langle i,j \rangle} \left(\hat{C}_{2,i+j} - \hat{C}_{2,i} - \hat{C}_{2,j} \right), \end{aligned} \tag{A.25}$$

since the SU(N) spin operators on different sites commute. The $\sum_a (T_i^a)^2 = \mathbf{T}_i \cdot \mathbf{T}_i = \hat{C}_{2,i}$ is the quadratic Casimir operator on site i (1.21), while $\sum_a (T_i^a + T_j^a)^2 = \mathbf{T}_{i+j} \cdot \mathbf{T}_{i+j} = \hat{C}_{2,i+j}$ is the quadratic Casimir operator of the subsystem composed of sites i and j. In the commutator

$$\begin{aligned} [T_T^a, \mathcal{H}] &= \left[\sum_{l=1}^{N_s} T_l^a, \frac{J}{2} \sum_{\langle i,j \rangle} \hat{C}_{2,i+j} - \hat{C}_{2,i} - \hat{C}_{2,j} \right] = \frac{J}{2} \sum_{\langle i,j \rangle} \sum_{l=1}^{N_s} [T_l^a, \hat{C}_{2,i+j} - \hat{C}_{2,i} - \hat{C}_{2,j}] \\ &= \frac{J}{2} \sum_{\langle i,j \rangle} \left(\sum_{l \notin \{i,j\}} \underbrace{[T_l^a, \hat{C}_{2,i+j} - \hat{C}_{2,i} - \hat{C}_{2,j}]}_{0} + [T_i^a + T_j^a, \hat{C}_{2,i+j} - \hat{C}_{2,i} - \hat{C}_{2,j}] \right). \end{aligned} \tag{A.26}$$

The $\hat{C}_{2,i}$ trivially commutes with T_j^a (since $i \neq j$), but it also commutes with T_i^a, because the Casimir operators at site i commute with all T_i^a (see Sec. 1.4.2). The only terms which do not commute are $[T_i^a, \hat{C}_{2,i+j}] \neq 0$ and $[T_j^a, \hat{C}_{2,i+j}] \neq 0$. However, the sum of the spin operators commutes $[T_i^a + T_j^a, \hat{C}_{2,i+j}] = \sum_b [T_i^a + T_j^a, (T_i^b + T_j^b)^2] = 0$, since $\hat{C}_{2,i+j}$ is a Casimir operator on the subsystem of sites i and j.

Thus, we conclude that $[T_T^a, \mathcal{H}] = 0$ for all $a \in \{1 \dots N^2-1\}$, implying $[U,\mathcal{H}]=0$ (equivalently to Eq. (A.20)), so that the Heisenberg Hamiltonian has global SU(N) spin rotation symmetry.

A.5 Young tableaux

As mentioned in Sections 1.4.2, and 2.1, the set of states $\{f_{i,\sigma}^\dagger |0\rangle | \sigma \in \{1 \dots N\}\}$ form an N dimensional basis for the fundamental representation of SU(N), meaning that the spin operators are represented by the matrices $\langle 0| f_{j,\sigma} T_j^a f_{j,\sigma'}^\dagger |0\rangle = \frac{1}{2}\lambda_{\sigma,\sigma'}^a$ (see Eq. (2.3)), and the basis states transform under the fundamental representation as $T_j^a f_{j,\sigma}^\dagger |0\rangle = \sum_{\sigma'=1}^{N} \frac{1}{2}\lambda_{\sigma',\sigma}^a f_{j,\sigma'}^\dagger |0\rangle$ (see Eq. (2.4)).

If we take the product of r such states on some sites $j_1, j_2 \dots j_r$, we get a multiparticle wavefunction $f_{j_1,\sigma_1}^\dagger f_{j_2,\sigma_2}^\dagger \dots f_{j_r,\sigma_r}^\dagger |0\rangle$. The set of these states for $\sigma_1, \sigma_2 \dots \sigma_r \in \{1 \dots N\}$ forms an N^r dimensional basis for a reducible representation of the su(N) Lie algebra. In this reducible representation, the total SU(N) spin operators $\sum_{j=1}^r T_j^a$ are represented by $N^r \times N^r$ matrices, with the matrix elements given by

$$\langle 0| f_{l_1,\rho_1} f_{l_2,\rho_2} \dots f_{l_r,\rho_r} \left(\sum_{j=1}^{r} T_j^a \right) f_{j_1,\sigma_1}^\dagger f_{j_2,\sigma_2}^\dagger \dots f_{j_r,\sigma_r}^\dagger |0\rangle. \tag{A.27}$$

These matrices can be simultaneously block diagonalized by a basis transformation, decomposing the reducible representation to a direct sum of irreducible representations. Such a basis transformation means taking the linear combinations of the r-particle product states as

$$|\psi^i\rangle \equiv \sum_{\sigma_1,\sigma_2,\ldots\sigma_r=1}^{N} \psi^i_{\sigma_1,\sigma_2,\ldots\sigma_r} f^\dagger_{j_1,\sigma_1} f^\dagger_{j_2,\sigma_2} \ldots f^\dagger_{j_r,\sigma_r}|0\rangle, \tag{A.28}$$

where $i \in \{1 \ldots N^r\}$. As claimed in the books [107, Sec. IV.4] and [109, Sec. 8.4], we get a decomposition to irreducible representations, if we symmetrize or antisymmetrize in every flavor index σ. In the su(2) case, constructing all symmetrized or antisymmetrized multiparticle wavefunctions reproduces the basis states of any irrep appearing in the Clebsh-Gordon decomposition.

The simplest example is the product of two particles $f^\dagger_{j_1,\sigma_1} f^\dagger_{j_2,\sigma_2}|0\rangle$, which can be antisymmetrized as $\frac{1}{\sqrt{2}}(f^\dagger_{j_1,\sigma_1} f^\dagger_{j_2,\sigma_2} - f^\dagger_{j_1,\sigma_2} f^\dagger_{j_2,\sigma_1})|0\rangle$ or symmetrized as $\frac{1}{\sqrt{2}}(f^\dagger_{j_1,\sigma_1} f^\dagger_{j_2,\sigma_2} + f^\dagger_{j_1,\sigma_2} f^\dagger_{j_2,\sigma_1})|0\rangle$. In the su(2) case, where both $\sigma_1, \sigma_2 \in \{1, 2\}$, antisymmetrization gives $|\psi^1\rangle \equiv \frac{1}{\sqrt{2}}(f^\dagger_{j_1,1} f^\dagger_{j_2,2} - f^\dagger_{j_1,2} f^\dagger_{j_2,1})|0\rangle$ (usually denoted as $1/\sqrt{2}(|\uparrow\downarrow\rangle - |\downarrow\uparrow\rangle)$), which is the one-dimensional basis of the $s = 0$ singlet irrep, while symmetrization yields the three states $|\psi^2\rangle \equiv f^\dagger_{j_1,1} f^\dagger_{j_2,1}|0\rangle$, $|\psi^3\rangle \equiv \frac{1}{\sqrt{2}}(f^\dagger_{j_1,1} f^\dagger_{j_2,2} + f^\dagger_{j_1,2} f^\dagger_{j_2,1})|0\rangle$, and $|\psi^4\rangle \equiv f^\dagger_{j_1,2} f^\dagger_{j_2,2}|0\rangle$ (usually denoted as $|\uparrow\uparrow\rangle$, $1/\sqrt{2}(|\uparrow\downarrow\rangle + |\downarrow\uparrow\rangle)$, and $|\downarrow\downarrow\rangle$), forming the three-dimensional basis for the $s = 1$ triplet irrep. The sets $\{|\psi^1\rangle\}$ and $\{|\psi^2\rangle, |\psi^3\rangle, |\psi^4\rangle\}$ transform separately under the action of the spin operators S^x, S^y, and S^z. Thus, the 4×4 matrices representing the spin operators in the basis of product states are block diagonalized to 1×1 and 3×3 blocks in the basis of $\{|\psi^1\rangle, |\psi^2\rangle, |\psi^3\rangle, |\psi^4\rangle\}$. The set of 1×1 block matrices form the singlet irrep and the set of 3×3 block matrices form triplet irrep. The sites j_1 and j_2 are arbitrary for the singlet, but $j_1 \neq j_2$ for the two triplet irrep.

In the su(3) case, $\sigma_1, \sigma_2 \in \{1, 2, 3\}$, so we get multiple states even after the antisymmetrization of two-particle wavefunctions, since we have $|\psi^1\rangle \equiv \frac{1}{\sqrt{2}}(f^\dagger_{j_1,1} f^\dagger_{j_2,2} - f^\dagger_{j_1,2} f^\dagger_{j_2,1})|0\rangle$, $|\psi^2\rangle \equiv \frac{1}{\sqrt{2}}(f^\dagger_{j_1,2} f^\dagger_{j_2,3} - f^\dagger_{j_1,3} f^\dagger_{j_2,2})|0\rangle$, and $|\psi^3\rangle \equiv \frac{1}{\sqrt{2}}(f^\dagger_{j_1,1} f^\dagger_{j_2,3} - f^\dagger_{j_1,3} f^\dagger_{j_2,1})|0\rangle$. To form a basis for the su(3) singlet, we have to antisymmetrize a 3-particle wavefunction as $(f^\dagger_{j_1,1} f^\dagger_{j_2,2} f^\dagger_{j_3,3} + f^\dagger_{j_1,3} f^\dagger_{j_2,1} f^\dagger_{j_3,2} + f^\dagger_{j_1,2} f^\dagger_{j_2,3} f^\dagger_{j_3,1} - f^\dagger_{j_1,3} f^\dagger_{j_2,2} f^\dagger_{j_3,1} - f^\dagger_{j_1,1} f^\dagger_{j_2,3} f^\dagger_{j_3,2} - f^\dagger_{j_1,2} f^\dagger_{j_2,1} f^\dagger_{j_3,3})|0\rangle$. Symmetrization of two-particle wavefunctions yields 6 independent linear combinations in the su(3) case, namely $f^\dagger_{j_1,1} f^\dagger_{j_2,1}|0\rangle$, $f^\dagger_{j_1,2} f^\dagger_{j_2,2}|0\rangle$, $f^\dagger_{j_1,3} f^\dagger_{j_2,3}|0\rangle$, $(f^\dagger_{j_1,2} f^\dagger_{j_2,1} + f^\dagger_{j_1,1} f^\dagger_{j_2,2})|0\rangle$, $(f^\dagger_{j_1,3} f^\dagger_{j_2,1} + f^\dagger_{j_1,1} f^\dagger_{j_2,3})|0\rangle$, and $(f^\dagger_{j_1,2} f^\dagger_{j_2,3} + f^\dagger_{j_1,3} f^\dagger_{j_2,2})|0\rangle$, the set of which form the six-dimensional basis for an irreducible representation of su(3).

In the case of su(N), to form a basis for the su(N) singlet representation, we have to antismmetrize an N particle wavefunction. We can not antisymmetrize more then N particles because we get 0, but we can symmetrize any number of particles. We can antisymmetrize subsets of a $2N$ particle wavefunction, so that we antisymmetrize in two subsets of N particles, which also forms a one-dimensional basis for the su(N) singlet representation (an example of this being the decoupled David star in chapter 3).

Hybrid symmetrization and antisymmetrization procedures are also possible, for example, we can symmetrize first in the first two flavors σ_1 and σ_2, and then antisymmetrize in the flavors σ_1 and σ_3 (which will destroy the symmetric feature in σ_1 and σ_2). In the su(3) case, the set of these hybrid three-particle wavefunctions forms a basis for the adjoint irreducible representation.

Due to the connection of the SU(N) group and the su(N) Lie algebra in Eq. (A.9), the set of states forming a basis for a given irrep of the su(N) Lie algebra also forms a basis for the same irrep of the SU(N) group. In general, the basis for every irreducible representation of the su(N) Lie algebra and the SU(N) group can be constructed by multiparticle wavefunctions.

In the books [107, Sec. IV.4] and [109, Sec. 8.4], the basis of each irreducible representation is formed by tensors. These tensors can have many upper and lower indices. Depending on

the convention, a tensor of r lower indices and no upper indices is equivalent to an r particle wavefunction. Antisymmetrizing $N-1$ lower indices is equivalent to introducing an upper index, therefore any tensor can be rewritten only with lower indices, and is thus equivalent to a multiparticle wavefunction. Antisymmetrizing $N-1$ particles on the same lattice site can be thought of as a hole, so that on the same site the upper indices can be analogies of the holes. However, we can also antisymmetrize $N-1$ particles residing on different sites, so we can have upper indices which are not analogs of holes. For the sake of clarity, we will not talk about tensors with upper and lower indices, only multiparticle wavefunctions.

A.5.1 Young tableau: a pictorial representation of symmetrization and antisymmetrization

In the following subsections, we follow section 8.4 of the book [109]. Every flavor index σ of the multiparticle wavefunction corresponds to a box, so the number of boxes is equal to the number of particles. The r boxes of the r particle wavefunction are arranged in a way to represent the symmetrization and antisymmetrization procedure of the σ indices, what we call a Young tableau (the Young tableaux is the plural). For the boxes in the same row the corresponding σ indices are symmetrized, while for the boxes in the same column the σ indices are antisymmetrized. We can not antisymmetrize more than N indices, therefore we can not have more than N boxes in a column. A single column of N boxes corresponds to the completely antisymmetric wavefunction, forming a one-dimensional basis for the SU(N) singlet irrep. All the rows must be arranged to the left, and every row must have less or equal number of boxes than the row on top of it.

We first label the boxes with the σ indices starting from the top row in increasing order to the right (as σ_1, $\sigma_2 \dots \sigma_l$), following with the second row (σ_{l+1}, $\sigma_{l+2} \dots \sigma_{l'}$)) and so on. Next, we symmetrize the multiparticle wavefunction in the indices of each row separately. Finally, we antisymmetrize the multiparticle wavefunction in the indices in the columns separately (which destroys the previous symmetrization).

A.5.2 Pictorial calculation of the dimension with a Young tableau

In this subsection, we follow section 8.4 (ii) of the book [109]. As already stated, the linear combinations of the elements of the r particle wavefunction form a basis for an irreducible representation. The number of linearly independent linear combinations is the dimension of the irreducible representation (it determines the sizes of the matrices representing the SU(N) spin operators in this irrep). The dimension can be written as a ratio of two numbers, which are both calculated from the Young tableau (for specific examples see Fig. A.1(a) and (b)). For this, we draw the shape of the Young tableau in both the numerator and the denominator, and we fill each box with one integer. In the denominator, the number in a given box is the number of boxes below it (in the same column) plus the number of boxes to the right of it (in the same row) plus 1 (see Fig. A.1(a) and (b)). In the numerator, we start from the leftmost box in the top row, and we write N in it. Next, we write integers in descending order in the boxes below it (so in the first column we will have the integers N, $N-1$, $N-2$ ... from top to bottom). Then, we fill the boxes in every row, starting from the leftmost box (which was already filled) to the right, and we write in integers in ascending order. The first row will contain the numbers N, $N+1$, $N+2 \dots$ from left to right. The second row will have $N-1$, N, $N+1, \dots$, the third row $N-2$, $N-1$, $N, \dots$ always in ascending order from left to right. Finally, the dimension of the irreducible representation is the product of all the numbers in the Young tableau of the numerator divided by the product of all the numbers in the Young tableau of the denominator.

(a) An example for the dimension of an irrep:

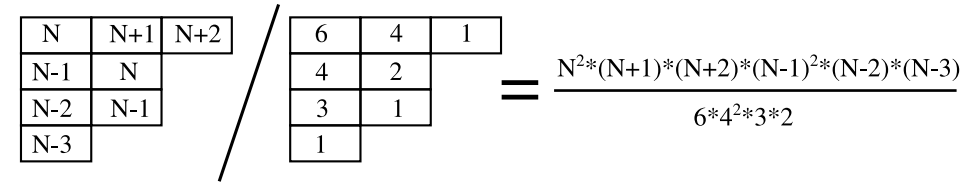

(b) The dimension of the adjoint representation:

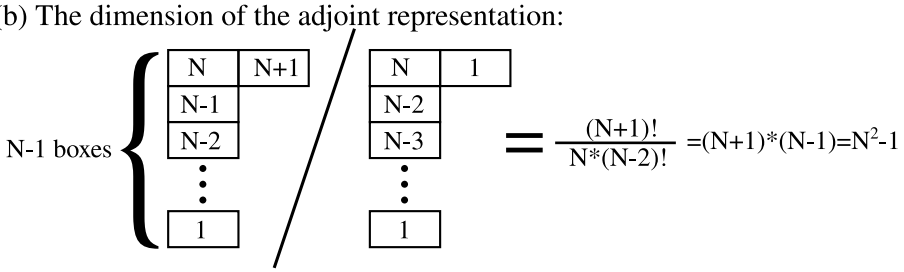

(c) The simplest decomposition to irreps:

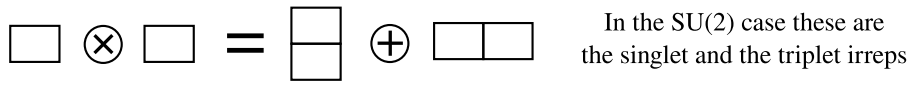

(d) Decomposition of the product of conjugate and fundamental irreps:

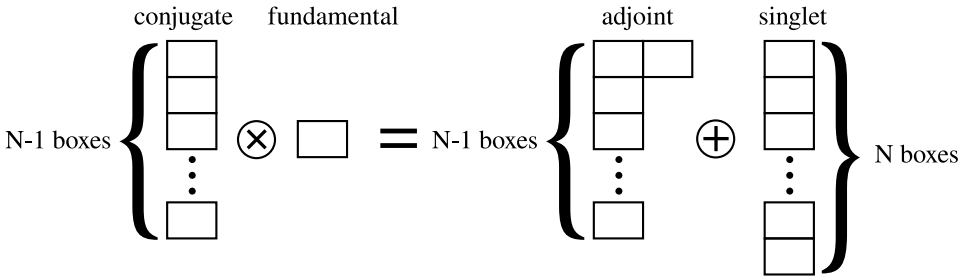

Figure A.1: (a) An example for the calculation of the dimension of an irrep, the basis for this irrep is formed by hybridly symmetrized and antisymmetrized eight-particle wavefunctions (rows show symmetrization, columns antisymmetrization). The rules for the calculation of the dimension are given in Appendix A.5.2
. (b) The Young tableau of the adjoint representation has a column of $N-1$ boxes and an additional box in the first row. Its dimension is N^2-1. (c) The direct product of the conjugate and fundamental irreps is reducible, therefore we can decompose it to a direct sum of irreps with a basis transformation (symmetrization and antisymmetrization). The irreps appearing in the decomposition can be constructed by adding the single box of the fundamental representation to the Young tableau of the conjugate representation in all possible ways. There are only two ways to do this while keeping a valid Young tableau, resulting in the singlet and the adjoint irreps.

A.5.3 Decomposition of a direct product of two Young tableaux

In this section, we follow section 8.4 (iii) of the book [109]. The direct product of two irreducible representations is reducible, so it can be decomposed into the direct sum of irreducible representations. In other words, if the r_1 particle wavefunctions $|\psi^i\rangle$ with $i \in \{1 \dots d_1\}$ form a d_1 dimensional basis for the first irreducible representation, and the r_2 particle wavefunctions $|\phi^j\rangle$ with $j \in \{1 \dots d_2\}$ form a d_2 dimensional basis for the second irreducible representation, then the $r_1 \times r_2$ particle wavefunctions $|\psi^i\rangle \otimes |\phi^j\rangle$ form a basis for the $d_1 \times d_2$ dimensional product representation, which is reducible. The decomposition to irreducible representations means a basis transformation (symmetrization or antisymmetrization), which simultaneously block diagonalizes every SU(N) spin operator. The symmetrized or antisymmetrized linear combinations transform separately under the action of the SU(N) spin operators, so that we can represent these linear combinations by Young tableaux too. There are rules for the decomposition of a direct product of two arbitrary Young tableau to a direct sum of Young tableaux, but these rules are quite complicated [109, Sec. 8.4 (iii)]. Here, we consider only a simple case, where the first Young tableau can be arbitrary, but the second is a single box forming a basis for the fundamental representation. In the decomposition to irreps, we get all possible Young tableaux which can be formed by adding a box to the first Young tableau. In the simplest case, both Young tableaux are single boxes. Then there are only two possibilities: we either antisymmetrize or symmetrize these two indices, resulting in a single column of two boxes or a single row of two boxes, respectively. In the case of SU(2), a box is a spin 1/2, antisymmetrization leads to the singlet irrep (a column of two boxes) while symmetrization to the triplet irrep (a row of two boxes), as shown in Fig. A.1(c). Another simple but important example is, when the first Young tableau is a column of $N-1$ boxes (conjugate irrep), and the second is a single box (fundamental irrep). In this case, there are only two possibilities to add a new box: we either add it to the bottom, getting a column of N boxes (singlet irrep), or we add it to the first row (adjoint irrep). We can not add the box to any other row than the first because in a legal Young tableau any row must have less or equal number of boxes than the row about it. Both the conjugate and the fundamental representation are N dimensional, so their direct product is $N \times N = N^2$ dimensional, matching the sum of the dimensions of the one-dimensional singlet representation and the $N^2 - 1$ dimensional adjoint representation (see Figs. A.1(b) and (d)), appearing in the decomposition.

A.6 Other irreducible representations of SU(N)

As stated in Appendices A.2 and A.3 the number of generators of the su(N) Lie algebra is always $N^2 - 1$, but the size of the matrices varies among different irreducible representations (irreps). The size of these matrices corresponds to the dimension of the Young tableau of the given irrep. In the case of the fundamental irrep, the Young tableau is a single box, meaning that the basis of this irrep is N dimensional, so the generators are represented by $N \times N$ matrices. Thinking in terms of the repulsive SU(N) Hubbard model in the $U/t \to \infty$ limit, the fundamental representation of the Heisenberg model emerges from the $1/N$ filling of the Hubbard model (with one fermion per site on average).

A.6.1 The conjugate representation

The conjugate representation has the same dimensionality N and the same eigenvalue of the quadratic Casimir operator (A.15) as the fundamental representation, but its Young tableau is a column of $N-1$ boxes, instead of a single box. Thinking in terms of the repulsive SU(N) Hubbard model in the $U/t \to \infty$ limit, the conjugate representation emerges from the $(N-1)/N$ filling corresponding to $N-1$ fermions per site (as having one hole at every site on average). In

the SU(2) case, the two representations are the same since one fermion per site is the same as one hole per site.

A.6.2 The self-conjugate representation

Another frequently used irrep in the literature is the self-conjugate representation of su(N) represented by a Young tableau of a column of $N/2$ boxes (self-conjugate because $N - N/2$ boxes give the same). Therefore, this irrep exists only for even N. In terms of the repulsive Hubbard model, it emerges from the half-filled case, with $N/2$ fermions per site on average. The one-dimensional basis of the SU(N) singlet is formed by the antisymmetrization of N fermions (a column of N boxes in the Young tableau). Therefore, the basis function of the singlet irrep can be formed by combining two lattice sites with the basis functions of the self-conjugate representation (forming a dimer) for any N, since the decomposition of the product of two identical Young tableaux with a column of $N/2$ boxes will contain a Young tableau of a column with N boxes. In contrast, for the formation of a basis function of an SU(N) singlet from the basis functions of the fundamental representation we have to combine N singly occupied sites since we have to take the product of N single boxes, to be able to construct a column of N boxes. For this reason, people frequently use it in the SU(N) expansion because it is possible to form a basis for the SU(N) singlet with two sites only for any N.

A.6.3 The adjoint representation

The adjoint representation is $N^2 - 1$ dimensional and is represented by a Young tableau shown in Fig. A.1(b). In the following, we will show that the matrices representing the total SU(N) spin operators $T^a_{\mathrm{T}} \equiv \sum_{j=1}^{N_s} T^a_j$ in this irrep are given by the structure constants of Eq. (1.19) as $\lambda^a_{b,c} = -if_{abc}$ (see "The adjoint representation of $SU(N)$" in [107, Sec. IV.4]). As we will show, the $(N^2-1)\times(N^2-1)$ matrices $\lambda^a_{b,c}$ are written in the basis of states $\{T^1_{\mathbf{k}}|\mathrm{GS}\rangle, T^2_{\mathbf{k}}|\mathrm{GS}\rangle \dots T^{N^2-1}_{\mathbf{k}}|\mathrm{GS}\rangle\}$, where $T^a_{\mathbf{k}} \equiv \frac{1}{\sqrt{N_s}}\sum_{\mathbf{R},s} e^{i\mathbf{k}\cdot(\mathbf{R}+\boldsymbol{\delta}_s)} T^a_{\mathbf{R},s}$ from Eq. (4.2), and the ground state $|\mathrm{GS}\rangle$ of the antiferromagnetic SU(N) Heisenberg model is supposed to transform as an SU(N) singlet, implying $T^a_{\mathrm{T}}|\mathrm{GS}\rangle = 0$ for any $a \in \{1 \dots N^2-1\}$. In the literature it is common to say that the states $T^a_{\mathbf{k}}|\mathrm{GS}\rangle$ transform under the adjoint representation, or that they belong to the adjoint representation. The adjoint transformation is significant for the calculation of the spectral weights $|\langle f|T^a_{\mathbf{k}}|\mathrm{GS}\rangle|^2$ in the dynamical spin structure factor of Eq. (4.5), as discussed in section 4.3.4.

First, let us calculate the commutator $[T^a_{\mathrm{T}}, T^b_{\mathbf{k}}]$, where we will use that $T^a_{\mathrm{T}} = \sum_{j=1}^{N_s} T^a_j = T^a_{\mathbf{k}=\mathbf{0}}$ as

$$[T^a_{\mathrm{T}}, T^b_{\mathbf{k}}] = [T^a_{\mathbf{0}}, T^b_{\mathbf{k}}] = \sum_{\mathbf{R},\bar{\mathbf{R}},s\bar{s}} e^{i\mathbf{0}\cdot(\mathbf{R}+\boldsymbol{\delta}_s)} e^{i\mathbf{k}\cdot(\mathbf{R}+\boldsymbol{\delta}_s)} [T^a_{\mathbf{R},s}, T^b_{\bar{\mathbf{R}},\bar{s}}] \tag{A.29}$$

$$= \sum_{\mathbf{R},\bar{\mathbf{R}},s\bar{s}} e^{i\mathbf{k}\cdot(\mathbf{R}+\boldsymbol{\delta}_s)} \delta_{\mathbf{R},\bar{\mathbf{R}}}\delta_{s,\bar{s}} i \sum_{c=1}^{N^2-1} f_{a,b,c} T^c_{\mathbf{R},s} \tag{A.30}$$

$$= i\sum_{c=1}^{N^2-1} f_{a,b,c} \sum_{\mathbf{R},s} e^{i\mathbf{k}\cdot(\mathbf{R}+\boldsymbol{\delta}_s)} T^c_{\mathbf{R},s} = i\sum_{c=1}^{N^2-1} f_{a,b,c} T^c_{\mathbf{k}}. \tag{A.31}$$

Using this commutator, we can calculate the action of the total SU(N) spin operators T^a_{T} on the basis states $\{T^1_{\mathbf{k}}|\mathrm{GS}\rangle, T^2_{\mathbf{k}}|\mathrm{GS}\rangle \dots T^{N^2-1}_{\mathbf{k}}|\mathrm{GS}\rangle\}$, as

$$T^a_{\mathrm{T}} T^b_{\mathbf{k}}|\mathrm{GS}\rangle = \underbrace{[T^a_{\mathrm{T}}, T^b_{\mathbf{k}}]}_{i\sum_c f_{abc} T^c_{\mathbf{k}}} |\mathrm{GS}\rangle + T^b_{\mathbf{k}} \underbrace{T^a_{\mathrm{T}}|\mathrm{GS}\rangle}_{0} = \sum_{c=1}^{N^2-1} \underbrace{if_{abc}}_{\Gamma^a_{c,b}} T^c_{\mathbf{k}}|\mathrm{GS}\rangle = \sum_{c=1}^{N^2-1} \Gamma^a_{c,b} T^c_{\mathbf{k}}|\mathrm{GS}\rangle \tag{A.32}$$

The above equation shows, that in the basis of states $\{T^1_{\mathbf{k}}|\mathrm{GS}\rangle, T^2_{\mathbf{k}}|\mathrm{GS}\rangle \dots T^{N^2-1}_{\mathbf{k}}|\mathrm{GS}\rangle\}$ the T^a_{T} is represented by the matrix Γ^a having matrix elements $\Gamma^a_{c,b} \equiv i f_{a,b,c}$. From now on, let us abbreviate the basis states as $|a\rangle \equiv T^a_{\mathbf{k}}|\mathrm{GS}\rangle$, so Eq. (A.32) simplifies to

$$T^a_{\mathrm{T}}|b\rangle = i \sum_{c=1}^{N^2-1} f_{abc}|c\rangle = \sum_{c=1}^{N^2-1} \Gamma^a_{c,b}|c\rangle. \tag{A.33}$$

As we will show below, the Γ^a matrices represent the total SU(N) spin operators T^a_{T} in the adjoint irreducible representation. Thus, the above equation shows that the states $|b\rangle \equiv T^b_{\mathbf{k}}|\mathrm{GS}\rangle$ transform under the action of the total SU(N) spin operators T^a_{T} as the adjoint irrep, since the action of T^a_{T} is equal to the multiplication with the matrix Γ^a. In the literature, this is often abbreviated as the states $T^b_{\mathbf{k}}|\mathrm{GS}\rangle$ transform under the adjoint irreducible representation.

We can derive the commutation relations of these Γ matrices from the commutation relations of the T^a_{T}, since

$$\begin{aligned}
[T^a_{\mathrm{T}}, T^b_{\mathrm{T}}]|c\rangle &= T^a_{\mathrm{T}} \sum_{d=1}^{N^2-1} \Gamma^b_{d,c}|d\rangle - T^b_{\mathrm{T}} \sum_{d=1}^{N^2-1} \Gamma^a_{d,c}|d\rangle \\
&= \sum_{d=1}^{N^2-1} \Gamma^b_{d,c} \sum_{e=1}^{N^2-1} \Gamma^a_{e,d}|e\rangle - \sum_{d=1}^{N^2-1} \Gamma^a_{d,c} \sum_{e=1}^{N^2-1} \Gamma^b_{e,d}|e\rangle \qquad \text{(A.34)} \\
&= \sum_{e=1}^{N^2-1} [\Gamma^a, \Gamma^b]_{e,c}|e\rangle \qquad \text{(A.35)} \\
&= i \sum_{d=1}^{N^2-1} f_{a,b,d} T^d_{\mathrm{T}}|c\rangle = i \sum_{d=1}^{N^2-1} f_{a,b,d} \sum_{e=1}^{N^2-1} \Gamma^d_{e,c}|e\rangle, \qquad \text{(A.36)}
\end{aligned}$$

where in the last row we used the Lie algebra $[T^a_{\mathrm{T}}, T^b_{\mathrm{T}}] = i \sum_{d=1}^{N^2-1} f_{a,b,d} T^d_{\mathrm{T}}$. Comparing the third and the fourth rows above, we get

$$[\Gamma^a, \Gamma^b]_{e,c} = i \sum_{d=1}^{N^2-1} f_{a,b,d} \Gamma^d_{e,c}, \tag{A.37}$$

showing that the Γ^a matrices satisfy the same commutation relations as the T^a_{T}, so the set of Γ^a matrices forms a representation of the su(N) Lie algebra. The number of basis states $T^a_{\mathbf{k}}|\mathrm{GS}\rangle$ is equal to the number of generators $N^2 - 1$, so the Γ^a are $(N^2 - 1) \times (N^2 - 1)$ matrices and the dimension of this representation is $d = N^2 - 1$. These matrices form the adjoint irreducible representation of su(N) [107, Sec. IV.4].

A.6.3.1 Particle-hole excitations

Similarly, a basis for the adjoint representation can also be formed by the following linear combinations of real-space-particle-hole excitations
$\{\sum_{\sigma,\bar{\sigma}=1}^{N} \lambda^a_{\sigma,\bar{\sigma}} f^\dagger_{\mathbf{R}+\mathbf{R}',s,\sigma} f_{\mathbf{R}',\bar{s},\bar{\sigma}}|\pi\mathrm{FS}\rangle | a \in \{1 \dots N^2 - 1\}\}$, where the $\lambda^a_{\sigma,\bar{\sigma}}$ are $N \times N$ matrices representing the SU(N) spin operators in the fundamental representation (see Appendix A.3). To show this, we will follow the same steps as for the states $T^1_{\mathbf{k}}|\mathrm{GS}\rangle$, since $|\pi\mathrm{FS}\rangle$ is also an SU(N) singlet.

First, using $T^a_{\rm T} \equiv \sum_{\tilde{\mathbf{R}},\tilde{s}} T^a_{\tilde{\mathbf{R}},\tilde{s}} = \frac{1}{2}\sum_{\tilde{\mathbf{R}},\tilde{s}}\sum_{\rho,\rho'=1}^{N} f^\dagger_{\tilde{\mathbf{R}},\tilde{s},\rho}\lambda^a_{\rho,\rho'} f_{\tilde{\mathbf{R}},\tilde{s},\rho'}$, we calculate the commutator

$$\begin{aligned}
\left[T^a_{\rm T}, \sum_{\sigma,\sigma'=1}^{N} \lambda^b_{\sigma,\sigma'} f^\dagger_{\mathbf{R}+\mathbf{R}',s,\sigma} f_{\mathbf{R}',s',\sigma'}\right] &= \left[\frac{1}{2}\sum_{\tilde{\mathbf{R}},\tilde{s}}\sum_{\rho,\rho'=1}^{N} f^\dagger_{\tilde{\mathbf{R}},\tilde{s},\rho}\lambda^a_{\rho,\rho'} f_{\tilde{\mathbf{R}},\tilde{s},\rho'}, \sum_{\sigma,\sigma'=1}^{N} \lambda^b_{\sigma,\sigma'} f^\dagger_{\mathbf{R}+\mathbf{R}',s,\sigma} f_{\mathbf{R}',s',\sigma'}\right] \\
&= \frac{1}{2}\sum_{\tilde{\mathbf{R}},\tilde{s}}\sum_{\rho,\rho'=1}^{N}\sum_{\sigma,\sigma'=1}^{N} \lambda^a_{\rho,\rho'}\lambda^b_{\sigma,\sigma'}\left[f^\dagger_{\tilde{\mathbf{R}},\tilde{s},\rho} f_{\tilde{\mathbf{R}},\tilde{s},\rho'}, f^\dagger_{\mathbf{R}+\mathbf{R}',s,\sigma} f_{\mathbf{R}',s',\sigma'}\right] \\
= \frac{1}{2}\sum_{\tilde{\mathbf{R}},\tilde{s}}\sum_{\rho,\rho'=1}^{N}\sum_{\sigma,\sigma'=1}^{N} \lambda^a_{\rho,\rho'}\lambda^b_{\sigma,\sigma'}&\left(\delta_{\tilde{\mathbf{R}},\mathbf{R}+\mathbf{R}'}\delta_{\tilde{s},s}\delta_{\sigma,\rho'} f^\dagger_{\tilde{\mathbf{R}},\tilde{s},\rho} f_{\mathbf{R}',s',\sigma'} - \delta_{\mathbf{R}',\tilde{\mathbf{R}}}\delta_{s',\tilde{s}}\delta_{\sigma',\rho} f^\dagger_{\mathbf{R}+\mathbf{R}',s,\sigma} f_{\tilde{\mathbf{R}},\tilde{s},\rho'}\right) \\
= \frac{1}{2}\sum_{\rho=1}^{N}\sum_{\sigma,\sigma'=1}^{N} \lambda^a_{\rho,\sigma}\lambda^b_{\sigma,\sigma'} f^\dagger_{\mathbf{R}+\mathbf{R}',s,\rho} f_{\mathbf{R}',s',\sigma'} &- \frac{1}{2}\sum_{\rho'=1}^{N}\sum_{\sigma,\sigma'=1}^{N} \lambda^b_{\sigma,\sigma'}\lambda^a_{\sigma',\rho'} f^\dagger_{\mathbf{R}+\mathbf{R}',s,\sigma} f_{\mathbf{R}',s',\rho'} \\
= \frac{1}{2}\sum_{\sigma,\sigma',\alpha=1}^{N} &\left(\lambda^a_{\sigma,\alpha}\lambda^b_{\alpha,\sigma'} f^\dagger_{\mathbf{R}+\mathbf{R}',s,\sigma} f_{\mathbf{R}',s',\sigma'} - \frac{1}{2}\lambda^b_{\sigma,\alpha}\lambda^a_{\alpha,\sigma'} f^\dagger_{\mathbf{R}+\mathbf{R}',s,\sigma} f_{\mathbf{R}',s',\sigma'}\right) \\
= \frac{1}{2}\sum_{\sigma,\sigma'=1}^{N} &\underbrace{\left(\sum_{\alpha=1}^{N}\lambda^a_{\sigma,\alpha}\lambda^b_{\alpha,\sigma'} - \lambda^b_{\sigma,\alpha}\lambda^a_{\alpha,\sigma'}\right)}_{2i\sum_{c=1}^{N^2-1} f_{abc}\lambda^c_{\sigma,\sigma'}} f^\dagger_{\mathbf{R}+\mathbf{R}',s,\sigma} f_{\mathbf{R}',s',\sigma'} \\
= i\sum_{c=1}^{N^2-1} f_{abc} &\sum_{\sigma,\sigma'=1}^{N} \lambda^c_{\sigma,\sigma'} f^\dagger_{\mathbf{R}+\mathbf{R}',s,\sigma} f_{\mathbf{R}',s',\sigma'},
\end{aligned} \tag{A.38}$$

where we used the commutation relation $\left[\frac{1}{2}\lambda^a, \frac{1}{2}\lambda^b\right] = i\sum_{c=1}^{N^2-1} f_{abc}\frac{1}{2}\lambda^c$ of Eq. (A.13). Using the above commutator we get

$$\begin{aligned}
T^a_{\rm T}\sum_{\sigma,\sigma'=1}^{N} \lambda^b_{\sigma,\sigma'} f^\dagger_{\mathbf{R}+\mathbf{R}',s,\sigma} f_{\mathbf{R}',s',\sigma'}|\pi{\rm FS}\rangle = &\underbrace{[T^a_{\rm T}, \sum_{\sigma,\sigma'=1}^{N} \lambda^b_{\sigma,\sigma'} f^\dagger_{\mathbf{R}+\mathbf{R}',s,\sigma} f_{\mathbf{R}',s',\sigma'}]}_{i\sum_{c=1}^{N^2-1} f_{abc}\sum_{\sigma,\sigma'=1}^{N}\lambda^c_{\sigma,\sigma'} f^\dagger_{\mathbf{R}+\mathbf{R}',s,\sigma} f_{\mathbf{R}',s',\sigma'}} |\pi{\rm FS}\rangle \\
&+ \sum_{\sigma,\sigma'=1}^{N} \lambda^b_{\sigma,\sigma'} f^\dagger_{\mathbf{R}+\mathbf{R}',s,\sigma} f_{\mathbf{R}',s',\sigma'} \underbrace{T^a_{\rm T}|\pi{\rm FS}\rangle}_{0} \\
= \sum_{c=1}^{N^2-1} &\underbrace{if_{abc}}_{\Gamma^a_{c,b}} \sum_{\sigma,\sigma'=1}^{N} \lambda^c_{\sigma,\sigma'} f^\dagger_{\mathbf{R}+\mathbf{R}',s,\sigma} f_{\mathbf{R}',s',\sigma'}|\pi{\rm FS}\rangle,
\end{aligned} \tag{A.39}$$

equivalently to Eqs. (A.32) and (A.33), from which Eqs. (A.36) and (A.37) follow the same way as in the previous section, so the basis states $|a\rangle \equiv \sum_{\sigma,\sigma'=1}^{N} \lambda^a_{\sigma,\sigma'} f^\dagger_{\mathbf{R}+\mathbf{R}',s,\sigma} f_{\mathbf{R}',s',\sigma'}$ form a basis for the $(N^2-1)\times(N^2-1)$ $\Gamma^a_{c,b} = if_{abc}$ matrices. In other words, the states $\sum_{\sigma,\sigma'=1}^{N} \lambda^a_{\sigma,\sigma'} f^\dagger_{\mathbf{R}+\mathbf{R}',s,\sigma} f_{\mathbf{R}',s',\sigma'}$ also transform under the adjoint irreducible representation.

Appendix B

Mean-field theory in the projective construction

Substituting the fermionic decomposition $T_i^a = \frac{1}{2}\sum_{\sigma,\sigma'=1}^{N} f_{i,\sigma}^\dagger \lambda_{\sigma,\sigma'}^a f_{i,\sigma'}$ of Eq. (2.2) into the Heisenberg Hamiltonian $\mathcal{H} = J\sum_{\langle i,j\rangle}\sum_{a=1}^{N^2-1} T_i^a T_j^a$ of Eq. (1.18) we get

$$\begin{aligned}\mathcal{H} &= J\sum_{\langle i,j\rangle}\sum_{a=1}^{N^2-1}\left(\frac{1}{2}\sum_{\alpha,\beta=1}^{N} f_{i,\alpha}^\dagger \lambda_{\alpha,\beta}^a f_{i,\beta}\right)\left(\frac{1}{2}\sum_{\gamma,\epsilon=1}^{N} f_{j,\gamma}^\dagger \lambda_{\gamma,\epsilon}^a f_{j,\epsilon}\right) \\ &= \frac{J}{4}\sum_{\langle i,j\rangle}\sum_{\alpha,\beta,\gamma,\epsilon=1}^{N}\left(\sum_{a=1}^{N^2-1}\lambda_{\alpha,\beta}^a\lambda_{\gamma,\epsilon}^a\right) f_{i,\alpha}^\dagger f_{i,\beta} f_{j,\gamma}^\dagger f_{j,\epsilon},\end{aligned} \tag{B.1}$$

which can be simplified using the relation [108]

$$\sum_{a=1}^{N^2-1}\lambda_{\alpha,\beta}^a\lambda_{\gamma,\epsilon}^a = 2\delta_{\alpha,\epsilon}\delta_{\beta,\gamma} - \frac{2}{N}\delta_{\alpha,\beta}\delta_{\gamma,\epsilon} \tag{B.2}$$

to

$$\begin{aligned}\mathcal{H} &= \frac{J}{2}\sum_{\langle i,j\rangle}\left(\sum_{\alpha,\beta=1}^{N} f_{i,\alpha}^\dagger f_{i,\beta} f_{j,\beta}^\dagger f_{j,\alpha} - \frac{1}{N}\sum_{\alpha,\beta=1}^{N} f_{i,\alpha}^\dagger f_{i,\alpha} f_{j,\beta}^\dagger f_{j,\beta}\right) \\ &= \frac{J}{2}\sum_{\langle i,j\rangle}\left[\sum_{\alpha,\beta=1}^{N}\left(f_{i,\alpha}^\dagger f_{i,\beta} f_{j,\beta}^\dagger f_{j,\alpha}\right) - \frac{1}{N}\right]\end{aligned} \tag{B.3}$$

where in the second step we used that $\sum_{\alpha,\beta=1}^{N} f_{i,\alpha}^\dagger f_{i,\alpha} f_{j,\beta}^\dagger f_{j,\beta} = n_i n_j = 1$, due to the single occupancy constraint of Eq. (2.5). It will be convenient to change the order of fermionic operators as $f_{i,\alpha}^\dagger f_{i,\beta} f_{j,\beta}^\dagger f_{j,\alpha} = f_{i,\alpha}^\dagger f_{i,\beta}\delta_{\alpha,\beta} - f_{i,\alpha}^\dagger f_{j,\alpha} f_{j,\beta}^\dagger f_{i,\beta}$, where again $\sum_{\alpha,\beta=1}^{N} f_{i,\alpha}^\dagger f_{i,\beta}\delta_{\alpha,\beta} = n_i = 1$. Taking out the minus sign, the Heisenberg Hamiltonian can be written as

$$\mathcal{H} = -\frac{J}{2}\sum_{\langle i,j\rangle}\left[\sum_{\alpha,\beta=1}^{N}\left(f_{i,\alpha}^\dagger f_{j,\alpha} f_{j,\beta}^\dagger f_{i,\beta}\right) + \frac{1}{N} - 1\right] \tag{B.4}$$

It is important to emphasize that Eq. (B.4) together with the single occupancy constraint $n_j = 1$ of Eq. (2.5), is an *exact* mapping of the Heisenberg Hamiltonian (1.18) to interacting fermions.

To obtain the mean-field approximation, let us first rewrite a pair of operators with their expectation value plus the fluctuation around the expectation value (in the hope that the fluctuation is much smaller than the expectation value) like $f_{i,\alpha}^\dagger f_{j,\alpha} = \langle f_{i,\alpha}^\dagger f_{j,\alpha}\rangle + \delta(f_{i,\alpha}^\dagger f_{j,\alpha})$ where the fluctuation is $\delta(f_{i,\alpha}^\dagger f_{j,\alpha}) \equiv f_{i,\alpha}^\dagger f_{j,\alpha} - \langle f_{i,\alpha}^\dagger f_{j,\alpha}\rangle$, and similarly $f_{j,\beta}^\dagger f_{i,\beta} = \langle f_{j,\beta}^\dagger f_{i,\beta}\rangle + \delta(f_{j,\beta}^\dagger f_{i,\beta})$.

Substituting these expressions into Eq. (B.4) we get

$$\begin{aligned}\mathcal{H} &= -\frac{J}{2}\sum_{\langle i,j\rangle}\Big(\sum_{\alpha,\beta=1}^{N}\Big[\langle f^\dagger_{i,\alpha}f_{j,\alpha}\rangle+\delta(f^\dagger_{i,\alpha}f_{j,\alpha})\Big]\Big[\langle f^\dagger_{j,\beta}f_{i,\beta}\rangle+\delta(f^\dagger_{j,\beta}f_{i,\beta})\Big]+\frac{1}{N}-1\Big)\\ &= -\frac{J}{2}\sum_{\langle i,j\rangle}\Big(\sum_{\alpha,\beta=1}^{N}\langle f^\dagger_{i,\alpha}f_{j,\alpha}\rangle\langle f^\dagger_{j,\beta}f_{i,\beta}\rangle+\langle f^\dagger_{i,\alpha}f_{j,\alpha}\rangle\delta(f^\dagger_{j,\beta}f_{i,\beta})+\delta(f^\dagger_{i,\alpha}f_{j,\alpha})\langle f^\dagger_{j,\beta}f_{i,\beta}\rangle\\ &\qquad+\delta(f^\dagger_{i,\alpha}f_{j,\alpha})\delta(f^\dagger_{j,\beta}f_{i,\beta})+\frac{1}{N}-1\Big),\end{aligned} \tag{B.5}$$

which is still an exact mapping of the Heisenberg Hamiltonian (1.18). The mean-field approximation is obtained by neglecting the second order term in the fluctuations $\delta(f^\dagger_{i,\alpha}f_{j,\alpha})\delta(f^\dagger_{j,\beta}f_{i,\beta})$, assuming that it is small, and taking all expectation values $\langle\dots\rangle=\langle\mathrm{FS}|\dots|\mathrm{FS}\rangle$ in the ground state $|\mathrm{FS}\rangle$ of the mean-field Hamiltonian. Dropping all constants, the mean-field Hamiltonian is

$$\mathcal{H}^{\mathrm{MF}} = -\frac{J}{2}\sum_{\langle i,j\rangle}\sum_{\alpha,\beta=1}^{N}\Big[\langle f^\dagger_{i,\alpha}f_{j,\alpha}\rangle\delta(f^\dagger_{j,\beta}f_{i,\beta})+\delta(f^\dagger_{i,\alpha}f_{j,\alpha})\langle f^\dagger_{j,\beta}f_{i,\beta}\rangle\Big] \tag{B.6}$$

$$\begin{aligned}&= -\frac{J}{2}\sum_{\langle i,j\rangle}\sum_{\alpha,\beta=1}^{N}\Big[\langle f^\dagger_{i,\alpha}f_{j,\alpha}\rangle f^\dagger_{j,\beta}f_{i,\beta}-\langle f^\dagger_{i,\alpha}f_{j,\alpha}\rangle\langle f^\dagger_{j,\beta}f_{i,\beta}\rangle\\ &\qquad+f^\dagger_{i,\alpha}f_{j,\alpha}\langle f^\dagger_{j,\beta}f_{i,\beta}\rangle-\langle f^\dagger_{i,\alpha}f_{j,\alpha}\rangle\langle f^\dagger_{j,\beta}f_{i,\beta}\rangle\Big].\end{aligned} \tag{B.7}$$

Leaving away the constants $\langle\dots\rangle\langle\dots\rangle$ gives us two terms, which are identical, up to an index change $\alpha\leftrightarrow\beta$, giving a factor of 2. The resulting Hamiltonian

$$\mathcal{H}^{\mathrm{MF}} = \sum_{\langle i,j\rangle}\sum_{\beta=1}^{N}\underbrace{\left(-J\sum_{\alpha=1}^{N}\langle f^\dagger_{i,\alpha}f_{j,\alpha}\rangle\right)}_{t_{i,j}}f^\dagger_{j,\beta}f_{i,\beta} \tag{B.8}$$

allows for the identification of the hoppings, as given in Eq. (2.7).

Appendix C

Sum rules

As we stated in Eqs. (6.2) and (6.3), the sum rules are different in the projected and the mean-field cases. This section shows how the charge fluctuations affect the sum rule in the mean-field case for a general SU(N) model in the fundamental representation. The sum rule is defined as

$$\begin{aligned}\sum_{\mathbf{k}\in\mathrm{eBZ}} S^{33}(\mathbf{k}) &= \sum_{\mathbf{k}\in\mathrm{eBZ}} \langle \mathrm{GS}|T^3_{-\mathbf{k}}T^3_{\mathbf{k}}|\mathrm{GS}\rangle \\ &= \sum_{\mathbf{k}\in\mathrm{eBZ}} \frac{1}{N_s}\sum_{\substack{\mathbf{R},s\\ \bar{\mathbf{R}},\bar{s}}} e^{-i\mathbf{k}\cdot(\mathbf{R}+\boldsymbol{\delta}_s-\bar{\mathbf{R}}-\boldsymbol{\delta}_{\bar{s}})}\langle \mathrm{GS}|T^3_{\mathbf{R},s}T^3_{\bar{\mathbf{R}},\bar{s}}|\mathrm{GS}\rangle,\end{aligned} \tag{C.1}$$

where we inserted the expression of Eq. (4.2). Using the relation

$$\sum_{\mathbf{k}\in\mathrm{eBZ}} e^{-i\mathbf{k}\cdot(\mathbf{R}+\boldsymbol{\delta}_s-\bar{\mathbf{R}}-\boldsymbol{\delta}_{\bar{s}})} = N_{\mathbf{k}}\delta_{\mathbf{R},\bar{\mathbf{R}}}\delta_{s,\bar{s}}, \tag{C.2}$$

where $N_{\mathbf{k}}$ is the number of wave vectors in the extended Brillouin zone, we get

$$\begin{aligned}\sum_{\mathbf{k}\in\mathrm{eBZ}} S^{33}(\mathbf{k}) &= \frac{N_{\mathbf{k}}}{N_s}\sum_{\mathbf{R},s}\langle \mathrm{GS}|T^3_{\mathbf{R},s}T^3_{\mathbf{R},s}|\mathrm{GS}\rangle \\ &= \frac{N_{\mathbf{k}}}{N_s}\sum_{\mathbf{R},s}\frac{1}{N^2-1}\sum_{a=1}^{N^2-1}\langle \mathrm{GS}|T^a_{\mathbf{R},s}T^a_{\mathbf{R},s}|\mathrm{GS}\rangle = \frac{N_{\mathbf{k}}}{N_s}\sum_{\mathbf{R},s}\frac{1}{N^2-1}\langle \mathrm{GS}|\hat{C}_{2,\mathbf{R},s}|\mathrm{GS}\rangle,\end{aligned} \tag{C.3}$$

where in the second row we assumed that the ground state does not break the SU(N) symmetry, so $\langle \mathrm{GS}|T^b_{\mathbf{R},s}T^b_{\mathbf{R},s}|\mathrm{GS}\rangle = \frac{1}{N^2-1}\sum_{a=1}^{N^2-1}\langle \mathrm{GS}|T^a_{\mathbf{R},s}T^a_{\mathbf{R},s}|\mathrm{GS}\rangle$ for every $b \in \{1\dots N^2-1\}$ (i.e., it transforms as an SU(N) singlet). The expression $\sum_{a=1}^{N^2-1} T^a_{\mathbf{R},s}T^a_{\mathbf{R},s}$ is the quadratic Casimir operator $\hat{C}_{2,\mathbf{R},s}$ of Eq. (1.21), so Eq. (C.3) is general and allows for different irreps on different sites. In case of the SU(N) Heisenberg model in the fundamental representation, $\mathrm{GS}|T^a_{\mathbf{R},s}T^a_{\mathbf{R},s}|\mathrm{GS}\rangle = (N^2-1)/2N$ on every site, as shown in Eq. (A.15). Thus, the sum rule of the Heisenberg model reads

$$\sum_{\mathbf{k}\in\mathrm{eBZ}} S^{33}(\mathbf{k}) = \frac{N_{\mathbf{k}}}{N_s}\sum_{\mathbf{R},s}\frac{1}{N^2-1}\langle \mathrm{GS}|\hat{C}_{2,\mathbf{R},s}|\mathrm{GS}\rangle = \frac{N_{\mathbf{k}}}{2N}. \tag{C.4}$$

As argued in the following section, we get the same sum rule, if we make the approximation $|\mathrm{GS}\rangle \approx P_{\mathrm{G}}|\mathrm{FS}\rangle$. As argued in Appendix H, $N_{\mathbf{k}} = \frac{3}{2}N_s$ for the honeycomb lattice, while $N_{\mathbf{k}} = \frac{4}{3}N_s$ for the kagome lattice.

C.1 Mean-field sum rule

In the case of the mean-field hopping Hamiltonian of Eq. (2.6), the value of the quadratic Casimir operator is reduced due to the charge fluctuations in $|\mathrm{FS}\rangle$. To calculate its precise value let us substitute the fermionic projective construction of the SU(N) spin operators (Eq. (2.2)) into the Casimir operator

$$\hat{C}_2 = \sum_{a=1}^{N^2-1} T^a T^a = \frac{1}{4}\sum_{a=1}^{N^2-1}\sum_{\substack{\alpha,\beta,\\ \gamma,\epsilon=1}}^{N} c^\dagger_\alpha \lambda^a_{\alpha,\beta} c_\beta c^\dagger_\gamma \lambda^a_{\gamma,\epsilon} c_\epsilon \tag{C.5}$$

where we omit the site indices for convenience. Using the completeness relation $\sum_{a=1}^{N^2-1} \lambda^a_{\alpha,\beta}\lambda^a_{\gamma,\epsilon} = 2\delta_{\alpha,\epsilon}\delta_{\beta,\gamma} - \frac{2}{N}\delta_{\alpha,\beta}\delta_{\gamma,\epsilon}$ of Eq. (B.2) we get

$$\sum_{a=1}^{N^2-1} T^a T^a = \sum_{\alpha,\gamma=1}^{N} \left(\frac{1}{2} c^\dagger_\alpha c_\gamma c^\dagger_\gamma c_\alpha - \frac{1}{2N} c^\dagger_\alpha c_\alpha c^\dagger_\gamma c_\gamma \right). \tag{C.6}$$

Rearranging the order of the fermionic operators results in

$$\hat{C}_{2,\mathbf{R},s} = \sum_{a=1}^{N^2-1} T^a_{\mathbf{R},s} T^a_{\mathbf{R},s} = \frac{N+1}{2} \mathrm{n}_{\mathbf{R},s} - \frac{N+1}{2N} \mathrm{n}^2_{\mathbf{R},s}, \tag{C.7}$$

where $\mathrm{n}_{\mathbf{R},s} \equiv \sum_{\sigma=1}^{N} c^\dagger_{\mathbf{R},s,\sigma} c_{\mathbf{R},s,\sigma}$ is the total fermion number operator on the site with lattice vector $\mathbf{r} = \mathbf{R} + \boldsymbol{\delta}_s$. The value of $\mathrm{n}_{\mathbf{R},s}$ determines the irreducible representation on a given site (see Appendices A.6 and A.5), so we get the eigenvalue of the quadratic Casimir operator of this irrep. On a singly occupied site ($\mathrm{n}_{\mathbf{R},s} = 1$), the quadratic Casimir operator takes on the same value $\frac{N^2-1}{2N}$ as in the fundamental representation of SU(N). This is not surprising, since the states $c^\dagger_{\mathbf{R},s,\sigma}|0\rangle$ form a basis for the fundamental representation. The Gutzwiller projector enforces single occupancy, so $\langle \mathrm{FS}|P_\mathrm{G}\hat{C}_{2,\mathbf{R},s}P_\mathrm{G}|\mathrm{FS}\rangle = \frac{N^2-1}{2N}$, and we get the same sum rule (C.4) as for the SU(N) Heisenberg model in the fundamental representation, just as we stated in Eq. (6.2).

However, to calculate the mean-field expectation value $\sum_{a=1}^{N^2-1}\langle \mathrm{FS}|T^a_{\mathbf{R},s}T^a_{\mathbf{R},s}|\mathrm{FS}\rangle$, we have to consider all the possible occupations with their probabilities. Consequently, the $|\mathrm{FS}\rangle$ without Gutzwiller projection mixes different irreducible representations, so that $|\mathrm{FS}\rangle$ is not an eigenstate of the Casimir operators. Since the fermions are uncorrelated in the mean-field approach (i.e., each flavor of fermions occupies a site independently of the other flavors), the probability that r fermions occupy a site is determined by the binomial distribution $P_\mathrm{binom}(r) = \binom{N}{r} p^r (1-p)^{N-r}$, where $p = 1/N$ is the probability that one of the flavors occupies this site. Thus

$$\begin{aligned} C^\mathrm{MF}_{2,\mathbf{R},s} &= \langle \mathrm{FS}|\hat{C}_{2,\mathbf{R},s}|\mathrm{FS}\rangle = \langle \mathrm{FS}| \left(\frac{N+1}{2} \mathrm{n}_{\mathbf{R},s} - \frac{N+1}{2N} \mathrm{n}^2_{\mathbf{R},s} \right) |\mathrm{FS}\rangle \\ &= \sum_{r=0}^{N} P_\mathrm{binom}(r) \left(\frac{N+1}{2} r - \frac{N+1}{2N} r^2 \right) \\ &= \left(\frac{N^2-1}{2N} \right) \left(1 - \frac{1}{N} \right), \end{aligned} \tag{C.8}$$

for any site with indeces $\mathbf{R}, s$. The above equation shows that the deviation from the proper value of the quadratic Casimir operator in the fundamental representation is a factor $1 - \frac{1}{N}$. We note that this is an average, as the probability of multiply occupied sites ($r > 1$) is non-zero even in the large-N limit, since the binomial distribution $P_\mathrm{binom}(r)$ approaches the Poisson distribution with parameter $\lambda = Np = 1$. Substituting the C^MF_2 from Eq. (C.8), to the general formula in Eq. (C.3) we get

$$\sum_{\mathbf{k}\in \mathrm{eBZ}} S^{33}_\mathrm{MF}(\mathbf{k}) = \frac{N_\mathbf{k}}{N_s} \sum_{\mathbf{R},s} \frac{1}{N^2-1} C^\mathrm{MF}_{2,\mathbf{R},s} = \frac{N_\mathbf{k}}{2N} \left(1 - \frac{1}{N} \right), \tag{C.9}$$

just as stated in Eq. (6.3).

Appendix D

Relation between the ground states of gauge equivalent mean-field Hamiltonians

In this appendix, we prove that if we take two gauge equivalent (2.33) Hamiltonians

$$\mathcal{H}_2^{\mathrm{MF}} = G\mathcal{H}_1^{\mathrm{MF}}G^{-1}, \tag{D.1}$$

which are further related by some invertible operator $\mathcal{O}$ as

$$\mathcal{H}_2^{\mathrm{MF}} = \mathcal{O}\mathcal{H}_1^{\mathrm{MF}}\mathcal{O}^{-1}, \tag{D.2}$$

then their ground states $|\mathrm{FS}_1\rangle$ and $|\mathrm{FS}_2\rangle$ are related as

$$|\mathrm{FS}_2\rangle = \mathcal{O}|\mathrm{FS}_1\rangle, \tag{D.3}$$

provided that both $|\mathrm{FS}_1\rangle$ and $|\mathrm{FS}_2\rangle$ are non-degenerate.

If $\mathcal{O} = G$, then Eqs. (D.1) and (D.2) are the same.

To prove Eq. (D.3), we start from the two eigenvalue equations

$$\mathcal{H}_1^{\mathrm{MF}}|\mathrm{FS}_1\rangle = E_{\mathrm{FS},1}^{\mathrm{MF}}|\mathrm{FS}_1\rangle \tag{D.4}$$

and

$$\mathcal{H}_2^{\mathrm{MF}}|\mathrm{FS}_2\rangle = E_{\mathrm{FS},2}^{\mathrm{MF}}|\mathrm{FS}_2\rangle. \tag{D.5}$$

We can use Eq. (D.2) as

$$\begin{aligned} \mathcal{H}_2^{\mathrm{MF}}|\mathrm{FS}_2\rangle = \mathcal{O}\mathcal{H}_1^{\mathrm{MF}}\mathcal{O}^{-1}|\mathrm{FS}_2\rangle = E_{\mathrm{FS},2}^{\mathrm{MF}}|\mathrm{FS}_2\rangle \\ \mathcal{H}_1^{\mathrm{MF}}\mathcal{O}^{-1}|\mathrm{FS}_2\rangle = E_{\mathrm{FS},2}^{\mathrm{MF}}\mathcal{O}^{-1}|\mathrm{FS}_2\rangle \end{aligned} \tag{D.6}$$

where in the second row we multiplied from the left with $\mathcal{O}^{-1}$. If we showed that $E_{\mathrm{FS},1}^{\mathrm{MF}} = E_{\mathrm{FS},2}^{\mathrm{MF}}$, then comparing the last equation above with the eigenvalue equation (D.4), the non-degeneracy of $|\mathrm{FS}_1\rangle$ would imply that $|\mathrm{FS}_2\rangle = \mathcal{O}^{-1}|\mathrm{FS}_2\rangle$. To prove $E_{\mathrm{FS},1}^{\mathrm{MF}} = E_{\mathrm{FS},2}^{\mathrm{MF}}$, it is enough to show that the one-particle energy spectra of the gauge equivalent $\mathcal{H}_1^{\mathrm{MF}}$ and $\mathcal{H}_2^{\mathrm{MF}}$ are the same (which is shown in Eq. (2.34)), since the mean-field ground state energy is just the sum of the one-particle energies below the Fermi energy ε_{F}.

Appendix E

Gauge transformations for projective symmetries

The projective symmetry $\mathcal{H}^{\mathrm{MF}} = G_{\mathsf{g}}\mathsf{g}\mathcal{H}^{\mathrm{MF}}\mathsf{g}^{-1}G_{\mathsf{g}}^{-1}$ of Eq. (2.32) can be rewritten for the hopping Hamiltonian (2.6) as

$$\sum_{\langle a,b\rangle}\sum_{\sigma=1}^{N} t_{a,b} f^{\dagger}_{a,\sigma} f_{b,\sigma} = \sum_{\langle i,j\rangle}\sum_{\sigma=1}^{N} t_{i,j} G_{\mathsf{g}}\mathsf{g} f^{\dagger}_{i,\sigma} f_{j,\sigma}\mathsf{g}^{-1}G_{\mathsf{g}}^{-1} \tag{E.1}$$

$$= \sum_{\langle i,j\rangle}\sum_{\sigma=1}^{N} t_{i,j} G_{\mathsf{g}}\mathsf{g} f^{\dagger}_{i,\sigma}\mathsf{g}^{-1}G_{\mathsf{g}}^{-1} G_{\mathsf{g}}\mathsf{g} f_{j,\sigma}\mathsf{g}^{-1}G_{\mathsf{g}}^{-1}$$

$$= \sum_{\langle i,j\rangle}\sum_{\sigma=1}^{N} t_{i,j} G_{\mathsf{g}} f^{\dagger}_{\mathsf{g}(i),\sigma} G_{\mathsf{g}}^{-1} G_{\mathsf{g}} f_{\mathsf{g}(j),\sigma} G_{\mathsf{g}}^{-1}$$

$$= \sum_{\langle i,j\rangle}\sum_{\sigma=1}^{N} t_{i,j} e^{i\phi_{\mathsf{g}}(\mathsf{g}(i))} f^{\dagger}_{\mathsf{g}(i),\sigma} f_{\mathsf{g}(j),\sigma} e^{-i\phi_{\mathsf{g}}(\mathsf{g}(j))} \tag{E.2}$$

Since the coefficients of a given pair of fermionic operators

$$f^{\dagger}_{a,\sigma} f_{b,\sigma}$$

must be equal, there must be a nearest neighbor pair of sites $\langle a,b\rangle = \langle \mathsf{g}(i), \mathsf{g}(j)\rangle$, for which

$$\begin{aligned} t_{a,b} f^{\dagger}_{a,\sigma} f_{b,\sigma} &= t_{i,j} e^{i\phi_{\mathsf{g}}(\mathsf{g}(i))} f^{\dagger}_{\mathsf{g}(i),\sigma} f_{\mathsf{g}(j),\sigma} e^{-i\phi_{\mathsf{g}}(\mathsf{g}(j))} \\ t_{a,b} f^{\dagger}_{a,\sigma} f_{b,\sigma} &= t_{\mathsf{g}^{-1}(a),\mathsf{g}^{-1}(b)} e^{i\phi_{\mathsf{g}}(a)} f^{\dagger}_{a,\sigma} f_{b,\sigma} e^{-i\phi_{\mathsf{g}}(b)} \\ e^{-i\phi_{\mathsf{g}}(a)} t_{a,b} e^{i\phi_{\mathsf{g}}(b)} &= t_{\mathsf{g}^{-1}(a),\mathsf{g}^{-1}(b)}, \end{aligned} \tag{E.3}$$

where in the second row we relabeled the indices as $a = \mathsf{g}(i)$ and $b = \mathsf{g}(j)$. The meaning of Eq. (E.3) is that $\mathcal{H}^{\mathrm{MF}}$ is invariant under a combined transformation $G_{\mathsf{g}}\mathsf{g}$, if the effect of g on the hoppings can be reversed by the gauge phases. For real hoppings, the phases of the gauge transformations can also be chosen to be real as $e^{i\phi_{\mathsf{g}}(a)} = \pm 1 = e^{-i\phi_{\mathsf{g}}(a)}$, so we will call them gauge signs. These gauge signs can be transferred to the hoppings, so the gauge transformation $G f^{\dagger}_{a,\sigma} G^{-1} = -f^{\dagger}_{a,\sigma}$ changes the signs of the hoppings $t_{a,b}$ that are connected to site a. The gauge signs for the generators of the space group formed by the D_6 point group (C_6 and σ) and the elementary translations ($\mathsf{T}_{1,2}$), are shown in Fig. E.1, for both the honeycomb and the kagome lattices, supposing periodic boundary conditions (for APBC see Appendix E.2). We can figure them out easily in the following way. We start from an arbitrary lattice site a_{start} (in Fig. E.1 we started from sublattice A), and we choose not to change the sign of the fermionic operator $f^{\dagger}_{a_{start},\sigma}$, meaning that its gauge sign is set to $e^{i\phi_{\mathsf{g}}(a_{start})} = +1$ (this choice can be changed at the end by multiplying every $f^{\dagger}_{a,\sigma}$ with minus signs simultaneously). First, we look at the transformed hoppings $t_{a_{start},b}$ connected to site a_{start} and compare them with the original hoppings $t_{\mathsf{g}^{-1}(a_{start}),\mathsf{g}^{-1}(b)}$, which were not yet affected by g. If a hopping was changed ($t_{a_{start},b} \neq t_{\mathsf{g}^{-1}(a_{start}),\mathsf{g}^{-1}(b)}$), then the fermionic operator at site b must be multiplied with a minus sign as $e^{i\phi_{\mathsf{g}}(b)} = -1$, to reverse the change of the hopping as $e^{-i\phi_{\mathsf{g}}(a_{start})} t_{a_{start},b} e^{i\phi_{\mathsf{g}}(b)} =$

$-t_{a_{start},b} = t_{\mathsf{g}^{-1}(a_{start}),\mathsf{g}^{-1}(b)}$. This way we can determine the gauge signs $e^{-i\phi_{\mathsf{g}}(b)}$ at the nearest neighbor sites b of a_{start}. Next, we repeat the same procedure for the nearest neighbor sites of b, and iterate it until we go through the entire cluster.

The label of the sites j can be changed to the Bravais lattice vector $\mathbf{R} = R_1\mathbf{a}_1 + R_2\mathbf{a}_2$ (specifying the unit cell of site j) and the sublattice index s. In the case of the honeycomb lattice, the gauge signs can be reformulated as $e^{i\phi_{\mathsf{C}_6}(\mathbf{R},s)} = (-1)^{\xi_s}$, $e^{i\phi_{\mathsf{T}_1}(\mathbf{R},s)} = (-1)^{R_1+\xi_s}$, $e^{i\phi_{\mathsf{T}_2}(\mathbf{R},s)} = (-1)^{R_1+R_2+\xi_s}$, and $e^{i\phi_{\sigma}(\mathbf{R},s)} = (-1)^{\xi_s(R_2+1)+(R_1+1)R_2}$, where $s \in \{A,B\}$, $\xi_A = 0$, and $\xi_B = 1$. The gauge signs of the translations can also be given with the plane waves $e^{i\phi_{\mathsf{T}_{1,2}}(\mathbf{R},s)} = e^{i\mathbf{Q}_{1,2}\cdot\mathbf{r}}$, where $\mathbf{Q}_1 = (\pi, \sqrt{3}\pi)$ and $\mathbf{Q}_2 = (\pi, -\sqrt{3}\pi)$ are wave vectors at the M′ points of the extended Brillouin zone, because these also give the same gauge signs as above, when evaluated on the lattice vector $\mathbf{r} = \mathbf{R} + \boldsymbol{\delta}_s$ of a given site. In the case of the kagome lattice, the gauge signs of translations can be reformulated as $e^{i\phi_{\mathsf{T}_1}(\mathbf{R},s)} = (-1)^{R_1}$ and $e^{i\phi_{\mathsf{T}_2}(\mathbf{R},s)} = (-1)^{R_1+R_2}$, and also as $e^{i\phi_{\mathsf{T}_1}(\mathbf{R},s)} = \sqrt{2}\cos(\mathbf{Q}_1\cdot\mathbf{r} - \pi/4)$ and $e^{i\phi_{\mathsf{T}_2}(\mathbf{R},s)} = \sqrt{2}\cos(\mathbf{Q}_2\cdot\mathbf{r} + \pi/4)$, where $\mathbf{Q}_1 = (\pi, \pi/\sqrt{3})$ and $\mathbf{Q}_1 = (-\pi, \pi/\sqrt{3})$, provided that $\mathbf{r}$ are lattice vectors.

E.1 Gauge transformations for combined geometrical transformations

We call combined geometrical transformations those which are not generators of the space group, meaning neither elementary translations ($\mathsf{T}_{1,2}$) nor generators of the point group (C_6, σ). The gauge transformation of a combined geometrical transformation can be figured out from the gauge transformations of the generators of the space group. Let us first consider a simple combined transformation $\mathsf{g}_1\mathsf{g}_2$ (where both g_1 and g_2 are some generators of the space group). The gauge transformation $G_{\mathsf{g}_1\mathsf{g}_2}$ should reverse the effect of $\mathsf{g}_1\mathsf{g}_2$ as $\mathcal{H}_{\mathrm{MF}} = G_{\mathsf{g}_1\mathsf{g}_2}\mathsf{g}_1\mathsf{g}_2\mathcal{H}_{\mathrm{MF}}(\mathsf{g}_1\mathsf{g}_2)^{-1}G^{-1}_{\mathsf{g}_1\mathsf{g}_2}$. We can find out the form of the gauge phases of $G_{\mathsf{g}_1\mathsf{g}_2}$ by the consecutive application of $G_{\mathsf{g}_1}\mathsf{g}_1$ and $G_{\mathsf{g}_2}\mathsf{g}_2$ as

$$\mathcal{H}_{\mathrm{MF}} = G_{\mathsf{g}_1}\mathsf{g}_1\left(G_{\mathsf{g}_2}\mathsf{g}_2\mathcal{H}_{\mathrm{MF}}\mathsf{g}_2^{-1}G^{-1}_{\mathsf{g}_2}\right)\mathsf{g}_1^{-1}G^{-1}_{\mathsf{g}_1}, \tag{E.4}$$

which transfers to the hoppings as

$$t_{a,b}f^{\dagger}_{a,\sigma}f_{b,\sigma} = t_{i,j}\underbrace{e^{i\phi_{\mathsf{g}_1}(\mathsf{g}_1\mathsf{g}_2(i))}e^{i\phi_{\mathsf{g}_2}(\mathsf{g}_2(i))}}_{e^{i\phi_{\mathsf{g}_1\mathsf{g}_2}(\mathsf{g}_1\mathsf{g}_2(i))}}f^{\dagger}_{\mathsf{g}_1\mathsf{g}_2(i),\sigma}f_{\mathsf{g}_1\mathsf{g}_2(j),\sigma}\underbrace{e^{-i\phi_{\mathsf{g}_2}(\mathsf{g}_2(j))}e^{-i\phi_{\mathsf{g}_1}(\mathsf{g}_1\mathsf{g}_2(j))}}_{e^{-i\phi_{\mathsf{g}_1\mathsf{g}_2}(\mathsf{g}_1\mathsf{g}_2(j))}} \tag{E.5}$$

Any geometric transformation g can be decomposed into a product of the generators of the space group as $\mathsf{g} = \mathsf{g}_1\mathsf{g}_2\ldots\mathsf{g}_L$. The gauge transformation for this product can be figured out the same way as above, which turns out to be

$$e^{i\phi_{\mathsf{g}_1\mathsf{g}_2\cdots\mathsf{g}_L}(\mathsf{g}_1\mathsf{g}_2\cdots\mathsf{g}_L(j))} = e^{i\phi_{\mathsf{g}_1}(\mathsf{g}_1\mathsf{g}_2\cdots\mathsf{g}_L(j))}e^{i\phi_{\mathsf{g}_2}(\mathsf{g}_2\mathsf{g}_3\cdots\mathsf{g}_L(j))}\ldots e^{i\phi_{\mathsf{g}_{L-1}}(\mathsf{g}_{L-1}\mathsf{g}_L(j))}e^{i\phi_{\mathsf{g}_L}(\mathsf{g}_L(j))} \tag{E.6}$$

Specifically, the translations $\mathsf{T}_{\mathbf{R}'}$ with Bravais lattice vectors $\mathbf{R}' = R'_1\mathbf{a}_1 + R'_2\mathbf{a}_2$ can be written as a product of the elementary translations $\mathsf{T}_{\mathbf{R}'} = \mathsf{T}_1^{R'_1}\mathsf{T}_2^{R'_2}$, where the order of T_1 and T_2 does not matter. In this case, the gauge transformation is

$$e^{i\phi_{\mathsf{T}_{\mathbf{R}'}}(\mathsf{T}_{\mathbf{R}'}(j))} = e^{i\phi_{\mathsf{T}_1}(\mathsf{T}_1^{R'_1}\mathsf{T}_2^{R'_2}(j))}\ldots e^{i\phi_{\mathsf{T}_1}(\mathsf{T}_1\mathsf{T}_2^{R'_2}(j))}e^{i\phi_{\mathsf{T}_2}(\mathsf{T}_2^{R'_2}(j))}\ldots e^{i\phi_{\mathsf{T}_2}(\mathsf{T}_2^{3}(j))}e^{i\phi_{\mathsf{T}_2}(\mathsf{T}_2^{2}(j))}e^{i\phi_{\mathsf{T}_2}(\mathsf{T}_2(j))}, \tag{E.7}$$

which looks complicated, but for the specific forms $e^{i\phi_{\mathsf{T}_1}(\mathbf{R},s)} = (-1)^{a_1R_1+b_1R_2+c_1\xi_s}$ and $e^{i\phi_{\mathsf{T}_2}(\mathbf{R},s)} = (-1)^{a_2R_1+b_2R_2+c_2\xi_s}$ (which applies on both the honeycomb and the kagome lattices, as shown at the end of the previous subsection) the above equation can be simplified. As mentioned in the previous subsection, the site index can be equivalently replaced with the Bravais lattice vector of the unit cell and the sublattice index as $j \leftrightarrow (\mathbf{R},s)$, so $e^{i\phi_{\mathsf{T}_{\mathbf{R}'}}(\mathsf{T}_{\mathbf{R}'}(j))} = e^{i\phi_{\mathsf{T}_{\mathbf{R}'}}(\mathsf{T}_{\mathbf{R}'}(\mathbf{R},s))} =$

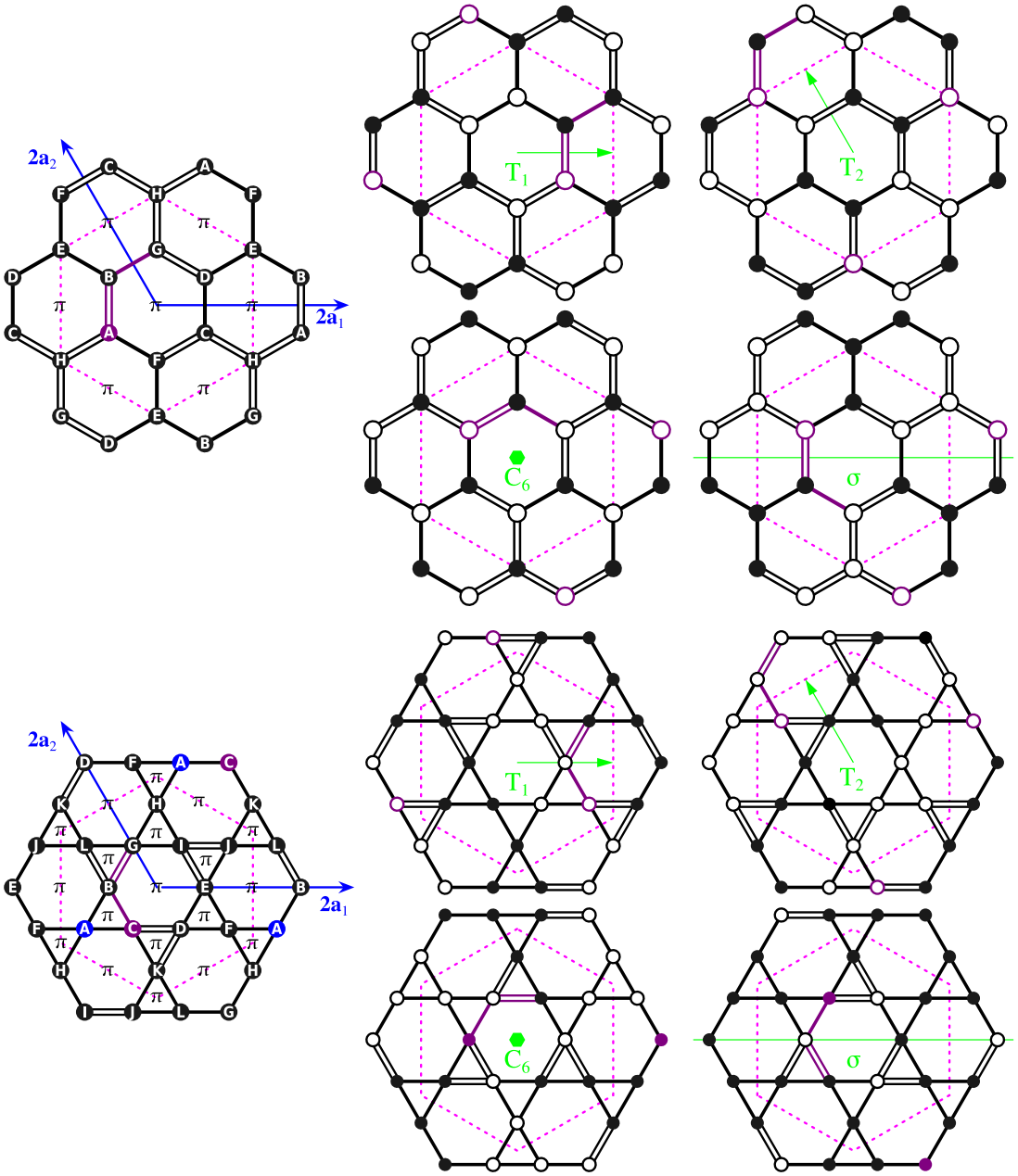

Figure E.1: In the leftmost column we show the hopping structure of the π-flux $\mathcal{H}^{\mathrm{MF}}$ of the Dirac spin liquid ansatz discussed in sections 2.3.1 and 2.3.2. The white and black bonds represent positive and negative hopping amplitudes, respectively. On the remaining figures, we show the gauge transformations G_{g} Eq. (2.16) reversing the effect of the corresponding geometrical transformations g, assuring that the π-flux $\mathcal{H}^{\mathrm{MF}}$ is invariant under the combined transformations $G_{\mathsf{g}}\mathsf{g}$ (see Eqs. (2.32) and (E.3)). As the hoppings are real, the gauge phases of the gauge transformations (2.16) become gauge signs. The lattice sites where the fermionic operators acquire minus signs are marked with white circles. These minus signs can be transferred to the surrounding hoppings, therefore the gauge transformations flip the signs of all those hoppings, which are connected only to a single white circle. The purple bonds are visualizing the effect of the geometrical transformations. The purple dashed hexagons show the quadrupled Wigner-Seitz unit cell.

$e^{i\phi_{\mathsf{T}_{\mathbf{R}'}}(\mathbf{R}+\mathbf{R}',s)}$. When we apply T_2 at site $j \leftrightarrow (\mathbf{R},s)$ the Bravais lattice vector $\mathbf{R} = R_1\mathbf{a}_1 + R_2\mathbf{a}_2$ is shifted with $\mathbf{a}_2$ as $\mathbf{R}+\mathbf{a}_2$, so the coordinate R_2 is raised with 1. Similarly, the action of T_1 shifts with $\mathbf{a}_1$, so it raises the coordinate R_1 with 1. In Eq. (E.7) we first shift site j by T_2 R_2' times, so we get $(-1)^{a_2R_1+b_2(R_2+1)+c_2\xi_s} \times (-1)^{a_2R_1+b_2(R_2+2)+c_2\xi_s} \times \cdots \times (-1)^{a_2R_1+b_2(R_2+R_2')+c_2\xi_s} = (-1)^{[a_2R_1+b_2R_2+c_2\xi_s]R_2'+b_2\sum_{n=1}^{R_2'} n}$. Next, starting from site $\mathsf{T}_2^{R_2'}(j)$ we apply T_1 R_1' times, and we get $(-1)^{a_1(R_1+1)+b_1(R_2+R_2')+c_1\xi_s} \times (-1)^{a_1(R_1+2)+b_1(R_2+R_2')+c_1\xi_s} \times \cdots \times (-1)^{a_1(R_1+R_1')+b_1(R_2+R_2')+c_1\xi_s} = (-1)^{\left[a_1R_1+b_1(R_2+R_2')+c_1\xi_s\right]R_1'+a_1\sum_{m=1}^{R_1'} m}$. Therefore, Eq. (E.7) simplifies to

$$\begin{aligned} e^{i\phi_{\mathsf{T}_{\mathbf{R}'}}(\mathbf{R}+\mathbf{R}',s)} &= (-1)^{\left[a_1R_1+b_1(R_2+R_2')+c_1\xi_s\right]R_1'+a_1\sum_{m=1}^{R_1'} m} \times (-1)^{[a_2R_1+b_2R_2+c_2\xi_s]R_2'+b_2\sum_{n=1}^{R_2'} n} \\ &= (-1)^{\left[a_1R_1+b_1(R_2+R_2')+c_1\xi_s\right]R_1'+a_1(1+R_1')R_1'/2} \times (-1)^{[a_2R_1+b_2R_2+c_2\xi_s]R_2'+b_2(1+R_2')R_2'/2}, \end{aligned} \tag{E.8}$$

where in the second row we used the formula $S_n = (a_1+a_n)n/2$ for the sums of both arithmetic series $\sum_{m=1}^{R_1} m$ and $\sum_{n=1}^{R_2} n$. The sums of these series $(1+R_1')R_1'/2$ and $(1+R_2')R_2'/2$ are both even, since either R_1' or $R_1'+1$ is even (similarly for R_2). Every even power of (-1) is $+1$, so it can be ignored. Ignoring all even terms, we get

$$\begin{aligned} e^{i\phi_{\mathsf{T}_{\mathbf{R}'}}(\mathbf{R}+\mathbf{R}',s)} &= (-1)^{\left[a_1R_1+b_1(R_2+R_2')+c_1\xi_s\right]R_1'} \times (-1)^{[a_2R_1+b_2R_2+c_2\xi_s]R_2'} \\ &= (-1)^{\left[a_1R_1+b_1(R_2+R_2')+c_1\xi_s\right]R_1'+[a_2R_1+b_2R_2+c_2\xi_s]R_2'} \end{aligned} \tag{E.9}$$

At the beginning we claimed that the order of the T_1 and T_2 in Eq. (E.7) is unimportant, but reversing the order of T_1 and T_2 in Eq. (E.7) yields a different expression as the one above, due to the term $b_1R_2'R_1'$. However, the additional gauge signs appearing in the expression of Gutzwiller-projected particle-hole excitations of the $|\pi\mathrm{FS}\rangle$ in Eq. (4.20) turn out to be independent of the order of T_1 and T_2, since the term $b_1R_2'R_1'$ falls out as

$$\begin{aligned} e^{i\phi_{\mathsf{T}_{\mathbf{R}'}}(\mathbf{R}+\mathbf{R}',s)}e^{-i\phi_{\mathsf{T}_{\mathbf{R}'}}(\mathbf{R}',\bar{s})} &= (-1)^{\left[a_1R_1+b_1(R_2+R_2')+c_1\xi_s\right]R_1'+[a_2R_1+b_2R_2+c_2\xi_s]R_2'} \\ &\quad \times (-1)^{\left[b_1R_2'+c_1\xi_{\bar{s}}\right]R_1'+[c_2\xi_{\bar{s}}]R_2'} \\ &= (-1)^{[a_1R_1+b_1R_2+c_1(\xi_s+\xi_{\bar{s}})]R_1'+[a_2R_1+b_2R_2+c_2(\xi_s+\xi_{\bar{s}})]R_2'} \end{aligned}$$

For the specific forms $e^{i\phi^H_{\mathsf{T}_1}(\mathbf{R},s)} = (-1)^{R_1+\xi_s}$ ($a_1=1$, $b_1=0$, $c_1=1$), $e^{i\phi^H_{\mathsf{T}_2}(\mathbf{R},s)} = (-1)^{R_1+R_2+\xi_s}$ ($a_2=1$, $b_2=1$, $c_2=1$) on the honeycomb, and $e^{i\phi^K_{\mathsf{T}_1}(\mathbf{R},s)} = (-1)^{R_1}$ ($a_1=1$, $b_1=0$, $c_1=0$) and $e^{i\phi^K_{\mathsf{T}_2}(\mathbf{R},s)} = (-1)^{R_1+R_2}$ ($a_2=1$, $b_2=1$, $c_2=0$) on the kagome lattices, we get

$$\begin{aligned} e^{i\phi^H_{\mathsf{T}_{\mathbf{R}'}}(\mathbf{R}+\mathbf{R}',s)}e^{-i\phi^H_{\mathsf{T}_{\mathbf{R}'}}(\mathbf{R}',\bar{s})} &= (-1)^{[R_1+(\xi_s+\xi_{\bar{s}})]R_1'+[R_1+R_2+(\xi_s+\xi_{\bar{s}})]R_2'} \\ e^{i\phi^K_{\mathsf{T}_{\mathbf{R}'}}(\mathbf{R}+\mathbf{R}',s)}e^{-i\phi^K_{\mathsf{T}_{\mathbf{R}'}}(\mathbf{R}',\bar{s})} &= (-1)^{[R_1]R_1'+[R_1+R_2]R_2'} \end{aligned} \tag{E.10}$$

respectively.

E.2 The effect of antiperiodic boundary condition

We impose antiperiodic boundary conditions as shown in Figs. 2.1(a) and (c), and Fig. E.2(a), which changes the sign of the hoppings crossing one of the cluster's boundaries. After these sign changes Eq. (E.3) will still hold for the T_2 translations and the two reflections about the antiperiodic boundary and perpendicular to it (the two reflections generate the D_2 point group, which also includes a C_2 rotation), but it will no longer hold for the T_1, C_6 and the remaining

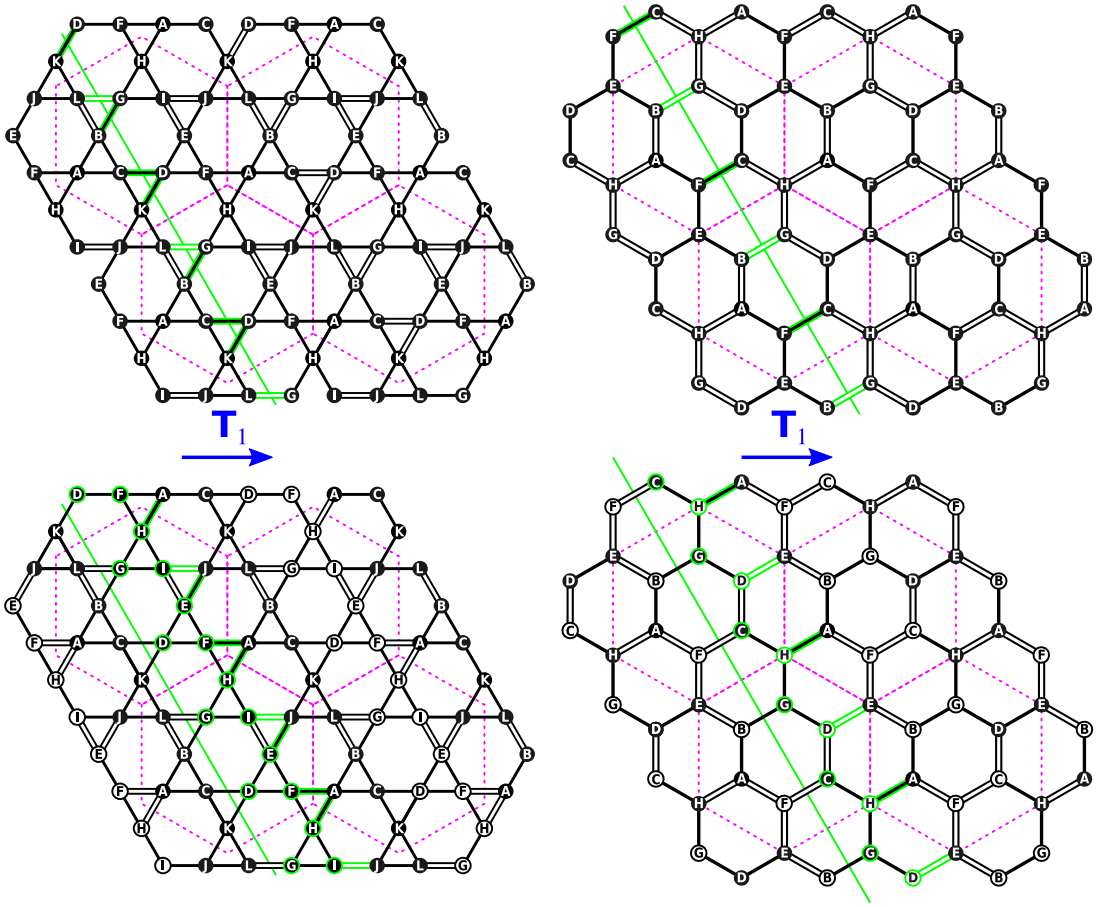

Figure E.2: A cluster containing four quadrupled unit cells (shown with dashed magenta hexagons) of the Dirac spin liquid ansätze shown in Figs. 2.1(a) and (c), where the black and white bonds represent negative and positive hopping amplitudes, respectively. In the left panels we show the effect of the antiperiodic boundary condition (APBC) (the green line), which flips the sign of the hoppings $t_{i,j}$ crossing it (highlighted in green). In the right panels the translation operator T_1 shifts the hoppings by the primitive vector $\mathbf{a}_1$. For periodic boundaries, the gauge transformation $G^{\mathrm{PBC}}_{\mathsf{T}_1}$ shown in Fig. E.1 restores the original hopping configuration, according to and Eq. (E.3). However, due to the APBC, we must modify the gauge transformation so that it restores the hopping configurations shown on the left panels. To do so, we change the $G^{\mathrm{PBC}}_{\mathsf{T}_1}$ so that we reverse the signs of the fermionic operators on the sites highlighted with green. The resulting gauge signs of $G^{\mathrm{APBC}}_{\mathsf{T}_1}$ are shown with white-filled circles, which can be transferred to the surrounding hoppings. In other words, the signs of the hoppings on the bonds connected to a single white circle are flipped.

reflections if we use the same gauge transformations as we used in the case of periodic boundary conditions. However, we can satisfy Eq. (E.3) for T_1 if we multiply by -1 the gauge phases $e^{i\phi_{\mathsf{T}_1}(j)}$ at the locations marked by green circles in Fig. E.2(d). Regarding the C_6 rotations and the reflections about the other axis, we could not find any gauge transformation restoring their effect. Indeed, the numerical calculation of the structure factor confirms the D_2 point group symmetry for antiperiodic boundary conditions, providing further support for the absence of gauge transformations that would restore the full D_6 point group.

Note that the boundary conditions of the fermionic operators do not affect the periodic boundary condition of the spin operators, as can be understood from Eq. (2.2).

Appendix F

Gauge equivalence of doubled and quadrupled unit cell ansätze

As stated in Sec. 2.3, the π-flux $\mathcal{H}^{\mathrm{MF}}$ requires at least a doubled unit cell to accommodate the hoppings creating the π-fluxes. In all articles we found, people used the doubled unit cell ansatz shown in the second column of Fig. F.1, for both the honeycomb, and the kagome lattices [6, 58]. The doubled unit cell ansätze are gauge equivalent to the quadrupled unit cell ansätze shown in the first column of Fig. F.1, but the gauge transformation connecting them requires the change of the boundary conditions (PBC↔APBC) for certain cluster sizes. The gauge transformation in a cluster containing a single quadrupled unit cell requires a change in the boundary conditions, as shown in the second column of Fig. F.1. However, the gauge transformation in a cluster containing four quadrupled unit cells does not involve the change of the boundary conditions, as shown in the third column of Fig. F.1. Repeating the quadrupled unit cell an odd number of times in the directions of the primitive vectors requires the change of the boundary conditions, while repeating it even times does not involve any change.

We applied the ansatz with the quadrupled unit cell on both lattices, to construct the gauge transformations G_{C_6} and G_σ restoring the C_6 and some σ symmetries as in Eq. (2.32). These gauge transformations can be constructed for PBC, but if we impose APBC, the gauge transformations G_{C_6} and G_σ do not exist anymore, so the C_6 and some σ projective symmetries are broken (see Appendix E.2).

As the quadrupled unit cell ansatz with PBC yields a degenerate Fermi sea, we are forced to impose APBC. Therefore, the doubled unit cell ansatz, which yields a non-degenerate Fermi sea, must be gauge equivalent to the quadrupled unit cell ansatz with APBC. Consequently, if the doubled unit cell ansatz for given boundary conditions gives a non-degenerate Fermi sea, then it is not possible to construct the gauge transformations restoring the C_6 and some σ symmetries. These gauge transformations could be constructed, if we changed the boundary conditions, but then the Fermi sea would become degenerate.

The number of energy bands in the mean-field spectrum (see Eqs. (2.26) and (2.31)) is equal to the number of basis sites, therefore the number of energy bands in the quadrupled unit cell ansatz is twice as much as in the doubled unit cell ansatz. However, as these are gauge equivalent, they are expected to have the same energy spectrum (see Eq. (2.34), which is possible only by doubling the degeneracy of every energy band. The number of available one-particle states in the whole reduced Brillouin zone will not be different, because even if the energy bands of the quadrupled unit cell are doubly degenerate, its reduced Brillouin zone is half as big as that of the doubled unit cell ansatz with non-degenerate bands (see Appendix H.3).

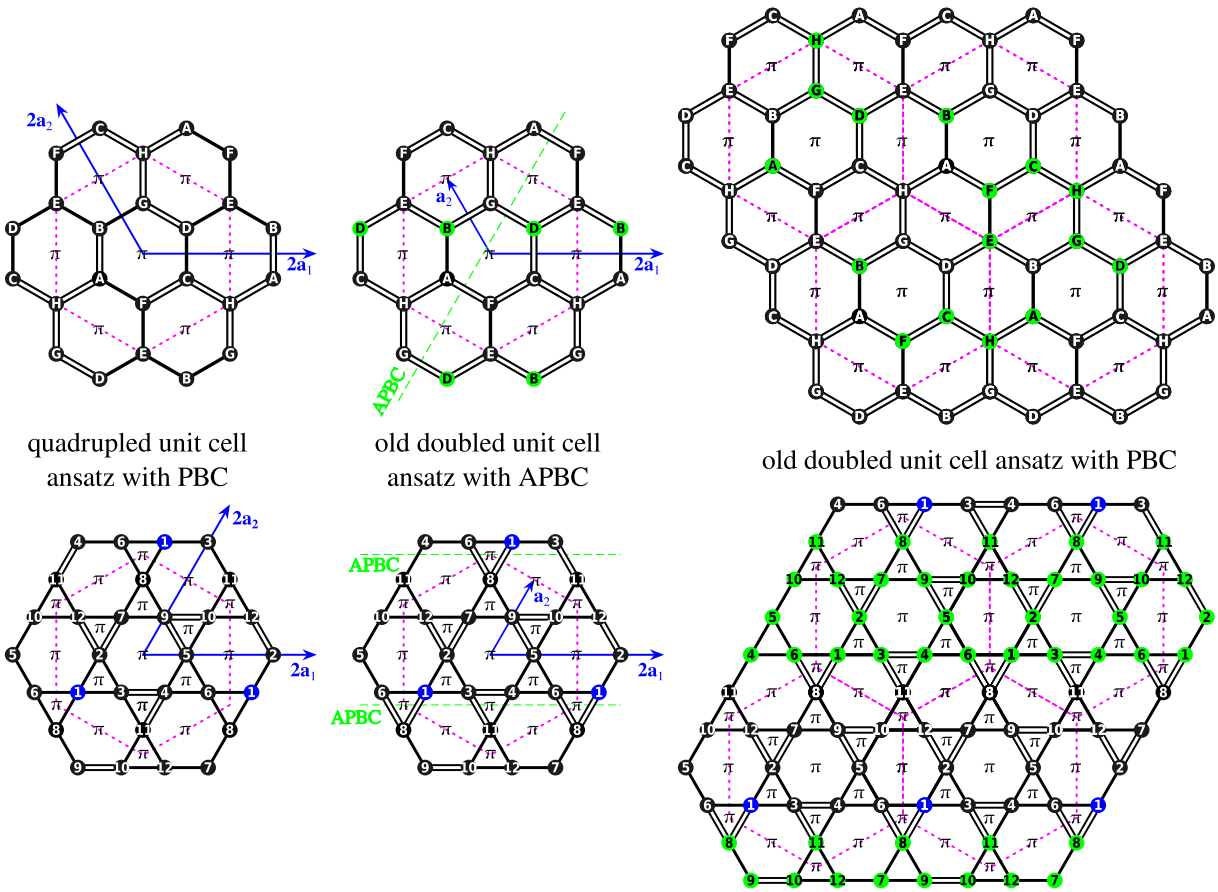

Figure F.1: The gauge equivalence of the quadrupled unit cell ansatz (first column) and the old π-flux ansatz with doubled unit cell (second and third columns). The magenta dashed hexagons denote the quadrupled Wigner-Seitz unit cells. The gauge transformation connecting these ansätze is tricky, because for certain clusters it involves the change of the boundary conditions from periodic to antiperiodic as shown with the green dashed lines in the second column. The signs of the hopping amplitudes intersected by the APBC are switched. The sites on which the gauge transformation changes the signs of the fermionic operators are denoted with green circles. These gauge signs can be transferred to the surrounding hoppings, so a hopping (not intersected by the APBC) changes sign if only one of the connected sites is green.

Appendix G

Invariance of the expectation values of spin operators in the mean-field ground state

Here we will prove Eq. (2.43). If the mean-field ground states $|\mathrm{FS}_1\rangle$ and $|\mathrm{FS}_2\rangle$ of the gauge equivalent Hamiltonians $\mathcal{H}_1^{\mathrm{MF}}$ and $\mathcal{H}_2^{\mathrm{MF}}$ are non-degenerate, we can show (see Appendix D) that they are related as $|\mathrm{FS}_2\rangle = G|\mathrm{FS}_1\rangle$ given in Eq. (2.36).

As the SU(N) spin operators T_j^a are insensitive to gauge transformations (2.17), their expectation values and correlations functions in the states $|\mathrm{FS}_1\rangle$ and $|\mathrm{FS}_2\rangle$ are equal, since

$$\langle \mathrm{FS}_1|T_j^a|\mathrm{FS}_1\rangle = \langle \mathrm{FS}_2|GT_j^aG^{-1}|\mathrm{FS}_2\rangle = \langle \mathrm{FS}_2|T_j^a|\mathrm{FS}_2\rangle \tag{G.1}$$

and

$$\langle \mathrm{FS}_1|T_i^aT_j^a|\mathrm{FS}_1\rangle = \langle \mathrm{FS}_2|GT_i^aT_j^aG^{-1}|\mathrm{FS}_2\rangle = \langle \mathrm{FS}_2|GT_i^aG^{-1}GT_j^aG^{-1}|\mathrm{FS}_2\rangle = \langle \mathrm{FS}_2|T_i^aT_j^a|\mathrm{FS}_2\rangle, \tag{G.2}$$

where we inserted the idendtity as $\mathcal{I} = G^{-1}G$. Now let us choose the two Hamiltonians so that $\mathcal{H}_1^{\mathrm{MF}}$ is gauge equivalent to $\mathcal{H}_2^{\mathrm{MF}} = \mathsf{g}\mathcal{H}_1^{\mathrm{MF}}\mathsf{g}^{-1}$ (so that $\mathcal{H}_1^{\mathrm{MF}}$ is invariant under G_{g}g). Due to the construction of $\mathcal{H}_2^{\mathrm{MF}}$, their ground states are related as $|\mathrm{FS}_2\rangle = \mathsf{g}|\mathrm{FS}_1\rangle$ (as argued in Appendix D), so following the same steps as above we get

$$\langle \mathrm{FS}_1|T_i^a|\mathrm{FS}_1\rangle = \langle \mathrm{FS}_2|\mathsf{g}T_i^a\mathsf{g}^{-1}|\mathrm{FS}_2\rangle = \langle \mathrm{FS}_2|T_{\mathsf{g}(i)}^a|\mathrm{FS}_2\rangle, \tag{G.3}$$

and

$$\langle \mathrm{FS}_1|T_i^aT_j^a|\mathrm{FS}_1\rangle = \langle \mathrm{FS}_2|\mathsf{g}T_i^a\mathsf{g}^{-1}\mathsf{g}T_j^a\mathsf{g}^{-1}|\mathrm{FS}_2\rangle = \langle \mathrm{FS}_2|T_{\mathsf{g}(i)}^aT_{\mathsf{g}(j)}^a|\mathrm{FS}_2\rangle. \tag{G.4}$$

Comparing these equations with Eqs. (G.1) and (G.2), we can conclude that

$$\langle \mathrm{FS}_2|T_i^a|\mathrm{FS}_2\rangle = \langle \mathrm{FS}_2|T_{\mathsf{g}(i)}^a|\mathrm{FS}_2\rangle, \;\; \langle \mathrm{FS}_2|T_i^aT_j^a|\mathrm{FS}_2\rangle = \langle \mathrm{FS}_2|T_{\mathsf{g}(i)}^aT_{\mathsf{g}(j)}^a|\mathrm{FS}_2\rangle, \tag{G.5}$$

and using $|\mathrm{FS}_2\rangle = \mathsf{g}|\mathrm{FS}_1\rangle$

$$\langle \mathrm{FS}_1|T_{\mathsf{g}^{-1}(i)}^a|\mathrm{FS}_1\rangle = \langle \mathrm{FS}_1|T_i^a|\mathrm{FS}_1\rangle, \;\; \langle \mathrm{FS}_1|T_{\mathsf{g}^{-1}(i)}^aT_{\mathsf{g}^{-1}(j)}^a|\mathrm{FS}_1\rangle = \langle \mathrm{FS}_1|T_i^aT_j^a|\mathrm{FS}_1\rangle, \tag{G.6}$$

which is just the same after relabeling the sites as $i' = \mathsf{g}^{-1}(i)$.

Appendix H

Brillouin zones: original, extended, reduced

H.1 Original Brillouin zone

Bravais lattices have only one basis site in their unit cell ($N_B = 1$), two-dimensional examples are the square and the triangular lattices. In these lattices every lattice site can be connected by translations by Bravais lattice vectors $\mathbf{R} = R_1\mathbf{a}_1 + R_2\mathbf{a}_2$, where $\mathbf{a}_1$ and $\mathbf{a}_2$ are the primitive vectors of the lattice and R_1, R_2 are integers. The reciprocal lattice, describing the periodicity of the direct lattice, is also a Bravais lattice with primitive vectors $\mathbf{b}_1$ and $\mathbf{b}_2$, defined by $\mathbf{b}_c \cdot \mathbf{a}_d = 2\pi\delta_{c,d}$ with $c, d \in \{1, 2\}$ in two dimensions. Therefore, the reciprocal primitive vectors $\mathbf{b}_1$ and $\mathbf{b}_2$ are the rows of the matrix $\frac{1}{2\pi}\left(\mathbf{a}_1 \middle| \mathbf{a}_2\right)^{-1}$. Namely, for the primitive vectors $\mathbf{a}_1 = (1, 0)$, and $\mathbf{a}_2 = (-1/2, \sqrt{3}/2)$, we get the reciprocal primitive vectors $\mathbf{b}_1 = (2\pi, 2\pi/\sqrt{3})$, and $\mathbf{b}_2 = (0, 4\pi/\sqrt{3})$. The Brillouin zone is the Wigner-Seitz unit cell of the reciprocal lattice.

H.2 Extended Brillouin zone

In non-Bravais lattices, the unit cell has more than one basis sites ($N_B > 1$), which we will label by letters in every unit cell. The set of a given type of basis sites (e.g. the sites with label A) form a Bravais sublattice (which is independent of the choice of the type of basis site), so the Bravais lattice connects the unit cells. A reciprocal lattice always describes the periodicity of a Bravais lattice, so we can not take the reciprocal lattice of a non-Bravais lattice. Instead, we can take the reciprocal lattice of the Bravais lattice connecting the unit cells, which will have less information than the direct lattice, because it does not contain the sublattice structure. The Brillouin zone of the Bravais lattice connecting the unit cells will be called the original Brillouin zone, or simply Brillouin zone, shown with the dark grey hexagons in Fig. H.1(c) and (d).

However, there is a way to construct a reciprocal lattice, which contains all the information of the direct lattice, even if it a non-Bravais lattice. To do so, we should take the reciprocal lattice of a different (artificial) Bravais lattice, which has smaller lattice spacing, so that we can connect the lattice sites of the direct lattice with translations by the lattice vectors of this artificial Bravais lattice. Clearly, this artifical Bravais lattice will have additional lattice sites even where the original direct lattice had no lattice sites, but at least all the lattice sites of the direct lattice will also be lattice sites of the artificial Bravais lattice. Specifically, we can associate artificial triangular Bravais lattices to both the honeycomb and the kagome lattices, by putting additional lattice sites in the centers of the hexagons, as shown in Fig. H.1(a) and (b). The resulting artificial triangular lattices have smaller lattice spacings and different primitive vectors than the original triangular lattices connecting the unit cells of the honeycomb, and kagome lattices. Namely, if we choose the primitive vectors of both the honeycomb and kagome lattices to be $\mathbf{a}_1 = (1, 0)$, $\mathbf{a}_2 = (-1/2, \sqrt{3}/2)$, then the primitive vectors of the artificial triangular lattices become $\tilde{\mathbf{a}}_1^H = (1/2, \sqrt{3}/4)$, $\tilde{\mathbf{a}}_2^H = (0, 1/\sqrt{3})$ and $\tilde{\mathbf{a}}_1^K = (1/2, 0)$, $\tilde{\mathbf{a}}_2^K = (-1/4, \sqrt{3}/4)$, which have been shrinked as $|\tilde{\mathbf{a}}_d^H| = \frac{1}{\sqrt{3}}|\mathbf{a}_d|$ and $|\tilde{\mathbf{a}}_d^K| = \frac{1}{2}|\mathbf{a}_d|$, respectively. The corresponding reciprocal primitive vectors of the original Bravais lattice are $\mathbf{b}_1 = (2\pi, 2\pi/\sqrt{3})$, and $\mathbf{b}_2 = (0, 4\pi/\sqrt{3})$, and for the artifical triangular lattices $\tilde{\mathbf{b}}_1^H = (4\pi, 0)$, $\tilde{\mathbf{b}}_2^H = (-2\pi, 2\sqrt{3}\pi)$ and $\tilde{\mathbf{b}}_1^K = (4\pi, 4\pi/\sqrt{3})$,

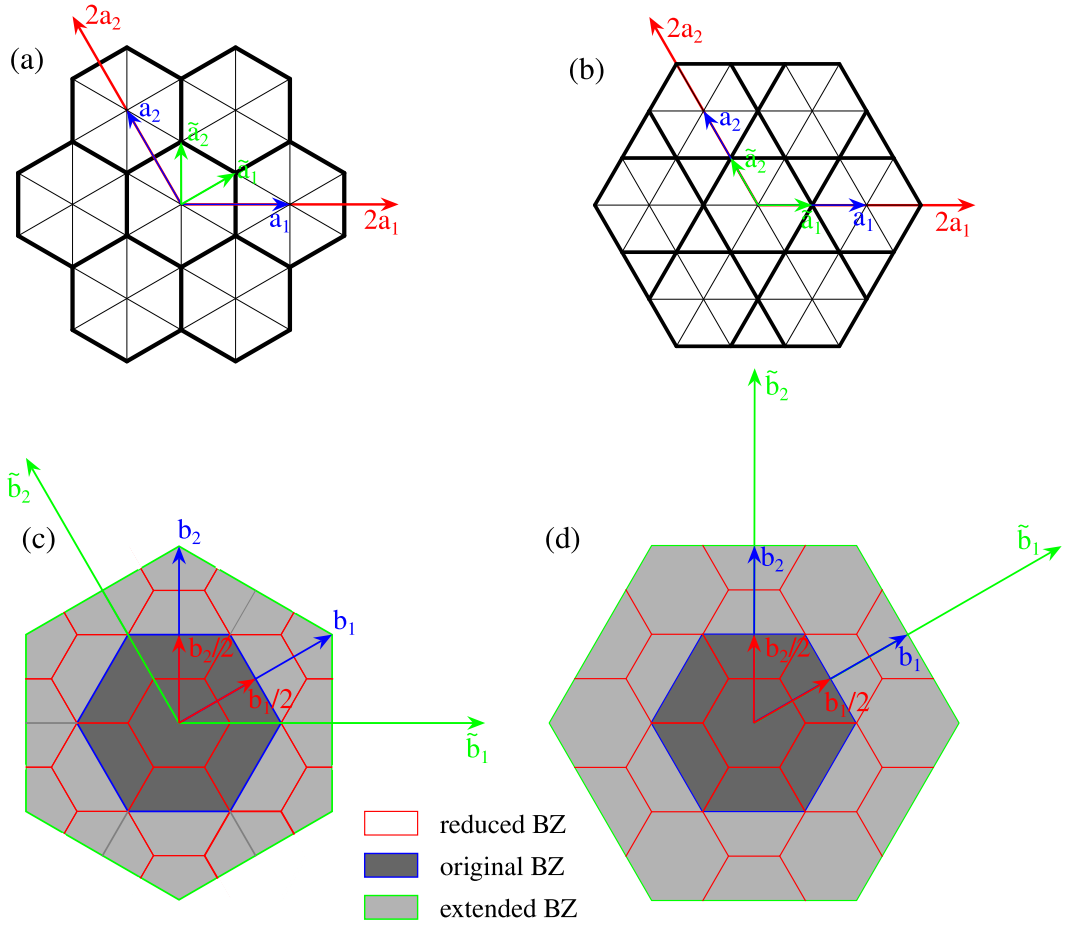

Figure H.1: (a) and (b) shows the artificial triangular lattices associated to the honeycomb, and kagome lattices, respectively. These triangular lattices contain every lattice site of the original lattice, so their reciprocal lattice will contain all information about the original lattices. (c) and (d) show the original, extended, and reduced Brillouin zones, with the color code shown between (c) and (d).

$\tilde{\mathbf{b}}_2^K = (0, 8\pi/\sqrt{3})$ (shown in Fig. H.1(c) and (d)), which have been elongated as $|\tilde{\mathbf{b}}_c^H| = \sqrt{3}|\mathbf{b}_c|$ and $|\tilde{\mathbf{b}}_c^K| = 2|\mathbf{b}_c|$, respectively. Consequently, the areas of the Brillouin zones of these artificial triangular lattices are three and four times bigger than those of the original Brillouin zones of the honeycomb and kagome lattices, respectively. Therefore, we will call them the extended Brillouin zones (eBZ), shown with the light grey hexagons in Fig. H.1(c) and (d).

H.3 Reduced Brillouin zone

The π-flux mean-field Hamiltonians of sections 2.3.1 and 2.3.2 break the translational invariance of the original lattice, requiring quadrupled unit cells to accomodate the hoppings. The hopping structure is periodic only in this quadrupled unit cell, so the primitive vectors get doubled. The Bravais lattice consists of vectors $\mathbf{R} = R_1 2\mathbf{a}_1 + R_2 2\mathbf{a}_2$, where R_1 and R_2 are integers. Consequently, the primitive vectors of the reciprocal lattice $\mathbf{b}_1^{\mathrm{MF}}$ and $\mathbf{b}_2^{\mathrm{MF}}$ get halved relative to the original ones, since they are the rows of the matrix $\frac{1}{2\pi}\left(2\mathbf{a}_1 \middle| 2\mathbf{a}_2\right)^{-1}$. Thus, the area of the Brillouin zone of this reciprocal lattice is the quarter of the area of the original Brillouin zone, and we will call it the reduced Brillouin zone (rBZ), shown with the red empty hexagons in Fig. H.1(c) and (d).

Appendix I

Derivation of $S^{33}_{\mathrm{MF}}(\mathbf{k},\omega)$

In this section, we will derive the formula (4.8) for a general mean-field Hamiltonian $\mathcal{H}_{\mathrm{MF}}$, with any unit cell and any band structure, supposing that the Fermi sea $|\mathrm{FS}\rangle$ fills complete bands (so that the Fermi energy is not inside an energy band). This derivation was presented in Ref. [II.].

The Bravais lattice vectors of the mean-field Hamiltonian $\mathcal{H}_{\mathrm{MF}}$ may be different from those of the original lattice, since the accommodation of the hoppings can require enlarged unit cells, like in the case of the π-flux $\mathcal{H}_{\mathrm{MF}}$ with a quadrupled unit cell (see Fig. 2.1), where the Bravais lattice vectors are $\mathbf{R}^{\mathrm{MF}} = R_1^{\mathrm{MF}}(2\mathbf{a}_1) + R_2^{\mathrm{MF}}(2\mathbf{a}_2)$ with $R_1^{\mathrm{MF}}, R_2^{\mathrm{MF}}$ integers (see Eq. (2.19)). For simplicity, we will leave away the MF superscripts and subscripts everywhere (except in $S^{33}_{\mathrm{MF}}(\mathbf{k},\omega)$) in this section.

Substituting $T^3_{\mathbf{k}} = \frac{1}{\sqrt{N_s}} \sum_{\mathbf{R},s} e^{i\mathbf{k}\cdot(\mathbf{R}+\boldsymbol{\delta}_s)} \frac{1}{2} \left(f^\dagger_{\mathbf{R},s,1} f_{\mathbf{R},s,1} - f^\dagger_{\mathbf{R},s,2} f_{\mathbf{R},s,2} \right)$ from Eq. (4.6) into $S^{33}(\mathbf{k},\omega)$ (4.5), we get

$$S^{33}_{\mathrm{MF}}(\mathbf{k},\omega) = \frac{1}{N_s} \sum_f \left| \sum_{\mathbf{R},s} e^{i\mathbf{k}\cdot(\mathbf{R}+\boldsymbol{\delta}_s)} \frac{1}{2} \langle f | f^\dagger_{\mathbf{R},s,1} f_{\mathbf{R},s,1} - f^\dagger_{\mathbf{R},s,2} f_{\mathbf{R},s,2} | \mathrm{FS} \rangle \right|^2 \delta(\omega + E_{\mathrm{FS}} - E_f), \quad \text{(I.1)}$$

where the $\sum_{\mathbf{R}}$ sums over all mean-field Bravais lattice vectors, and the $\sum_s$ sums over all mean-field sublattice indices $s \in \{A, B, \dots\}$. Using $f^\dagger_{\mathbf{R},s,\sigma} = \frac{1}{\sqrt{N_C}} \sum_{\mathbf{q}\in \mathrm{rBZ}} e^{-i\mathbf{q}\cdot\mathbf{R}} f^\dagger_{\mathbf{q},s,\sigma}$ of Eq. (2.21) (where N_C is the number of mean-field unit cells), we obtain

$$\begin{aligned} S^{33}_{\mathrm{MF}}(\mathbf{k},\omega) = \frac{1}{N_s} \sum_f \Bigg| \frac{1}{N_C} \sum_{\substack{s \\ \mathbf{q},\mathbf{q}'\in \mathrm{rBZ}}} e^{i\mathbf{k}\cdot\boldsymbol{\delta}_s} \sum_{\mathbf{R}} e^{i(\mathbf{k}-\mathbf{q}'+\mathbf{q})\cdot\mathbf{R}} \frac{1}{2} \langle f | f^\dagger_{\mathbf{q}',s,1} f_{\mathbf{q},s,1} - f^\dagger_{\mathbf{q}',s,2} f_{\mathbf{q},s,2} | \mathrm{FS} \rangle \Bigg|^2 \\ \times \delta(\omega + E_{\mathrm{FS}} - E_f) \,, \end{aligned} \quad \text{(I.2)}$$

where $\mathbf{q}$ and $\mathbf{q}'$ are wave vectors in the reduced Brillouin zone (rBZ), but $\mathbf{k}$ can be anywhere in the extended Brillouin zone (eBZ), see the argument in Sec. 4.2. The sum $\sum_{\mathbf{R}} e^{i(\mathbf{k}-\mathbf{q}'+\mathbf{q})\cdot\mathbf{R}}$ would usually lead to $\delta_{\mathbf{k}-\mathbf{q}'+\mathbf{q},0}$, but that happens when all wave vectors are restricted to the rBZ, see Appendix F of the Solid state physics book of Ashcroft and Mermin. Repeating that derivation, the sum $\sum_{\mathbf{R}} e^{i(\mathbf{k}-\mathbf{q}'+\mathbf{q})\cdot\mathbf{R}}$ is not modified by adding a Bravais lattice vector $\mathbf{R}_0$ to every $\mathbf{R}$ as $\sum_{\mathbf{R}} e^{i(\mathbf{k}-\mathbf{q}'+\mathbf{q})\cdot\mathbf{R}} = \sum_{\mathbf{R}} e^{i(\mathbf{k}-\mathbf{q}'+\mathbf{q})\cdot(\mathbf{R}+\mathbf{R}_0)}$, since it corresponds to relabeling the Bravais lattice vectors (due to periodic or antiperiodic boundary conditions). Consequently, the $e^{i(\mathbf{k}-\mathbf{q}'+\mathbf{q})\cdot\mathbf{R}_0}$ must be equal to 1 for any Bravais lattice vector $\mathbf{R}_0$. This is possible only if

$$\mathbf{k} - \mathbf{q}' + \mathbf{q} = \mathbf{Q}, \quad \text{(I.3)}$$

where $\mathbf{Q} = Q_1 \mathbf{b}_1^{\mathrm{MF}} + Q_2 \mathbf{b}_2^{\mathrm{MF}}$ (see Appendix H.3) is a reciprocal Bravais lattice vector, with Q_1 and Q_2 integers. In the usual case, when all wave vectors are in the rBZ, $\mathbf{Q}$ must be zero, since that is the only reciprocal Bravais lattice vector in the rBZ. However, in our case, $\mathbf{Q}$ can be anywhere in the eBZ, allowing for more possibilities. If we restrict both wave vectors $\mathbf{q}$ and $\mathbf{q}'$ to the rBZ, then rearranging Eq. (I.3) we get $\mathbf{q}' = \mathbf{k} + \mathbf{q} - \mathbf{Q}$, meaning that $\mathbf{Q}$ is the reciprocal Bravais lattice vector, which maps back the wave vector $\mathbf{k} + \mathbf{q}$ to the rBZ. Therefore, we get $\sum_{\mathbf{R}} e^{i(\mathbf{k}-\mathbf{q}'+\mathbf{q})\cdot\mathbf{R}} = N_C \delta_{\mathbf{q}',\mathbf{k}+\mathbf{q}-\mathbf{Q}}$. We will hide the wave vector $\mathbf{Q}$ and write everywhere only

$\mathbf{k}+\mathbf{q}$, which is meant to be mapped back into the rBZ. Consequently,

$$S^{33}_{\mathrm{MF}}(\mathbf{k},\omega)=\frac{1}{4N_s}\sum_f\left|\sum_s e^{i\mathbf{k}\cdot\boldsymbol{\delta}_s}\sum_{\mathbf{q}}\langle f|f^\dagger_{\mathbf{k}+\mathbf{q},s,1}f_{\mathbf{q},s,1}-f^\dagger_{\mathbf{k}+\mathbf{q},s,2}f_{\mathbf{q},s,2}|\mathrm{FS}\rangle\right|^2\delta(\omega+E_{\mathrm{FS}}-E_f)\ . \tag{I.4}$$

The one-particle eigenstate of $\mathcal{H}_{\mathrm{MF}}$ with wave vector $\mathbf{q}$ and energy $\varepsilon_b(\mathbf{q})$ can be written as $f^\dagger_{\mathbf{q},b,\sigma}|0\rangle=\sum_s v_{\mathbf{q},b,s}f^\dagger_{\mathbf{q},s,\sigma}|0\rangle$ (see Eq. (2.27)), where $b\in\{1\dots N_B\}$ is the band index, and N_B is the number of basis sites in the mean-field unit cell. Inverting this relation we have $f^\dagger_{\mathbf{q},s,\sigma}|0\rangle=\sum_{b=1}^{N_B}v^{-1}_{\mathbf{q},s,b}f^\dagger_{\mathbf{q},b,\sigma}|0\rangle=\sum_{b=1}^{N_B}v^*_{\mathbf{q},b,s}f^\dagger_{\mathbf{q},b,\sigma}|0\rangle$, where we used that the matrix composed of the coefficients $v_{\mathbf{q},b,s}$ is unitary, namely $v^{-1}_{\mathbf{q},s,b}=v^*_{\mathbf{q},b,s}$. From these relations, we get

$$f^\dagger_{\mathbf{k}+\mathbf{q},s,\sigma}f_{\mathbf{q},s,\sigma}|\mathrm{FS}\rangle=\left(\sum_{b'=1}^{N_B}v^*_{\mathbf{k}+\mathbf{q},b',s}f^\dagger_{\mathbf{k}+\mathbf{q},b',\sigma}\right)\left(\sum_{b=1}^{N_B}v_{\mathbf{q},b,s}f_{\mathbf{q},b,\sigma}\right)|\mathrm{FS}\rangle.$$

Therefore, we can write

$$\begin{aligned}S^{33}_{\mathrm{MF}}(\mathbf{k},\omega)=\frac{1}{4N_s}\sum_f\Bigg|\sum_s e^{i\mathbf{k}\cdot\boldsymbol{\delta}_s}\sum_{\mathbf{q}}\sum_{b,b'}v^*_{\mathbf{k}+\mathbf{q},b',s}v_{\mathbf{q},b,s}\langle f|f^\dagger_{\mathbf{k}+\mathbf{q},b',1}f_{\mathbf{q},b,1}-f^\dagger_{\mathbf{k}+\mathbf{q},b',2}f_{\mathbf{q},b,2}|\mathrm{FS}\rangle\Bigg|^2\\ \times\delta(\omega+E_{\mathrm{FS}}-E_f)\ .\end{aligned} \tag{I.5}$$

The states $|1\rangle=f^\dagger_{\mathbf{k}+\mathbf{q},b',1}f_{\mathbf{q},b,1}|\mathrm{FS}\rangle$ and $|2\rangle=f^\dagger_{\mathbf{k}+\mathbf{q},b',2}f_{\mathbf{q},b,2}|\mathrm{FS}\rangle$ are multiparticle eigenstates of $\mathcal{H}_{\mathrm{MF}}$, which are non-zero only if b and b' are such, that $\varepsilon_b(\mathbf{q})<\varepsilon_{\mathrm{F}}$ and $\varepsilon_{b'}(\mathbf{k}+\mathbf{q})>\varepsilon_{\mathrm{F}}$ (meaning that a particle is hopped out of the Fermi sea), since in $|\mathrm{FS}\rangle$ only the bands below the Fermi energy ε_{F} are filled, see Eq. (2.8). Specifically, for the $|\pi\mathrm{FS}\rangle$ discussed in sections 2.3.1 and 2.3.2, $b\in\{1,2\}$ and $b'>2$ (see Eqs. (2.26) and (2.31)). With these notations, we can rewrite the overlap in Eq. (I.5) as $\langle f|1\rangle-\langle f|2\rangle$. Since the particle-hole excited eigenstates of $\mathcal{H}^{\mathrm{MF}}$ are orthogonal to each other, all the $|f\rangle$ giving non-zero overlaps must either be equal to $|1\rangle$ or they must be equal to $|2\rangle$. If $|1\rangle=|2\rangle$, then we get zero anyway, what happens when $\mathbf{k}=\mathbf{0}$, and $b=b'$. Thus, all $|f\rangle$ eigenstates giving non-zero overlaps, must be single particle-hole excitations of the form $|f\rangle=f^\dagger_{\mathbf{k}+\tilde{\mathbf{q}},\tilde{b}',\tilde{\sigma}}f_{\tilde{\mathbf{q}},\tilde{b},\tilde{\sigma}}|\mathrm{FS}\rangle$, and the $\sum_f$ can be replaced by $\sum_{\tilde{\sigma}=1,2}\sum_{\tilde{\mathbf{q}}}\sum_{\tilde{b}',\varepsilon_{\tilde{b}'}(\mathbf{k}+\mathbf{q})>\varepsilon_{\mathrm{F}}}\sum_{\tilde{b},\varepsilon_{\tilde{b}}(\mathbf{q})<\varepsilon_{\mathrm{F}}}$. Consequently, we get

$$\langle f|\left(f^\dagger_{\mathbf{k}+\mathbf{q},b,1}f_{\mathbf{q},b',1}-f^\dagger_{\mathbf{k}+\mathbf{q},b,2}f_{\mathbf{q},b',2}\right)|\mathrm{FS}\rangle=(1-\delta_{\mathbf{k},\mathbf{0}}\delta_{b,b'})\delta_{\tilde{\mathbf{q}},\mathbf{q}}\delta_{\tilde{b},b}\delta_{\tilde{b}',b'}(\delta_{\tilde{\sigma},1}-\delta_{\tilde{\sigma},2}), \tag{I.6}$$

which kills the sums $\sum_{\mathbf{q}}\sum_{b,b'}$ in Eq. (I.5). The sum $\sum_{\tilde{\sigma}=1}^{2}$ together with the term $\delta_{\tilde{\sigma},1}-\delta_{\tilde{\sigma},2}$ gives a factor of 2 since the absolute value squared is the same for both $\tilde{\sigma}=1,2$. Eventually, the dynamical spin structure factor in the mean-field case becomes

$$S^{33}_{\mathrm{MF}}(\mathbf{k},\omega)=\frac{1}{2N_s}\sum_{\tilde{\mathbf{q}}}\sum_{\substack{\tilde{b}'\\ \varepsilon_{\tilde{b}'}(\mathbf{k}+\tilde{\mathbf{q}})>\varepsilon_{\mathrm{F}}}}\sum_{\substack{\tilde{b}\\ \varepsilon_{\tilde{b}}(\tilde{\mathbf{q}})<\varepsilon_{\mathrm{F}}}}\left|\sum_{s\in\{A,B,\dots\}}e^{i\mathbf{k}\cdot\boldsymbol{\delta}_s}v^*_{\mathbf{k}+\tilde{\mathbf{q}},\tilde{b}',s}v_{\tilde{\mathbf{q}},\tilde{b},s}\right|^2\times\delta(\omega+E_{\mathrm{FS}}-E_f)\ , \tag{I.7}$$

Both the E_{FS} and E_f are sums of the filled one-particle energies, and they differ only in the $\varepsilon_b(\mathbf{q})$ that was changed by the single-particle-hole excited eigenstate $|f\rangle=f^\dagger_{\mathbf{k}+\tilde{\mathbf{q}},\tilde{b}',\tilde{\sigma}}f_{\tilde{\mathbf{q}},\tilde{b},\tilde{\sigma}}|\mathrm{FS}\rangle$. This excited state removes the particle with energy $\varepsilon_{\tilde{b}}(\tilde{\mathbf{q}})$ from the Fermi sea, and puts it into the one-particle state with energy $\varepsilon_{\tilde{b}'}(\mathbf{k}+\tilde{\mathbf{q}})$. Therefore, $E_f-E_{\mathrm{GS}}=\varepsilon_{\tilde{b}'}(\mathbf{k}+\tilde{\mathbf{q}})-\varepsilon_{\tilde{b}}(\tilde{\mathbf{q}})$, so we can change the Dirac delta to $\delta(\omega+E_{\mathrm{FS}}-E_f)=\delta(\omega-\varepsilon_{\tilde{b}'}(\mathbf{k}+\tilde{\mathbf{q}})+\varepsilon_{\tilde{b}}(\tilde{\mathbf{q}}))$.

Finally, we can leave off the ˜ notation for convenience, ending up with Eq. (4.8).

Appendix J

Monte Carlo sampling

An expectation value of a quantity B can be written as

$$\langle B \rangle = \sum_x B(x) P(x), \tag{J.1}$$

where $P(x)$ is some probability distribution, and $B(x)$ is the value to be averaged for all possible configurations x. Every probability distribution must satisfy $P(x) \geq 0 \ \forall x$ and $\sum_x P(x) = 1$. This allows us to use Monte Carlo sampling to evaluate such an expectation value, by sampling the configurations with probabilities $P(x)$. We can sample the configurations x with these probabilities using the Metropolis algorithm [110]. For such an algorithm, we need to construct some elementary steps that do not change the configuration x very much, we use pair exchanges of fermions between randomly chosen sites i and j. We start from a random configuration x, and propose a new configuration by randomly choosing a pair of sites for the pair exchange. Every pair is proposed with the same probability, and we accept the proposed configuration with the acceptance probability

$$A(x \to x') = \begin{cases} \dfrac{P(x')}{P(x)}, & \text{if } P(x') < P(x), \\ 1, & \text{if } P(x') > P(x). \end{cases} \tag{J.2}$$

If the configuration x' was accepted, then we propose a new randomly chosen configuration from this state, and iterate this process. If we start from a random configuration, then we need to perform some warmup steps before counting the $B(x)$ to the average, because we can start from a configuration having a very small probability, so counting it to the average would increase the error. After applying some warmup steps, the frequency of sampling a configuration is proportional to its probability $P(x)$ (called thermalization), so averaging the quantities $B(x)$ for many configurations will give an estimate of the expectation value $\langle B \rangle$. The more configurations we sample, the better the estimate of $\langle B \rangle$ becomes. We can characterize how good this estimate is, by the Monte Carlo error (the way to estimate the Monte Carlo error is presented in Appendix J.3).

Usually, people determine the number of warmup steps necessary to achieve thermalization by calculating the autocorrelation time of some quantity. Here we use a different approach, we believe that the sampling was already thermalized after a few times N_s accepted pair exchanges (we emphasize the word accepted), where N_s is the number of lattice sites. We believe so, because starting from a random permutation of the numbers $1 \dots N_s$, we can reach any other permutation with only N_s pair exchanges (Fisher-Yates shuffles).

Similarly, when we average $B(x)$ for different configurations x, to be able to estimate the Monte Carlo errors correctly, we need to average the values of $B(x)$ on uncorrelated configurations x. Since an elementary step (the pair exchanges) does not change the configuration much, the configurations connected with a single elementary step can not be considered to be uncorrelated. For this reason, calculations of $B(x)$ should be done after many elementary steps, when the new configuration is already not correlated with the previous one. Using the argument of Fisher-Yates shuffles again, we believe that N_s pair exchanges are enough to get an uncorrelated configuration.

In some cases, we can use Monte Carlo sampling to estimate sums that are not written in the form of Eq. (J.1), by defining something to be a probability distribution.

J.1 Sampling of the static properties

The expectation value of some quantity B in the state $|\psi\rangle$ can be expressed in the form of Eq. (J.1) as

$$\begin{aligned}\frac{\langle\psi|B|\psi\rangle}{\langle\psi|\psi\rangle} &= \frac{1}{\sum_{x'}\langle\psi|x'\rangle\langle x'|\psi\rangle}\sum_x\langle\psi|B|x\rangle\langle x|\psi\rangle \\ &= \frac{1}{\sum_{x'}|\langle x'|\psi\rangle|^2}\sum_x\langle\psi|x\rangle\langle x|B|x\rangle\langle x|\psi\rangle \\ &= \frac{1}{\sum_{x'}|\langle x'|\psi\rangle|^2}\sum_x\langle x|B|x\rangle|\langle x|\psi\rangle|^2 \\ &= \sum_x\langle x|B|x\rangle P(x) \end{aligned} \tag{J.3}$$

where we inserted the identity as $I=\sum_x|x\rangle\langle x|$ many times, and in the second row we supposed that B is diagonal in the basis $\{|x\rangle\}$. In the last step we defined the probability distribution $P(x)=|\langle x|\psi\rangle|^2/\left(\sum_{x'}|\langle x'|\psi\rangle|^2\right)$ (clearly satisfying $P(x)\geq 0\ \forall x$ and $\sum_x P(x)=1$). When we calculate the ratio of the probabilities in Eq. (J.2), we do not need to calculate the denominator of $P(x)=|\langle x|\psi\rangle|^2/\left(\sum_{x'}|\langle x'|\psi\rangle|^2\right)$, since $P(x')/P(x)=|\langle x'|\psi\rangle|^2/|\langle x|\psi\rangle|^2$. If we use the basis of product states defined in Eq. (2.9) as configurations, and the state $|\psi\rangle$ is a Gutzwiller projected Fermi sea (see Eq. (2.13)), then the $\langle x|\psi\rangle$ is a product of slater determinants of every flavor, so the ratio $|\langle x'|\psi\rangle|^2/|\langle x|\psi\rangle|^2$ involves only the slater determinants of those flavors which were changed in the pair exchange. The update of a Slater determinant in which only the k-th column was changed can be done efficiently with the Sherman-Morrison formula ([111, 112])

$$\det\tilde{A}=\det A\sum_j A^{-1}_{k,j}\tilde{A}_{j,k}, \tag{J.4}$$

where A and $\tilde{A}$ are the old and new Slater matrices, respectively. This efficient update also requires the storage and update of the inverse of the Slater matrix

$$\begin{aligned}\tilde{A}^{-1}_{k,j} &= \frac{\det A}{\det\tilde{A}}A^{-1}_{k,j} \\ \tilde{A}^{-1}_{i,j} &= A^{-1}_{i,j}-\frac{A^{-1}_{k,j}\det A}{\det\tilde{A}}\sum_l A^{-1}_{i,l}\tilde{A}_{l,k}. \end{aligned} \tag{J.5}$$

Furthermore, the Monte Carlo sampling of the configurations makes possible the easy application of the Gutzwiller projection, since all we have to do is to consider only singly occupied product states of the form (2.9), which were denoted as $|x_{P_\mathrm{G}}\rangle$ in Eq. (2.13). In the product basis of states like (2.9) the total fermion number operator $n_i\equiv\sum_{\sigma=1}^N f^\dagger_{i,\sigma}f_{i,\sigma}$ is diagonal, therefore the diagonal spin operators (which can be expressed with the total fermion number operator) are also diagonal (see Eq. (2.2)), allowing us to calculate $\langle\mathrm{FS}|P_\mathrm{G}T^3_iT^3_jP_\mathrm{G}|\mathrm{FS}\rangle=\frac{1}{4}\langle\mathrm{FS}|P_\mathrm{G}(n_{i,1}-n_{i,2})(n_{j,1}-n_{j,2})P_\mathrm{G}|\mathrm{FS}\rangle$.

J.2 Sampling of the dynamical structure factor

In order to evaluate the matrices $\tilde{\mathcal{H}}^{\mathbf{k}}=\langle\mathbf{k},\mathbf{R},\sigma|\mathcal{H}|\mathbf{k},\mathbf{R}',\sigma'\rangle$ and $\tilde{\mathcal{H}}^{\mathbf{k}}=\langle\mathbf{k},\mathbf{R},\sigma|\mathcal{H}|\mathbf{k},\mathbf{R}',\sigma'\rangle$ (where we have hidden the indices $s,\bar{s}$ of the states (4.20) for simplicity) we first insert the

identity operator $\mathbf{I} = \sum_x |x\rangle\langle x|$

$$\tilde{\mathcal{H}}^{\mathbf{k}}_{\mathbf{R},\sigma;\mathbf{R}',\sigma'} = \sum_x \langle \mathbf{k},\mathbf{R},\sigma|x\rangle\langle x|\mathcal{H}|\mathbf{k},\mathbf{R}',\sigma'\rangle$$
$$\mathcal{O}^{\mathbf{k}}_{\mathbf{R},\sigma;\mathbf{R}',\sigma'} = \sum_x \langle \mathbf{k},\mathbf{R},\sigma|x\rangle\langle x|\mathbf{k},\mathbf{R}',\sigma'\rangle, \tag{J.6}$$

where the orthonormal basis $\{|x\rangle\}$ is formed by the product states $|x\rangle$ of Eq. (2.9), with the constraint that every site must be singly occupied (denoted as $|x_{P_G}\rangle$ in Eq. (2.13)) to account for the action of P_G in Eq. 4.20.

For small system sizes (see Figs. 5.1(a)) the expressions above can be evaluated exactly by going through each configuration $|x\rangle$ of the Hilbert space and calculating $\langle x|\mathcal{H}|\mathbf{k},\mathbf{R},\sigma\rangle$ and $\langle x|\mathbf{k},\mathbf{R},\sigma\rangle$. This is what we called the exact variational method in Sections 4.3 and 5.

However, for larger system sizes the direct evaluation becomes difficult, as the size of the Hilbert space grows exponentially. Instead, one can use a Monte Carlo method to evaluate the Hamiltonian and overlap matrix Eqs. (J.6) by random sampling the states $|x\rangle$. To make the sampling efficient, we have to introduce a probability distribution $P(x)$, which should not be small for the configurations for which the quantities $\langle x|\mathcal{H}|\mathbf{k},\mathbf{R},\sigma\rangle$ and $\langle x|\mathbf{k},\mathbf{R},\sigma\rangle$ are not small. In other words, if $P(x)$ is very small for a configuration $\tilde{x}$, then this configuration probably will not sampled, and the values $\langle \tilde{x}|\mathcal{H}|\mathbf{k},\mathbf{R},\sigma\rangle$ and $\langle \tilde{x}|\mathbf{k},\mathbf{R},\sigma\rangle$ will not be counted to the average, even if they are big. The simplest way to introduce the probability distribution $P(x)$ is the reweighting technique, in which we multiply and divide Eqs. (J.6) by $P(x)$ as

$$\tilde{\mathcal{H}}^{\mathbf{k}}_{\mathbf{R},\sigma,\mathbf{R}',\sigma'} = \sum_x \frac{\langle \mathbf{k},\mathbf{R},\sigma|x\rangle}{\sqrt{P(x)}} \frac{\langle x|\mathcal{H}|\mathbf{k},\mathbf{R}',\sigma'\rangle}{\sqrt{P(x)}} P(x) \ ,$$
$$\mathcal{O}^{\mathbf{k}}_{\mathbf{R},\sigma,\mathbf{R}',\sigma'} = \sum_x \frac{\langle \mathbf{k},\mathbf{R},\sigma|x\rangle}{\sqrt{P(x)}} \frac{\langle x|\mathbf{k},\mathbf{R}',\sigma'\rangle}{\sqrt{P(x)}} P(x), \tag{J.7}$$

meaning that we can use $P(x)$ for the importance sampling of the configurations x, and calculate the quantities $\frac{\langle \mathbf{k},\mathbf{R},\sigma|x\rangle}{\sqrt{P(x)}} \frac{\langle x|\mathcal{H}|\mathbf{k},\mathbf{R}',\sigma'\rangle}{\sqrt{P(x)}}$ and $\frac{\langle \mathbf{k},\mathbf{R},\sigma|x\rangle}{\sqrt{P(x)}} \frac{\langle x|\mathbf{k},\mathbf{R}',\sigma'\rangle}{\sqrt{P(x)}}$ to be averaged. $P(x)$ must satisfy $P(x) \geq 0 \ \forall x$ and $\sum_x P(x) = 1$, otherwise we can not use it for importance sampling (not even if we use the Metropolis algorithm). The normalization condition would be a problem, because when we introduce some $\tilde{P}(x)$ we have to divide it with its norm to get $P(x) = \tilde{P}(x)/\sum_{x'} \tilde{P}(x')$, which we can not calculate due to the enormous size of the Hilbert space. This would not be a problem for the importance sampling, because the Metropolis algorithm needs only the ratios $P(x')/P(x)$, but the $P(x)$ appears even in the quantities to be averaged. Luckily, the matrices $\mathcal{H}^{\mathbf{k}}$ and $\mathcal{O}^{\mathbf{k}}$ are used in the generalized eigenvalue problem $\mathcal{H}^{\mathbf{k}}|f^{\mathbf{k}}\rangle = E^{\mathbf{k}}_f \mathcal{O}^{\mathbf{k}}|f^{\mathbf{k}}\rangle$, implying that we can multiply both $\mathcal{H}^{\mathbf{k}}$ and $\mathcal{O}^{\mathbf{k}}$ with the same number (which must be independent of x) without changing the $E^{\mathbf{k}}_f$ or the $|f^{\mathbf{k}}\rangle$. Therefore, we can multiply both with the norm $\sum_{x'} \tilde{P}(x')$ to get the unnormalized $\tilde{P}(x)$ in the denominators as

$$\tilde{\mathcal{H}}^{\mathbf{k}}_{\mathbf{R},\sigma,\mathbf{R}',\sigma'} = \sum_x \frac{\langle \mathbf{k},\mathbf{R},\sigma|x\rangle}{\sqrt{\tilde{P}(x)}} \frac{\langle x|\mathcal{H}|\mathbf{k},\mathbf{R}',\sigma'\rangle}{\sqrt{\tilde{P}(x)}} P(x) \ ,$$
$$\mathcal{O}^{\mathbf{k}}_{\mathbf{R},\sigma,\mathbf{R}',\sigma'} = \sum_x \frac{\langle \mathbf{k},\mathbf{R},\sigma|x\rangle}{\sqrt{\tilde{P}(x)}} \frac{\langle x|\mathbf{k},\mathbf{R}',\sigma'\rangle}{\sqrt{\tilde{P}(x)}} P(x), \tag{J.8}$$

The probability distribution $P(x)$ can be chosen in many ways, before presenting our choice we give a brief overview of the choices used in previous papers. In Refs. [88, 89], Li and Yang chose the probability distribution

$$P^{\mathbf{k}}(x) = \frac{\sum_{\mathbf{q},\sigma} |\langle x|\mathbf{k},\mathbf{q},\sigma\rangle|^2}{\sum_x \sum_{\mathbf{q},\sigma} |\langle x|\mathbf{k},\mathbf{q},\sigma\rangle|^2}, \tag{J.9}$$

also followed by [90], where the states $|\mathbf{k},\mathbf{q},\sigma\rangle = P_{\mathrm{G}} f^{\dagger}_{\mathbf{k}+\mathbf{q},\sigma} f_{\mathbf{q},\sigma}|\mathrm{FS}\rangle$ were introduced in Eq. (4.9). This probability distribution was used to sample the block matrices $\tilde{\mathcal{H}}^{\mathbf{k}}$ and $\mathcal{O}^{\mathbf{k}}$, which meant a separate Monte Carlo simulation for each $\mathbf{k}$.

On the other hand, Ferrari *et al.* [91] sampled according to the weight of $|x\rangle$ in the approximating ground state,

$$P(x) = \frac{|\langle x|P_{\mathrm{G}}|\mathrm{FS}\rangle|^2}{\sum_x |\langle x|P_{\mathrm{G}}|\mathrm{FS}\rangle|^2}, \tag{J.10}$$

where $\langle x|P_{\mathrm{G}}|\mathrm{FS}\rangle$ is a product of real Slater determinants (2.10). The advantage is the ability to sample all the block matrices $\tilde{\mathcal{H}}^{\mathbf{k}}$ and $\mathcal{O}^{\mathbf{k}}$ simultaneously. Furthermore, the terms

$$\frac{\langle x|\mathcal{H}|\mathbf{k},\mathbf{R},\sigma\rangle}{\langle x|P_{\mathrm{G}}|\mathrm{FS}\rangle} = \frac{1}{\sqrt{L}} \sum_{\mathbf{R}'} e^{i\mathbf{k}\cdot\mathbf{R}'} \frac{\langle x|\mathcal{H} P_{\mathrm{G}} f^{\dagger}_{\mathbf{R}+\mathbf{R}',\sigma} f_{\mathbf{R}',\sigma}|\mathrm{FS}\rangle}{\langle x|P_{\mathrm{G}}|\mathrm{FS}\rangle} \tag{J.11}$$

and

$$\frac{\langle x|\mathbf{k},\mathbf{R},\sigma\rangle}{\langle x|P_{\mathrm{G}}|\mathrm{FS}\rangle} = \frac{1}{\sqrt{L}} \sum_{\mathbf{R}'} e^{i\mathbf{k}\cdot\mathbf{R}'} \frac{\langle x|P_{\mathrm{G}} f^{\dagger}_{\mathbf{R}+\mathbf{R}',\sigma} f_{\mathbf{R}',\sigma}|\mathrm{FS}\rangle}{\langle x|P_{\mathrm{G}}|\mathrm{FS}\rangle}\ , \tag{J.12}$$

appearing in the expressions (J.8) can be calculated very efficiently using the Sherman-Morrison formula, since they reduce to quotients of real Slater determinants (2.11) which differ in a single column only. However, configurations which are important for the excited states, but unimportant for the ground state will be sampled rarely: the $|\langle x_1|P_{\mathrm{G}}|\mathrm{FS}\rangle| \gg |\langle x_2|P_{\mathrm{G}}|\mathrm{FS}\rangle|$ condition does not imply $|\langle x_1|\mathbf{k},\mathbf{R},\sigma\rangle| \gg |\langle x_2|\mathbf{k},\mathbf{R},\sigma\rangle|$ nor $|\langle x_1|\mathcal{H}|\mathbf{k},\mathbf{R},\sigma\rangle| \gg |\langle x_2|\mathcal{H}|\mathbf{k},\mathbf{R},\sigma\rangle|$. Thus, the $|x_2\rangle$ may be just as important for some excited states as $|x_1\rangle$ is for the ground state, yet it will be sampled with a much smaller probability.

Mei and Wen used an importance sampling similar to (J.10), with the difference of working in the subspace of $S^z_T = 1$, and replacing the $P_{\mathrm{G}}|\mathrm{FS}\rangle$ with the lowest energy mean-field particle-hole state in this subspace [113].

We used the probability distribution

$$P(x) = \frac{\max_{\mathbf{R},\mathbf{R}',\sigma} |\langle x|\mathbf{R},\mathbf{R}',\sigma\rangle|}{\sum_x \max_{\mathbf{R},\mathbf{R}',\sigma} |\langle x|\mathbf{R},\mathbf{R}',\sigma\rangle|}, \tag{J.13}$$

where the states

$$|\mathbf{R},\mathbf{R}',\sigma\rangle \equiv P_{\mathrm{G}} f^{\dagger}_{\mathbf{R},\sigma} f_{\mathbf{R}',\sigma}|\mathrm{FS}\rangle \tag{J.14}$$

were introduced in Eq. (4.11).

As noted in Sec. (4.3) these states are connected with the states $|\mathbf{k},\mathbf{R},\sigma\rangle$ as

$$|\mathbf{k},\mathbf{R},\sigma\rangle = \frac{1}{\sqrt{L}} \sum_{\mathbf{R}'} e^{i\mathbf{k}\cdot\mathbf{R}'} |\mathbf{R}+\mathbf{R}',\mathbf{R}',\sigma\rangle. \tag{J.15}$$

Therefore, if the weight $\max_{\mathbf{R},\mathbf{R}',\sigma} |\langle x|\mathbf{R},\mathbf{R}',\sigma\rangle|$ is small for a given configuration $|x\rangle$, the weights $|\langle x|\mathbf{k},\mathbf{R},\sigma\rangle|$ will also be small $\forall \mathbf{k},\mathbf{R}$. Since the weights $\langle x|\mathbf{k},\mathbf{R},\sigma\rangle$ appears in both $\tilde{\mathcal{H}}^{\mathbf{k}}$ and $\tilde{\mathcal{O}}^{\mathbf{k}}$, if $\max_{\mathbf{R},\mathbf{R}',\sigma} |\langle x|\mathbf{R},\mathbf{R}',\sigma\rangle|$ is small, the contribution of this configuration to the matrices $\tilde{\mathcal{H}}^{\mathbf{k}}$ and $\tilde{\mathcal{O}}^{\mathbf{k}}$ will also be small, implying that every important configuration will be sampled with large probability.

The choice of the maximum norm in (J.13) is arbitrary. Any norm of $\langle x|\mathbf{R},\mathbf{R}',\sigma\rangle$ is suitable for importance sampling. The norm in Eq. (J.13) is a special case of the p-norm

$$P(x) = \frac{\left(\sum_{|\mathbf{R},\mathbf{R}',\sigma\rangle} |\langle x|\mathbf{R},\mathbf{R}',\sigma\rangle|^p\right)^{1/p}}{\sum_x \left(\sum_{|\mathbf{R},\mathbf{R}',\sigma\rangle} |\langle x|\mathbf{R},\mathbf{R}',\sigma\rangle|^p\right)^{1/p}}, \tag{J.16}$$

with $p = \infty$.

On the one hand, this importance sampling is slower than that of Eq. (J.10) used by Ferrari *et al.* in Ref. [91], since in each elementary step we have to calculate the NN_s^2 elements of $\langle x|\mathbf{R}, \mathbf{R}', s, \bar{s}, \sigma\rangle$ (here we have taken back the hidden sublattice indices). But these elements are products of Slater determinants out of which one differs from those in $\langle x|P_{\mathrm{G}}|\mathrm{FS}\rangle$ in a single column only, so they can be calculated efficiently using Eqs. (J.4) and (J.5), provided that the inverse matrix exists (which is not always the case). On the other hand, the configurations that are important only for some of the states $|\mathbf{k}, \mathbf{R}, \sigma$, but are not important for the $P_{\mathrm{G}}|\mathrm{FS}\rangle$, are sampled with higher probabilities.

As already mentioned, the numerator $\sum_x \max_{\mathbf{R}',\mathbf{R}'',\sigma} |\langle x|\mathbf{R}', \mathbf{R}'', \sigma\rangle|$ of Eq. (J.13) is independent of $|x\rangle$ and it multiplies both the $\tilde{\mathcal{H}}^{\mathbf{k}}$ and the $\tilde{\mathcal{O}}^{\mathbf{k}}$, so it falls out from the generalized eigenvalue problem, and we do not have to measure it at all. Thus, the measurement of $\tilde{\mathcal{H}}^{\mathbf{k}}$ and $\tilde{\mathcal{O}}^{\mathbf{k}}$ for a given configuration $|x\rangle$ consists of calculating the quantities

$$\frac{\langle x|\mathcal{H}|\mathbf{k}, \mathbf{R}, \sigma\rangle}{\sqrt{\max_{\mathbf{R}',\mathbf{R}'',\sigma} |\langle x|\mathbf{R}', \mathbf{R}'', \sigma\rangle|}} \tag{J.17}$$

and

$$\frac{\langle x|\mathbf{k}, \mathbf{R}, \sigma\rangle}{\sqrt{\max_{\mathbf{R}',\mathbf{R}'',\sigma} |\langle x|\mathbf{R}', \mathbf{R}'', \sigma\rangle|}}. \tag{J.18}$$

The difficulty is in measuring $\langle x|\mathcal{H}|\mathbf{k}, \mathbf{R}, \sigma\rangle$, since $\langle x|\mathbf{k}, \mathbf{R}, \sigma\rangle$ can be calculated from $\langle x|\mathbf{R}, \mathbf{R}', \sigma\rangle$ using Eq. (J.15), and $\langle x|\mathbf{R}, \mathbf{R}', \sigma\rangle$ was already calculated during importance sampling.

J.3 Estimation of Monte Carlo errors

We run the program typically a hundred times for each system size. Let us denote the number of runs by $M(N_s)$ for a system with N_s sites. In the i^{th} run we obtained the subaverage $Q_i(N_s)$, and we have $M(N_s)$ runs so $i = 1, \ldots, M(N_s)$. The total average

$$\langle Q(N_s)\rangle = \frac{1}{M(N_s)} \sum_{i=1}^{M(N_s)} Q_i(N_s) \tag{J.19}$$

is the result of the MC calculation, with the standard error

$$\sigma_Q(N_s) = \sqrt{\frac{\sum_{i=1}^{M(N_s)} [Q_i(N_s) - \langle Q(N_s)\rangle]^2}{M(N_s)[M(N_s) - 1]}}. \tag{J.20}$$

We plot the above standard errors in the figures.

Some quantities were calculated by fitting functions to the data and optimizing the parameters of the functions by the non-linear least squares method, using scipy.curve_fit. The errors of the optimized parameters were estimated by passing the $\sigma_Q(N_s)$ of the data we wanted to fit on, setting the flag absolute_sigma = True, and taking the square root of the returned variance.

For the estimation of the error of the central charge (in Sec. 5) we used the error propagation formula

$$\sigma_{\frac{A}{B}} = \frac{A}{B}\sqrt{\left(\frac{\sigma_A}{A}\right)^2 + \left(\frac{\sigma_B}{B}\right)^2}, \tag{J.21}$$

where in our case $A = vc$ and $B = v$.

Appendix K

Details of the generalized eigenvalue problem

Not all of the states (4.9) or (4.20) are linearly independent. The linear dependencies show up as zero eigenvalues of the overlap matrix. To solve the generalized eigenvalue problem, the overlap matrix has to be positive definite (it can not have zero eigenvalues), therefore we have to perform a basis transformation to remove the numerically zero eigenvalues. This could be problematic if some of the positive eigenvalues of the overlap matrix were so small, that we could not distinguish between positive eigenvalues and zero eigenvalues, due to the Monte Carlo error. Fortunately, the positive eigenvalues of the overlap matrix are separated from the zero eigenvalues with a gap of many orders of magnitude.

To eliminate the zero eigenvalues of the overlap matrix, following Appendix F.2 in the PhD thesis https://hdl.handle.net/20.500.11767/103865, we first diagonalize $\tilde{\mathcal{O}}^{\mathbf{k}}$ as

$$\overline{\mathcal{O}}^{\mathbf{k}} = \mathcal{U}^{\dagger\mathbf{k}}\tilde{\mathcal{O}}^{\mathbf{k}}\mathcal{U}^{\mathbf{k}}, \tag{K.1}$$

where $\overline{\mathcal{O}}^{\mathbf{k}}$ is a diagonal matrix containing the sorted eigenvalues of $\tilde{\mathcal{O}}^{\mathbf{k}}$ in decreasing order, and $\mathcal{U}^{\mathbf{k}}$ is the matrix having the eigenstates of $\tilde{\mathcal{O}}^{\mathbf{k}}$ in its columns, in the order of the corresponding eigenvalues in $\overline{\mathcal{O}}^{\mathbf{k}}$. The eigenstates of $\tilde{\mathcal{O}}^{\mathbf{k}}$ in the columns of $\mathcal{U}^{\mathbf{k}}$ are expressed in the basis of Gutzwiller projected particle-hole excitations (4.20) as $|\overline{\mathbf{k}, \mathbf{R}, s, \bar{s}, \sigma}\rangle = \sum_{\mathbf{R}',s',\bar{s}',\sigma'} \mathcal{U}^{\mathbf{k}}_{\mathbf{R},s,\bar{s},\sigma,\mathbf{R}',s',\bar{s}',\sigma'} |\mathbf{k}, \mathbf{R}', s', \bar{s}', \sigma'\rangle$. Next, we calculate $\overline{\mathcal{H}}^{\mathbf{k}} \equiv \mathcal{U}^{\dagger\mathbf{k}}\tilde{\mathcal{H}}^{\mathbf{k}}\mathcal{U}^{\mathbf{k}}$ (which is not diagonal) and we reduce both $\overline{\mathcal{H}}^{\mathbf{k}}$ and $\overline{\mathcal{O}}^{\mathbf{k}}$ to the subspace of positive eigenvalues. To achieve this, if $\overline{\mathcal{O}}^{\mathbf{k}}$ has n_z zero eigenvalues, then we remove the n_z last rows and the n_z last columns of $\overline{\mathcal{H}}^{\mathbf{k}}$ and $\overline{\mathcal{O}}^{\mathbf{k}}$ (meaning that we eliminate the last n_z states $|\overline{\mathbf{k}, \mathbf{R}, s, \bar{s}, \sigma}\rangle$). Denoting the reduced matrices as $\overline{\mathcal{H}}^{\mathbf{k},R}$ and $\overline{\mathcal{O}}^{\mathbf{k},R}$ we solve the generalized eigenvalue problem

$$\overline{\mathcal{H}}^{\mathbf{k},R}|\overline{f}^{\mathbf{k}}\rangle = \overline{\mathcal{O}}^{\mathbf{k},R}|\overline{f}^{\mathbf{k}}\rangle. \tag{K.2}$$

This way, we get the approximating eigenstates $|\overline{f}^{\mathbf{k}}\rangle$ in the reduced basis of the eigenstates of the overlap matrix as

$$|\overline{f}^{\mathbf{k}}\rangle = \sum_{\mathbf{R},s,\bar{s},\sigma} \overline{A}^{f,\mathbf{k}}_{\mathbf{R},s,\bar{s},\sigma} |\overline{\mathbf{k}, \mathbf{R}, s, \bar{s}, \sigma}\rangle \tag{K.3}$$

To get the approximating eigenstates in the original basis $|\mathbf{k}, \mathbf{R}, s, \bar{s}, \sigma\rangle$ given in Eq. (4.34), we first complete the coefficients $\overline{A}^{f,\mathbf{k}}_{\mathbf{R},s,\bar{s},\sigma}$ with n_z zeros, so that we take back the eliminated eigenstates $|\overline{\mathbf{k}, \mathbf{R}, s, \bar{s}, \sigma}\rangle$ in the subspace of zero eigenvalues, and use

$$\begin{aligned} |\overline{f}^{\mathbf{k}}\rangle &= \sum_{\substack{\mathbf{R},s,\bar{s},\sigma \\ \mathbf{R}',s',\bar{s}',\sigma'}} \overline{A}^{f,\mathbf{k}}_{\mathbf{R},s,\bar{s},\sigma} \mathcal{U}^{\mathbf{k}}_{\mathbf{R},s,\bar{s},\sigma,\mathbf{R}',s',\bar{s}',\sigma'} |\mathbf{k}, \mathbf{R}', s', \bar{s}', \sigma'\rangle \\ &= \sum_{\mathbf{R},s,\bar{s},\sigma} A^{f,\mathbf{k}}_{\mathbf{R},s,\bar{s},\sigma} |\mathbf{k}, \mathbf{R}, s, \bar{s}, \sigma\rangle. \end{aligned} \tag{K.4}$$

This means, that the coefficients in Eq. (4.34) are given by

$$A^{f,\mathbf{k}}_{\mathbf{R},s,\bar{s},\sigma} = \sum_{\mathbf{R}',s',\bar{s}',\sigma'} \overline{A}^{f,\mathbf{k}}_{\mathbf{R},s,\bar{s},\sigma} \mathcal{U}^{\mathbf{k}}_{\mathbf{R},s,\bar{s},\sigma,\mathbf{R}',s',\bar{s}',\sigma'}. \tag{K.5}$$

Bibliography

[1] D. C. Tsui, H. L. Stormer, and A. C. Gossard, "Two-dimensional magnetotransport in the extreme quantum limit," *Phys. Rev. Lett.*, vol. 48, pp. 1559–1562, May 1982. [Online]. Available: https://link.aps.org/doi/10.1103/PhysRevLett.48.1559

[2] X.-G. Wen, *Quantum Field Theory of Many-Body Systems: From the Origin of Sound to an Origin of Light and Electrons*. Oxford University Press, 09 2007. [Online]. Available: https://doi.org/10.1093/acprof:oso/9780199227259.001.0001

[3] ——, "Quantum orders and symmetric spin liquids," *Phys. Rev. B*, vol. 65, p. 165113, Apr 2002. [Online]. Available: https://link.aps.org/doi/10.1103/PhysRevB.65.165113

[4] P. Fazekas, *Lecture Notes on Electron Correlation and Magnetism*. WORLD SCIENTIFIC, 1999. [Online]. Available: https://www.worldscientific.com/doi/abs/10.1142/2945

[5] Y. Ran and X.-G. Wen, "Continuous quantum phase transitions beyond Landau's paradigm in a large-N spin model," *arXiv: Strongly Correlated Electrons*, 2006. [Online]. Available: https://api.semanticscholar.org/CorpusID:116902931

[6] P. Corboz, M. Lajkó, A. M. Läuchli, K. Penc, and F. Mila, "Spin-orbital quantum liquid on the honeycomb lattice," *Phys. Rev. X*, vol. 2, p. 041013, Nov 2012. [Online]. Available: https://link.aps.org/doi/10.1103/PhysRevX.2.041013

[7] M. C. Gutzwiller, "Effect of correlation on the ferromagnetism of transition metals," *Phys. Rev. Lett.*, vol. 10, pp. 159–162, Mar 1963. [Online]. Available: https://link.aps.org/doi/10.1103/PhysRevLett.10.159

[8] J. Hubbard and B. H. Flowers, "Electron correlations in narrow energy bands," *Proceedings of the Royal Society of London. Series A. Mathematical and Physical Sciences*, vol. 276, no. 1365, pp. 238–257, 1963. [Online]. Available: https://royalsocietypublishing.org/doi/abs/10.1098/rspa.1963.0204

[9] J. Kanamori, "Electron correlation and ferromagnetism of transition metals," *Progress of Theoretical Physics*, vol. 30, no. 3, pp. 275–289, 09 1963. [Online]. Available: https://doi.org/10.1143/PTP.30.275

[10] M. Lewenstein, A. Sanpera, and V. Ahufinger, *Ultracold Atoms in Optical Lattices: Simulating quantum many-body systems*. Oxford University Press, 03 2012. [Online]. Available: https://doi.org/10.1093/acprof:oso/9780199573127.001.0001

[11] D. Jaksch, C. Bruder, J. I. Cirac, C. W. Gardiner, and P. Zoller, "Cold bosonic atoms in optical lattices," *Phys. Rev. Lett.*, vol. 81, pp. 3108–3111, Oct 1998. [Online]. Available: https://link.aps.org/doi/10.1103/PhysRevLett.81.3108

[12] W. Hofstetter, J. I. Cirac, P. Zoller, E. Demler, and M. D. Lukin, "High-temperature superfluidity of fermionic atoms in optical lattices," *Phys. Rev. Lett.*, vol. 89, p. 220407, Nov 2002. [Online]. Available: https://link.aps.org/doi/10.1103/PhysRevLett.89.220407

[13] G. Modugno, F. Ferlaino, R. Heidemann, G. Roati, and M. Inguscio, "Production of a fermi gas of atoms in an optical lattice," *Phys. Rev. A*, vol. 68, p. 011601, Jul 2003. [Online]. Available: https://link.aps.org/doi/10.1103/PhysRevA.68.011601

[14] M. Köhl, H. Moritz, T. Stöferle, K. Günter, and T. Esslinger, "Fermionic atoms in a three dimensional optical lattice: Observing fermi surfaces, dynamics, and interactions," *Phys. Rev. Lett.*, vol. 94, p. 080403, Mar 2005. [Online]. Available: https://link.aps.org/doi/10.1103/PhysRevLett.94.080403

[15] A. V. Gorshkov, M. Hermele, V. Gurarie, C. Xu, P. S. Julienne, J. Ye, P. Zoller, E. Demler, M. D. Lukin, and A. M. Rey, "Two-orbital su(n) magnetism with ultracold alkaline-earth atoms," *Nature Physics*, vol. 6, no. 4, pp. 289–295, feb 2010. [Online]. Available: https://doi.org/10.1038/nphys1535

[16] B. J. DeSalvo, M. Yan, P. G. Mickelson, Y. N. Martinez de Escobar, and T. C. Killian, "Degenerate fermi gas of ^{87}Sr," *Phys. Rev. Lett.*, vol. 105, p. 030402, Jul 2010. [Online]. Available: https://link.aps.org/doi/10.1103/PhysRevLett.105.030402

[17] M. K. Tey, S. Stellmer, R. Grimm, and F. Schreck, "Double-degenerate bose-fermi mixture of strontium," *Phys. Rev. A*, vol. 82, p. 011608, Jul 2010. [Online]. Available: https://link.aps.org/doi/10.1103/PhysRevA.82.011608

[18] T. Fukuhara, Y. Takasu, M. Kumakura, and Y. Takahashi, "Degenerate fermi gases of ytterbium," *Phys. Rev. Lett.*, vol. 98, p. 030401, Jan 2007. [Online]. Available: https://link.aps.org/doi/10.1103/PhysRevLett.98.030401

[19] M. A. Cazalilla, A. F. Ho, and M. Ueda, "Ultracold gases of ytterbium: ferromagnetism and Mott states in an SU(6) Fermi system," *New Journal of Physics*, vol. 11, no. 10, p. 103033, oct 2009. [Online]. Available: https://dx.doi.org/10.1088/1367-2630/11/10/103033

[20] S. Taie, Y. Takasu, S. Sugawa, R. Yamazaki, T. Tsujimoto, R. Murakami, and Y. Takahashi, "Realization of a SU(2) × SU(6) system of fermions in a cold atomic gas," *Phys. Rev. Lett.*, vol. 105, p. 190401, Nov 2010. [Online]. Available: https://link.aps.org/doi/10.1103/PhysRevLett.105.190401

[21] S. Taie, R. Yamazaki, S. Sugawa, and Y. Takahashi, "An su(6) mott insulator of an atomic fermi gas realized by large-spin pomeranchuk cooling," *Nature Physics*, vol. 8, no. 11, pp. 825–830, sep 2012. [Online]. Available: https://doi.org/10.1038/nphys2430

[22] G. Pagano, M. Mancini, G. Cappellini, P. Lombardi, F. Schäfer, H. Hu, X.-J. Liu, J. Catani, C. Sias, M. Inguscio, and L. Fallani, "A one-dimensional liquid of fermions with tunable spin," *Nature Physics*, vol. 10, no. 3, pp. 198–201, feb 2014. [Online]. Available: https://doi.org/10.1038/nphys2878

[23] C. Hofrichter, L. Riegger, F. Scazza, M. Höfer, D. R. Fernandes, I. Bloch, and S. Fölling, "Direct probing of the mott crossover in the SU(n) fermi-hubbard model," *Phys. Rev. X*, vol. 6, p. 021030, Jun 2016. [Online]. Available: https://link.aps.org/doi/10.1103/PhysRevX.6.021030

[24] B. Song, C. He, S. Zhang, E. Hajiyev, W. Huang, X.-J. Liu, and G.-B. Jo, "Spin-orbit-coupled two-electron fermi gases of ytterbium atoms," *Phys. Rev. A*, vol. 94, p. 061604, Dec 2016. [Online]. Available: https://link.aps.org/doi/10.1103/PhysRevA.94.061604

[25] B. Song, Y. Yan, C. He, Z. Ren, Q. Zhou, and G.-B. Jo, "Evidence for bosonization in a three-dimensional gas of SU(n) fermions," *Phys. Rev. X*, vol. 10, p. 041053, Dec 2020. [Online]. Available: https://link.aps.org/doi/10.1103/PhysRevX.10.041053

[26] B. Abeln, K. Sponselee, M. Diem, N. Pintul, K. Sengstock, and C. Becker, "Interorbital interactions in an su(2) $\bigotimes$ su(6)-symmetric fermi-fermi mixture," *Phys. Rev. A*, vol. 103, p. 033315, Mar 2021. [Online]. Available: https://link.aps.org/doi/10.1103/PhysRevA.103.033315

[27] S. Taie, E. Ibarra-García-Padilla, N. Nishizawa, Y. Takasu, Y. Kuno, H.-T. Wei, R. T. Scalettar, K. R. A. Hazzard, and Y. Takahashi, "Observation of antiferromagnetic correlations in an ultracold su(n) hubbard model," *Nature Physics*, vol. 18, no. 11, pp. 1356–1361, sep 2022. [Online]. Available: https://doi.org/10.1038/s41567-022-01725-6

[28] C. Wu, "Competing orders in one-dimensional spin-3/2 fermionic systems," *Phys. Rev. Lett.*, vol. 95, p. 266404, Dec 2005. [Online]. Available: https://link.aps.org/doi/10.1103/PhysRevLett.95.266404

[29] A. V. Gorshkov, M. Hermele, V. Gurarie, C. Xu, P. S. Julienne, J. Ye, P. Zoller, E. Demler, M. D. Lukin, and A. M. Rey, "Two-orbital SU(N) magnetism with ultracold alkaline-earth atoms," *Nature Physics*, vol. 6, no. 4, pp. 289–295, 2010. [Online]. Available: https://doi.org/10.1038/nphys1535

[30] K. I. Kugel' and D. I. Khomskiĭ, "The jahn-teller effect and magnetism: transition metal compounds," *Soviet Physics Uspekhi*, vol. 25, no. 4, p. 231, apr 1982. [Online]. Available: https://dx.doi.org/10.1070/PU1982v025n04ABEH004537

[31] C. Castellani, C. R. Natoli, and J. Ranninger, "Magnetic structure of v_2o_3 in the insulating phase," *Phys. Rev. B*, vol. 18, pp. 4945–4966, Nov 1978. [Online]. Available: https://link.aps.org/doi/10.1103/PhysRevB.18.4945

[32] Castellani, C. and Natoli, C. R. and Ranninger, J., "Insulating phase of V_2O_3: An attempt at a realistic calculation," *Phys. Rev. B*, vol. 18, pp. 4967–5000, Nov 1978. [Online]. Available: https://link.aps.org/doi/10.1103/PhysRevB.18.4967

[33] N. F. Q. Yuan and L. Fu, "Model for the metal-insulator transition in graphene superlattices and beyond," *Phys. Rev. B*, vol. 98, p. 045103, Jul 2018. [Online]. Available: https://link.aps.org/doi/10.1103/PhysRevB.98.045103

[34] J. W. F. Venderbos and R. M. Fernandes, "Correlations and electronic order in a two-orbital honeycomb lattice model for twisted bilayer graphene," *Phys. Rev. B*, vol. 98, p. 245103, Dec 2018. [Online]. Available: https://link.aps.org/doi/10.1103/PhysRevB.98.245103

[35] M. Angeli and A. H. MacDonald, "Γ valley transition metal dichalcogenide moiré bands," *Proceedings of the National Academy of Sciences*, vol. 118, no. 10, p. e2021826118, 2021. [Online]. Available: https://www.pnas.org/doi/abs/10.1073/pnas.2021826118

[36] L. Xian, M. Claassen, D. Kiese, M. M. Scherer, S. Trebst, D. M. Kennes, and A. Rubio, "Realization of nearly dispersionless bands with strong orbital anisotropy from destructive interference in twisted bilayer MoS2," *Nature Communications*, vol. 12, no. 1, p. 5644, 2021. [Online]. Available: https://doi.org/10.1038/s41467-021-25922-8

[37] Y.-H. Zhang, D. N. Sheng, and A. Vishwanath, "SU(4) chiral spin liquid, exciton supersolid, and electric detection in Moiré bilayers," *Phys. Rev. Lett.*, vol. 127, p. 247701, Dec 2021. [Online]. Available: https://link.aps.org/doi/10.1103/PhysRevLett.127.247701

[38] M. G. Yamada, M. Oshikawa, and G. Jackeli, "Emergent SU(4) Symmetry in $\alpha-ZrCl_3$ and Crystalline Spin-Orbital Liquids," *Phys. Rev. Lett.*, vol. 121, p. 097201, Aug 2018. [Online]. Available: https://link.aps.org/doi/10.1103/PhysRevLett.121.097201

[39] Yamada, Masahiko G. and Oshikawa, Masaki and Jackeli, George, "SU(4)-symmetric quantum spin-orbital liquids on various lattices," *Phys. Rev. B*, vol. 104, p. 224436, Dec 2021. [Online]. Available: https://link.aps.org/doi/10.1103/PhysRevB.104.224436

[40] B. Swaroop and S. N. Flengas, "The synthesis of anhydrous zirconium trichloride," *Canadian Journal of Chemistry*, vol. 42, no. 6, pp. 1495–1498, 1964. [Online]. Available: https://doi.org/10.1139/v64-228

[41] ——, "Crystal structure of zirconium trichloride," *Canadian Journal of Physics*, vol. 42, no. 10, pp. 1886–1889, 1964. [Online]. Available: https://doi.org/10.1139/p64-177

[42] R. L. Daake and J. D. Corbett, "Synthesis and nonstoichiometry of the zirconium trihalides," *Inorganic Chemistry*, vol. 17, no. 5, pp. 1192–1195, 1978. [Online]. Available: https://doi.org/10.1021/ic50183a020

[43] A. V. Ushakov, I. V. Solovyev, and S. V. Streltsov, "Can the highly symmetric su(4) spin-orbital model be realized in α-zrcl$_3$?" *Pis'ma Zh. Eksp. Teor. Fiz.*, vol. 112, no. 686, 2020. [Online]. Available: https://www.elibrary.ru/item.asp?id=44216306

[44] K. I. Kugel, D. I. Khomskii, A. O. Sboychakov, and S. V. Streltsov, "Spin-orbital interaction for face-sharing octahedra: Realization of a highly symmetric SU(4) model," *Phys. Rev. B*, vol. 91, p. 155125, Apr 2015. [Online]. Available: https://link.aps.org/doi/10.1103/PhysRevB.91.155125

[45] H. E. Haber, "Useful relations among the generators in the defining and adjoint representations of SU(N)," *SciPost Phys. Lect. Notes*, p. 21, 2021. [Online]. Available: https://scipost.org/10.21468/SciPostPhysLectNotes.21

[46] M. Gell-Mann, "Symmetries of baryons and mesons," *Phys. Rev.*, vol. 125, pp. 1067–1084, Feb 1962. [Online]. Available: https://link.aps.org/doi/10.1103/PhysRev.125.1067

[47] G. Baskaran, Z. Zou, and P. Anderson, "The resonating valence bond state and high-tc superconductivity — a mean field theory," *Solid State Communications*, vol. 63, no. 11, pp. 973–976, 1987. [Online]. Available: https://www.sciencedirect.com/science/article/pii/0038109887906429

[48] G. Baskaran, "The resonating valence bond state and high temperature superconductivity," *Physica B+C*, vol. 148, no. 1, pp. 200–203, 1987. [Online]. Available: https://www.sciencedirect.com/science/article/pii/0378436387901914

[49] I. Affleck and J. B. Marston, "Large-N limit of the Heisenberg-Hubbard model: Implications for high-T_c superconductors," *Phys. Rev. B*, vol. 37, pp. 3774–3777, Mar 1988. [Online]. Available: https://link.aps.org/doi/10.1103/PhysRevB.37.3774

[50] J. B. Marston and I. Affleck, "Large-N limit of the Hubbard-Heisenberg model," *Phys. Rev. B*, vol. 39, pp. 11 538–11 558, Jun 1989. [Online]. Available: https://link.aps.org/doi/10.1103/PhysRevB.39.11538

[51] G. Baskaran and P. W. Anderson, "Gauge theory of high-temperature superconductors and strongly correlated fermi systems," *Phys. Rev. B*, vol. 37, pp. 580–583, Jan 1988. [Online]. Available: https://link.aps.org/doi/10.1103/PhysRevB.37.580

[52] E. Dagotto, E. Fradkin, and A. Moreo, "Su(2) gauge invariance and order parameters in strongly coupled electronic systems," *Phys. Rev. B*, vol. 38, pp. 2926–2929, Aug 1988. [Online]. Available: https://link.aps.org/doi/10.1103/PhysRevB.38.2926

[53] X.-G. Wen and P. A. Lee, "Theory of underdoped cuprates," *Phys. Rev. Lett.*, vol. 76, pp. 503–506, Jan 1996. [Online]. Available: https://link.aps.org/doi/10.1103/PhysRevLett.76.503

[54] T. Senthil and M. P. A. Fisher, "Z_2 gauge theory of electron fractionalization in strongly correlated systems," *Phys. Rev. B*, vol. 62, pp. 7850–7881, Sep 2000. [Online]. Available: https://link.aps.org/doi/10.1103/PhysRevB.62.7850

[55] M. C. Gutzwiller, "Effect of correlation on the ferromagnetism of transition metals," *Phys. Rev. Lett.*, vol. 10, pp. 159–162, Mar 1963. [Online]. Available: https://link.aps.org/doi/10.1103/PhysRevLett.10.159

[56] P. Horsch and T. A. Kaplan, "Exact and monte carlo studies of gutzwiller's state for the localised-electron limit in one dimension," *Journal of Physics C: Solid State Physics*, vol. 16, no. 35, p. L1203, dec 1983. [Online]. Available: https://dx.doi.org/10.1088/0022-3719/16/35/002

[57] C. Gros, R. Joynt, and T. M. Rice, "Antiferromagnetic correlations in almost-localized fermi liquids," *Phys. Rev. B*, vol. 36, pp. 381–393, Jul 1987. [Online]. Available: https://link.aps.org/doi/10.1103/PhysRevB.36.381

[58] Y. Ran, M. Hermele, P. A. Lee, and X.-G. Wen, "Projected-Wave-Function Study of the Spin-1/2 Heisenberg Model on the Kagomé Lattice," *Phys. Rev. Lett.*, vol. 98, p. 117205, Mar 2007. [Online]. Available: https://link.aps.org/doi/10.1103/PhysRevLett.98.117205

[59] M. Lajkó and K. Penc, "Tetramerization in a su(4) heisenberg model on the honeycomb lattice," *Phys. Rev. B*, vol. 87, p. 224428, Jun 2013. [Online]. Available: https://link.aps.org/doi/10.1103/PhysRevB.87.224428

[60] D. Jakab, E. Szirmai, M. Lewenstein, and G. Szirmai, "Competing valence bond and symmetry-breaking mott states of spin-$\frac{3}{2}$ fermions on a honeycomb lattice," *Phys. Rev. B*, vol. 93, p. 064434, Feb 2016. [Online]. Available: https://link.aps.org/doi/10.1103/PhysRevB.93.064434

[61] W. M. H. Natori, R. Nutakki, R. G. Pereira, and E. C. Andrade, "SU(4) Heisenberg model on the honeycomb lattice with exchange-frustrated perturbations: Implications for twistronics and mott insulators," *Phys. Rev. B*, vol. 100, p. 205131, Nov 2019. [Online]. Available: https://link.aps.org/doi/10.1103/PhysRevB.100.205131

[62] X.-P. Yao, R. L. Luo, and G. Chen, "Intertwining su(n) symmetry and frustration on a honeycomb lattice," *Phys. Rev. B*, vol. 105, p. 024401, Jan 2022. [Online]. Available: https://link.aps.org/doi/10.1103/PhysRevB.105.024401

[63] H.-K. Jin, W. M. H. Natori, and J. Knolle, "Twisting the Dirac cones of the SU(4) spin-orbital liquid on the honeycomb lattice," *Phys. Rev. B*, vol. 107, p. L180401, May 2023. [Online]. Available: https://link.aps.org/doi/10.1103/PhysRevB.107.L180401

[64] M. G. Yamada and S. Fujimoto, "Thermodynamic signature of SU(4) spin-orbital liquid and symmetry fractionalization from Lieb-Schultz-Mattis theorem," *Phys. Rev. B*, vol. 105, p. L201115, May 2022. [Online]. Available: https://link.aps.org/doi/10.1103/PhysRevB.105.L201115

[65] M. Yamada, private communication.

[66] D. L. Bergman, C. Wu, and L. Balents, "Band touching from real-space topology in frustrated hopping models," *Phys. Rev. B*, vol. 78, p. 125104, Sep 2008. [Online]. Available: https://link.aps.org/doi/10.1103/PhysRevB.78.125104

[67] J. K. Jain, "Theory of the fractional quantum Hall effect," *Phys. Rev. B*, vol. 41, pp. 7653–7665, Apr 1990. [Online]. Available: https://link.aps.org/doi/10.1103/PhysRevB.41.7653

[68] X. G. Wen, "Non-Abelian statistics in the fractional quantum Hall states," *Phys. Rev. Lett.*, vol. 66, pp. 802–805, Feb 1991. [Online]. Available: https://link.aps.org/doi/10.1103/PhysRevLett.66.802

[69] X.-G. Wen, "Projective construction of non-Abelian quantum Hall liquids," *Phys. Rev. B*, vol. 60, pp. 8827–8838, Sep 1999. [Online]. Available: https://link.aps.org/doi/10.1103/PhysRevB.60.8827

[70] Y.-M. Lu and Y. Ran, "$\mathbb{Z}_2$ spin liquid and chiral antiferromagnetic phase in the hubbard model on a honeycomb lattice," *Phys. Rev. B*, vol. 84, p. 024420, Jul 2011. [Online]. Available: https://link.aps.org/doi/10.1103/PhysRevB.84.024420

[71] Y.-M. Lu, Y. Ran, and P. A. Lee, "$\mathbb{Z}_2$ spin liquids in the $s = \frac{1}{2}$ heisenberg model on the kagome lattice: A projective symmetry-group study of schwinger fermion mean-field states," *Phys. Rev. B*, vol. 83, p. 224413, Jun 2011. [Online]. Available: https://link.aps.org/doi/10.1103/PhysRevB.83.224413

[72] T. Appelquist, D. Nash, and L. C. R. Wijewardhana, "Critical behavior in (2+1)-dimensional qed," *Phys. Rev. Lett.*, vol. 60, pp. 2575–2578, Jun 1988. [Online]. Available: https://link.aps.org/doi/10.1103/PhysRevLett.60.2575

[73] D. Nash, "Higher-order corrections in (2+1)-dimensional qed," *Phys. Rev. Lett.*, vol. 62, pp. 3024–3026, Jun 1989. [Online]. Available: https://link.aps.org/doi/10.1103/PhysRevLett.62.3024

[74] T. Appelquist and D. Nash, "Critical behavior in (2+1)-dimensional qcd," *Phys. Rev. Lett.*, vol. 64, pp. 721–724, Feb 1990. [Online]. Available: https://link.aps.org/doi/10.1103/PhysRevLett.64.721

[75] X.-Y. Song, C. Wang, A. Vishwanath, and Y.-C. He, "Unifying description of competing orders in two-dimensional quantum magnets," *Nature Communications*, vol. 10, no. 1, p. 4254, 2019. [Online]. Available: https://doi.org/10.1038/s41467-019-11727-3

[76] S. Sachdev, *Quantum Phase Transitions*, 2nd ed. Cambridge University Press, 2011.

[77] P. W. Leung and V. Elser, "Numerical studies of a 36-site kagome´ antiferromagnet," *Phys. Rev. B*, vol. 47, pp. 5459–5462, Mar 1993. [Online]. Available: https://link.aps.org/doi/10.1103/PhysRevB.47.5459

[78] M. B. Hastings, "Dirac structure, rvb, and goldstone modes in the kagomé antiferromagnet," *Phys. Rev. B*, vol. 63, p. 014413, Dec 2000. [Online]. Available: https://link.aps.org/doi/10.1103/PhysRevB.63.014413

[79] M. Hermele, Y. Ran, P. A. Lee, and X.-G. Wen, "Properties of an algebraic spin liquid on the kagome lattice," *Phys. Rev. B*, vol. 77, p. 224413, Jun 2008. [Online]. Available: https://link.aps.org/doi/10.1103/PhysRevB.77.224413

[80] U. F. P. Seifert, J. Willsher, M. Drescher, F. Pollmann, and J. Knolle, "Spin-Peierls instability of the U(1) Dirac spin liquid," *Nature Communications*, vol. 15, no. 1, p. 7110, Dec. 2024. [Online]. Available: https://doi.org/10.1038/s41467-024-51367-w

[81] K. Matan, T. Ono, Y. Fukumoto, T. J. Sato, J. Yamaura, M. Yano, K. Morita, and H. Tanaka, "Pinwheel valence-bond solid and triplet excitations in the two-dimensional deformed kagome lattice," *Nature Physics*, vol. 6, no. 11, pp. 865–869, 2010. [Online]. Available: https://doi.org/10.1038/nphys1761

[82] D. P. Arovas, "Simplex solid states of SU(n) quantum antiferromagnets," *Phys. Rev. B*, vol. 77, p. 104404, Mar 2008. [Online]. Available: https://link.aps.org/doi/10.1103/PhysRevB.77.104404

[83] P. Corboz, K. Penc, F. Mila, and A. M. Läuchli, "Simplex solids in su(n) heisenberg models on the kagome and checkerboard lattices," *Phys. Rev. B*, vol. 86, p. 041106, Jul 2012. [Online]. Available: https://link.aps.org/doi/10.1103/PhysRevB.86.041106

[84] H. T. Diep, *Frustrated Spin Systems*, 3rd ed. WORLD SCIENTIFIC, 2020. [Online]. Available: https://www.worldscientific.com/doi/abs/10.1142/11660

[85] S. Hoinka, M. Lingham, M. Delehaye, and C. J. Vale, "Dynamic Spin Response of a Strongly Interacting Fermi Gas," *Phys. Rev. Lett.*, vol. 109, p. 050403, Aug 2012. [Online]. Available: https://link.aps.org/doi/10.1103/PhysRevLett.109.050403

[86] R. Senaratne, D. Cavazos-Cavazos, S. Wang, F. He, Y.-T. Chang, A. Kafle, H. Pu, X.-W. Guan, and R. G. Hulet, "Spin-charge separation in a one-dimensional fermi gas with tunable interactions," *Science*, vol. 376, no. 6599, pp. 1305–1308, 2022. [Online]. Available: https://www.science.org/doi/abs/10.1126/science.abn1719

[87] P. T. Ernst, S. Götze, J. S. Krauser, K. Pyka, D.-S. Lühmann, D. Pfannkuche, and K. Sengstock, "Probing superfluids in optical lattices by momentum-resolved Bragg spectroscopy," *Nature Physics*, vol. 6, no. 1, pp. 56–61, Jan. 2010. [Online]. Available: https://doi.org/10.1038/nphys1476

[88] T. Li and F. Yang, "Variational study of the neutron resonance mode in the cuprate superconductors," *Phys. Rev. B*, vol. 81, p. 214509, Jun 2010. [Online]. Available: https://link.aps.org/doi/10.1103/PhysRevB.81.214509

[89] F. Yang and T. Li, "Theory of the quasiparticle excitation in high-T_c cuprates: Quasiparticle charge and nodal-antinodal dichotomy," , vol. 83, no. 6, p. 064524, Feb. 2011. [Online]. Available: https://doi.org/10.1103/PhysRevB.83.064524

[90] B. Dalla Piazza, M. Mourigal, N. B. Christensen, G. J. Nilsen, P. Tregenna-Piggott, T. G. Perring, M. Enderle, D. F. McMorrow, D. A. Ivanov, and H. M. Rønnow, "Fractional excitations in the square-lattice quantum antiferromagnet," *Nature Physics*, vol. 11, no. 1, pp. 62–68, Jan. 2015. [Online]. Available: https://doi.org/10.1038/nphys3172

[91] F. Ferrari, A. Parola, S. Sorella, and F. Becca, "Dynamical structure factor of the $J_1 - J_2$ Heisenberg model in one dimension: The variational Monte Carlo approach," *Phys. Rev. B*, vol. 97, p. 235103, Jun 2018. [Online]. Available: https://link.aps.org/doi/10.1103/PhysRevB.97.235103

[92] F. Ferrari and F. Becca, "Dynamical Structure Factor of the J_1–J_2 Heisenberg Model on the Triangular Lattice: Magnons, Spinons, and Gauge Fields," *Physical Review X*, vol. 9, no. 3, p. 031026, Jul. 2019. [Online]. Available: https://doi.org/10.1103/PhysRevX.9.031026

[93] F. Ferrari and F. Becca, "Spectral signatures of fractionalization in the frustrated heisenberg model on the square lattice," *Phys. Rev. B*, vol. 98, p. 100405, Sep 2018. [Online]. Available: https://link.aps.org/doi/10.1103/PhysRevB.98.100405

[94] V. G. Knizhnik and A. B. Zamolodchikov, "Current algebra and Wess-Zumino model in two dimensions," *Nuclear Physics B*, vol. 247, no. 1, pp. 83–103, Dec. 1984. [Online]. Available: https://doi.org/10.1016/0550-3213(84)90374-2

[95] J. Dufour, P. Nataf, and F. Mila, "Variational Monte Carlo investigation of SU (N) Heisenberg chains," , vol. 91, no. 17, p. 174427, May 2015. [Online]. Available: https://doi.org/10.1103/PhysRevB.91.174427

[96] E. R. Gagliano and C. A. Balseiro, "Dynamical properties of quantum many-body systems at zero temperature," , vol. 59, no. 26, pp. 2999–3002, Dec. 1987. [Online]. Available: https://doi.org/10.1103/PhysRevLett.59.2999

[97] M. Binder and T. Barthel, "Low-energy physics of isotropic spin-1 chains in the critical and Haldane phases," , vol. 102, no. 1, p. 014447, Jul. 2020. [Online]. Available: https://doi.org/10.1103/PhysRevB.102.014447

[98] B. Sutherland, "Model for a multicomponent quantum system," , vol. 12, no. 9, pp. 3795–3805, Nov. 1975. [Online]. Available: https://doi.org/10.1103/PhysRevB.12.3795

[99] W. Yu and S. Haas, "Dynamical properties of spin-orbital chains in a magnetic field," *Phys. Rev. B*, vol. 63, p. 024423, Dec 2000. [Online]. Available: https://link.aps.org/doi/10.1103/PhysRevB.63.024423

[100] J. L. Cardy, "Conformal invariance and universality in finite-size scaling," *Journal of Physics A Mathematical General*, vol. 17, no. 7, pp. L385–L387, May 1984. [Online]. Available: https://doi.org/10.1088/0305-4470/17/7/003

[101] H. W. J. Blöte, J. L. Cardy, and M. P. Nightingale, "Conformal invariance, the central charge, and universal finite-size amplitudes at criticality," , vol. 56, no. 7, pp. 742–745, Feb. 1986. [Online]. Available: https://doi.org/10.1103/PhysRevLett.56.742

[102] I. Affleck, "Universal term in the free energy at a critical point and the conformal anomaly," , vol. 56, no. 7, pp. 746–748, Feb. 1986. [Online]. Available: https://doi.org/10.1103/PhysRevLett.56.746

[103] F. Ferrari and F. Becca, "Spectral signatures of fractionalization in the frustrated heisenberg model on the square lattice," *Phys. Rev. B*, vol. 98, p. 100405, Sep 2018. [Online]. Available: https://link.aps.org/doi/10.1103/PhysRevB.98.100405

[104] F. Ferrari and F. Becca, "Dynamical properties of Néel and valence-bond phases in the J_1-J_2 model on the honeycomb lattice," *Journal of Physics Condensed Matter*, vol. 32, no. 27, p. 274003, Jun. 2020. [Online]. Available: https://doi.org/10.1088/1361-648X/ab7f6e

[105] D. Kiese, F. Ferrari, N. Astrakhantsev, N. Niggemann, P. Ghosh, T. Müller, R. Thomale, T. Neupert, J. Reuther, M. J. P. Gingras, S. Trebst, and Y. Iqbal, "Pinch-points to half-moons and up in the stars: The kagome skymap," *Phys. Rev. Res.*, vol. 5, p. L012025, Feb 2023. [Online]. Available: https://link.aps.org/doi/10.1103/PhysRevResearch.5.L012025

[106] W. Rantner and X.-G. Wen, "Spin correlations in the algebraic spin liquid: Implications for high-T_c superconductors," *Phys. Rev. B*, vol. 66, p. 144501, Oct 2002. [Online]. Available: https://link.aps.org/doi/10.1103/PhysRevB.66.144501

[107] A. Zee, *Group Theory in a Nutshell for Physicists*. Princeton University Press, 41 William Street, Princeton, New Jersey 08540: Princeton University Press, 2016.

[108] R. Cutler and D. Sivers, "Quantum-chromodynamic gluon contributions to large-p_T reactions," *Phys. Rev. D*, vol. 17, pp. 196–211, Jan 1978. [Online]. Available: https://link.aps.org/doi/10.1103/PhysRevD.17.196

[109] H. F. Jones, *Groups, Representations and Physics*, 2nd ed. Institute of Physics Publishing, Dirac House, Temple Back, Bristol BSI 6BE, UK: IOP Publishing, 1990.

[110] N. Metropolis, A. W. Rosenbluth, M. N. Rosenbluth, A. H. Teller, and E. Teller, "Equation of State Calculations by Fast Computing Machines," *The Journal of Chemical Physics*, vol. 21, no. 6, pp. 1087–1092, 06 1953. [Online]. Available: https://doi.org/10.1063/1.1699114

[111] J. Sherman and W. J. Morrison, "Adjustment of an inverse matrix corresponding to changes in the elements of a given column or a given row of the original matrix," *Annals of Mathematical Statistics*, vol. 20, no. 4, p. Abstract 161, 1949. [Online]. Available: https://projecteuclid.org/journals/annals-of-mathematical-statistics/volume-20/issue-4/Abstracts-of-Papers/10.1214/aoms/1177729959.full

[112] Sherman, Jack and Morrison, Winifred J., "Adjustment of an inverse matrix corresponding to a change in one element of a given matrix," *Annals of Mathematical Statistics*, vol. 21, no. 1, pp. 124–127, 1950. [Online]. Available: https://projecteuclid.org/journals/annals-of-mathematical-statistics/volume-21/issue-1/Adjustment-of-an-Inverse-Matrix-Corresponding-to-a-Change-in/10.1214/aoms/1177729893.full

[113] J.-W. Mei and X.-G. Wen, "Fractionalized spin-wave continuum in spin liquid states on the kagome lattice," *arXiv e-prints*, p. arXiv:1507.03007, Jul. 2015. [Online]. Available: https://arxiv.org/abs/1507.03007